UNIVERSITÀ DI PARMA

UNIVERSITA' DEGLI STUDI DI PARMA

DOTTORATO DI RICERCA IN

"INGEGNERIA INDUSTRIALE"

CICLO XXXIV

DESIGN OF ENGINEERED SURFACE FOR PERFORMANCE IMPROVEMENTS OF HYDRAULIC PUMPS

Coordinatore:
Chiar.mo Prof. GIANNI ROYER CARFAGNI

Tutore:
Chiar.mo Prof. PAOLO CASOLI

Dottorando: FABIO SCOLARI

Anni Accademici 2018/2019 – 2020/2021

Table of contents

List of symbols

Symbol	Description	Unit
p	Pressure	[Pa]
V	Volume	[m^3]
T	Temperature	[K]
β	Isothermal compressibility module	[bar]
γ	isobaric cubic expandability	[K^{-1}]
m	Mass	[kg]
ρ	Density	[kg/m3]
τ	Shear stress	[Pa]
μ	Dynamic viscosity	[Pa s]
v	Velocity	[m/s]
v	Cinematic viscosity	[mm^2/s]
h	Gap height	[m]
U	Velocity	[m/s]
L	Length	[m]
α	Bunsen coefficient	[-]
σ	Normal stress	[Pa]
R	Bubble radius	[m]
r	Radial distance	[m]

N	Bubbles per unit volume	[-]
$\dot{m}$	Mass flow rate	[kg/s]
F	Proportional coefficient	[-]
R_{nuc}	Volume fraction of the nucleation sites	[-]
f	Mass fraction	[-]
H	Henry's constant	
M	Molar mass	[kg/mol]
x	Gas volume fraction	[-]
B	Compressibility module	[Pa]
θ	Fraction of free air	[-]
φ	Vapor to liquid mass fraction	[-]
R_G	Universal gas constant	J/mol K
c_{id}	Ideal fluid velocity	[m/s]
c_{sound}	Sound speed	[m/s]
Ω	Area	[m^2]
t	Time	[s]
i	Measurement uncertainty	
η	Efficiency	[-]

Abstract

The main target of this research activity is the development of techniques for increasing the performance of external gear pumps.

Gear pumps are fixed displacement machines widely used in fluid power systems since they have low cost and high reliability. Some components are very critical to be designed, such as the lateral plates, on whose characteristics the efficiency of the entire pump depends.

This research activity focuses on increasing the hydrodynamic bearing capacity in the meatus between gear wheels and lateral plates by means of engineered surfaces, in order to reduce the wear of the components and increase the useful life of the machine.

The analysis of the fluid meatus was carried out by means of CFD analysis. Numerical simulations made it possible to evaluate the effect that the creation of a textured surface on the lateral plates has in increasing the hydrodynamic bearing capacity of the lubricated coupling.

Great attention has been paid to the study of cavitation phenomenon, with the implementation of a cavitation model within the CFD code that allows to simulate both gaseous and vaporous cavitation. The model was validated through experimental activity on the flow through an orifice placed in a hydraulic circuit.

Numerical simulations made it possible to identify the best geometric characteristics on which to concentrate a wide experimental activity. The samples of the lateral plates have been made by laser marking and the geometric characteristics were verified by means of an optical profilometer. Subsequently, bench tests have been conducted to obtain the efficiency values of pumps with textured lateral plates, to be compared with those of standard pumps. The experimental activity required the definition of a running-in cycle and a specific test cycle; special components made particularly for this research activity have been also used, in order to obtain reliable results, but with test times compatible with those of the university laboratory, also considering the high number of samples tested.

The results obtained are very promising showing that pumps with textured components inside perform better than the standard and create the basis for future developments.

Chapter 1. Introduction

This chapter introduces the topic of fluid power technology and illustrates the background and the motivation behind the research presented in this Ph.D. Thesis. This introductory chapter details the contributions of this research activity to the applications of engineered surfaces to increase the performance of mechanical components and the numerical modeling techniques for their study.

1.1 Background and Motivation

Fluid power systems are widely used in many range of applications, stationary and mobile, including the sector of construction and agricultural, where is necessary to handle large quantities of material. Generally, the fluid power is used for both machine propulsion and as a working fluid. Hydraulic systems have many important advantages that make them preferable to other power transmission systems, such as mechanical and electrical ones. Hydraulic systems have high power density, the possibility of separating the fluid power generation unit and connecting it to the users thanks to the simplicity of energy distribution through flexible pipes. Moreover, they permit to have high controllability of movements of the users with also high reliability.

Most of the fixed displacement machines used to generate flow in hydraulic systems are gear pumps, since they have high reliability and low cost due to the reduced number of components. Although they are conceptually simple machines and made up of a limited number of components, the design is often difficult, especially to obtain high performance. The most critical components to be designed are the lateral plates, on whose characteristics the efficiency of the entire pump depends.

This work of Thesis fits precisely in the perspective of pump performance. During the working life of an external gear pump, very severe conditions could occur which tend to reduce the performance of the machine, due to greater wear of the internal components, mainly the lateral plates. The purpose of the research presented in this Thesis is to investigate and propose solutions for improving the performance of external gear pumps.

The lateral plates modification has been investigated by introducing texturized surfaces, in order to increase the tribological properties inside the machine. Starting from a careful bibliographic analysis of the scientific literature, the problem has been studied by means of CFD tools to evaluate which are the best characteristics of the textured surface to obtain the greatest benefits.

1.2 Original Contributions

This section summarizes the primarily contribution of this Thesis in the field of improving the efficiency of a hydraulic gear pump.

- Application of textured surfaces to components of hydraulic machines.
- Detailed analysis of the influence of engineered surfaces within a fluid meatus and study of the effect of the texture characteristics on the bearing capacity.
- Modelling of the phenomenon of cavitation and implementation of a complete cavitation model within a CFD software.

1.3 Dissertation Organization

After the introduction given in this chapter, a review of the state of the art about gear pumps, hydraulic fluids properties, information on tribology and applications of engineered surfaces are reported in Chapter 2.

Chapter 3 presents the first numerical results regarding the influence of a texturized surface on the pressure field within the calculation domain and the discussion about the obtainable bearing capacity.

Chapter 4 offers a comprehensive description of the cavitation phenomenon: starting from the information present in the scientific literature, the modeling techniques of both gaseous and vaporous cavitation applied to textured surfaces are shown, the results of which are also presented in Chapter 5. Furthermore, a lumped parameter model has been developed and described.

Chapter 6 concerns the experimental activity. After a brief description of the laser technology, the samples made and their measurement by means of an optical profilometer are shown. The wide experimental campaign conducted in order to verify the performance of the pumps with textured components inside is described and discussed in detail.

Then a summary and a final discussion about the proposed solutions presented in this Thesis are given.

Chapter 2. State of the art

In this chapter a review of the state of the art concerning gear pumps, the main target of this Thesis, is reported. Details are also provided on the properties of hydraulic fluids and their dependence on the main variables of a hydraulic system, such as pressure and temperature.

Furthermore, information is provided about the branch of engineering that deals with tribology, as well as a classification and description of the different wear processes in mechanical components, with particular attention to the importance that lubricated contacts have in reducing and limiting the degradation of mechanisms. Finally, the textured surfaces are analysed: in recent years, many researchers have studied the engineered surface benefits in various fields of application, including the food sector, that of glued joints and also the improvement of lubricated contacts, allowing to enhance the tribological properties of the coupling.

2.1 Gear pumps

Most of the fixed displacement machines used to generate flow in hydraulic systems are gear pumps, as they have a high reliability and a low cost thanks to the reduced number of components. These benefits have allowed the spread of this type of machine to many fields of application. Usually, gear pumps are used for simple applications, especially in mobile hydraulics [2.1]. In the automotive field, for example, they are used as lubrication pumps for internal combustion engines [2.2] and as fuel pumps [2.3]. Recently, gear pumps could be used as variable displacement electric units, as the costs of variable speed motors are decreasing [2.4, 2.5] and this should allow for even greater diffusion.

This type of machine could be divided into pumps with external gears or internal gears. The first consists of two external toothed rotors, the second is composed of an internally toothed ring driven by an external gear wheel. Moreover, internal gear pumps are classified as gerotors, if there is a difference in the number of gear teeth, or as crescent pumps, so called due to the presence of a fixed sealing element with a half-moon shape.

In this Thesis work, the attention has been paid to external gear pumps with spur gear. The Figure 2.1a shows a sectional image of an external gear pump, while the Figure 2.1b schematically displays the working. In this type of machine, the driving wheel and the driven gear rotate in opposite directions. It is a volumetric machine that allows to transfer the fluid from a low pressure environment to a high one. The fluid is carried in the volume between two adjacent teeth along the periphery of the two wheels: the meshing between the two wheels and the small radial gap between the wheels and the stator case allow to separate the low and high pressure regions.

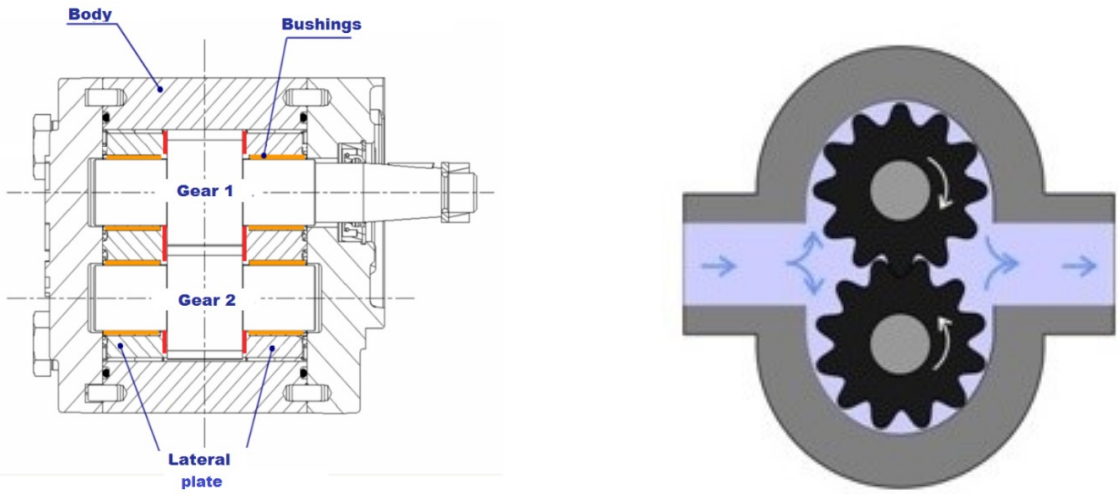

(a) (b)

Figure 2.1. (a) Sectional view of an external gear pump. (b) Image of the working of an external gear pump.

The lateral plate are two fundamental elements for obtaining good performance from the machine. They are axial compensation plates mounted with a small clearance with respect to the case in order to allow small axial movements. On the side facing the gears, Figure 2.2a, there are two grooves with the purpose of avoiding that there is fluid trapped in the meshing area: a fine design of the grooves is essential for a good efficiency of the machine; the detailed discussion could be found in [2.6, 2.7]. On the back, however, Figure 2.2b, a seal delimits two areas: one at high pressure and one at low pressure connected to the inlet and delivery by means of grooves made on the lateral plates. The position of equilibrium of the lateral plate is given by the balance of the forces acting on it. The correct sizing of the balancing areas on the lateral plates allows to have minimum gap heights in order to reduce losses due to leakage, and therefore to obtain high volumetric efficiency, and at the same time to prevent the lateral plates from coming into direct contact with the gear wheels [2.6], minimizing the shear stress and avoiding wear of the elements. There are also circumferential grooves, called back flow grooves, which regulate the pressurization of the chamber during rotation: they are used to control the radial forces acting on the gear wheels, both as direction and as module [2.8].

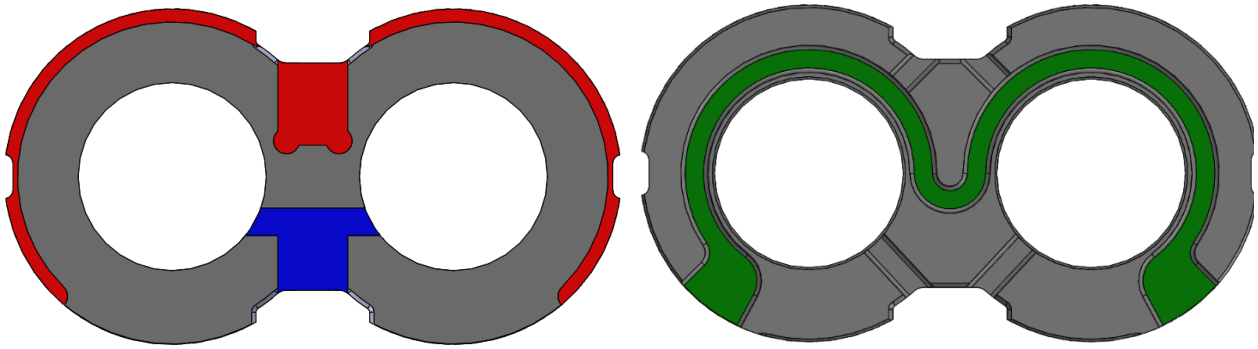

(a) (b)

Figure 2.2. Lateral plate of an external gear pump. (a) View from the gear wheels side: the low pressure area is highlighted in blue, while the high pressure is highlighted in red. (b) View of the back, highlighting the portion where the seal is inserted.

The forces acting on the lateral plates strongly depend on the operating conditions of the machine, and in the first place on the delivery pressure. Since there is a significant difference in pressure between delivery and suction, the lateral plates tend to be inclined more towards the low pressure area, reducing the height of the gap in the inlet zone. Furthermore, the discharge pressure is discontinuous because of the not continuous delivered flow rate, since a gear pump is a displacement machine. It follows that the lateral plates have an oscillatory motion around an equilibrium position, inclined towards low pressure.

To know the position assumed by the lateral plates during operation conditions, the detailed study of the axial balancing of the lateral plates is needed. In the scientific literature there are few works that present a detailed report of the dynamic evolution of the fluid gap that exists between the lateral plates and the gear wheels. Dhar et Al. [2.6], thanks to a numerical simulation tool, calculate the pressure distribution on the lateral plates including the hydrodynamic effects within the gap and the effects due to the squeeze, allowing to obtain the instant positions of the components. As confirmation, they actually obtained from simulation how the low pressure portion of the lateral plates is the one closest to the gear wheels, as shown in the Figure 2.3.

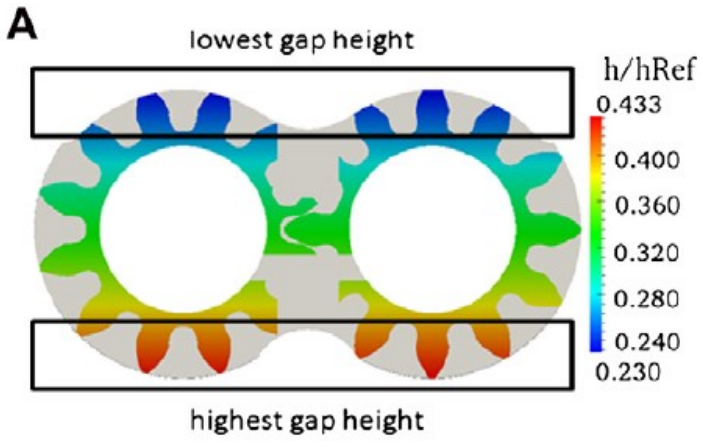

Figure 2.3. Height of the gap between wheels and lateral plates the value is dimensionless. The image is taken from Dhar et Al. [2.6].

Dhar et Al. [2.7] also conducted an accurate experimental analysis by inserting various non-contact position sensors into the covers of an external gear pump that permit to measure the mutual position between gears wheels and lateral plates during working. The Figure 2.4 shows the position of the different measurement points and a contour showing the dimensionless gap height obtained experimentally. This interesting experimental activity confirms what has been obtained numerically, i.e. that the low pressure zone is the one with the smallest gap height.

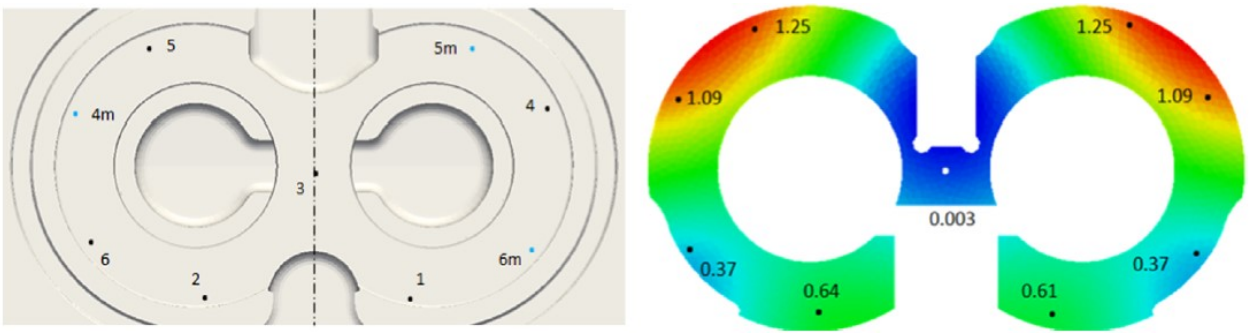

Figure 2.4. Position measurement points and dimensionless contour of the measured gap height. Image taken from Dhar et Al. [2.7].

2.2 Hydraulic fluid

The working fluid is the means for transferring the power of the prime mover to the users and therefore represents one of the main components of the hydraulic system.

The characteristic properties such as pressure p, volume V and temperature T are linked by an equation of state $V = V(p, T)$ that could be expressed at an equilibrium point, indicated by subscript 0 in Equation (2.1).

$$V = V_0 \cdot \left[1 + \frac{1}{V_0}\left(\frac{\partial V}{\partial p}\right)_T \cdot (p - p_0) + \frac{1}{V_0}\left(\frac{\partial V}{\partial T}\right)_p \cdot (T - T_0)\right] \tag{2.1}$$

By defining β the isothermal compressibility module, which expresses the pressure change following a volume change and γ the isobaric cubic expandability, which represents the volume change due to an increase in temperature, the equation of state could be expressed as:

$$V = V_0 \cdot \left[1 + \frac{1}{\beta} \cdot (p - p_0) + \gamma \cdot (T - T_0)\right] \tag{2.2}$$

Where:

$$k = -V_0\left(\frac{\partial V}{\partial p}\right)_T \tag{2.3}$$

And

$$\gamma = \frac{1}{V_0}\left(\frac{\partial V}{\partial T}\right)_p \tag{2.4}$$

The density of the fluid depends on both pressure and temperature. Considering a constant mass of fluid with density:

$$\rho_0 = \frac{m_0}{V_0} \tag{2.5}$$

It is possible to express the density as a function of the pressure or temperature variation, keeping the other variable constant. To evaluate the density as both variables change, it is sufficient to apply the superimposition of the effects.

Thus, two functions that represent the density could be obtained:

$$\rho_p = \frac{m_0}{V_0 + \Delta V|_T} = \frac{\rho_0}{1 - \frac{\Delta p|_p}{\beta}}$$
$$\rho_T = \frac{m_0}{V_0 + \Delta V|_p} = \frac{\rho_0}{1 + \gamma \cdot \Delta T} \tag{2.6}$$

The graphs in Figure 2.5 and in Figure 2.6 show the trends of the density as a function of the pressure or the temperature, also indicating the values of β and γ used.

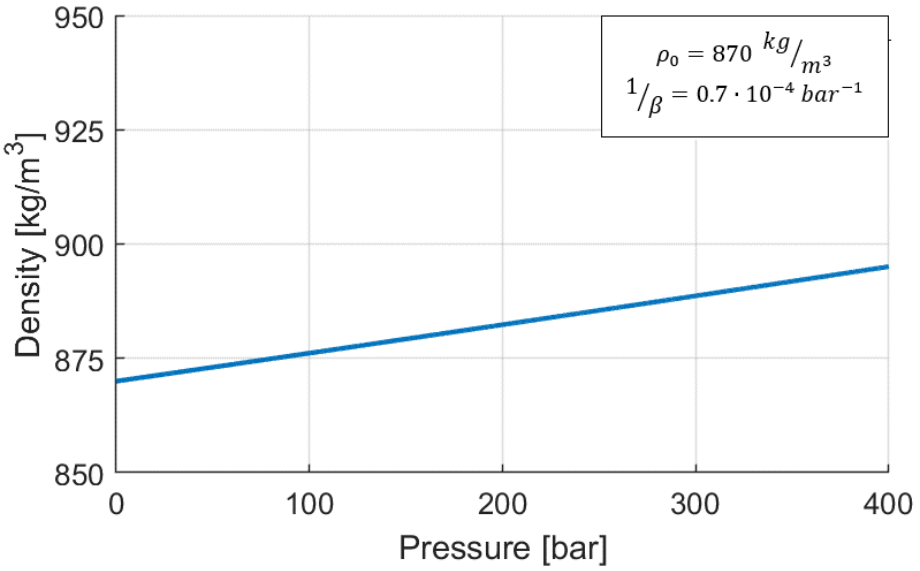

Figure 2.5. Density as a function of pressure.

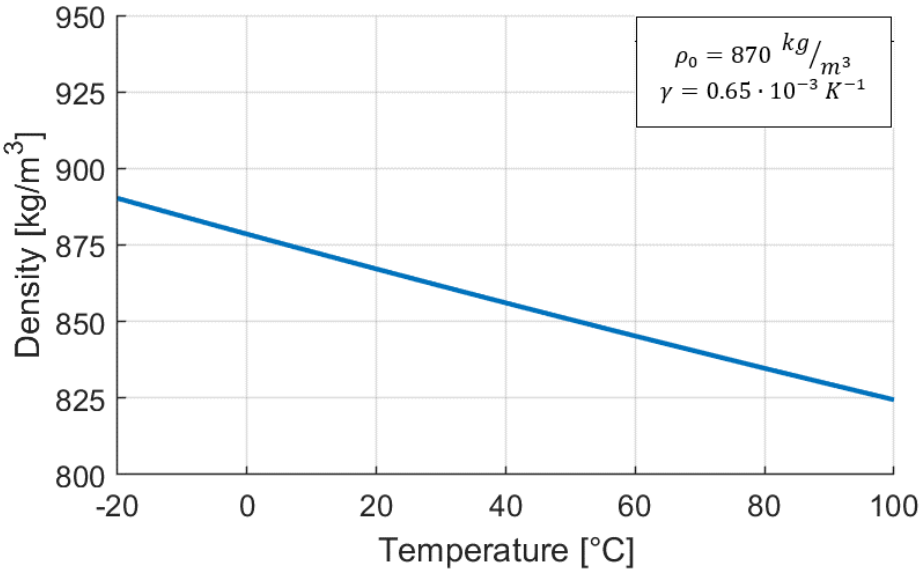

Figure 2.6. Density as a function of temperature.

2.3 Fluid viscosity

During the movement of a fluid, the particles that compose it slide over each other. However, this movement is limited by the presence of tangential stresses, parallel to the velocity of the fluid, which are characteristic of the fluid and constitute the so-called viscosity.

Considering a layer of fluid of height h on whose surface a flat plate moves at speed v_x, as shown in Figure 2.7: the plate for the adherence condition drags the fluid on the upper part, which in turn drags the fluid of the lower layers.

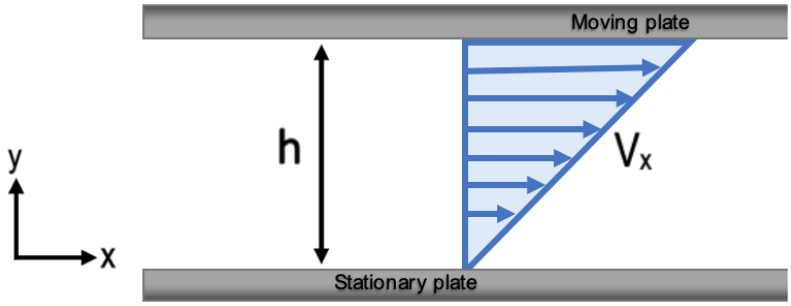

Figure 2.7. Flat surface moving on a fluid meatus with velocity v_x

In Newtonian fluids the tangential stress is given by:

$$\tau = \mu \cdot \frac{dv_x}{dy} \tag{2.7}$$

Where μ is the dynamic viscosity of the fluid.

The viscosity of mineral hydraulic oils decreases significantly with increasing temperature. The Ubbelhode-Walter relation is generally valid:

$$\log_{10} \log_{10}(v + a) = k - m \cdot \log_{10} T \tag{2.8}$$

Where v is the kinematic viscosity, k and m are constants of the fluid type and a is a universal constant that is 0.8. Usually, two viscosity values are given for a hydraulic oil, at 40 °C and at 100 °C from which it is possible to calculate the constants k and m. In scientific literature there are some variants of the Equation (2.8), reported in [2.11], developed to obtain a better agreement between numerical models and experimental results. Anyhow, the formulation (2.8) is useful for representing the dependence of viscosity on temperature on a dual-logarithm graph that appears linear, as shown in the Figure 2.8 for mineral oils of different viscosity grades. The viscosity grade in the ISO classification of hydraulic fluids indicates the viscosity of the oil at 40 °C with a margin of 10%.

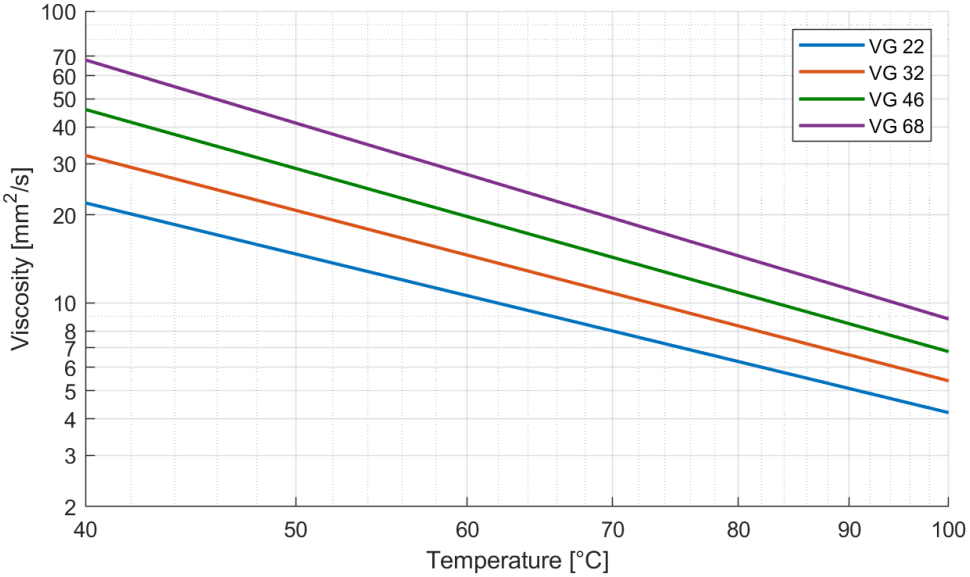

Figure 2.8. Double logarithmic diagram of viscosity as a function of temperature for hydraulic oils with different viscosity grades.

2.4 Tribology and wear

Tribology is a field of science that focuses on the study of friction phenomena, wear mechanisms and the lubrication of coupled surfaces in relative motion. It is a fairly recent branch of science defined in 1967 by a committee of the Organization for Economic Cooperation and Development and which became popular following strong industrial growth. “Tribology” comes from the greek word “tribos” (*Τρίβος*) which means rubbing or sliding. A more suitable definition could be referred to as the comprehensive study of the interaction between surfaces in relative motion, involving many fields, from physics and chemistry to mechanical engineering, including its technological impact.

At present, the knowledge is far from ensuring an exhaustive knowledge of the mechanisms of friction and wear, but many progresses have been made due to the numerous recently researches. Therefore, tribology is destined to be crucial for scientists today, mainly due to the significant impact on machinery that relies on sliding and rolling contacts.

Wear is the main source of material loss and reduction of mechanical performance in the industrial sector and therefore any reduction in wear could lead to significant savings, especially in terms of energy. One of the main causes of wear and energy dissipation is friction: it follows that better friction control allows for significant savings. Recent estimates have shown that a third of the world’s energy resources in use are required exclusively to overcome frictions. Lubrication is a useful tool to reduce friction and consequently limit wear. In fact, surfaces in relative motion, i.e. subject to sliding, rolling and normal approach or separation, are very crucial because they control the operation of practically every human-developed device. Everything man does wears out, almost always by relative motion between surfaces. The failure analysis of the machines shows that in most cases the failures and stops are due to the interacting between moving components like gears, cams, clutches, bearings, etc. Most of the problems considered are of a tribological nature.

A general finding derived from countless researches is that tribology includes the study of the films of material interposed between components in contact and the consequences of a collapsing, or the absence, of a lubricating film, which usually manifest themselves with strong friction and wear.

The practical aim of tribology is to reduce the main drawbacks of solid-to-solid contact: friction and wear. Actually, this depends a lot on the applications and is not always what it is wanted. For example, in brakes and clutches a reduction in wear is desirable but not in friction.

To enhance the smoothness of movement between the coupled surfaces and therefore to prevent damage, thin films of gas, liquid or solid with low shear strength are interposed between the two

surfaces. These films separate solid bodies avoiding direct contact and they are typically very thin. Usually, the thicknesses of the layers vary from 1 to 100 μm, even though thinner or thicker films could also be present in some applications. Lubrication is commonly known as the knowledge relating to the improvement or diagnosis of the effectiveness in preventing damage between coupled components. The type of material that forms the lubricating film determines the effectiveness of the lubrication, but there is no limitation on the type of material that could form a lubricating film, since gases, liquids and certain solids are all effective. The study of liquid or gaseous films is frequently referred to as “hydrodynamic lubrication”.

2.4.1 Wear

The breaking of the film leads to direct contact between the two coupled surfaces, with the consequence of inevitably causing severe damage to the contact surfaces and therefore compromising the relative movement between the components. Wear is defined as the process of removing material from a surface due to the interaction between the coupled surfaces, and it is the main reason for the loss of durability and reliability of almost all machines.

The traces of removed material, the shape and consistency of the debris produced, the surface roughness, provide information in the characterization of wear, which is generally quantified by evaluating the amount of volume lost and qualified by the state of the worn surface. The argument is very complex and so there is no complete and exhaustive theory that can predict all the different possibilities of wear. For this reason, the traditional approach with which the subject is dealt with is the classification of the many wear mechanisms, though they are not always differentiated, but are frequently interconnected.

The best classification is based on the classification of the deformation states, and therefore of the mechanics that govern the contact. Four main wear modes can be distinguished, following the classification proposed by Burwell [2.14], shown schematically in the Figure 2.9:

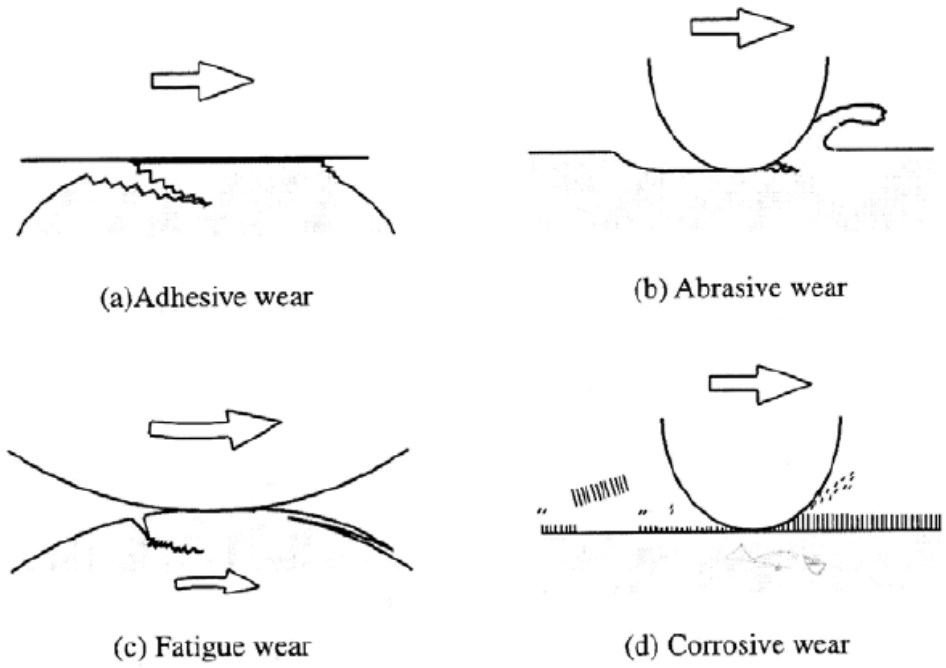

Figure 2.9. Different ways of wear. (a) Adhesive wear; (b) abrasive wear; (c) fatigue wear; (d) corrosive wear.

- Adhesive wear, Figure 2.9a: the failure of the lubricating film causes severe wear due to the adhesion between the two bodies in contact. It is generated by a contact characterized by an adhesion force sufficient to resist the relative sliding which produces a large plastic deformation caused by dislocation under compression at the inlet and shear at the outlet. Due to the deformation in the contact region, cracking phenomena are generated by mechanically induced stresses and deformations and then propagate in the combined tensile and shear fracture mode.
- Abrasive wear, Figure 2.9b: the contact takes place between materials of different hardness where the harder penetrates the softer one causing grooves. When the wear material is ductile, a long ribbon-shaped debris is generated; while in the case of brittle material, crack propagation produces wear particles. Therefore, in abrasive wear, the mechanical properties of the two coupled surfaces greatly influence the wear behavior.
- Fatigue wear, Figure 2.9c: generated by repeated friction cycles on both elastic and plastic contacts. In metals subjected to cyclic loads, surface and subsurface cracks could be generated, which after a critical number of cycles cause severe wear, with large debris leaving the surface.
- Corrosive wear, Figure 2.9d: unlike the previous cases, corrosive wear does not occur because of the mechanical interaction between coupled surfaces, but the removal of

material happens by the development of chemical reactions. Oxidation is the most representative example, and in this case it is also called oxidative wear.

There are two other forms of wear: erosive wear due to particle impact and cavitation wear caused by liquids that flow quickly.

2.5 Textured surfaces

Texturing a surface means introducing identical and repeated defined geometries, like dimples or grooves, in order to increase certain features, such as wettability, antibacterial properties, etc. and for this reason they are also called engineered surfaces. Figure 2.10 shows some examples of textured surfaces measured at microscope from the research of Gachot et Al. [2.15].

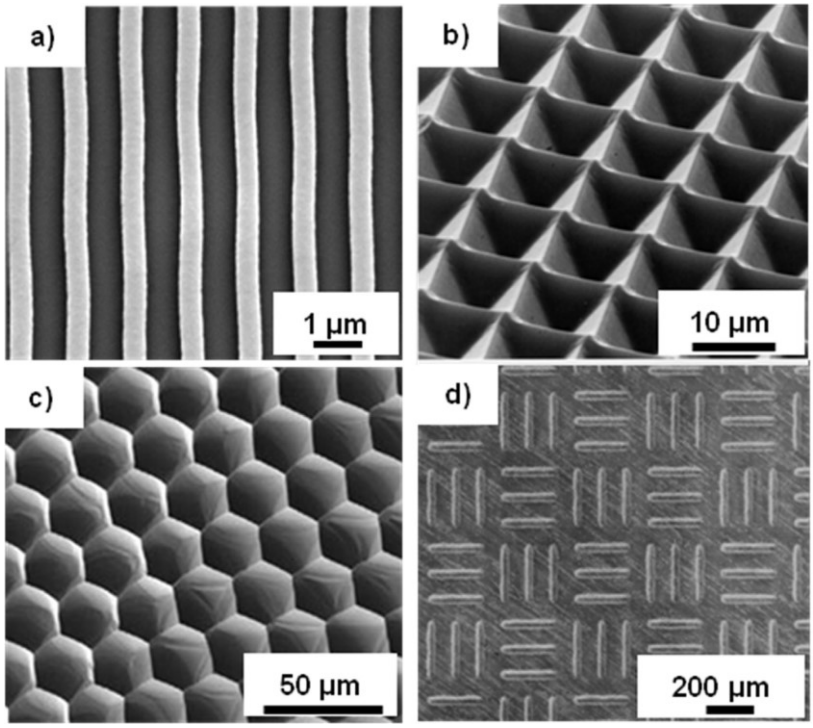

Figure 2.10. Various texture examples. (a) line patterns, (b) pyramidal texturing; (c) honeycomb patterns; (d) lines with different orientations. Images from Gachot et Al. [2.15]

Improving contact performance by means of textured surfaces is not a recent concept. There are examples in nature where special surface geometries permit to increase adhesion, allowing the tree frogs to walk on wet surfaces [2.16] or to reduce fluid dynamic resistance, making the movement of sharks in water more efficient [2.17]. Considering other applications, the surface of a golf ball has dimples that are intended to significantly reduce air resistance and allow to reach distances up to four times greater than a golf ball with a smooth surface [2.18].

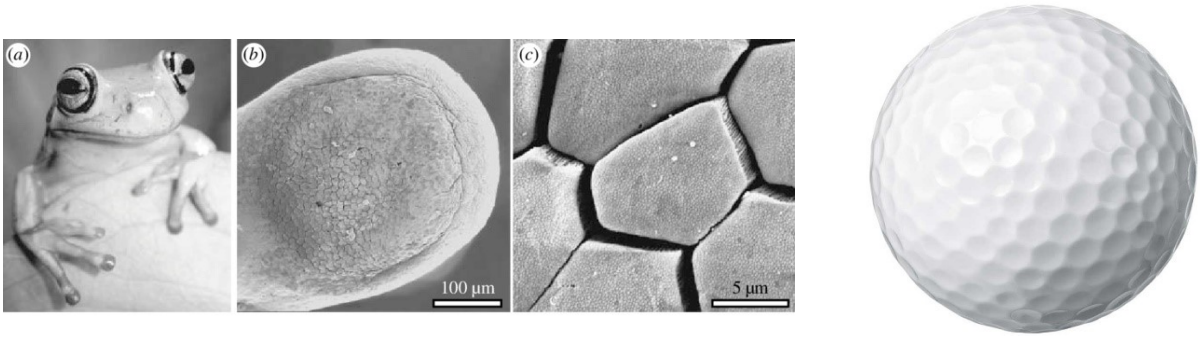

(a) (b)

Figure 2.11. (a) Morphology of tree frog toe pads and enlargement on epidermis with hexagonal epithelial cells. Image from Bhushan et Al. [2.16]; (b) Surface of a golf ball with hexagonal shaped dimples.

In recent years, laser technologies have had a strong diffusion, especially aimed at the creation of textured surfaces. Among the various fields of use, several researchers have studied the possibility that engineered surfaces have in increasing the adhesion force between two surfaces [2.19 - 2.21]. The sample on which an adhesive is placed is previously treated by laser marking: in this way, the surface on which the adhesive acts is greater and the results show an increase in the strength of adhesion compared to untreated samples. The choice of laser processing parameters is a critical factor in achieving the maximization of adhesive properties.

Another field of application is the creation by laser processing of antibacterial surfaces, very useful in the food industry, in order to obtain self-cleaning surfaces. The idea is to create an extremely fine texture on the component, with the dimensional order of a bacterium, on which the bacteria remain suspended, without being able to cling to the surface. In various scientific articles [2.22 - 2.25] several geometries of textures made on different materials are presented. The experimental activity shows how it is possible to reduce the presence of bacteria on treated surfaces, compared to traditional surfaces. Also in this case, a very carefully calibration of the laser parameters is needed in order to obtain the best possible performance.

Surface texturing could also influence the tribological properties of lubricated contacts. The surface structures could act as lubricant reservoirs [2.26], supplying lubricant upon contact in the event of a lack of lubrication and trap the particles produced by wear, minimizing abrasion. Furthermore, a textured surface has a lower overall contact surface due to the creation of the texture, which could lead to a reduction in friction, also due to a higher average height of the fluid meatus. These effects that occur simultaneously could reduce the overall wear of the components and therefore increase the life of the machine.

However, the predominant effect, the only studied using mathematical models, is the generation of an additional hydrodynamic force that could increase the bearing capacity of the coupling in cases of mixed and hydrodynamic lubrication.

The first studies in this regard date back to the mid-1960s, when Hamilton et Al. [2.26] found that the micro-irregularities on the surfaces of the rotating shaft seals are able to generate a hydrodynamic effect that creates a load capacity. The proposed explanation justifying the mechanism responsible for supporting the observed load was due to local cavitation phenomena. In fact, they were able to directly observe the establishment of cavitation in the divergent part of the asperities using a transparent rotor. Anno et Al. [2.27, 2.28] took up this theory by applying it to mechanical seals and parallel thrust bearings, concluding that the introduction of micro-roughness could be an effective solution to improve lubrication. A successful applications of surface texturing was that of the cylinder liners of combustion engines [2.29]. The grooves on the surface of the coating created by the sanding process can hold oil and block debris due to wear and therefore increase the component life.

After nearly 30 years, Etsion and his collaborators have published one of the new articles regarding surface texture [2.30]. They used the two-dimensional Reynolds equation for the case of incompressible fluid to numerically examine the textured mechanical seals by introducing hemispherical dimples on one of the coupling surfaces. The result was an increase in load capacity, justified by the onset of local cavitation; furthermore, they concluded that performance depended heavily on defining texture size and density. They also carried out experiments to compare the performance of non-textured versus textured seals and demonstrated that the texture might increase the life of the seal by three times [2.31]. These results have given a strong impetus to the study of applications of engineered surfaces in the industrial field.

A large range of applications has been investigated, such as various types of bearings, piston pins and drill bits.

In the various studies, promising results have generally been achieved, but finding the optimal texturing parameters is still very difficult, since many variables are involved and the equations governing the process are complex. Furthermore, the optimal design of the texture strongly depends on the type of contact and the working conditions in which it is used. For these reasons, in case the textures are designed incorrectly [2.32, 2.33], it is not uncommon to find that the textures could be harmful and with undesirable effects. The issues already mentioned have conducted to differing conclusions generating a lot of scepticism regarding the use of textured surfaces, making it still

difficult for a successful industrial diffusion. Many researchers have broadened the knowledge on engineering surface; but there are still very few examples of successful industrial applications and confirm the great difficulties still present.

The analysis of the scientific literature relating to applications involving textured surfaces, in recent years more refined numerical models have been developed for solving fluid dynamics problems, thanks also to the increase in computing power.

Many researchers have devoted themselves to the mainly numerical study of the influence that engineered surfaces have on the tribological properties of coupling. In [2.34] the effects on the distribution of pressure within the meatus due to the introduction of dimples of different geometry and orientation are analysed. In [2.35] the mechanical techniques to obtain the particular geometries of the dimples are studied, taking into consideration laser technologies, micro-casting or electrochemical machining. Other studies have numerically analysed, by applying the Reynolds equation, various configurations of textured surfaces, concluding that the engineered surfaces are able to increase the tribological performance [2.36 - 2.38], and in particular the reduction of tangential forces and friction coefficient [2.39]. Another article also included the local cavitation effects that may occur and the relationship with the fluid temperature variation [2.40]. Tahmani et Al. [2.41] carried out a numerical study in order to obtain the best geometric arrangement of a texture formed by square section dimples and the best geometric characteristics of the dimples. Among the results there is confirmation that it is possible to obtain improvements in the tribological properties of the coupling by optimizing the geometry of the dimples, also confirming what was obtained by previous researchers.

With regard to the experimental validation of the numerous numerical results, there are few articles in the scientific literature, mainly relating to the application of engineered surfaces to thrust bearings. Brizmer et Al. [2.42] studied numerically, using the Reynold equation, the influence of the various geometric parameters of the textured surface, such as the dimensions of the dimples and their depth, on the tribological performance of an axial thrust bearing formed by parallel plates. From the conclusion of the numerical study, it is possible that a series of regular micro dimples are able to provide a positive bearing capacity in this type of bearings. The experimental verification of this useful and interesting theoretical treatment is reported in another scientific work published by the same authors [2.43]. This research group therefore focused on an axial bearing, both unidirectional and bidirectional, formed by two parallel discs: one smooth and flat while the second was divided into six sectors, by means of radial grooves. On this last disc, a regular texturing was created by laser marking, which consists of a succession of hemispherical dimples. The experimental

campaign confirmed the possibility of surface texturing to increase the operating performance of a parallel thrust bearing, also finding good correlations with the theoretical model. The fluid meatus of the textured case increased in height by almost three times compared to the case without texture in all test conditions, with a consequent lower friction coefficient.

Despite the promising numerical results and the few experimental confirmations, possible applications of textured surfaces to improve the lubricated contacts inside hydraulic pumps are very scarce and recent. Chen et Al. [2.44] dealt with an axial piston pump for aeronautical use. For reasons of size and weight they must be compact units, but to guarantee the required capacity it is necessary that the rotation speed is high. These factors lead to severe wear of the components that also show signs of abrasion, burns up to even plastic deformation, with consequent loss of efficiency. A rectangular section prismatic dimples texture was then created on the retainer's bottom plate in order to increase its performance and durability. The results obtained showed that the volumetric and mechanical efficiencies increased up to 7.4% for high speeds. Deng et Al. [2.45] studied the effects produced by micro-wells made on another component of an axial piston pump, the port plate. This is heavily stressed and texturing could be adopted in order to increase the tribological performance of the component, reducing friction and wear. The conclusions reached by the researchers are in line with what has been observed in the other articles, confirming the potential of engineered surfaces. Similar results are found in [2.46, 2.47], where texturing is applied to internal components of axial piston pumps, such as the port plate or the tilting cylinder. Also in these cases, an exhaustive theoretical discussion and an experimental analysis show benefits from the point of view of machine performance and a lower degree of wear of the textured components compared to the standard ones.

A very interesting application of engineered surfaces is the texturing of the teeth of the gear wheels. This is a non-conforming and usually heavily loaded contact, in the range of several GPa, where between the gear tooth surfaces there are usually boundary or mixed lubrication conditions due to poor lubricant retention and the maximum film thickness is less than the peak-valley distance, with interactions between the roughnesses. Consequently, there is a need for techniques that could help effectively support a lubricating film between gears to improve lubrication conditions. The friction on the contacts of the sliding and rolling teeth is responsible for most of the losses in the gear pairs. Gupta et Al. [2.48] investigated the tribological performance of texturing on spur gear teeth. Unlike the other papers, the texturing has been produced by chemical processing and was localized on the face of the gear teeth, as shown in Figure 2.12.

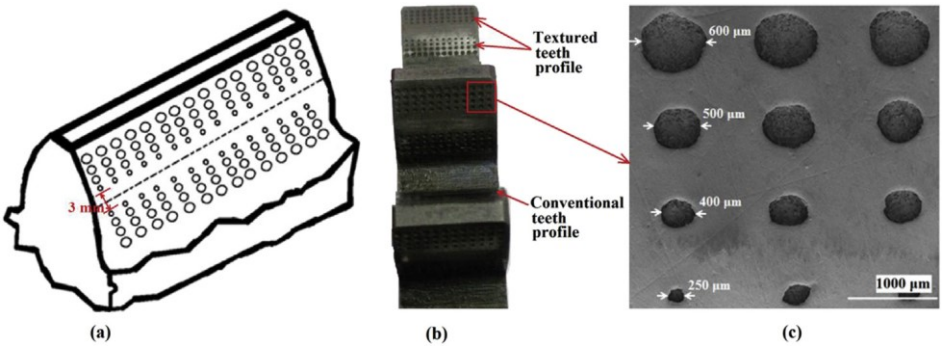

Figure 2.12. Textured teeth surface; (a) Schematic view, (b) Photographic view, (c) SEM image. Image from Gupta et Al. [2.48]

Dimple sizes vary, getting larger near the tip of the tooth, where the maximum scrolling. Tests on textured gears revealed less wear than non-textured samples and this could give new impetus to the application of textured surfaces. In fact, gears are not only used in power transmission, but are also used in volumetric hydraulic gear pumps, which are very common and widespread in many industrial fields, including earthmoving machinery, agricultural machinery and machinery for lifting and transport. These are all sectors that would benefit from an increase in the performance of the fluid power unit.

List of references

2.1 Ivantysyn J., Ivantysynova M. Hydrostatic Pumps and Motors, Principles, Designs, Performance, Modelling, Analysis, Control and Testing. Akademia Books International. New Delhi, India, 2002.

2.2 Rundo M., Nervegna N. Lubrication Pumps for Internal Combustion Engines: A Review. International Journal of Fluid Power. 2015. Doi: 10.1080/14399776.2015.1050935

2.3 Ruvalcaba M. A., Hu X. Gerotor fuel pump performance and leakage study. Proceedings of the ASME 2011 International Mechanical Engineering Congress & Exposition, Denver, USA. 2011. Doi: 10.1115/IMECE2011-62226

2.4 Malvasi A., Squarcini R., Armenio G., Brömmel A. Design process of an electric powered oil pump. Autotechreview. 2014. Doi: 10.1007/s38313-012-0236-0

2.5 Kim J. H., Kim S. G. The Flow Rate Characteristics of External Gear Pump for EHPS. Proceedings of the 4th International Conference on Intelligent Systems, Modelling and Simulation, Bangkok, Thailand. 2013. Doi: 10.1109/ISMS.2013.113

2.6 Dhar S., Vacca A. A fluid structure interaction-EHD model of the lubricating gaps in external gear machines: Formulation and validation. Tribology International. 2013. Doi: 0.1016/j.triboint.2013.02.008

2.7 Dhar S., Vacca A. A novel FSI–thermal coupled TEHD model and experimental validation through indirect film thickness measurements for the lubricating interface in external gear machines. Tribology International. 2015. Doi: 10.1016/j.triboint.2014.10.007

2.8 Vacca A., Guidetti M. Modelling and experimental validation of external spur gear machines for fluid power applications. Simulation Modelling Practice and Theory. 2011. Doi: 10.1016/j.simpat.2011.05.009

2.9 Dhar S., Vacca A. A novel CFD – Axial motion coupled model for the axial balance of lateral bushings in external gear machines. Simulation Modelling Practice and Theory. 2012. Doi: 10.1016/j.simpat.2012.03.008

2.10 Nervegna N., Rundo M. Passi nell'oleodinamica. Epics. 2020

2.11 Seeton C. J. Viscosity–temperature correlation for liquids. Tribology Letters. 2006. Doi: 10.1007/s11249-006-9071-2

2.12 Rundo M. Models for flow rate simulation in gear pumps: a review. Energies. 2017. Doi: 10.3390/en10091261

2.13 Zardin B., Natali E., Borghi M. Evaluation of the hydro-mechanical efficiency of external gear pumps. Energies. 2019. Doi: 0.3390/en12132468

2.14 Burwell J. T. Survey of possible wear mechanism. Wear. 1957. Doi: 10.1016/0043-1648(57)90005-4

2.15 Gachot C., Rosenkranz A., Hsu S. M., Costa H. L. A critical assessment of surface texturing for friction and wear improvement. Wear. 2017. Doi: 10.1016/j.wear.2016.11.020

2.16 Bhushan B. Biomimetics: lessons from nature – an overview. 2009. Philosophical Transaction of the Royal Society A. Doi: 10.1098/rsta.2009.0011

2.17 Dean B., Bhushan B. Shark-skin surfaces for fluid-drag reduction in turbulent flow: a review. 2010. Philosophical Transaction of the Royal Society A. Doi: 10.1098/rsta.2010.0201

2.18 Jearl W. More on boomerangs, including their connection with the dimpled golf ball. 1979. Scientific American. https://www.jstor.org/stable/10.2307/24965181

2.19 Maressa P., Anodio L., Bernasconi L., Demir A. G., Previtali B. Effect of surface texture on the adhesion performance of laser treated Ti6Al4V alloy. The Journal of Adhesion. 2014. Doi: 0.1080/00218464.2014.933809

2.20 Romoli L., Moroni F., Khan M. M. A. A study on the influence of surface laser texturing on the adhesive strength of bonded joints in aluminium alloys. CIRP Annals - Manufacturing Technology. 2017. Doi: 10.1016/j.cirp.2017.04.123

2.21 Moroni F., Romoli L., Khan M. M. A. Design of laser-textured surfaces to enhance the strength of adhesively bonded joints. International Journal of Adhesion and Adhesives. 2018. Doi: 10.1016/j.ijadhadh.2018.06.001

2.22 Lutey A. H. A., Gemini L., Romoli L., Lazzini G., Fuso F., Faucon M., Kling R. Towards laser-textured antibacterial surfaces. Scientific reports. 2018. Doi: 10.1038/s41598-018-28454-2

2.23 Pan Q., Cao Y., Xue W., Zhu D., Liu W. Picosecond laser-textured stainless steel superhydrophobic surface with an antibacterial adhesion property. Langmuir. 2019. Doi: 10.1021/acs.langmuir.9b01333

2.24 Villapún V. M., Gomez A. P., Wei W., Dover L. G., Thompson J. R., Barthels T., Rodriguez J., Cox S., González S. Development of antibacterial steel surfaces through laser texturing. APL Materials. 2020. Doi: 10.1063/5.0017580

2.25 Yusufa Y., Ghazalia M. J., Otsukac Y., Ohnumad K., Morakule S., Nakamuraf S., Abdollah M. F. Antibacterial properties of laser surface-textured TiO2/ZnO ceramic coatings. Ceramics International. 2020. Doi: 10.1016/j.ceramint.2019.10.124

2.26 Hamilton D. B., Walowit J. A., Allen C. M. A theory of lubrication by microirregularities. Journal of Fluids Engineering. 1966. Doi: 10.1115/1.3645799

2.27 Anno J. N., Walowit J. A., Allen C. M. Microasperity lubrication. Journal of Tribology. 1968. Doi: 10.1115/1.3601568

2.28 Anno J. N., Walowit J. A., Allen C. M. Load support and leakage from microasperity-lubricated face seals. Journal of Tribology. 1969. Doi: 10.1115/1.3555030

2.29 Willis E. Surface finish in relation to cylinder liners. Wear. 1986. Doi: 10.1016/0043-1648(86)90278-4

2.30 Etsion I., Burstein L. A model for mechanical seals with regular microsurface structure. Tribology Transactions. 1996. Doi: 10.1080/10402009608983582

2.31 Etsion I. State of the art in laser surface texturing. Journal of Tribology. 2005. Doi: 10.1115/1.1828070

2.32 Dobrica M. B., Fillon M., Pascovici M. D., Cicone T. Optimizing surface texture for hydrodynamic lubricated contacts using a mass-conserving numerical approach. Journal of Engineering Tribology. 2010. Doi: 10.1243/13506501JET673

2.33 Fowell M. T., Medina S., Olver A. V., Spikes H. A., Pegg I. G. Parametric study of texturing in convergent bearings. Tribology International. 2012. Doi: 10.1016/j.triboint.2012.02.013

2.34 Iban T., Uddin M., Chowdhury M. Recent development on surface texturing in enhancing tribological performance of bearing sliders. Surface & Coatings Technology. 2015. Doi: 10.1016/j.surfcoat.2015.04.017

2.35 Yu H., Wang X., Zhou F. Geometric shape effects of surface texture on the generation of hydrodynamic pressure between conformal contacting surfaces. Tribology Letters. 2010. Doi: 10.1007/s11249-009-9497-4

2.36 de Kraker A., van Ostayen R. A. J., van Beek A., Rixen D. J. A multiscale method modeling surface texture effects. Journal of Tribology. 2007. Doi: 10.1115/1.2540156

2.37 Li K., Jing D., Hu J., Ding X., Yao Z. Numerical investigation of the tribological performance of micro-dimple textured surfaces under hydrodynamic lubrication. Beilstein Journal of Nanotechnology. 2017. Doi: 10.3762/bjnano.8.232

2.38 Caramia G., Carbone G., De Palma P. Hydrodynamic lubrication of micro-textured surfaces: Two dimensional CFD-analysis. Tribology International. 2015. Doi: 10.1016/j.triboint.2015.03.019

2.39 Vilhena L., Sedlacek M., Podgornik B., Rek Z., Žun I. CFD modeling of the effect of different surface texturing geometries on the frictional behavior. Lubricants. 2018. Doi: 10.3390/lubricants6010015

2.40 Guzek A., Podsiadlo P., Stachowiak G. W. Optimization of textured surface in 2D parallel bearings governed by the Reynolds equation including cavitation and temperature. Tribology online. 2013. Doi: 10.2474/trol.8.7

2.41 Rahmani R., Shirvani A., Shirvani H. Optimization of partially textured parallel thrust bearings with square-shaped micro-dimples. Tribology Transactions. 2008. Doi: 10.1080/10402000701429261.

2.42 Brizmer V., Kligerman Y., Etsion I. A laser surface textured parallel thrust bearing. Tribology Transactions. 2003. Doi: 10.1080/10402000308982643

2.43 Etsion I., Halperin G., Brizmer V., Kligerman Y. Experimental investigation of laser surface textured parallel thrust bearings. Tribology Letters. 2004. Doi: 10.1023/B:TRIL.0000032467.88800.59

2.44 Chen Y., Zhang J., Xu B., Wang F., Li H. Investigation of laser surface texturing for integrated PV (pressure×velocity)-value-decreased retainer in an EHA pump. The 11th International Fluid Power Conference, IFK. 2018.

2.45 Deng H., He S., Mao F., Wang C. Effects of micropit depths on tribology performance of textured port plate pair. Advances in Materials Science and Engineering. 2018. Doi: 10.1155/2018/9501708

2.46 Wang Z., Hu S., Zhang H., Ji H., Yang J., Liang W. Effect of surface texturing parameters on the lubrication characteristics of an axial piston pump valve plate. Lubricants. 2018. Doi: 10.3390/lubricants6020049

2.47 Zhang J., Chen Y., Xu B., Chao Q., Zhu Y., Huang X. Effect of surface texture on wear reduction of the tilting cylinder and the valve plate for a high-speed electro-hydrostatic actuator pump. Wear. 2018. Doi: 10.1016/j.wear.2018.08.003

2.48 Gupta N., Tandon N., Pandey R. K. An exploration of the performance behaviors of lubricated textured and conventional spur gearsets. Tribology International. 2018. Doi: 10.1016/j.triboint.2018.07.044

Chapter 3. Simulation results

This chapter presents the numerical modelling of a reference domain with textured surfaces. After a description of the case study, the simulations performed in ANSYS® CFX environment are presented. The analysis is carried out in steps, starting from a configuration with a single dimple, the full texturing configuration is studied and finally the attention is turned to partial texturing.

Numerical results of more complex domain applications are also provided, characterized by a circular sector geometry.

1.1 Three-dimensional CFD model description

The low pressure area of the lateral plates inside an external gear pump is the most critical portion. Due to a variation in the working conditions, often associated with sudden changes in the delivery pressure, it is possible that the gap between the lateral plates and the gear wheels is reduced to the point of allowing the direct contact between the two components, since the gap is smaller in this area. During normal operation, direct contact between the components is avoided thanks to the establishment of a hydrodynamic bearing capacity that allows to counterbalance the tendency to approach the two surfaces. However, if the applied load is greater than the force that could be generated by the coupling, the contact is no longer avoidable.

It is evident that direct contact between aluminum components, the lateral plates, and cemented steel gear wheels produces wear in the lateral plates, which, if the contact persists and is long-lasting, risks seriously damaging the component, causing great decreases in the performance of the pump.

Starting from the many fields of application of engineered surfaces described in the paragraph 2.5, in this research activity the possibility and effectiveness of creating a textured surface on the lateral plates has been studied. The aim is to generate an additional hydrodynamic bearing capacity that allows to avoid, or in any case limit, direct contact between wheels and lateral plates. Since the critical area is the low pressure one, the attention has been focused on the suction area, limiting the introduction of texturing only on this portion of the lateral plates.

The study concentrates on the fluid gap existing between the gear wheels and the lateral plates inside a gear pump, highlighted in the Figure 3.1.

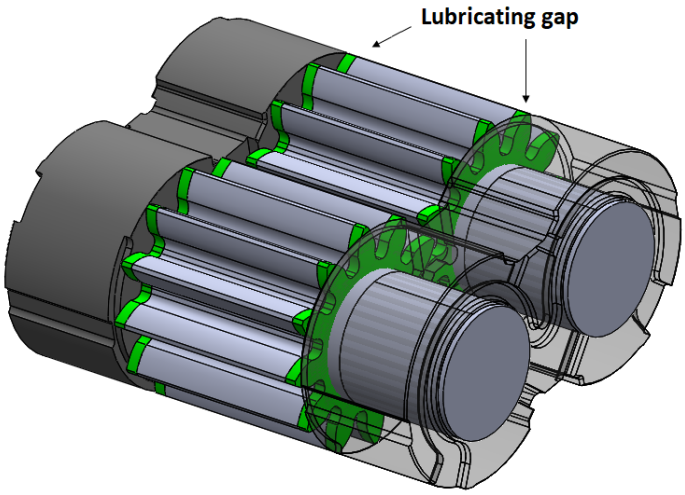

Figure 3.1. Assembly of gear wheels and lateral plates. The fluid gap that allows the coupling to be lubricated is highlighted in green.

To study the effects due to the introduction of a textured surface on the lateral plates, a numerical study by means of CFD simulations has been conducted. The simulations have been carried out in ANSYS® CFX environment, a commercial software widely used in the industrial field that discretizes the governing equations using a finite volume method.

The geometry of the gap, as already mentioned, is of complex definition due to the position assumed by the lateral plates during working. It has been therefore assumed that the gap is delimited by two parallel surfaces, one of which in relative motion with respect to the other. This simplification permits to evaluate the influence of only the texturing on the bearing capacity within the gap. Furthermore, the principle of superimposition of effects is still valid, whereby the overall bearing capacity in the gap is the sum of the force given by the hydrodynamic lubrication of the original coupling of wheels and lateral plates plus that generated by the texture.

The strategy with which the simulations have been carried out initially focuses on a very simple reference fluid domain, composed of two parallel plane surfaces in relative translational motion. These first simulations aim to evaluate the geometric influences of the texturing and the distribution of the texture in the domain in order to maximize the coupling performance, [3.1, 3.2]. Only later, the analysis has been addressed to the gap existing between the gear wheels and the lateral plates.

3.1 Single dimple

To evaluate the influence that an engineered surface exerts within a lubricating gap, the analysis has been started with a single dimple located at the centre of a reference domain, characterized by two parallel planes, one of which is in translational motion with respect to the other. A square-based prismatic dimple has been chosen as the reference geometry. The Figure 3.2 shows schematically the simulated fluid domain with the main geometric characteristics indicated.

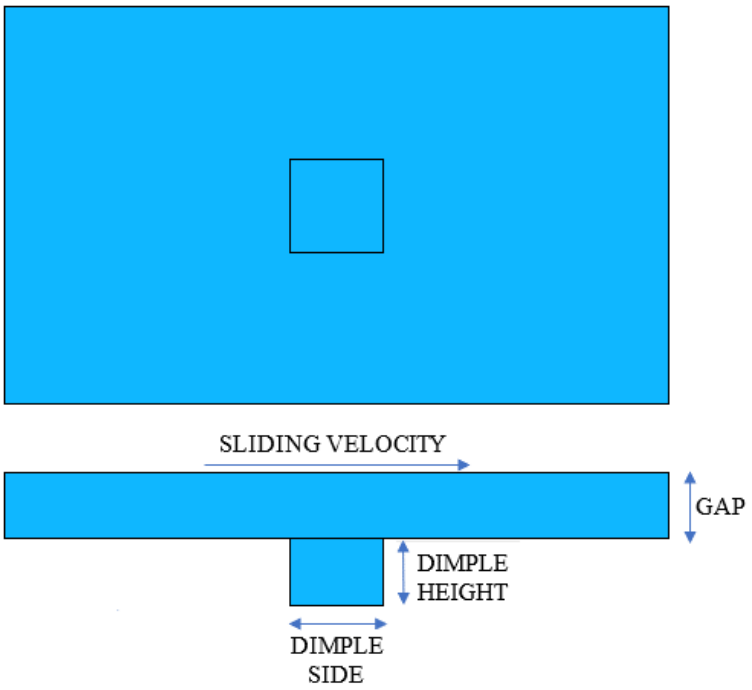

Figure 3.2. Graphic representation of the single dimple configuration with the main geometric features indicated.

The simulations have been carried out to define the influence of the geometric characteristics of the dimple, such as the size of the side and the depth, in relation to the characteristics of the two coupled surfaces, such as the height of the gap and the translational speed of the moving surface.

The dimensions of the reference domain are such as to ensure that the pressure gradient established by the presence of the dimple reaches the zero value in both directions, in this way the size of the domain does not affect the results obtained, [3.2].

The boundary conditions are open boundary with zero relative pressure for the perimeter walls of the domain, while the upper plane is a moving wall with no-slip condition. The speed of moving plane is a characteristic of the lubricated coupling and depends on the operating conditions of the hydraulic machine: in the simulations performed, the speed is assumed to be 5 m/s. Simulations are considered convergent when the residuals of each equation are less than 10^{-5}. Generally, the motion

of fluids in industrial applications is turbulent; however, since the height of the gap is in the order of micron and the viscosity of the hydraulic oil is high, the simulations have been performed considering the motion of the fluid laminar.

The fluid modelled in the CFD simulations is an ISO VG-46 hydraulic oil, which is a complex mixture of hydrocarbons, the properties of which are shown in Table 3.1.

Table 3.1. Properties of hydraulic oil used in numerical simulations.

Parameter	Value
Density	850 kg/m^3
Viscosity (40 °C)	46 mm^2/s

The fluid domain has been discretized using a structured mesh, the characteristics of which were established following a sensitivity analysis. Of the different meshes tested, the three most significant are shown in the Table 3.2.

Table 3.2. Sets adopted for the sensitivity analysis of the mesh.

	Min Element size	Max Element size	Average Element quality	Average Aspect ratio	Average Orthogonal quality	Average Skewness
Mesh 1	1e-6	1e-5	0.30	6.02	0.998	2.24e-2
Mesh 2	1e-7	4e-6	0.68	2.42	0.998	1.42e-2
Mesh 3	1e-7	1e-6	0.83	1.67	0.999	5.94e-5

The maximum pressure value has been used as a parameter to evaluate the influence of the mesh on the numerical solution. As could be seen from the Figure 3.3, the results obtained with Mesh 2 differ slightly from those obtained with Mesh 3, which has a greater number of elements: the deviation is only 0.8%. In the following simulations, Mesh 2 has been therefore adopted.

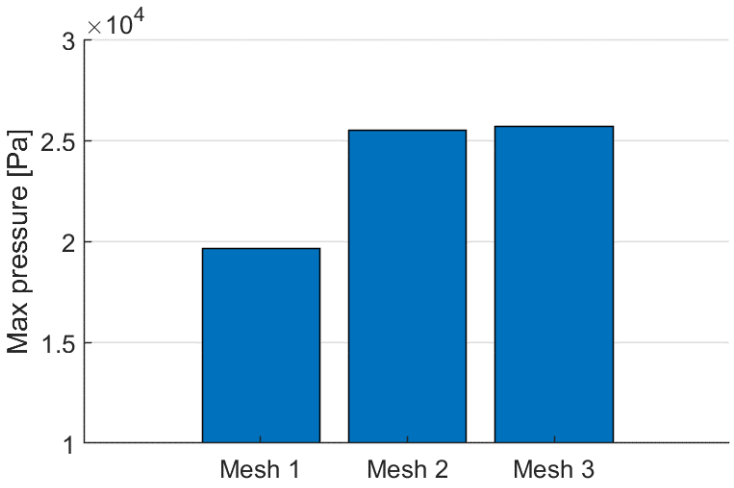

Figure 3.3. Influence of the mesh on the maximum pressure reached.

The introduction of a dimple in a domain characterized by two parallel surfaces distorts the pressure field inside the gap. The pressure decreases near the diverging section, since there is an increasing of the average gap height; the pressure then increases close to the converging area. The Figure 3.4 shows the pressure contour on the moving surface relative to the case of a square dimple with side equal to 50 µm and sliding speed equal to 5 m/s. The direction of the moving plane is indicated by the arrow.

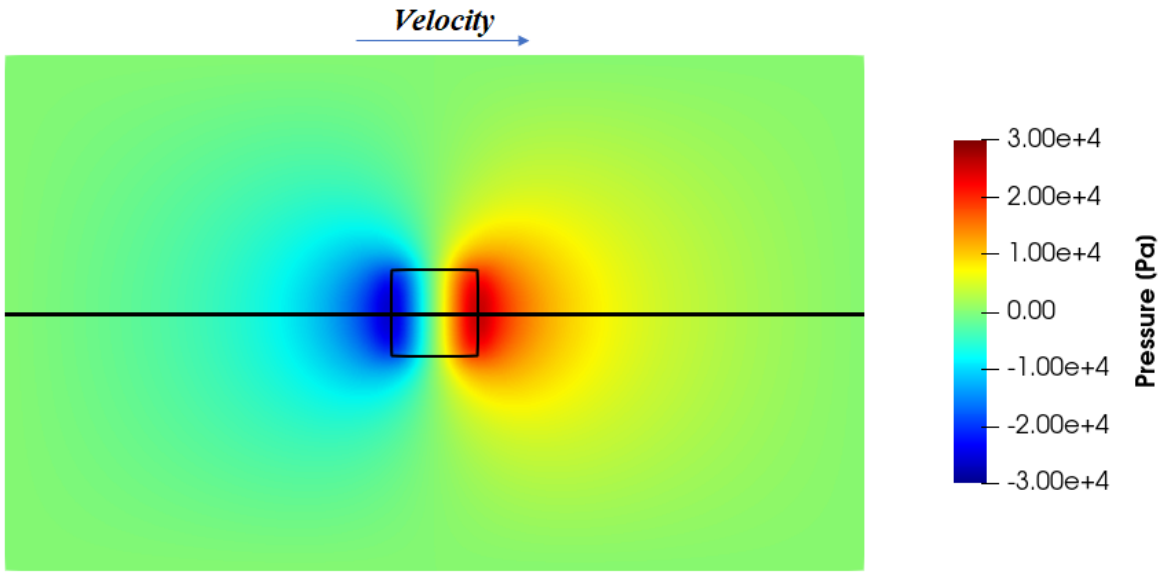

Figure 3.4. Pressure contour of a square dimple with side 50 µm and depth 10 µm. Gap 10 µm, sliding velocity 5 m/s.

Consequently, a perturbation of the pressure field has been introduced which however is antisymmetric with respect to the centre of the dimple: the minimum value reached is equal to the maximum overpressure value. The Figure 3.5 shows the pressure profile on the moving plane

calculated along the black line in Figure 3.4: the graph deliberately displays the relative pressure in order to emphasize the symmetry of the curve, since the pressure on the boundary walls is zero. It follows that the average pressure inside the gap is zero, making no contribution in terms of bearing capacity, defined as the integral of the pressure on the surface of the plane in motion.

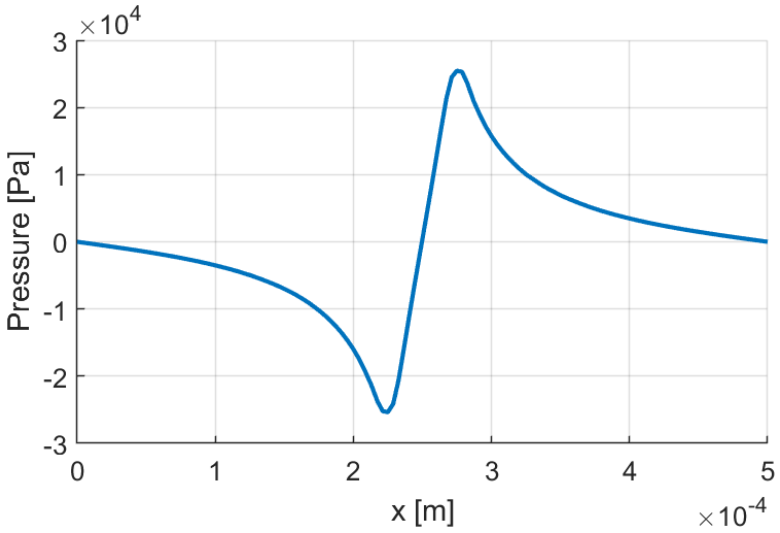

Figure 3.5. The pressure profile perturbation generated by a square dimple. Dimple side 50 µm and depth 10 µm. Gap 10 µm, sliding velocity 5 m/s.

This result is also valid for any other pressure value imposed as a boundary condition: in fact, the pressure set represents the average value within the meatus.

The fact that the pressure oscillates symmetrically around the average value is a direct consequence of the geometric symmetry of the dimple. As confirmation, simulations have been also carried out on prismatic dimples with a circular and rectangular section, characterized by the same surface area as the previous square dimple. The Figure 3.6 and the Figure 3.7 show the relative pressure contours on the moving plane respectively in the case of circular and rectangular dimple. The graph in the Figure 3.8 shows the relative pressure along the median line on the moving plane (the black line in the contours) and confirms the perfect symmetry of pressure within the domain.

It could be concluded that the perfect geometric symmetry of the dimple does not allow to obtain any bearing capacity in the gap.

This result is confirmed in the scientific literature: Li et Al. [3.3] by studying the effect of micro-dimples (geometrically symmetrical) on the pressure distribution using the Navier-Stokes equations, obtained an antisymmetric trend, which could be slightly distorted as the Reynolds number varies. Vilhena et Al. [3.4] have also obtained similar results with symmetrical dimples of different geometry.

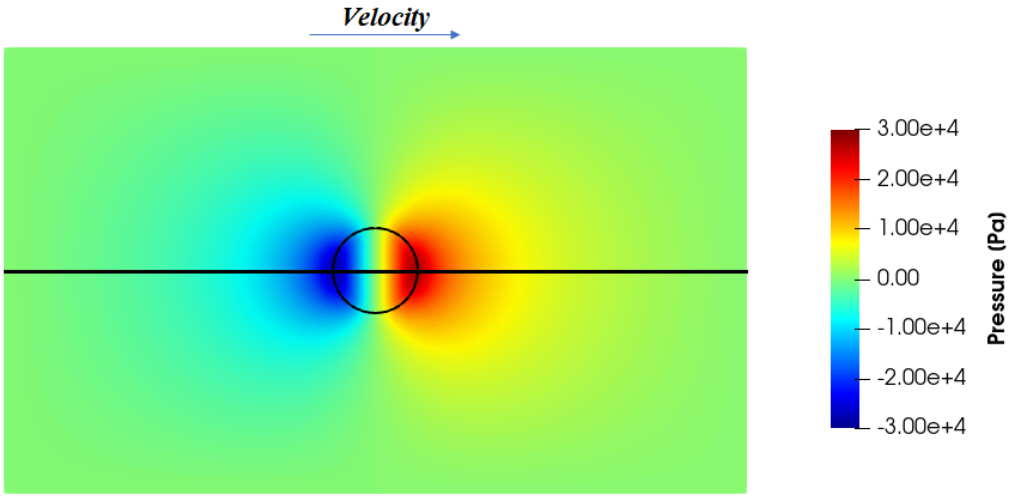

Figure 3.6. Pressure contour of a circle dimple with diameter 56.4 µm and depth 10 µm. Gap 10 µm, sliding velocity 5 m/s.

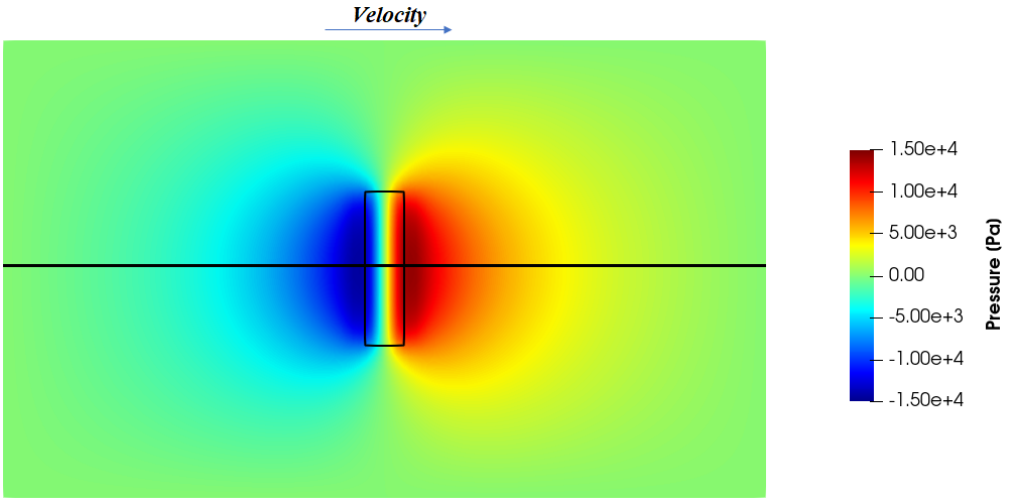

Figure 3.7. Pressure contour of a rectangular dimple with sides 100 µm and 25 µm, depth 10 µm. Gap 10 µm, sliding velocity 5 m/s.

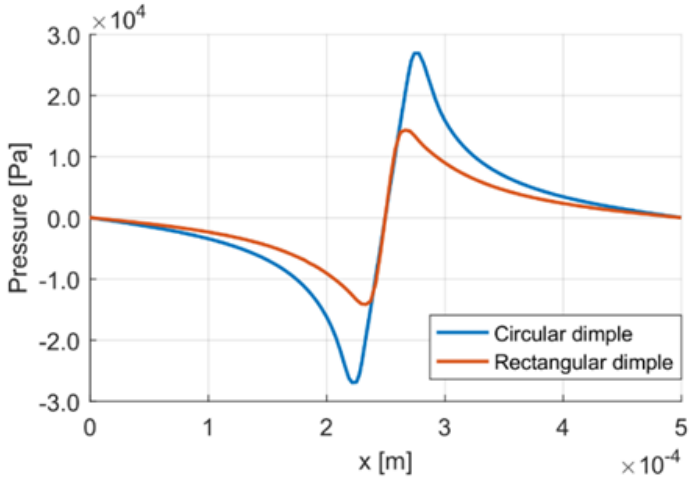

Figure 3.8. Pressure distributions relative to the circle and rectangular case of Figure 3.6 and Figure 3.7, calculated along the dimples median line.

The size of the dimple is an important factor in the perturbation of pressure in the gap. Larger dimples generate a pressure profile characterized by a greater amplitude, with higher depression and overpressure peaks, as shown in Figure 3.9.

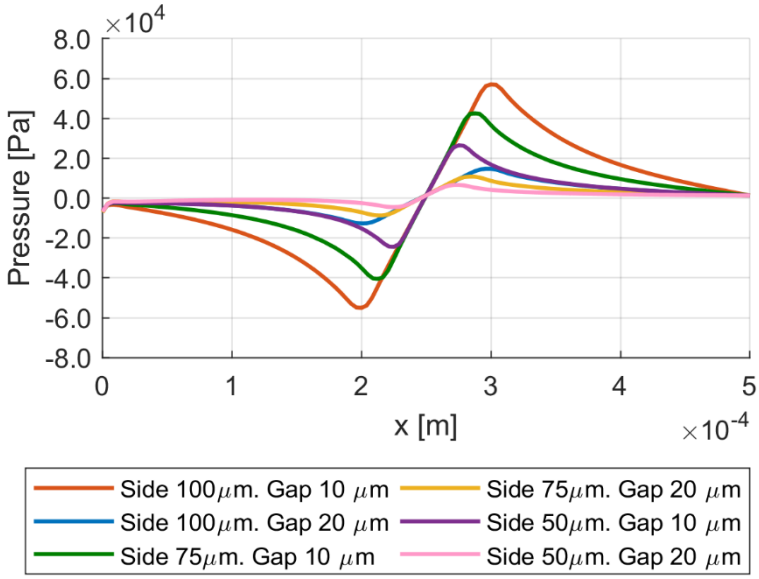

Figure 3.9. The pressure profile perturbation is generated by a square dimple and characterized by different sides and values of the gap. Dimple depth 10 μm, sliding velocity 5 m/s.

A similar result is also given by the reduction of the gap between the two coupled surfaces: this is due to a higher average speed within the domain.

These simulations have been performed not including the cavitation effects of the fluid: for this reason, the minimum pressure is not limited in any way. The in-depth study of the influence of cavitation will be dealt with later in this Thesis. In this first phase, the focus was mainly on the perturbation of pressure due to the insertion of a dimple in the domain and the influence of its geometric characteristics. Furthermore, the results without cavitation are still valid if the boundary conditions are different. The boundary pressure is the average value around which the pressure profile oscillates: using a higher pressure value as a boundary condition simply involves a translation of the pressure profile to a higher average pressure value, but the trend remains unchanged, generating no bearing capacity.

According to the Reynolds equation, Equation (3.1), which represents the theory of lubrication, the dependence of pressure on the sliding speed of the moving plane is linear: therefore, the amplitude of the pressure profile will be greater for higher sliding speeds.

$$\frac{\partial}{\partial x}\left(h^3\frac{\partial p}{\partial x}\right) = 6U\eta\frac{dh}{dx} \tag{3.1}$$

From the Reynolds equation it is also observed that the dependence of pressure on the viscosity of the working fluid is linear. Viscosity is a property of the fluid that strongly depends on temperature: the higher the temperature, the lower the viscosity, as shown in the Paragraph 2.3. It follows that by increasing the temperature, the amplitude of the pressure profile will be reduced.

The depth of the dimple is another design parameter of the textured surface and its influence on the pressure profile has been evaluated. From the simulations conducted, the depth of the dimple is rather marginal on the bearing capacity, since it does not significantly change the pressure profile. The Figure 3.10 shows the pressure profile on the moving plane due to a square dimple with a side of 50 µm and a depth of 5 - 10 - 20 µm; the gap is 10 µm high. The difference between the three curves is minimal. This fact find confirmation in the scientific literature. Brizmer et Al. after a parametric numerical study to also evaluate the influence of the depth of the dimple applied to a thrust bearing, concluded that the depth of the dimples should be the same as the thickness of the fluid film in order to ensure the best performance of the bearing [3.5].

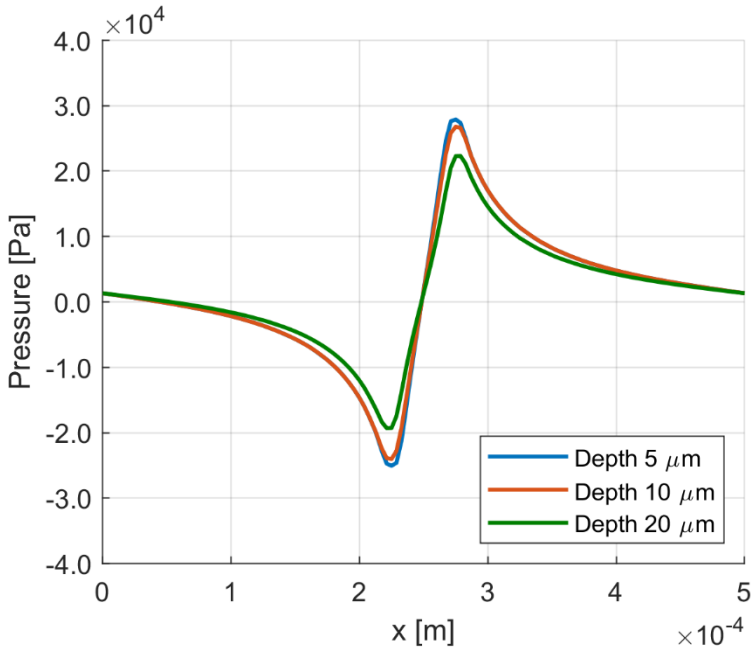

Figure 3.10. Influence of the dimple depth on the pressure profile. Square dimple with side 50 µm and gap 10 µm, sliding velocity 5 m/s.

As already noted, the symmetry in pressure is the consequence of perfect geometric symmetry. Using a non-symmetrical geometry, such as a prismatic dimple with a trapezoidal section, the pressure contours shown in the Figure 3.11 are obtained. Two cases are reported: the first is a

geometry characterized by an isosceles trapezoid with bases 100 µm and 50 µm, 50 µm high, Figure 3.11a; the second has the bases 100 µm and 25 µm long, always 50 µm high, Figure 3.11b. The depth of the dimple is 10 µm for both configurations. The results show that in fact the average pressure on the moving plane is greater than zero, but only a few hundred Pascals, and consequently the bearing capacity is very small. The force generated therefore does not justify the greater geometric complexity of the dimple. Furthermore, the behavior of an asymmetrical geometry depends on the direction of the speed of the moving plane: by inverting the velocity, a very small average negative pressure is obtained, which would tend to bring the two coupled surfaces closer together, as shown in the Figure 3.12 for the two same configurations of Figure 3.11.

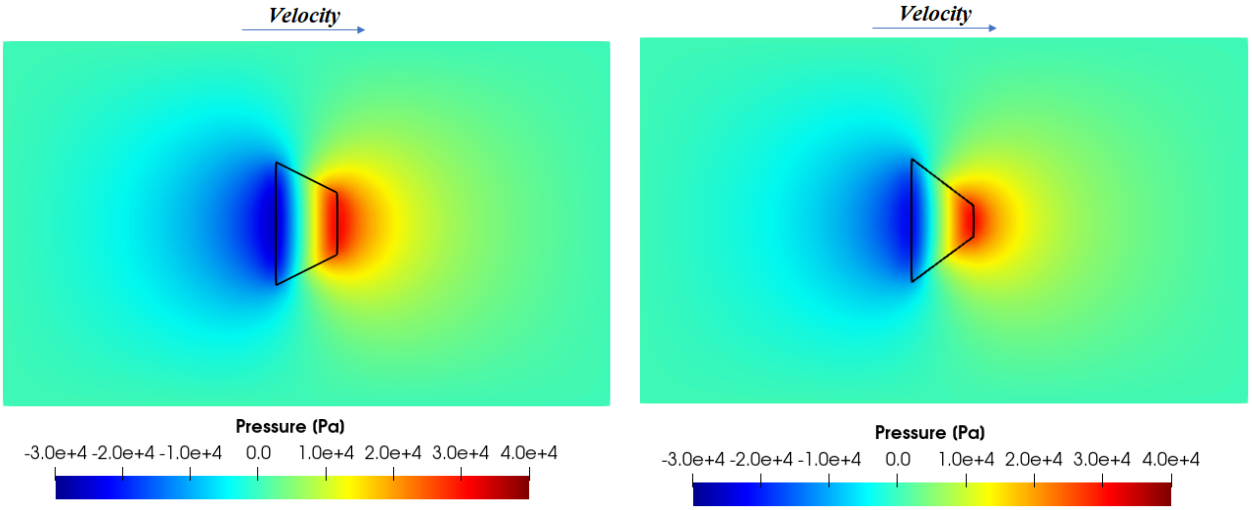

(a) (b)

Figure 3.11. (a) Pressure contour of a trapezoidal dimple with sides 100 µm and 50 µm; height of the trapezoid 50 µm. Depth 10 µm. (b) Pressure contour of a trapezoidal dimple with sides 100 µm and 25 µm; height of the trapezoid 50 µm. Depth 10 µm. Gap 10 µm, sliding velocity 5 m/s.

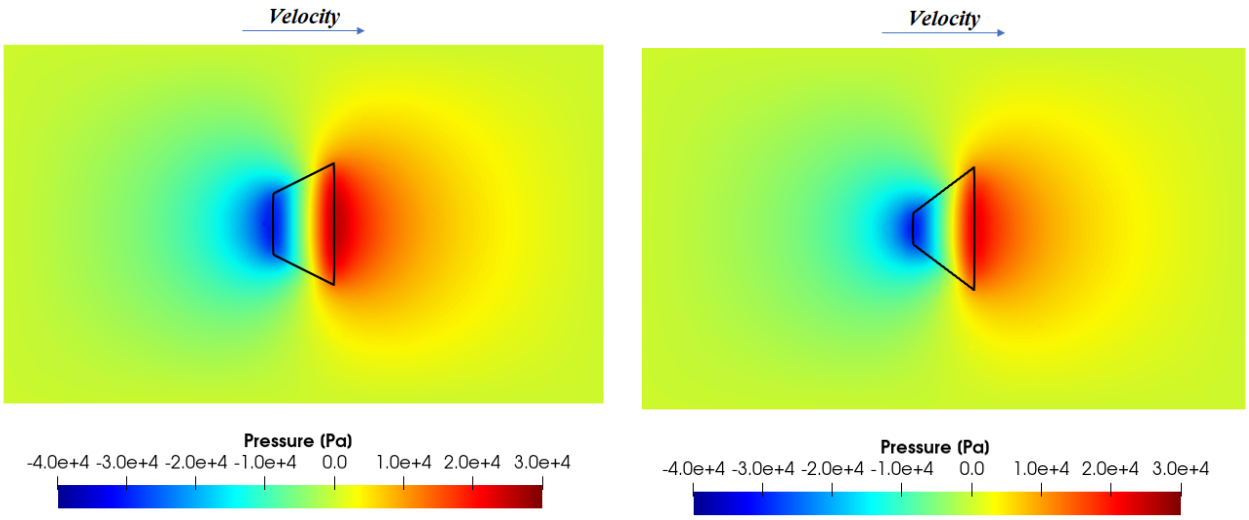

(a) (b)

Figure 3.12. (a) Pressure contour of a trapezoidal dimple with sides 100 µm and 50 µm; height of the trapezoid 50 µm. Depth 10 µm. (b) Pressure contour of a trapezoidal dimple with sides 100 µm and 25 µm; height of the trapezoid 50 µm. Depth 10 µm. Gap 10 µm, sliding velocity 5 m/s.

3.2 Full texturing

A full texturing configuration is characterized by a succession of dimple equally distributed over the entire available domain. The Figure 3.13 shows a schematically representation of this configuration in which there is only one row of dimples.

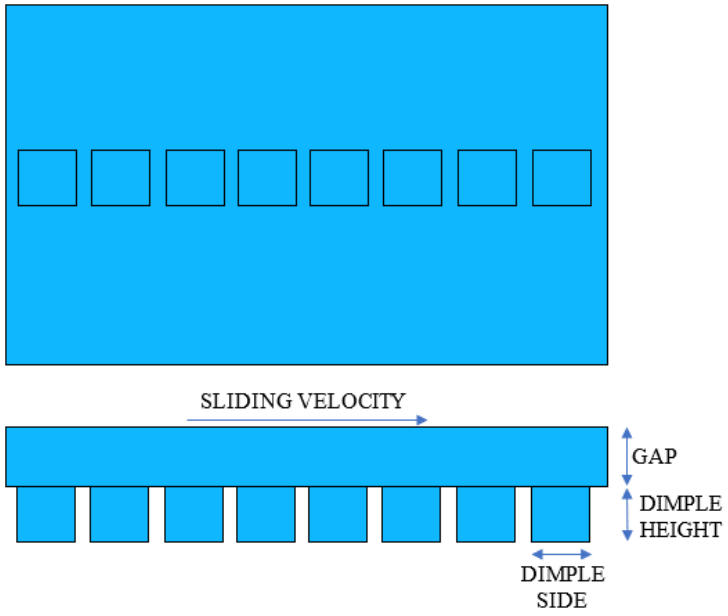

Figure 3.13. Graphic representation of the full texturing configuration with the main geometric features reported.

In this configuration, with the same boundary conditions used in the previous paragraph, the perturbation of the pressure profile introduced by each dimple is similar to the single dimple case. The pressure field has a trend characterized by a periodic oscillation around the average value, which is the value imposed as a boundary condition. To better understand the trend, the Figure 3.14a shows the pressure contours of a full texture configuration with a single row of dimples, while in Figure 3.14b the pressure profile calculated along the dimples' median line is plotted.

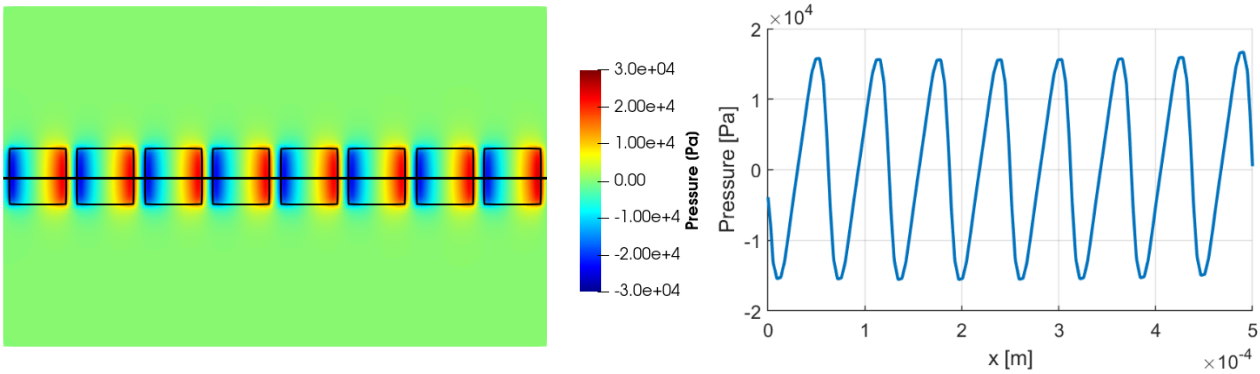

(a) (b)

Figure 3.14. (a) Pressure contour of the full texturing configuration. Square dimples with side 50 µm and depth 10 µm. Gap 10 µm, sliding velocity 5 m/s. (b) Pressure profile calculated along the dimples' median line shown in the contour.

A geometry thus characterized does not allow to obtain any improvement in terms of additional load capacity due to a hydrodynamic effect.

In a full texturing configuration, the domain should be textured in both directions, with dimples placed over the entire surface, but for simplicity, the simulations have been performed considering only one row of dimples. For completeness, the case of a multi-row configuration is reported, where all the dimples are equal to each other and equally spaced in both directions. The Figure 3.15 shows the pressure contour on the moving surface of a configuration with two textured lines. The Figure 3.16 instead shows the pressure profiles extracted on the median line of the dimples on the moving plane both for the single row case and for each of the two rows of the multi-row configuration: the pressure profile is almost identical and therefore it is possible to study the full texturing configuration simplifying it to a single row of dimples.

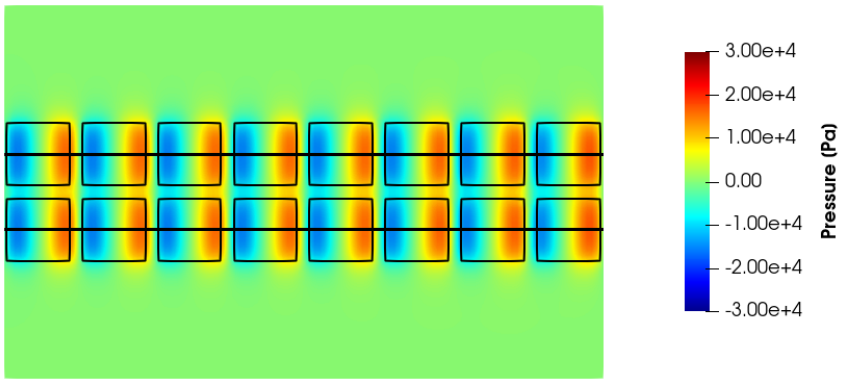

Figure 3.15. Pressure contour of a multi-row configuration. Square dimples with side 50 µm and depth 10 µm. Gap 10 µm, sliding velocity 5 m/s.

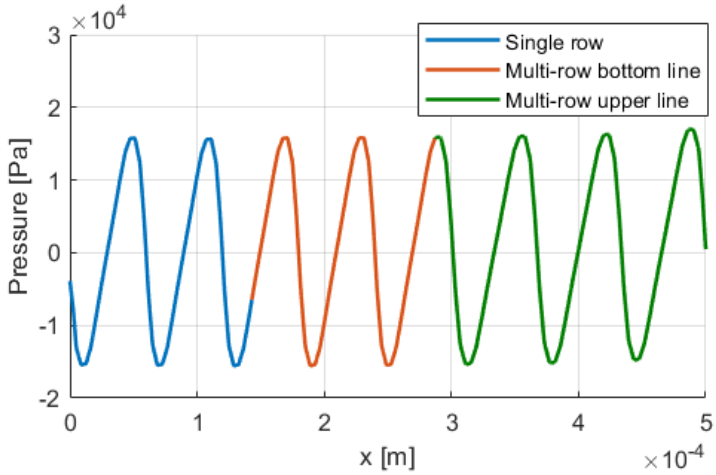

Figure 3.16. Pressure profiles of a full texturing surface with dimples side 50 µm and gap 10 µm, sliding velocity 5 m/s. Comparison between a single-row configuration and a multi-row.

From the analysis of the results regarding the single dimple and full texturing configurations it emerges that the possibility of generating a bearing capacity inside the gap capable of opposing the approach of the two surfaces is very limited. In fact, this occurs exclusively with dimples characterized by asymmetrical geometry in the direction of motion. This still represents an interesting result, but unfortunately the achievable forces are very low.

A texture configuration that permits to obtain a great bearing capacity due to the hydrodynamic effect has been investigated, acting exclusively on the geometric arrangement of the dimples: this configuration is called partial texturing.

3.3 Partial texturing

Partial texturing refers to a configuration in which the dimples are arranged only in a portion of the entire available domain. The Figure 3.17 shows schematically this type of configuration with a single row of dimples.

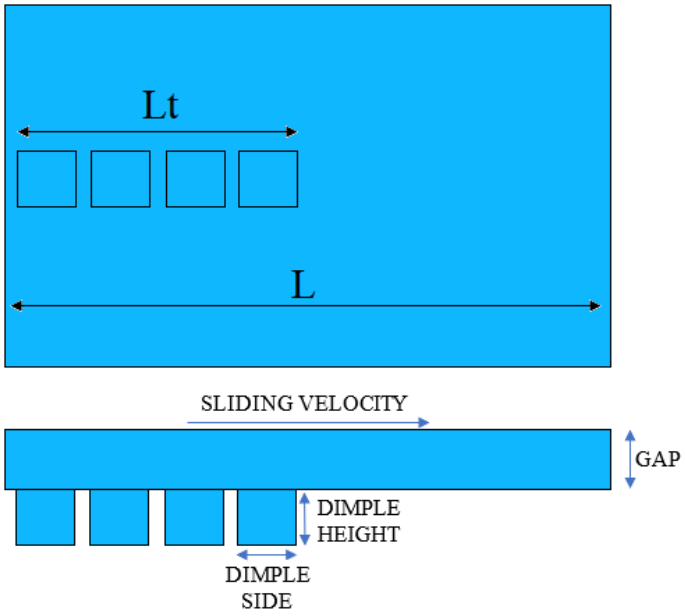

Figure 3.17. Graphic representation of the partial texturing configuration with the main geometric features indicated.

The textured portion, which indicates how much surface is textured, is defined as:

$$\alpha = \frac{L_t}{L} \tag{3.2}$$

The pressure contour on the moving plane relative to the case of texturing half domain (α = 50%) is shown in the Figure 3.18a. In this configuration, unlike the previous ones, the pressure does not oscillate symmetrically around the zero mean value, imposed as boundary condition. As could be seen from the pressure profile calculated along the black line indicated in the contour, Figure 3.18b, each dimple provides a contribution that locally raises the pressure so that the overall effect is an increasing pressure ramp. Near the last dimple, a large overpressure value is reached which gradually decreases: in this configuration, therefore, it is possible to obtain a significant bearing capacity.

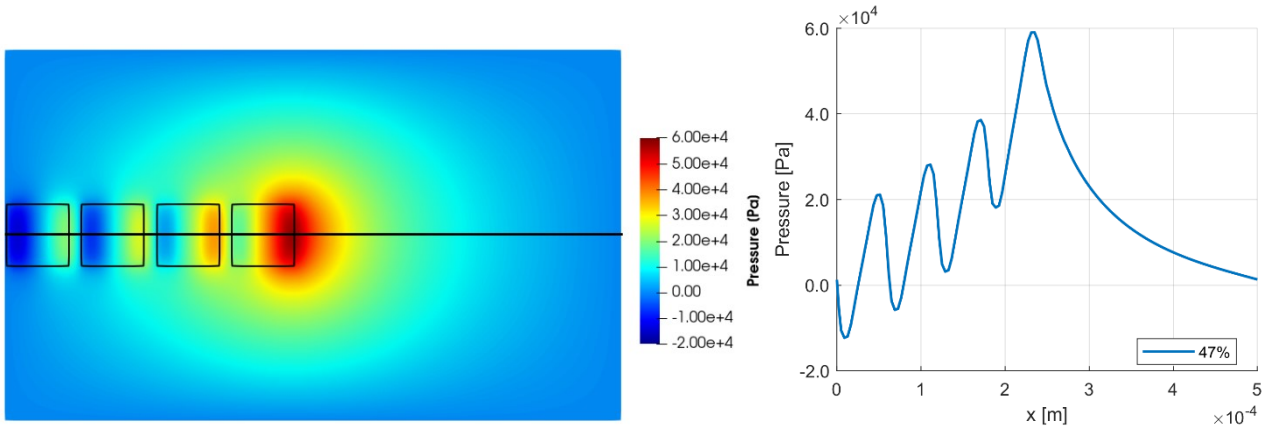

(a) (b)

Figure 3.18. Pressure contour of a partial texturing configuration realized by square dimples with side 50 µm and depth 10 µm. Gap 10 µm, sliding velocity 5 m/s. (b) Pressure profiles calculated along the dimples median line, textured portion of 47%. Square dimples with side 50 µm and gap 10 µm, sliding velocity 5 m/s.

The portion of the textured surface strongly influences the overall bearing capacity generated by the hydrodynamic effect. The Figure 3.19 shows the integral of the pressure on the reference domain as the texturized portion varies, expressed as a percentage: the best condition, which allows to obtain maximum force, is when the domain is 45-60% texturized.

Also in this case, for simplicity, a single row of dimples has been studied because the same considerations for the multi-row configuration made for the case of full texturing are still valid.

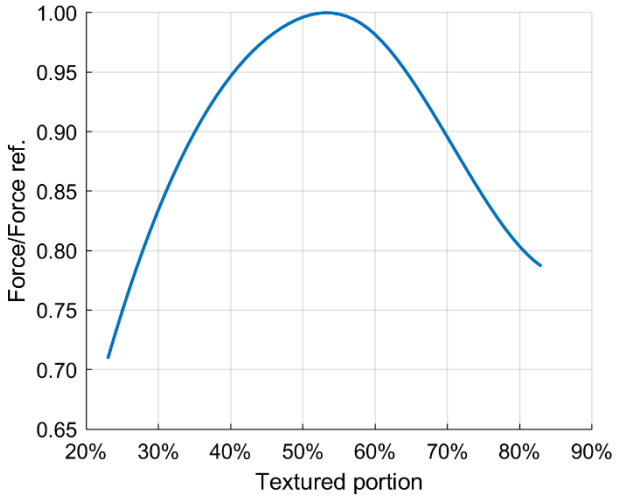

Figure 3.19. Force generated by the partial texturing surface as a function of the textured portion. Square dimples with side 50 µm and gap 10 µm, sliding velocity 5 m/s

These results are also confirmed by the work of other researchers. Etsion's team [3.5] concluded that full texturing can not generate any bearing capacity. However, they believe it could still have benefits in terms of increased surface lubrication. On the contrary, they have determined that the partial texturing configuration could greatly improve the tribological performance through what they define a "collective dimple effect". Partial texturing is able to generate a considerable bearing capacity and they have calculated that the optimal condition is to texturize 60% of the available surface. This important result agrees with the simulations carried out during this Thesis activity.

Partial texturing could also have other benefits, acting as reservoirs of lubricant and trapping wear debris. Partial texturing is therefore more efficient than full texturing and is the only way to significantly improve performance in a lubricated contact.

3.3.1 Partial texturing - Domain with circular sector

A more in-depth analysis has been carried out on partial texturing configuration, since it is the only way that allows obtaining a hydrodynamic benefit.

To get closer to the conditions inside a gear pump, the domain adopted in these simulations is a circular sector, assumed to be 10° wide. The motion of the moving plane is no longer translational, but rotary with an angular speed equal to 2500 r/min. In the following simulations, a clockwise rotation of the upper plane has been set. The internal radius and the external radius of the domain refer to the gear wheel present in the type of pump considered and are respectively R1 and R2 indicated in the Figure 3.20. For confidentiality reasons it is not possible to provide the actual geometric dimension.

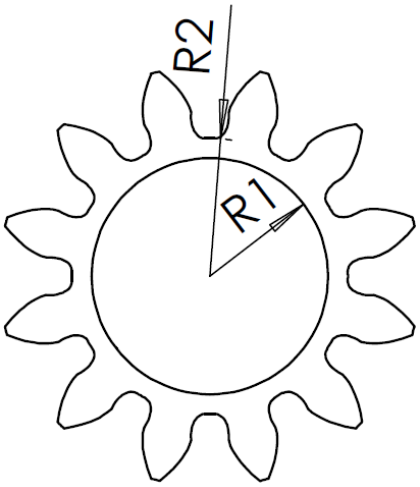

Figure 3.20. Gear wheel indicating the internal and external radius of the circular sector.

The circular sector has a partial texturing, comprised between 50% and 60% of the available surface, formed by prismatic dimples with a square section.

A structured mesh has been used to discretize the domain, the characteristics have been established following a sensitivity analysis. Three different types of mesh have been tested, indicated in the Table 3.3.

Table 3.3. Parameters of the sets adopted for the sensitivity analysis of the mesh.

	Min Element size	Max Element size	Average Element quality	Average Aspect ratio	Average Orthogonal quality	Average Skewness
Mesh 1	1e-5	1e-4	3.13e-2	59.80	0.955	8.74e-2
Mesh 2	1e-5	1e-6	0.30	6.06	0.996	2.65e-2
Mesh 3	5e-6	5e-7	0.57	3.02	0.997	2.33e-2

The parameter used to evaluate the influence of the mesh on the numerical results is the force generated by the surface. The Figure 3.21 shows the trend of the force, divided by a reference value for confidential reasons, as the mesh changes: Mesh 2 has a final value that differs only by 0.8% compared to Mesh 3. For this reason, Mesh 2 has been adopted.

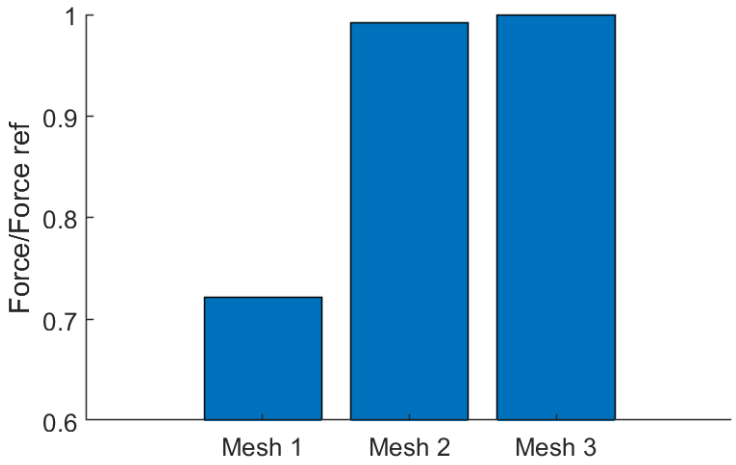

Figure 3.21. Influence of the mesh on the force generated by the sequence of dimples.

In the following simulation results, the influence of the size of the dimples in the circumferential direction has been evaluated. The Figure 3.22 shows the pressure contours related to three cases: side with dimension 0.05 mm, 0.1 mm and 0.2 mm. The height of the gap is equal to 10 μm, equal to the depth of the dimples. The textured portion is the same in the three cases, so as the size of the dimple decreases, the number of dimples increases. The Figure 3.23 shows the pressure graph as a function of the angle calculated along the black line highlighted in the pressure contours. The pressure trend in the three cases has the characteristic of being an increasing ramp where the contributions of the individual dimples are visible. The circumferential size of the dimples is a factor that greatly affects the performance of the surface. In general, larger dimples have a ramp that reaches higher pressures, with a consequent greater integral on the surface, i.e. a greater bearing capacity.

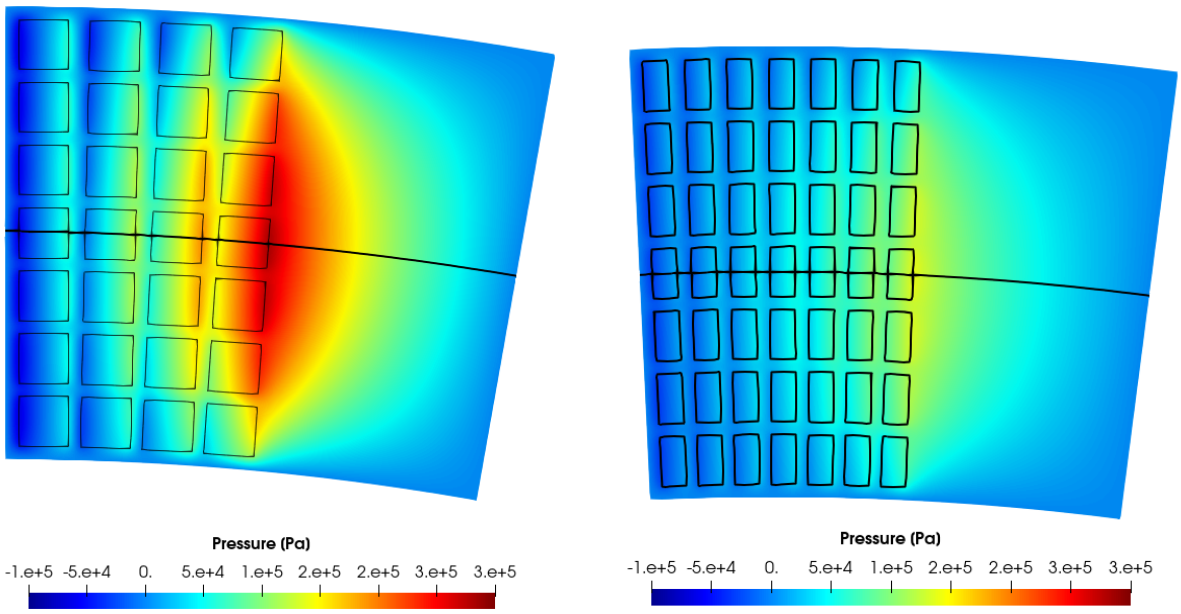

(a) (b)

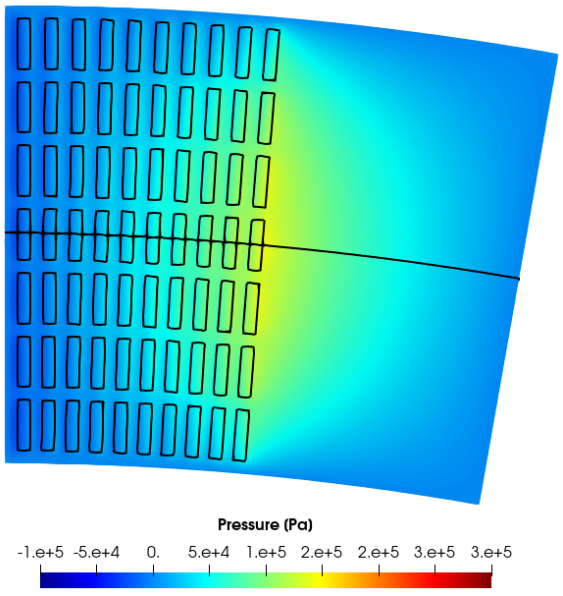

(c)

Figure 3.22. Pressure contour of a partial texturing configuration realized by: (a) square dimples with side 0.2 mm and depth 10 μm; (b) rectangular dimples with side 0.2 mm and 0.1 mm, depth 10 μm; (c) rectangular dimples with side 0.2 mm and 0.05 mm, depth 10 μm. Gap 10 μm, rotating speed 2500 r/min.

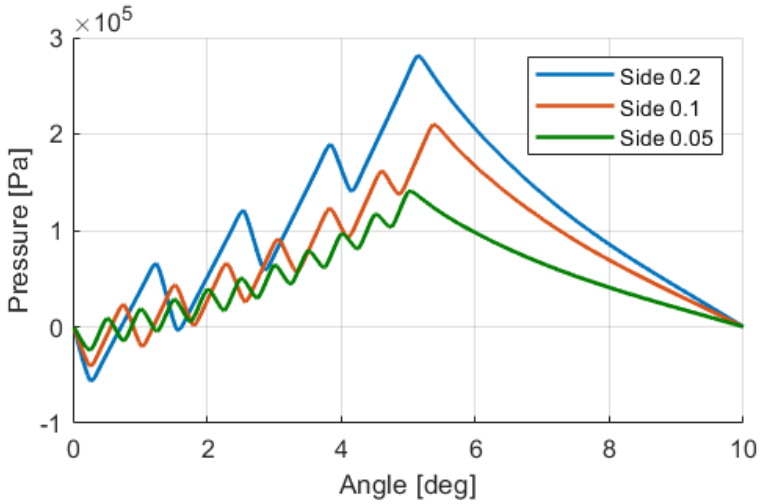

Figure 3.23. Pressure profiles calculated along the domain median line of the cases of Figure 3.22.

The effect of the size of the dimple in the direction of motion is very important, regardless of whether it is translational or rotational. In fact, the force generated growths as this dimension increases, as already pointed out in the paragraph 3.1. It would therefore be natural to increase the size of the dimples in order to maximize the performance of the surface, with the constraint, however, of working only 50-60% of the available surface. A condition would be reached such as to have only a single dimple, no longer a succession, and a step would be created.

In fact, what happens is that the (partial) texturing represents a solution whose effects, from the point of view of hydrodynamic bearing capacity, are always lower than those achieved by a step bearing, whatever the operating conditions, as shown in Figure 3.24, taken from the article by Gropper et Al. [3.6].

Circular sectors in which a step has been created have also been simulated, in order to compare the bearing capacity generated by the step configuration with that generated by the succession of dimples.

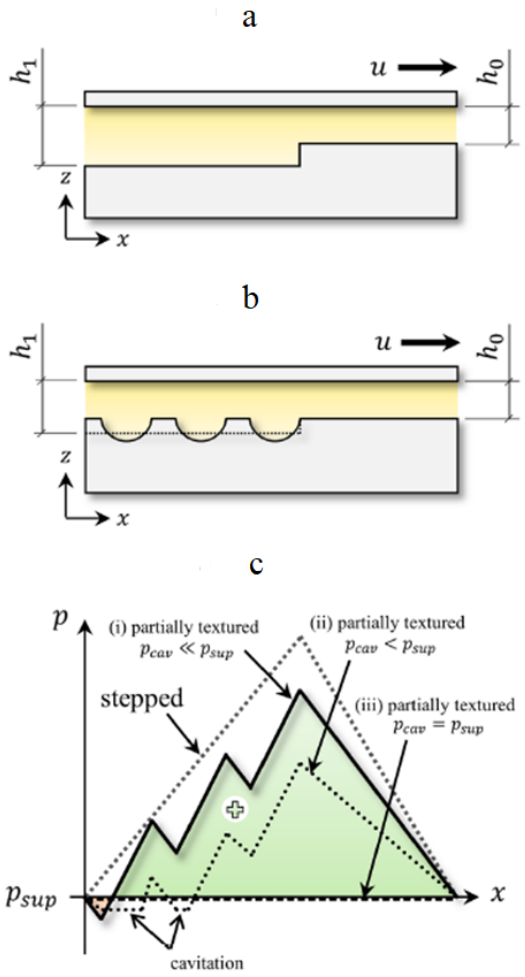

Figure 3.24. Schematic representation of: (a) stepped slider; (b) partially textured slider. (c) Typical pressure distributions over a stepped and partially textured slider. Image taken from Gropper et Al. [3.6]

Also in the case of geometry with step, it was checked that the mesh used in the previous case, Mesh 2 in the Table 3.3, was adequate. Similarly to the previous case, the Figure 3.25 shows the trend of the force as the mesh adopted varies: Mesh 2 is still adequate since the deviation from Mesh 3 is only 2.8%.

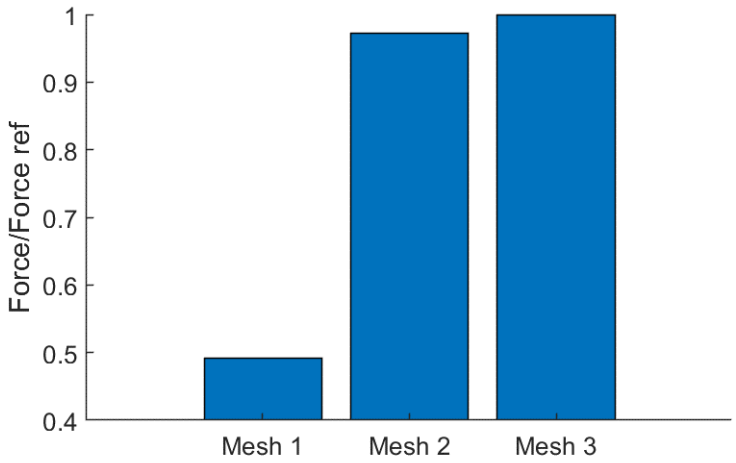

Figure 3.25. Influence of the mesh on the force generated by the step.

Figure 3.26 shows the pressure contour of a step with dimensions equal to 60% of the entire domain, 10 μm deep. The step is delimited by the internal and external radius to keep the oil confined inside, preventing it from dispersing due to the pressure difference that is established. The boundary conditions, speed and pressures, are the same as in the previous case, that is open boundary with zero relative pressure and rotation speed of the moving plane equal to 2500 r/min. As shown in Figure 3.27a, the pressure trend in the case of a step has a maximum that is more than double that of the case of a succession of dimples: it is therefore evident that even the bearing capacity is much greater in the case of a step. The Figure 4.24b shows a column chart that emphasize this aspect: the force that could be expressed by a step bearing is considerably greater than that obtainable with the sequence of dimples, with the same textured portion and boundary conditions.

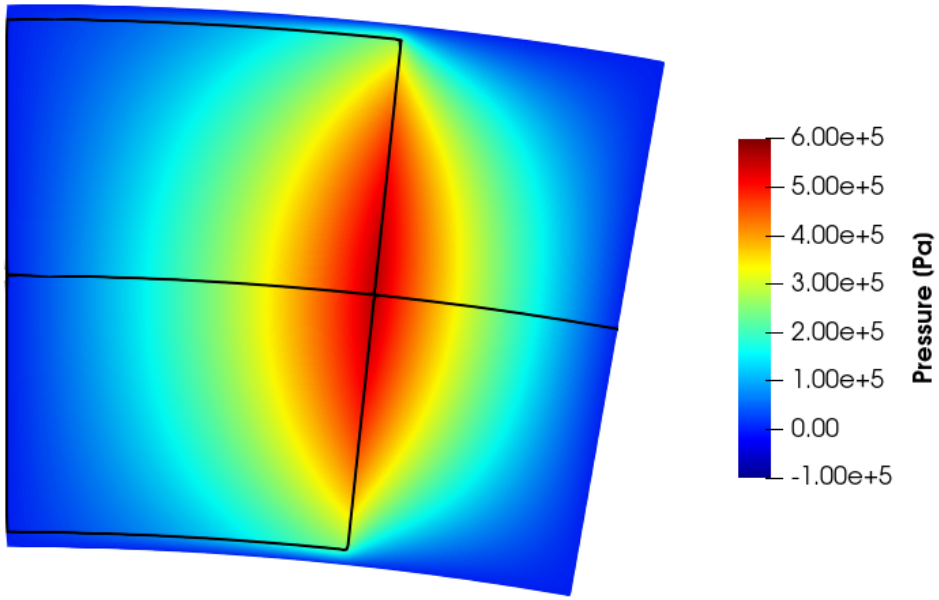

Figure 3.26. Pressure contour of a stepped sector 60% wide of the domain, depth 10 µm. Gap 10 µm and rotating speed 2500 r/min

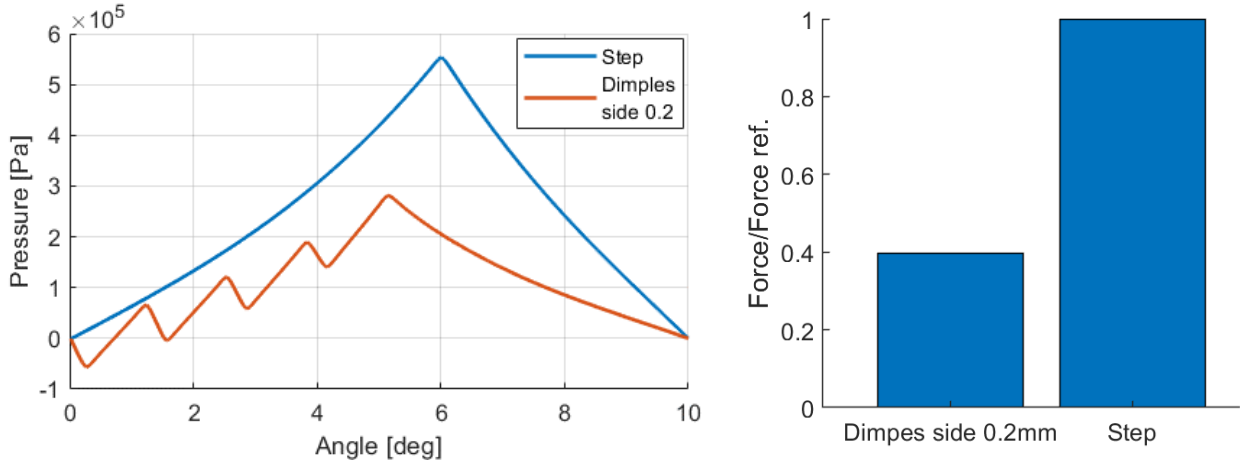

(a) (b)

Figure 3.27. (a) Pressure profiles calculated along the domain median line of the cases of Figure 3.22.a and Figure 3.26. (b) Comparison between the force generated by the step configuration and that with the dimples.

As also shown in the Figure 3.24, the step bearing has the advantage of starting the step on the inlet edge of the domain: this allows to avoid the divergence of the gap and therefore to avoid having a negative pressure at the beginning of the domain, allowing to reach even higher pressures. The negative pressure could reach values such as to trigger cavitation, as will be discussed later; avoiding depressurizing the gap with an accurate arrangement of the geometry is an excellent solution.

This geometry configuration represents the best textured surface condition able to guarantee the maximum hydrodynamic bearing capacity in a gap characterized by parallel surfaces in relative motion.

3.3.2 Multi sector surface

Generally, the surface to be texturized is large compared to the dimensions of dimples or steps. In this case, defining a sequence of steps is needed, whose geometric arrangement has to be defined to obtain the best possible performance. The overall effect will therefore be the sum of the contributions of each step.

Figure 3.28 shows the case of a circular sector with a width of 30° where there are three steps with the geometric characteristics of the previous case. Already from the pressure map it is evident that the first step generates a large overpressure, while the following two, in addition to the overpressure, also show a corresponding decrease in pressure in proximity of the divergent zone. This aspect is clarified by the pressure diagram of Figure 3.29. The result is that only the first step gives a contribution on the hydrodynamic bearing capacity, while the other two cancel each other out.

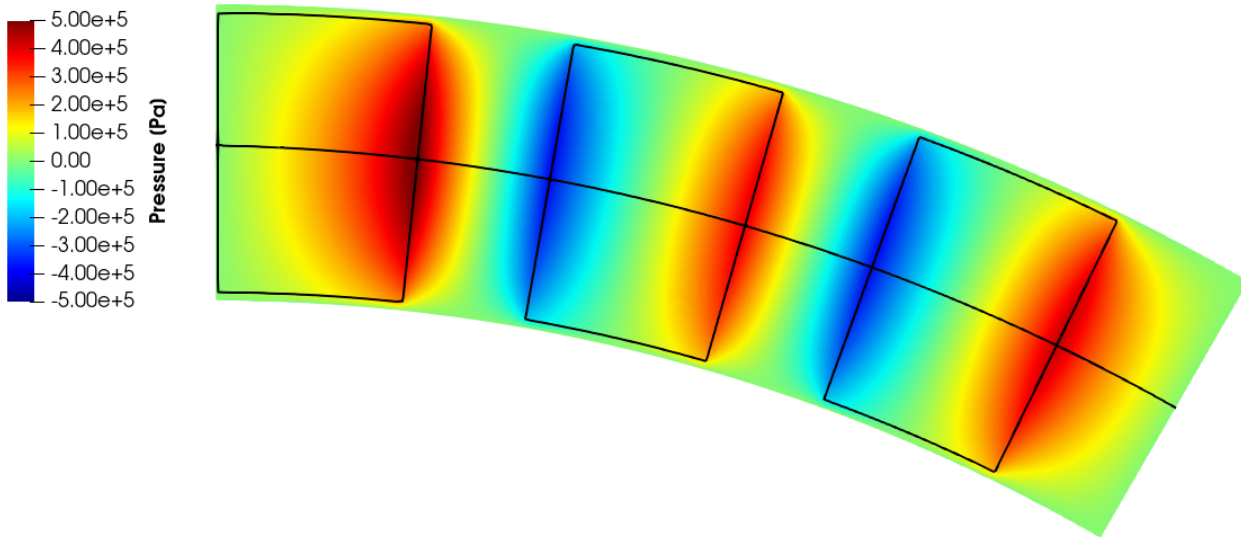

Figure 3.28. Pressure contour of a surface with three steps equal to each other's and equal distributed. Step depth 10 µm. Gap 10 µm and rotating speed 2500 r/min

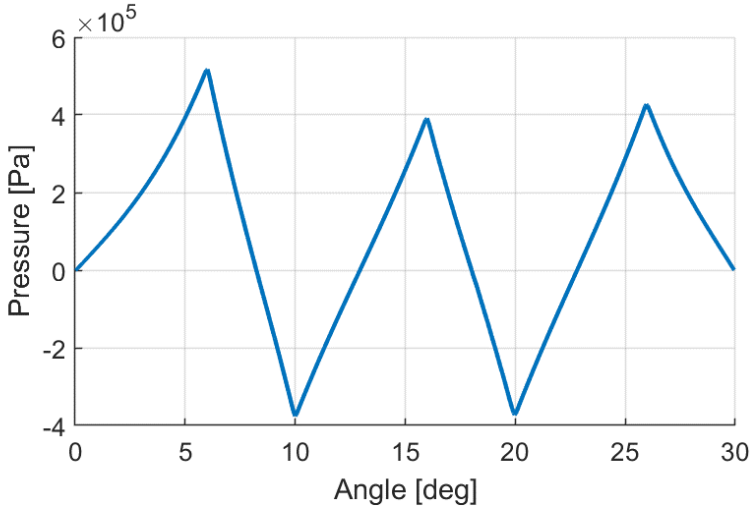

Figure 3.29. Pressure profiles calculated along the domain median line in a multi-stepped configuration.

In order to also include the effect of the steps subsequent to the first, the creation of a channel that allows the available surface to be divided into different sectors is required. This channel has an essential role: it permits to restore the pressure conditions at the inlet and outlet of each portion of the domain, in this case the relative pressure is zero, creating a sectoral structure in which each sector is independent of each other, as shown in the pressure contour in Figure 3.30. In each sector, a step is then introduced which covers 60% of the available surface. For this reason, it has been decided to call it the "recovery channel". The Figure 3.31 shows the comparison between the pressure profile without and with the recovery channel: this limits the minimum pressure reached, allowing to greatly increase the generated bearing capacity. In addition, it also plays a fundamental role in reducing the minimum pressure reached, letting fluid to be drawn from the outside, preventing, or at least reducing, the onset of cavitation. Unlike the single step configuration, in this case there is an area where the gap diverges: this zone is where it is possible for the oil to cavitate, as will be shown later in this Thesis.

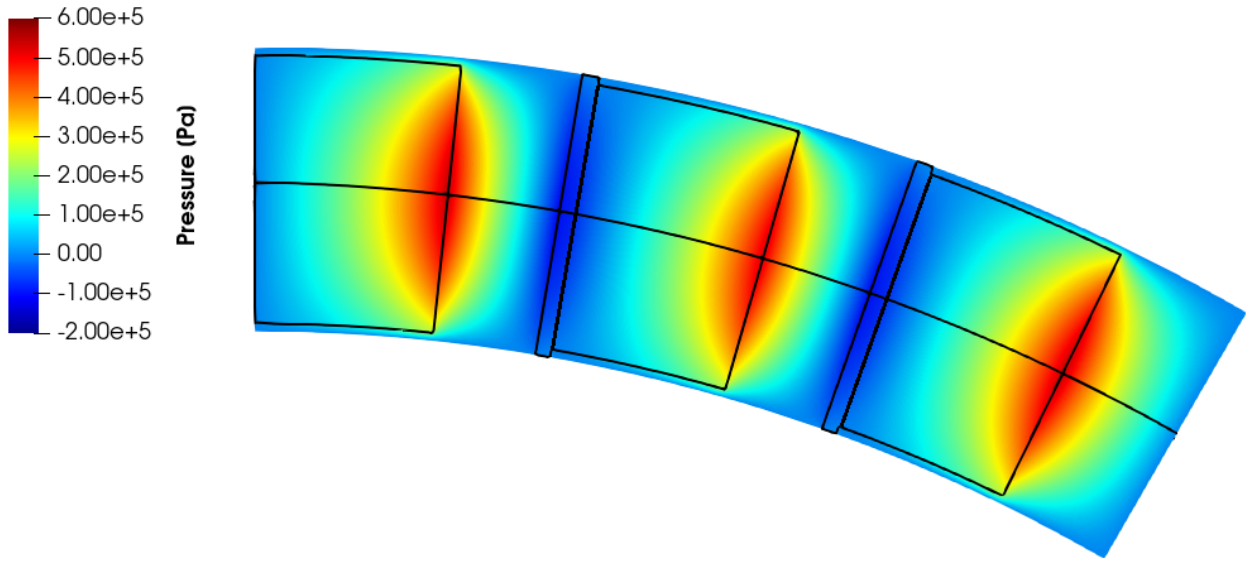

Figure 3.30. Pressure contour of a surface with three sectors equal to each other's and equal distributed delimitated by the recovery channels. Step width 60% and depth 10 µm. Gap 10 µm and rotating speed 2500 r/min

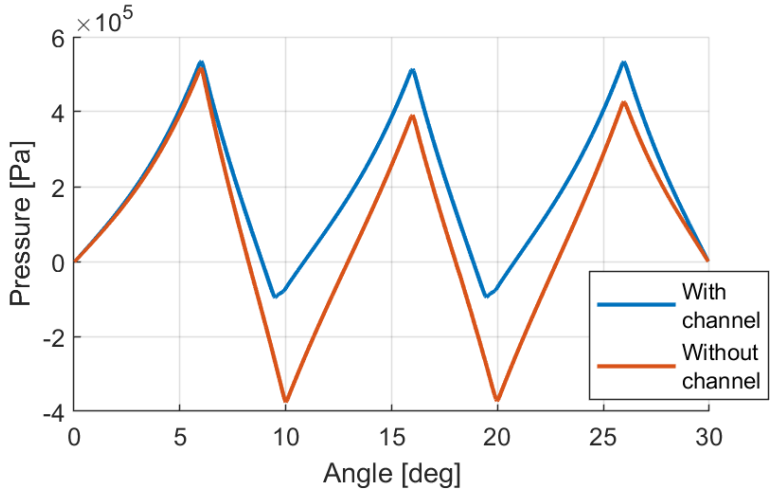

Figure 3.31. Pressure profiles calculated along the domain median line in a multi-stepped configuration with and without the recovery channels.

The need to introduce a recovery channel is independent of the type of texturing considered: even in the case of a succession of individual dimples, the recovery channel is necessary. Similarly to the case of the succession of steps, the Figure 3.32 shows a surface characterized by a sequence of dimples. The pressure profile in the Figure 3.33 highlights the same problem described above.

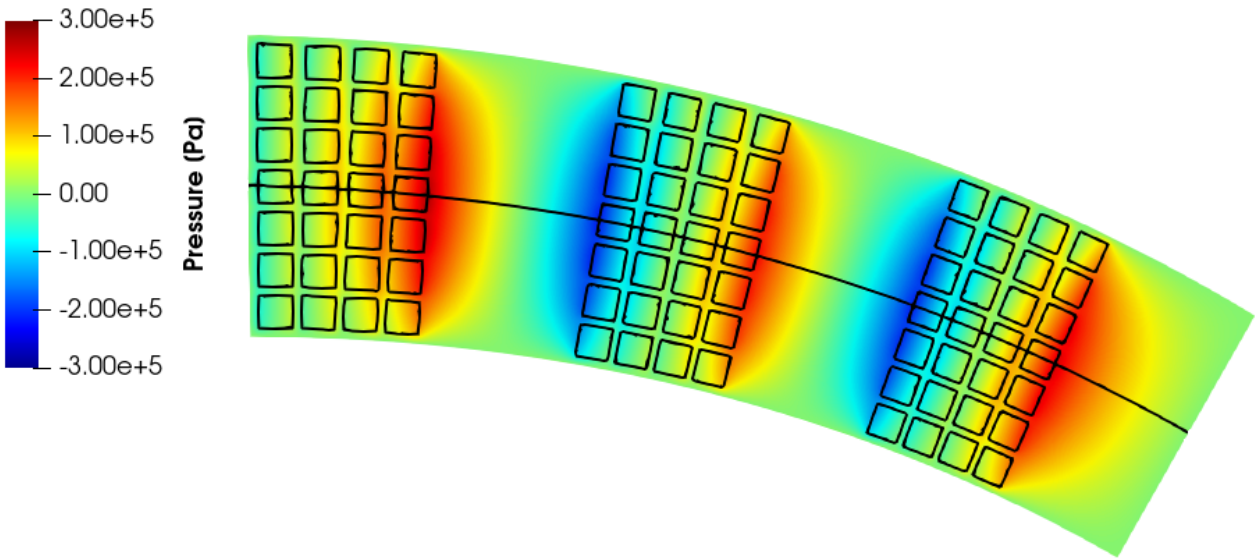

Figure 3.32. Pressure contour of a surface with three sequences of square dimples equal to each other's and equal distributed delimitated by the recovery channels. Dimples side 0.2 mm and depth 10 µm. Gap 10 µm and rotating speed 2500 r/min

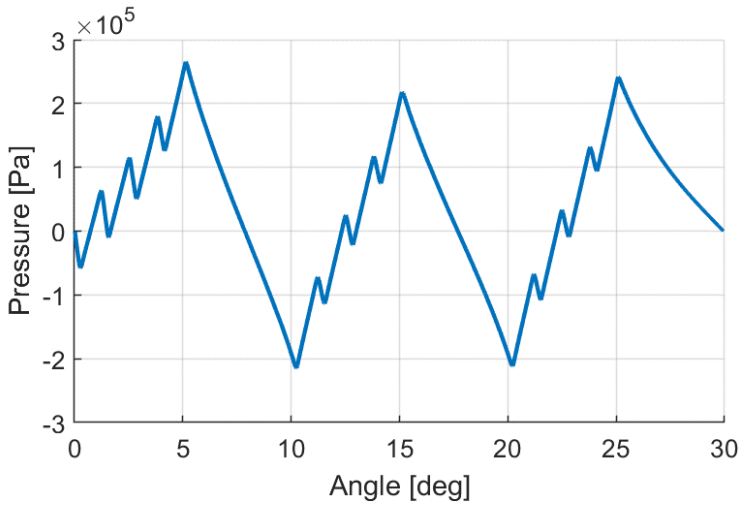

Figure 3.33. Pressure profiles calculated along the domain median line in a multi-sequence of dimples configuration.

However, thanks to the introduction of recovery channels that divide the domain into sectors of equal width, as shown in Figure 3.34, it is also possible in this case to limit the minimum pressure and guarantee a good bearing capacity, as confirmed by the pressure profile reported in the Figure 3.35.

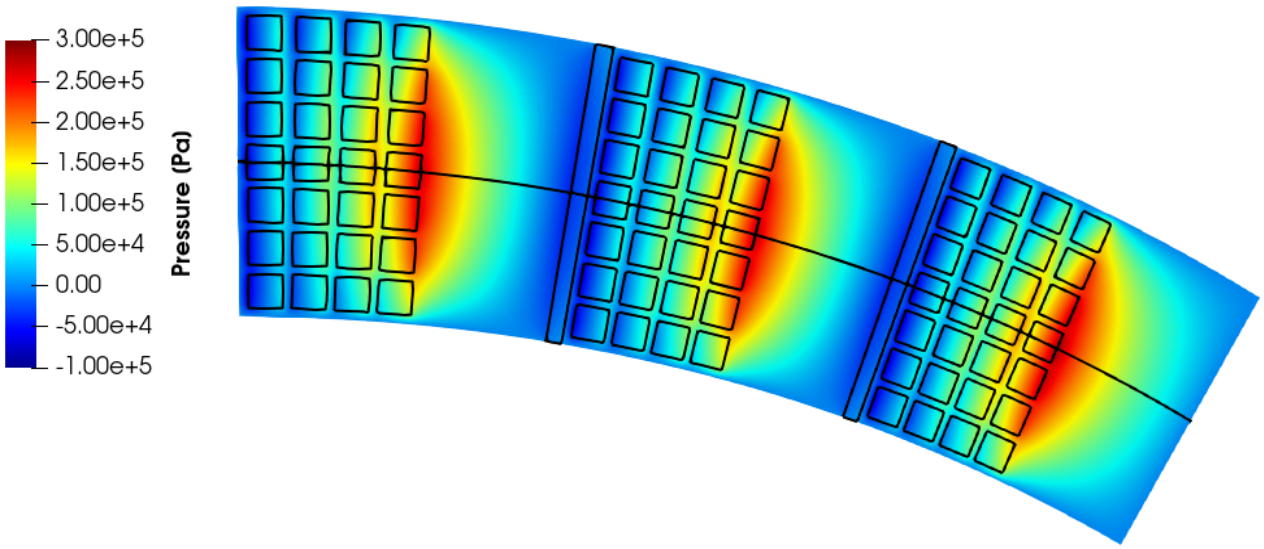

Figure 3.34. Pressure contour of a surface with three sectors equal to each other's and equal distributed delimitated by the recovery channels. Dimples side 0.2 mm and depth 10 µm. Gap 10 µm and rotating speed 2500 r/min

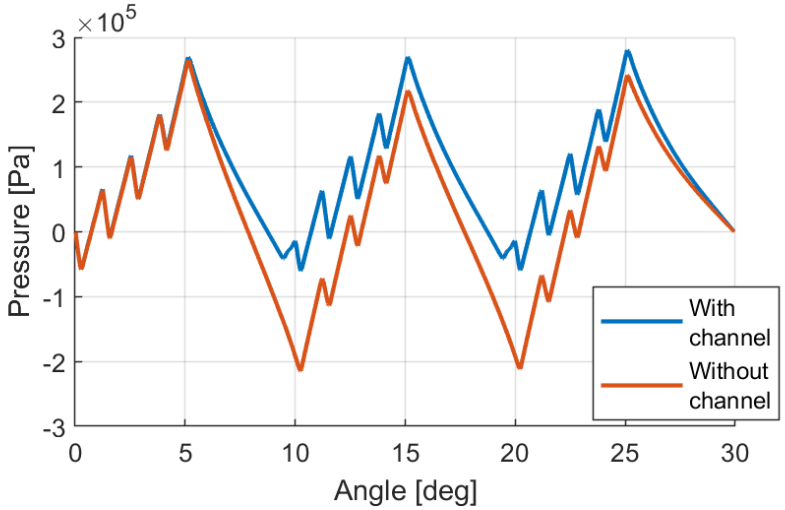

Figure 3.35. Comparison between the pressure profiles calculated along the domain median with and without the recovery channels.

The bar graph in the Figure 3.36 shows the comparison between the force generated by the configuration with the steps and that with the dimples, in the presence of the recovery channels. The force is always positive and greater than zero, however, the geometry with the steps permits to obtain a much greater force, twice as high as the succession of dimples. The force value is dimensionless for confidential reasons.

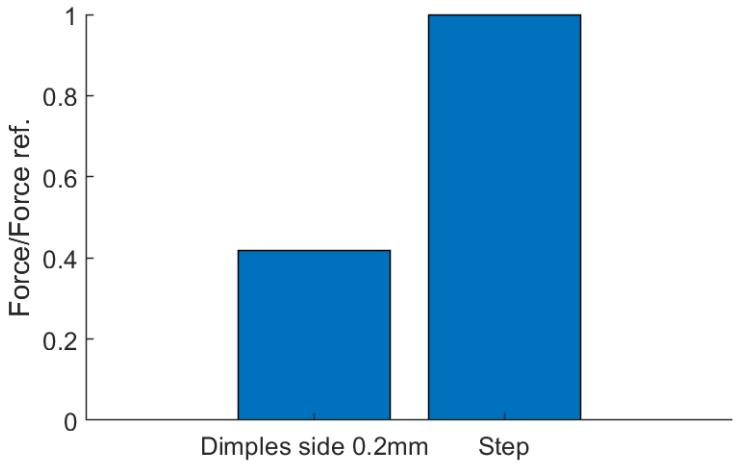

Figure 3.36. Comparison between the force generated by the step configuration and that with the dimples over a three sector surface delimitated by recovery channels.

List of references

3.1 Casoli P., Scolari F., Rossi C., Rigosi M. A cfd design of engineered surface for tribological performance improvements in hydraulic pumps. 12th International Fluid Power Conference, Dresden. 2020. Doi: 10.25368/2020.41

3.2 Casoli P., Scolari F., Rundo M., Lettini A., Rigosi M. CFD analyses of textured surfaces for tribological improvements in hydraulic pumps. Energies. 2020. Doi: 10.3390/en13215799

3.3 Li1 K., Jing K., Hu J., Ding X., Yao Z. Numerical investigation of the tribological performance of micro-dimple textured surfaces under hydrodynamic lubrication. Beilstein Journal of Nanotechnology. 2017. Doi: 10.3762/bjnano.8.232

3.4 Vilhena L., Sedlacek M., Podgornik B., Rek Z., Zun I. CFD modeling of the effect of different surface texturing geometries on the frictional behavior. Lubricants. 2018. Doi: 10.3390/lubricants6010015

3.5 Brizmer V., Kligerman Y., Etsion I. A laser surface textured parallel thrust bearing. Tribology Transactions. 2003. Doi: 10.1080/10402000308982643

3.6 Gropper D., Wang L., Harvey T. J. Hydrodynamic lubrication of textured surfaces: A review of modelling techniques and key findings. Tribology International. 2016. Doi: 10.1016/j.triboint.2015.10.009

Chapter 4. Cavitation

This chapter provides details regarding cavitation. Initially the theory of the phenomenon is proposed, and then the equations that describe it are reported.

The cavitation modeling techniques within the CFD software are explained in detail, and the simulation results and any limitations of the models are discussed.

Finally, a lumped parameter model for the simulation of gaseous and vapor cavitation is illustrated in detail and the results are compared with experimental data.

4.1 Introducing the phenomenon

The liquid used in hydraulic systems always contains gas, usually air. This gas is dissolved in the liquid and generally does not affect the performance of the fluid when operating at high pressures. The hydraulic circuits are characterized by high pressures, however conditions may occur such that the pressure inside the pipe drops below the atmospheric pressure: for example, it could occur at the inlet of a pump [4.1, 4.2]. If the pressure decreases below atmospheric pressure, the gas dissolved in the liquid tends to be released in free form, in the shape of bubbles: this process is called aeration. Conversely, if the pressure increases, the free gas tends to dissolve back into the liquid (dissolution). The hydraulic properties of the fluid are significantly changed only when the gas is present in undissolved form, [4.3 - 4.5].

In addition to the release and dissolution of air, the hydraulic fluid itself could vaporize due to cavitation (decrease in pressure) or boiling (increase in temperature). The Figure 4.1 summarizes the different processes that could affect the fluid as the pressure decreases.

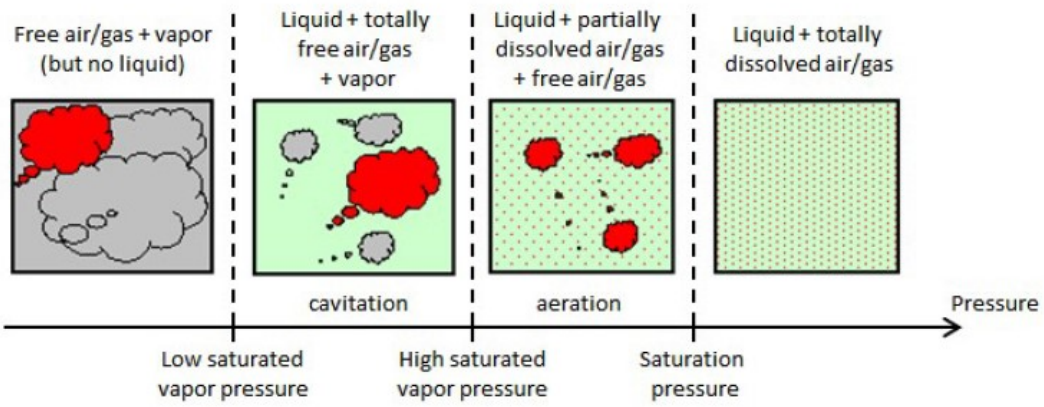

Figure 4.1. Evolution of the gas phases as the pressure varies.

The presence of a gas phase due to cavitation in a hydraulic system is a great problem. Vapor is unstable and, when reaches a higher pressure region, usually collapses violently because the pressure inside the vapor bubbles is generally similar to the vapor pressure. As a result, there are many consequences depending on the type of application:

- alteration of system performance, like a reduction in the efficiency in turbomachinery, energy dissipation;
- the presence of additional forces on the components;
- generation of noise and vibrations;
- wall erosion, in case of fully developed cavitation.

The damage produced by cavitation could be considerable and it is therefore very important to know whether conditions for the onset of cavitation are reached in the study application and where any gas phase is concentrated.

For these reasons it is required to have an accurate cavitation model, which allows to simulate in a realistic way the behavior of the fluid, especially in low pressure areas.

4.1.1 Gaseous cavitation

The liquid used in hydraulic systems usually contains gas, which could be dissolved or undissolved. The maximum amount of gas dissolved in a liquid (the solvent) is called solubility. The maximum volume of air dissolved at a given pressure and temperature is constant: a volume of liquid V_0 is able to dissolve in solution, depending on the pressure to which it is subjected, a volume of air V_g which could be known according to Henry-Dalton law, Equation (4.1):

$$V_g = V_0 \cdot \alpha \cdot \frac{p}{p_0} \tag{4.1}$$

The expression shows a linear dependence of the air solubility in the liquid with pressure. The proportionality coefficient α is called Bunsen coefficient. The Bunsen coefficient is generally used to express the solubility of a gas in the liquid: it is defined as the volume of gas V_g reduced under standard conditions (p_{atm} = 1.013 barA and T_0 = 273.15 K) dissolved per unit volume of liquid V_l:

$$\alpha = \frac{V_g(p_{atm}, T_0)}{V_l} \tag{4.2}$$

Table 4.1 gives some values of the Bunsen coefficient for air in various liquids, from [4.1].

Table 4.1. Bunsen coefficient for air in several liquids.

Liquid	Bunsen coefficient
Fuels	0.15 – 0.25
Mineral oil	0.06 – 0.12
Water	0.02

The Figure 4.2 shows the solubility of a gas in a liquid. The saturation limit separates the region for which the gas is completely dissolved in the liquid and the region for which the gas is both dissolved and undissolved. The graph is given at the equilibrium condition.

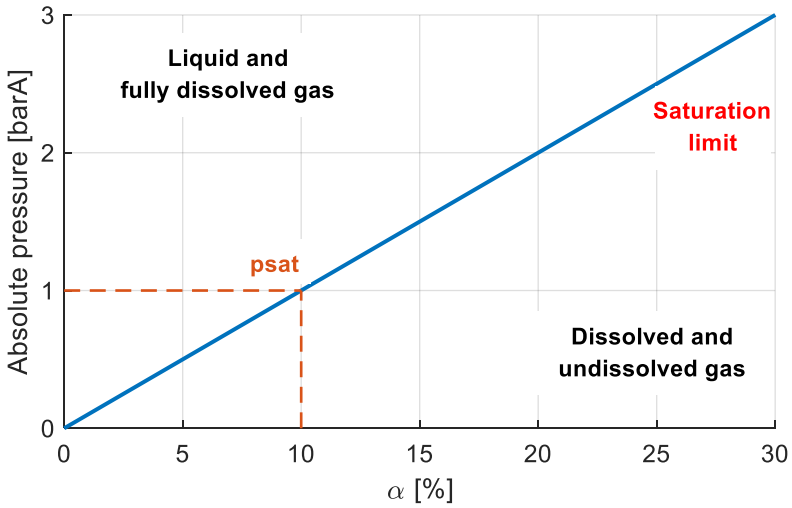

Figure 4.2. Solubility of a gas in a liquid at equilibrium condition.

The processes of solution and separation of air in oil are complex phenomena and do not even occur instantaneously, but they are characterized by different time constants: in general, the dissolution process is much slower than the separation.

4.1.2 Vapor cavitation

The concept of vapor pressure is simpler to consider from the point of view of classical thermodynamics. Considering the water, in the phase diagram shown in Figure 4.3, the line from the triple point T_r to the critical point C distinguishes the liquid and vapor regions.

The crossing of this curve represents a reversible transformation in equilibrium conditions, that is condensation or evaporation of the fluid at pressure p_v, which is the vapor pressure, a function of the temperature T.

As a result, vapor cavitation in a liquid could happen by dropping the pressure remaining at a nearly constant temperature, a condition that frequently occurs locally in real flows. Therefore, the vapor cavitation phenomenon looks similar to boiling, with the difference that the cause is not a temperature variations but a pressure changes due to the flow dynamics.

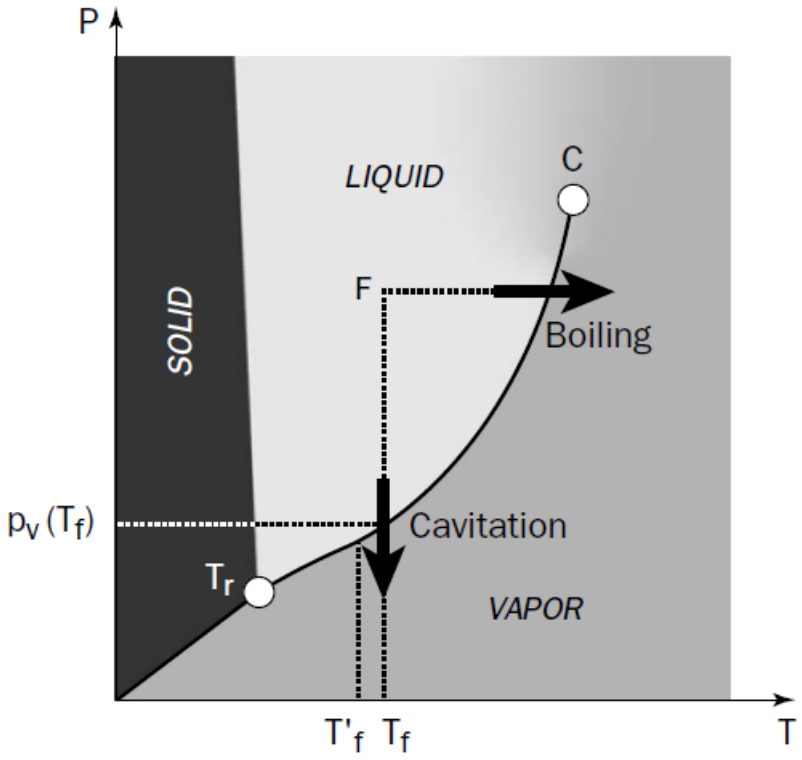

Figure 4.3. Phase diagram of water.

The consequences of vapor cavitation are the erosion of metal components due to the implosion of vapor bubbles.

4.1.3 Rayleigh-Plesset equation

The Rayleigh-Plesset equation governs the dynamics of a spherical bubble immersed in a liquid and is applied to various practical cases such as the formation of a bubble from nuclei, the collapse of a bubble, etc.

The main hypotheses for obtaining the Rayleigh-Plesset equation are:

- Spherical bubbles;
- Incompressible liquid;
- Gravity is neglected;
- The amount of air inside a bubble is constant and does not exchange heat with the outside;
- The partial pressure of the vapor inside the bubble is the vapor pressure at the temperature of the liquid.

In the liquid domain $r \geq R(t)$, the expressions of the velocity *u(r, t)* and of the pressure *p(r, t)* induced by the evolution of the bubble, Figure 4.4, will be calculated.

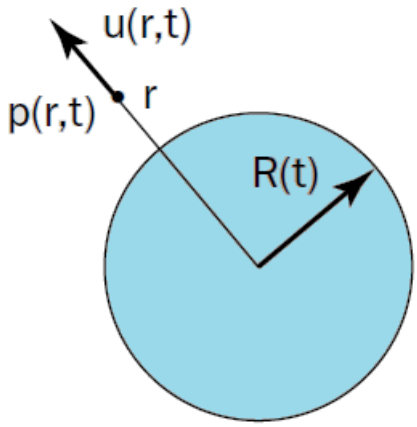

Figure 4.4. Spherical bubble immersed in a liquid.

Boundary conditions

The mass transfer to the interface is ignored and for this reason the speed of the liquid u at the interface is equal to the speed of the interface $\dot{R} = {dR}/{dt}$.

The normal stress at the interface in the case of fluid with kinematic viscosity υ is:

$$\sigma|_{r=R} = -p(R) + 2\mu \left.\frac{\partial u}{\partial r}\right|_{r=R} \tag{4.3}$$

The normal force balance leads to:

$$-\sigma|_{r=R} = p_v - \frac{2S}{R} \tag{4.4}$$

Therefore, the pressure at the interface is given by:

$$p(R) = p_v - \frac{2S}{R} + 2\mu \left.\frac{\partial u}{\partial r}\right|_{r=R} \tag{4.5}$$

Rayleigh-Plesset equation

The conservation equation of mass for an incompressible fluid is:

$$u(r,t) = \frac{dR}{dt} \cdot \frac{R^2}{r^2} \tag{4.6}$$

In this case, the viscous term of the Navier-Stokes equation is zero and therefore reduces to:

$$\frac{\partial u}{\partial t} + u\frac{\partial u}{\partial r} = -\frac{1}{\rho}\frac{\partial p}{\partial r} \tag{4.7}$$

From which, replacing the expression of speed, it could be obtained:

$$\frac{d^2R}{dt^2}\frac{R^2}{r^2} + 2\left(\frac{dR}{dt}\right)^2\left[\frac{R}{r^2} - \frac{R^4}{r^5}\right] = -\frac{1}{\rho}\frac{\partial p}{\partial r} \tag{4.8}$$

Integrating with respect to *r* leads to:

$$\frac{p(r,t) - p_\infty(t)}{\rho} = \frac{d^2R}{dt^2}\frac{R^2}{r} + 2\left(\frac{dR}{dt}\right)^2\left[\frac{R}{r} - \frac{R^4}{4r^4}\right] \tag{4.9}$$

Which at the interface for $r = R$ becomes:

$$\frac{p(R,t) - p_\infty(t)}{\rho} = \frac{d^2R}{dt^2}R + \frac{3}{2}R\left(\frac{dR}{dt}\right)^2 \tag{4.10}$$

Considering that:

$$\left.\frac{\partial u}{\partial r}\right|_{r=R} = -\frac{2}{R}\frac{dR}{dt} \tag{4.11}$$

The expression obtained is:

$$\rho\left[\frac{d^2R}{dt^2}R + \frac{3}{2}R\left(\frac{dR}{dt}\right)^2\right] = p_v - p_\infty(t) - \frac{2S}{R} - \frac{4\mu}{R}\frac{dR}{dt} \tag{4.12}$$

This is the Rayleigh-Plesset equation that allows to know the temporal evolution of the bubble radius and the pressure in the liquid. Generally, the term containing viscosity is neglected and the most common equation is:

$$\rho\left[\frac{d^2R}{dt^2}R + \frac{3}{2}R\left(\frac{dR}{dt}\right)^2\right] = p_v - p_\infty(t) - \frac{2S}{R} \tag{4.13}$$

4.1.4 Zwart model

A popular and widespread cavitation model implemented in many numerical simulation software has been proposed by Zwart et Al. [4.7]. The model has been derived from the Rayleight-Plesset equation, described above, which controls the dynamics of a spherical bubble immersed in a liquid.

The formulation assumes there are two phases within the fluid domain, one of which is liquid and the other is gaseous.

Starting from the Rayleigh-Plesset, Equation (4.13), the rate of variation of bubble volume could be expressed as follows:

$$\frac{dV_B}{dt} = \frac{d}{dt}\left(\frac{4}{3}\pi R_B^3\right) = 4\pi R_B^2 \sqrt{\frac{2}{3}\frac{p_v - p}{\rho_f}} \tag{4.14}$$

while the rate of change of bubble mass is given by multiplying the Equation (4.14) for the air density. Assuming that N_B are the bubbles present per unit volume, the volume fraction r_g could be expressed as follows:

$$r_g = V_B N_B = \frac{4}{3}\pi R_B^3 N_B \tag{4.15}$$

and the interphase mass transfer rate expressed per unit volume is:

$$\dot{m}_{fg} = F\frac{3 r_g \rho_g}{R_B}\sqrt{\frac{2}{3}\frac{|p_v - p|}{\rho_f}}\; sign(p_v - p) \tag{4.16}$$

The Equation (4.16) refers to the case of condensation, while in the case of vaporisation it should be modified. The process is originated at nucleation sites, but when the vapor volume fraction increases, the nucleation site density should decrease: in the case of vaporisation, r_g is replaced by $R_{nuc}(1\text{-}r_g)$.

$$\dot{m}_{fg} = F\frac{3 R_{nuc}(1 - r_g) \rho_g}{R_B}\sqrt{\frac{2}{3}\frac{|p_v - p|}{\rho_f}}\; sign(p_v - p) \tag{4.17}$$

Where R_{nuc} is the volume fraction of the nucleation sites. In Equations (4.16) and (4.17) F is an empirical parameter which controls the process velocity and might be different in the case of

vaporisation, F_v or condensation, F_c,: in general vaporisation is a process that happens faster than condensation and this aspect is quantified with the F parameter.

4.2 Gaseous cavitation – Application to textured surfaces

In the simulation results shown in Chapter 3, the amplitude of the pressure profile is such that the minimum pressure value reached could be below absolute zero, which is obviously not physical. Therefore, introducing a cavitation model in the simulations is needed.

As previously described, the first phenomenon that happens when the pressure decreases below the atmospheric pressure is gaseous cavitation. In the scientific literature there are articles that use the model proposed by Zwart et Al. [4.7] to study gaseous cavitation. In fact, although the Zwart model has been developed for vaporization and condensation applied to water, it could also be applied to the release and absorption of gas since the theory behind the two phenomena is the same, namely the dynamics of bubbles [4.8]. The values of the parameters that characterize the cavitation model could be found in literature and are listed in Table 4.2. Zhou et Al. [4.8] suggest different values, Set A, focusing on the cavitation phenomenon applied to an orifice using a hydraulic oil as fluid and they find good agreement between experimental data and simulations results. Instead, Zwart et Al. [4.7] propose a different set of values, Set B, mainly related to water, but the authors assert that they could be also valid for different fluids and applications. These two sets have been also used by Del Campo et Al. [4.9], who conducted numerical simulations of an external gear pump under cavitating conditions.

The volume of the dissolved air in the hydraulic oil is given by the Bunsen coefficient, which represents the ratio between the volume of gas and the volume of liquid at normal and equilibrium conditions, which is 0.09 for mineral oil (from Table 4.1). Consequently, the nucleation sites density has been kept fixed and the value is the Bunsen coefficient [4.9]. The density value of the nucleation sites has been kept constant also to highlight the great variability of the results that derives from the uncertainty about the air parameters. The bubble radius R_B has been set equal to 0.5 μm, since the heights of the gap considered are of the same order of magnitude.

Table 4.2. Different cavitation sets of coefficients used in the simulations.

	R_b	R_{nuc}	F_r	F_a
Set A	0.5 μm	0.09	0.09	0.01
Set B	0.5 μm	0.09	50	0.01

With the model adopted, when the pressure decreases and reaches the saturation value the pressure remains constant instead of further decreasing. In this Chapter to overcome this question and to present a general overview of the behavior of textured surfaces in the presence of gaseous cavitation, the simulations have been carried out using different saturation pressures, [4.10]. The aim of this paragraph is to investigate the effect of the gas formation on the bearing capacity generated by the textured surface with the fluid model available, also considering the great uncertainty of the cavitation parameters present in the literature.

4.2.5 Single dimple

The onset of the cavitation phenomenon modifies the pressure field generated by the presence of the dimple. The Figure 4.5 shows the pressure profile generated by a square dimple as the height of the gap decreases, using the cavitation parameters of Set A with a saturation pressure of -0.7 bar. From the graph it could be observed that if the gap height is 5 microns or less, the pressure drops below the oil saturation threshold, allowing cavitation to begin. When the pressure reaches the saturation value, the model formulation blocks the minimum pressure with the consequence that the pressure profile is no longer symmetrical. Considering that the maximum value is slightly affected by the onset of cavitation, within the domain the average pressure is no longer zero, but assumes a positive value: this allows for a positive integral on the moving plane, generating a positive bearing capacity.

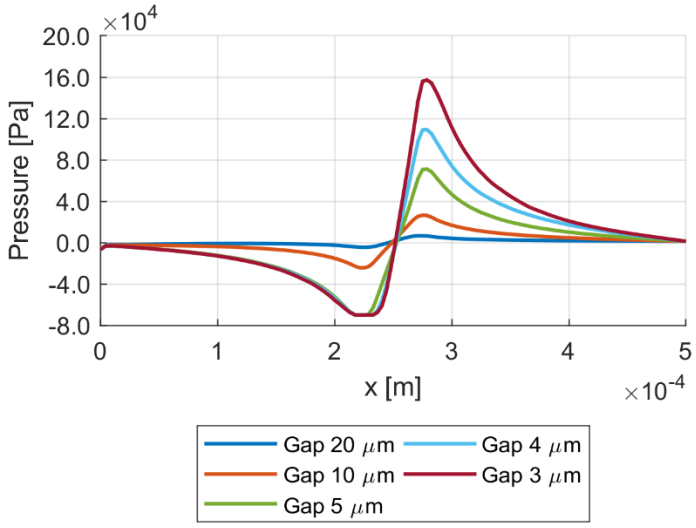

Figure 4.5. Pressure profile of a square dimple with side of 50 μm and depth 10 μm for different values of the gap. Sliding velocity 5 m/s. Set A parameters of cavitation.

The Figure 4.6 shows the bearing capacity as a function of the gap height for several dimples size. The tendency, in general, is an increasing of the generated force as the gap decreases and the trend is more than linear. The rising of the bearing capacity due to a gap height reduction is a useful aspect to counteract a possible approach between the two coupled surfaces and could avoid an eventual condition of direct contact. The force values are divided by a reference value for confidential reasons.

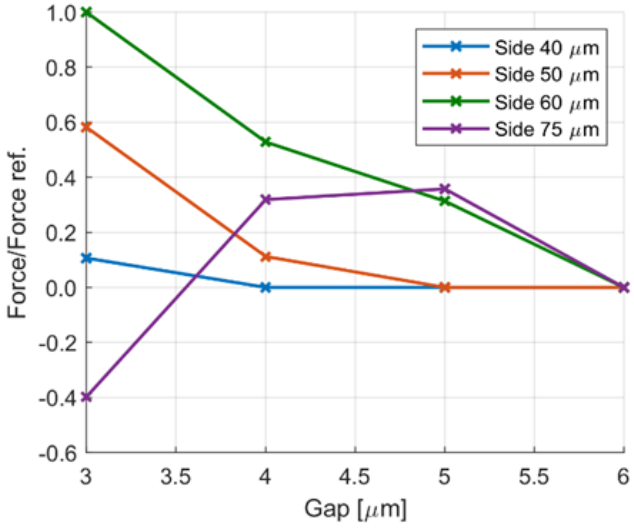

Figure 4.6. Bearing capacity is generated by a square dimple. Influence of the gap for different sizes of the dimple. Dimple depth 10 μm, sliding velocity 5 m/s. Set A parameters of cavitation.

The Figure 4.6 also shows the influence of the size of the dimple on the bearing capacity. A larger dimple provides a greater contribution; however, a limit exists, beyond which the bearing capacity decreases, modifying the trend until negative forces are obtained. The reason is that larger dimples are characterized by a greater quantity of released air, at the saturation pressure, which fills almost the entire dimple; air that does not have time to be reabsorbed and this strongly limits the overpressure peak that could be reached, conditioning the bearing force that could be expressed by the surface. To better understand this specific condition, the Figure 4.7 shows the volume fraction of free air in the case of square dimple with side 75 μm and gap 3 μm, highlighting only the portion of the mesh where the air volume fraction is greater than 1‰. Almost the entire volume available inside the dimple is filled with free air at the saturation pressure: the bearing capacity could only be negative and this justifies the trend of the curve in Figure 4.6. With smaller dimples, the amount of air released is less and has the time required to be reabsorbed, allowing to obtain a positive bearing capacity.

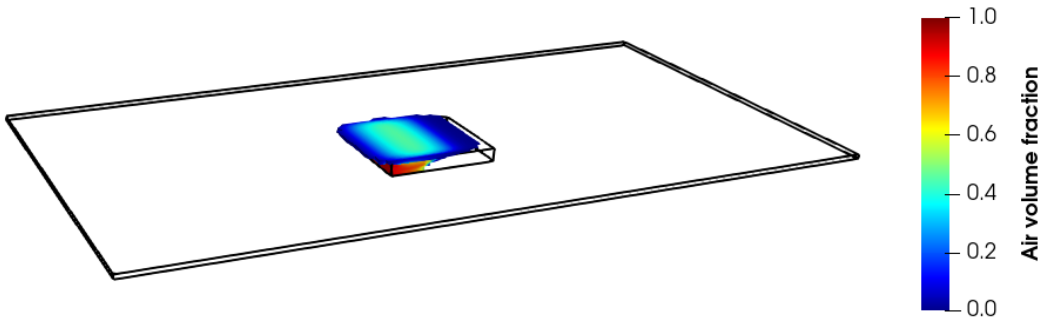

Figure 4.7. The air volume fraction generated by a square dimple with side of 75 µm and depth 10 µm. Gap 3 µm, sliding velocity 5 m/s. The volumes of the mesh where the volume fraction of air is greater than 1‰ are highlighted.

Using Set B of parameters from Table 4.2 the results are similar: the asymmetry of the pressure profile induced by cavitation allows to obtain a positive bearing capacity. A comparison between the two sets of parameters is not reported because the bearing capacity generated by a single dimple is very small, but will be shown for subsequent cases.

4.2.6 Full texturing

As the gap decreases, the pressure profile tends to increase in amplitude, as in the case of the single dimple.

Also for this configuration, cavitation is established as the gap decreases or the sliding speed of the moving surface increases. The Figure 4.8 shows the pressure contour in the case of a domain with a gap equal to 3 µm, using the parameters of Set A, with a saturation pressure of -0.7 bar.

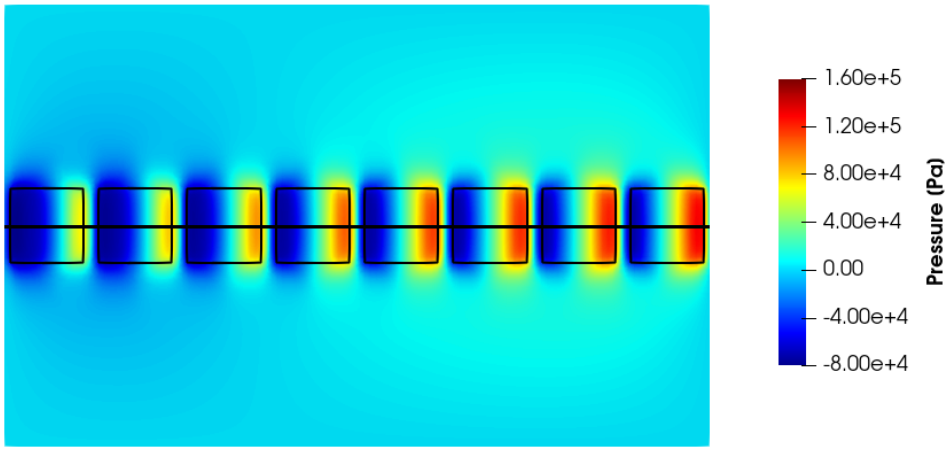

Figure 4.8. Pressure contour of the full texturing configuration under cavitation condition. Square dimples with side 50 µm and depth 10 µm. Gap 3 µm, sliding velocity 5 m/s. Set A of cavitation parameters.

In this working condition, the first dimples show a considerable area involved in the cavitation process, which progressively decreases until it disappears completely. After the first dimples, the fluid pressure tends to increase from dimple to dimple, since each makes a positive contribution. The onset of cavitation disturbs the symmetry of the pressure profile due to geometric symmetry, generating an increasing pressure ramp within the domain, as shown in the Figure 4.9 where the pressure profile calculated on the moving plane along the black line of the contour is plotted. However, the overpressure generated at the end of the domain is not sufficient to balance the highly negative effects of cavitation with the final result that the force generated is negative.

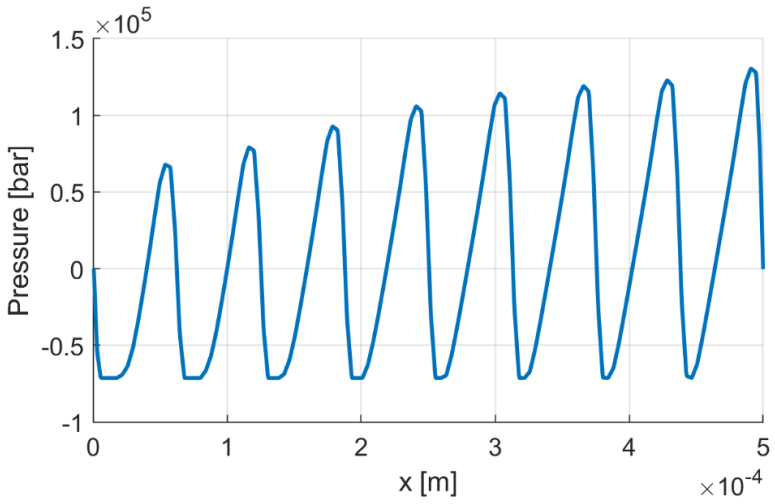

Figure 4.9. Pressure profile of a full textured configuration under cavitation condition. Dimple with side of 50 µm and depth 10 µm for different values of the gap. Sliding velocity 5 m/s. Set A parameters of cavitation.

The overall bearing capacity is negative because with the Set A cavitation parameters, a great amount of air is released in proximity of every dimple, as shown in Figure 4.10, which negatively affects the integral over the entire surface.

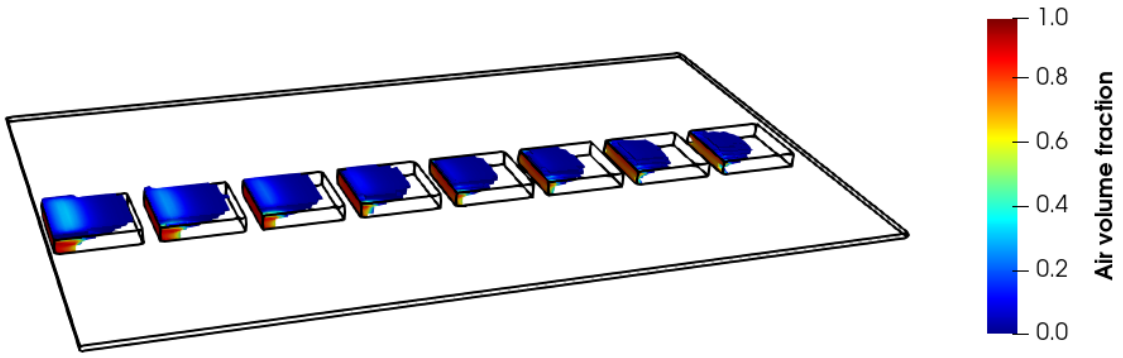

Figure 4.10. The air volume fraction: dimples side 50 µm and gap 3 µm, sliding velocity 5 m/s. Set A of the cavitation coefficients. Only the portions of the mesh where the volume fraction of air is greater than 1‰ are highlighted.

Using the Set B cavitation coefficients, the results are even worst, Figure 4.11. Compared to Set A the air absorption coefficient is the same, while the release one is much higher: consequently, a much more quantity of air is released in the domain. The result is that the fluid approaches the following dimple with a fraction of pre-existent air, limiting the pressure increasing near the convergent zone of the dimple. There is a propagation of the cavitation process with the release of a great amount of air on the entire domain.

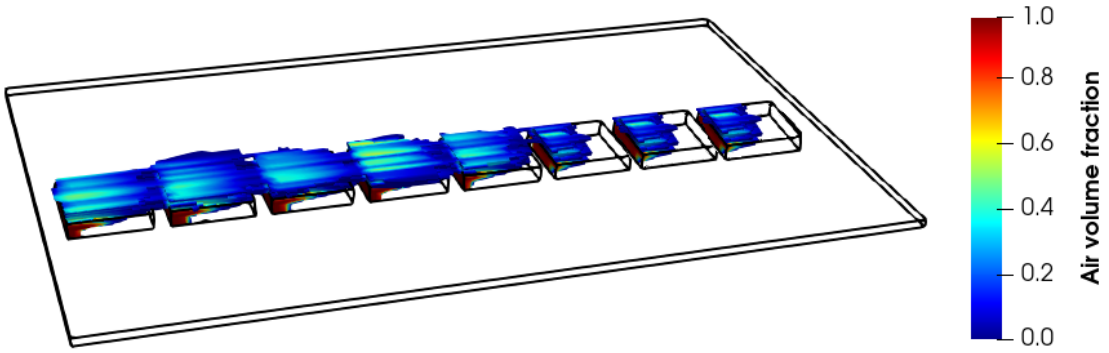

Figure 4.11. The air volume fraction: dimples side 50 µm and gap 3 µm, sliding velocity 5 m/s. Set B of the cavitation coefficients. Only the portions of the mesh where the volume fraction of air is greater than 1‰ are highlighted.

No cases are reported in which the saturation pressure changes, because in the full texturing configuration the bearing capacity generated in the presence of cavitation is always negative.

4.2.7 Partial texturing

Similarly to the other configurations previously described, also in a partial texture configuration a reduction of the gap or an increase in the sliding speed between the two surfaces leads to an increase in the amplitude of the pressure profile, which could trigger the cavitation phenomenon.

In this section the sliding speed has been increased to 10 m/s to better highlight the effects on the pressure distribution.

The behaviour of a partially textured surface varies with respect to the set of parameters and the air saturation pressure.

The Figure 4.12 shows the force as a function of the gap using Set A as cavitation parameters. Given the formulation of the cavitation model used, the trend is strongly influenced by the cavitation pressure. The values are divided by a reference value for confidential reasons.

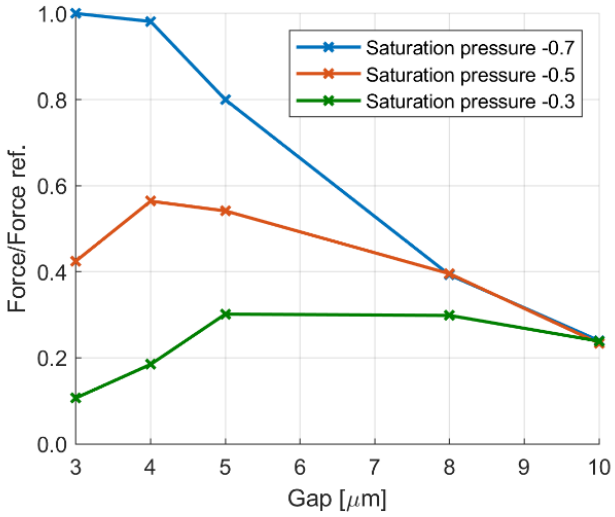

Figure 4.12. Bearing capacity generated by a partial texturing configuration. Influence of the gap for different values of saturation pressure. Set A cavitation coefficients. Square dimple with side 50 µm and depth 10 µm, sliding velocity 10 m/s

For gap heights greater than 10 µm the trend is the same, regardless of the saturation pressure: the amount of air formed is negligible since the saturation pressure is not reached. By decreasing the gap, the trend varies according to the saturation pressure. If a higher saturation pressure is considered, a greater quantity of air is released which tends to occupy almost the entire volume of the dimple: the consequence is a lower force generated by the surface. For high gap values (e.g. 8 µm) the best condition is reached if a low saturation pressure is assumed (-0.7 bar), since less gas is released, allowing to generate a greater bearing capacity, as shown in Figure 4.13.

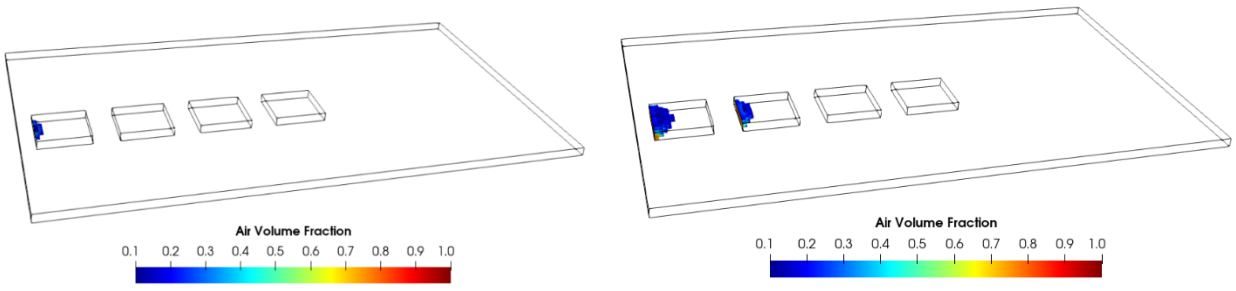

(a) (b)

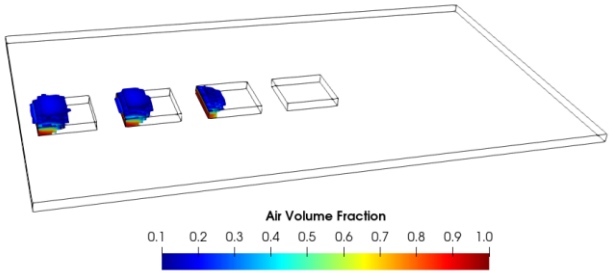

(c)

Figure 4.13. Air volume fraction; dimples side 50 µm and gap 8 µm, sliding velocity 10 m/s. Set A of cavitation coefficients. Only the portions of the mesh where the volume fraction of air is greater than 10% are highlighted. (a) Saturation pressure -0.7 bar; (b) Saturation pressure -0.5 bar; (c) Saturation pressure -0.3 bar

Figure 4.14 shows the pressure trends in the case of a gap equal to 8 µm. To confirm the previous air maps, the fluid remains at saturation conditions for a longer time if a higher saturation pressure is considered and this leads to a greater quantity of air released. On the contrary, with a lower saturation pressure, less air is free, and the pressurization ramp of the oil starts at an earlier stage of the texturized domain and this permits to obtain a higher pressure.

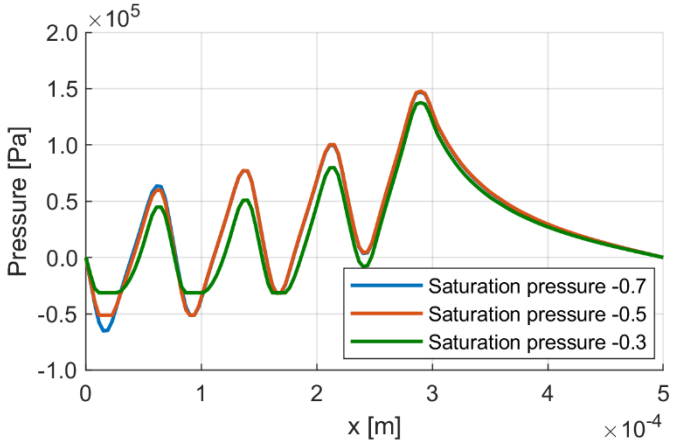

Figure 4.14. Pressure profiles calculated along the dimples median line, considering different saturation pressure values. Square dimples with side 50 µm and gap 8 µm, sliding velocity 10 m/s. Set A of cavitation coefficients.

As the height of the gap decreases, a greater amount of air is released, regardless of the saturation pressure considered. In fact, Figure 4.15 shows the case of a 3 µm gap where cavitation affects almost all the dimples present in the domain.

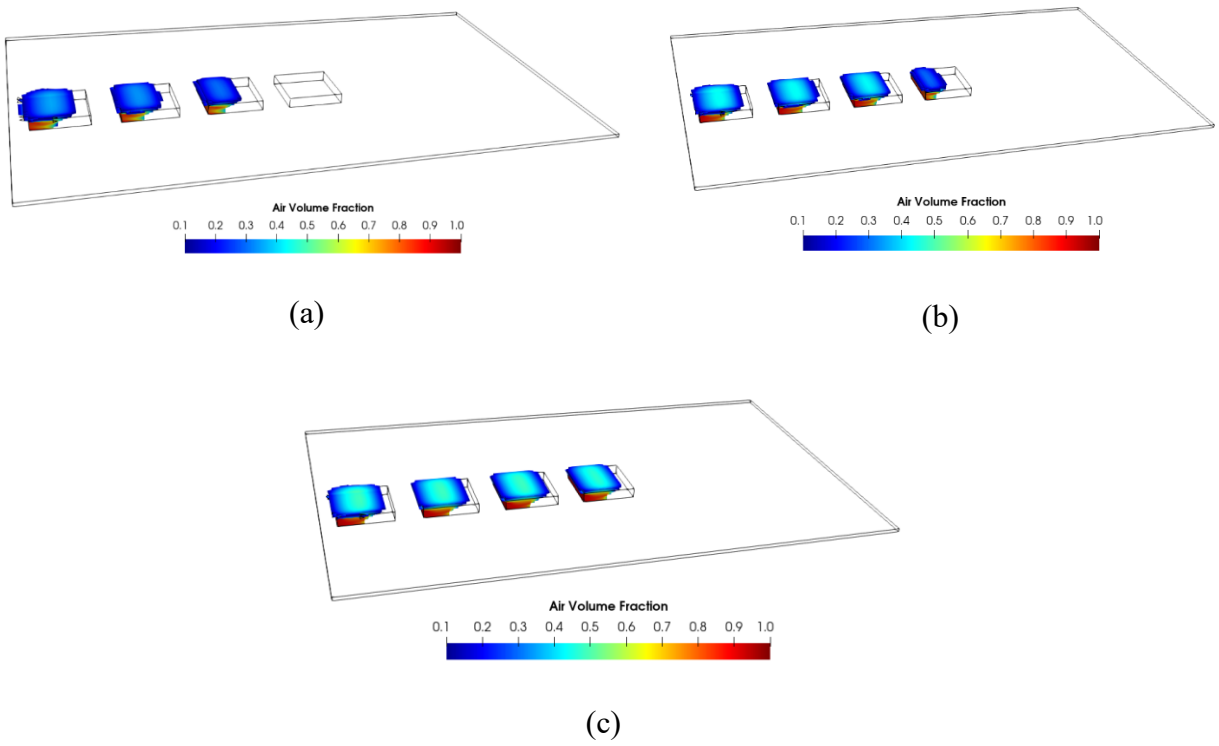

Figure 4.15. Air volume fraction; dimples side 50 µm and gap 3 µm, sliding velocity 10 m/s. Set A of cavitation coefficients. Only the portions of the mesh where the volume fraction of air is greater than 10% are highlighted. (a) Saturation pressure -0.7 bar; (b) Saturation pressure -0.5 bar; (c) Saturation pressure -0.3 bar.

For low gap values the behavior depends on the quantity of air released. The saturation pressure value impacts the time during which the fluid remains at low pressure, Figure 4.16. With a low saturation pressure (-0.7 bar) a large overpressure could be obtained, which tends to limit the cavitation effects, mainly on the last dimple. On the contrary, with a high saturation pressure (-0.3 bar) there is a great amount of air, even in the last dimple, reducing the maximum pressure that could be reached with the consequent reduction of the bearing capacity.

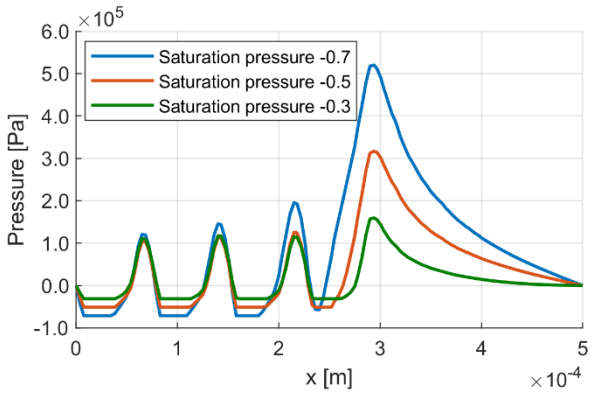

Figure 4.16. Pressure profiles calculated along the dimples median line at different saturation pressures. Square dimples with side 50 µm and gap 3 µm, sliding velocity 10 m/s. Set A of cavitation coefficients

To investigate the effects due to the different cavitation coefficients, the simulations have been also conducted using the parameters of Set B. Figure 4.17 shows the bearing force as a function of the gap and saturation pressure, with the coefficients of Set B. Compared to the case relating to Set A, the trends are very different. The cause is that in Set B the absorption coefficient is the same as in Set A, while the air release parameter is much greater.

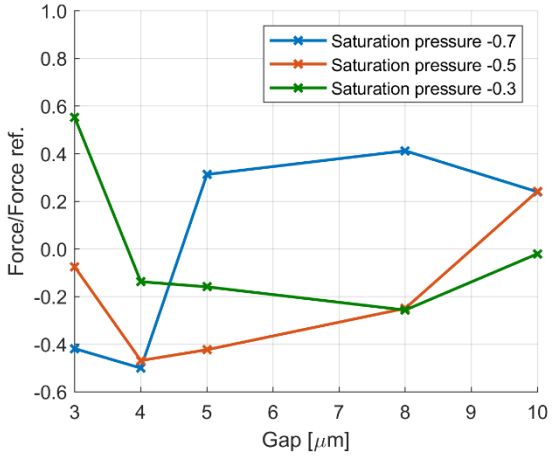

Figure 4.17. Bearing capacity generated by a partial texturing configuration. Influence of the gap for different values of saturation pressure. Set B cavitation coefficients. Square dimple with side 50 μm and depth 10 μm, sliding velocity 10 m/s

The quantity of air released conditions the trend for high gap values; unlike before, the force is positive only considering the lowest saturation pressure. Figure 4.18 shows the volume fraction of air with a gap of 8 μm: with a low saturation pressure (-0.7 bar) the results are very similar to the case of Set A: a small amount of air is released and for this reason both the pressure profile, Figure 4.19, and the force generated are the same as before. But, with a high saturation pressure (-0.3 bar) the cavitation happens in a very intense way and the consequence is that in some cases the air does not have enough time to be reabsorbed before the next dimple. There is a propagation of the cavitation phenomenon which compromises the performance of the coupling. As a result, the force generated with a high saturation pressure (-0.3 ÷ -0.5 bar) is negative.

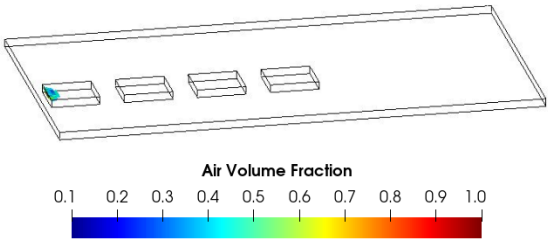

(a)

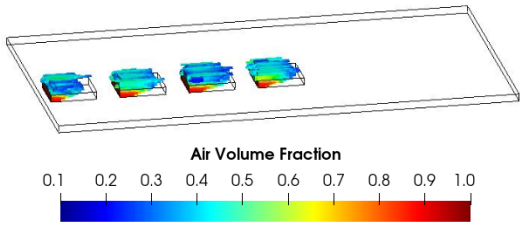

(b)

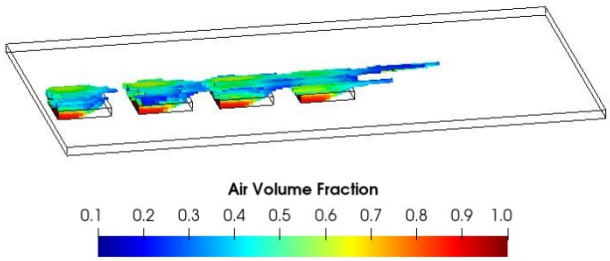

(c)

Figure 4.18. Air volume fraction: dimples side 50 µm and gap 8 µm, sliding velocity 10 m/s. Set B of cavitation coefficients. Only the portions of the mesh where the volume fraction of air is greater than 10% are highlighted. (a) Saturation pressure -0.7 bar; (b) Saturation pressure -0.5 bar; (c) Saturation pressure -0.3 bar.

Figure 4.19 shows the pressure profile for the 8 µm gap case. Cavitation takes place in a very intense way and for high saturation pressure values (-0.3 bar) the partial texturing is not able to generate an overpressure capable of reducing the negative effects of cavitation. With a lower saturation pressure (-0.7 bar), the phenomenon happens slightly, remaining restricted only to a small area of the first dimple. The pressure profile is an increasing curve, generating an overpressure that permits to have a positive integral of the pressure on the moving plane.

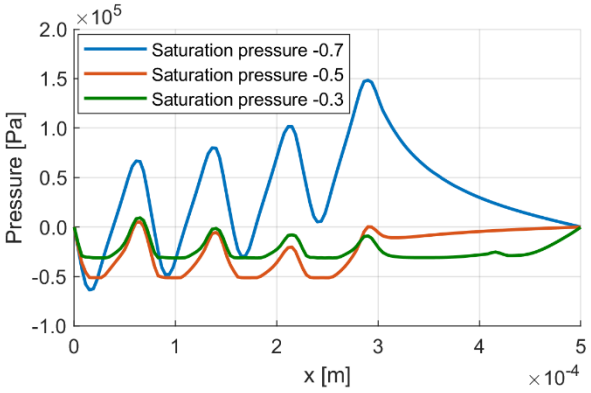

Figure 4.19. Pressure profiles calculated along the dimples median line at different saturation pressures. Square dimples with side 50 µm and gap 8 µm, sliding velocity 10 m/s. Set B of cavitation coefficients.

The trend changes by further decreasing the gap: for each configuration, the bearing capacity increases, especially when the saturation pressure is higher. In these conditions, the amount of air released is similar between the different cases, as could be seen from Figure 6.15: consequently, the surface generates a bearing capacity in case the minimum pressure is the highest (-0.3 bar).

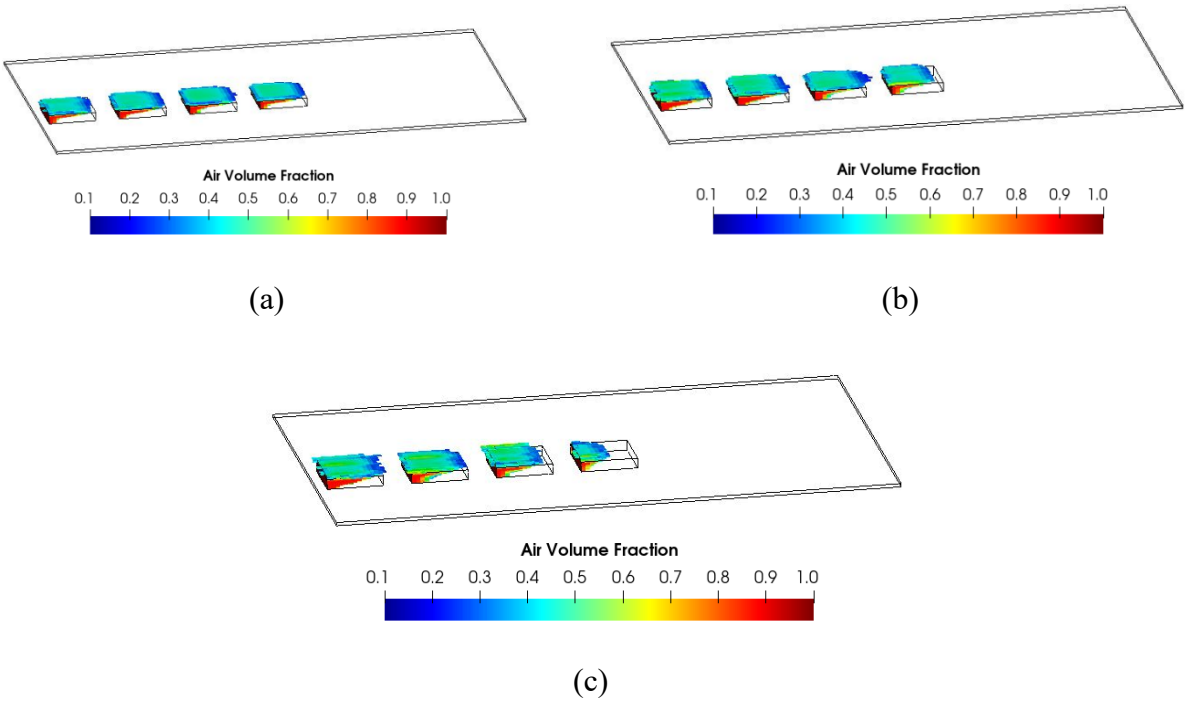

Figure 4.20. Air volume fraction: dimples side 50 µm and gap 3 µm, sliding velocity 10 m/s. Set B of cavitation coefficient. Only the portions of the mesh where the volume fraction of air is greater than 10% are highlighted. (a) Saturation pressure -0.7 bar; (b) Saturation pressure -0.5 bar; (c) Saturation pressure -0.3 bar

The Figure 4.21 shows the pressure profile for the case of a gap equal to 3 µm. Since the release coefficient is very high, the air release condition is reached almost instantaneously, while reabsorption is always slower. The contribution of each dimple on the pressure profile is greater if the saturation pressure is high (-0.3 bar). The overall effect is generating a greater overpressure that reduces the effect of cavitation, especially on the last dimple.

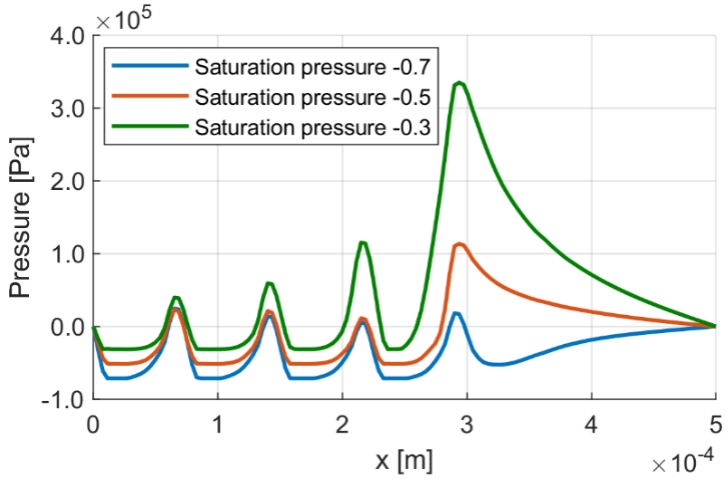

Figure 4.21. Pressure profiles calculated along the dimples median line at different saturation pressures. Square dimples with side 50 µm and gap 3 µm, sliding velocity 10 m/s. Set B of cavitation coefficient.

The temporal aspect of the air release and absorption processes has been further investigated to verify if a greater distance between the dimples, which means more time for the fluid, could reduce the quantity of air present in the domain. The Figure 4.22 shows a case where the dimension of the dimples along the moving direction has been decreased: since the textured portion has been kept unaltered, a greater spacing between the dimples has been obtained. So, the free air has more time to be completely reabsorbed between one dimple and the next. The force generated by the surface is almost the same as the original configuration, but with the advantage of having less free air.

The onset of cavitation and its possible propagation through the surface pose a further aspect to be investigated in the design phase, since the geometric characteristics of the texture influence the tribological behaviour of the coupling. In addition, an accurate fluid model is essential, as even slight variations in the air release and absorption coefficients greatly change the pressure distribution.

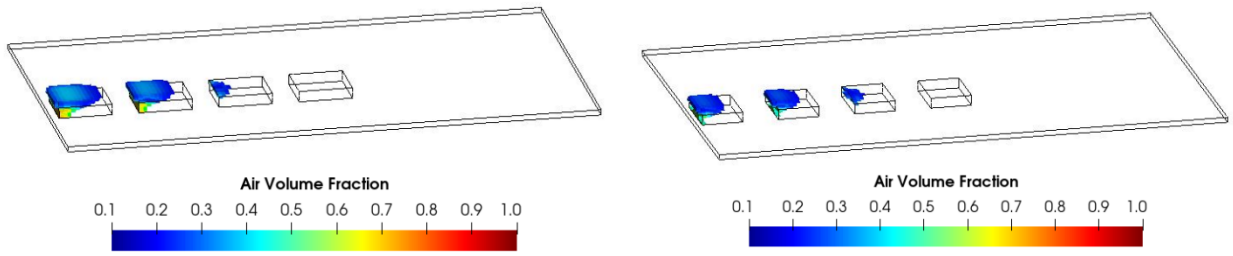

(a) (b)

Figure 4.22. Air volume fraction generated by a partial texturing configuration using Set A cavitation coefficients and a saturation pressure of -0.7 bar. Gap 5 µm, sliding velocity 10 m/s. Highlighted only the volumes of the mesh where the volume fraction of air is greater than 1%. (a) Dimples side 50 µm. (b) Dimples side 40 µm. The textured portion remains constant.

This section uses the best literature references on this complex topic, but the lack of knowledge of the exact composition of the fluid leads to a relevant uncertainty of the characteristic parameters of the models, as shown in Table 4.2.

The results presented in this paragraph help to highlight how the dynamic characteristics of the cavitation phenomenon become relevant when the fluid process involves transient phenomena, due to the geometric variation which, being very small, occur in a very short time.

The next paragraph describes a cavitation model that allows simulating both gaseous and vaporous cavitation at the same time, partially managing to overcome the limitations of the model adopted in this paragraph.

4.3 Full cavitation model

The cavitation model adopted in the previous paragraph has two strong limitations:

- It does not allow simulating both gaseous and vaporous cavitation at the same time.
- Limits the minimum pressure obtainable at the saturation value.

This last condition is not physically correct when applied to the release of dissolved gases. In fact, it is a progressive phenomenon as the pressure decreases, but it can not limit its minimum value; only vaporous cavitation sets a limit on the minimum pressure.

The Figure 4.23 provides a schematic representation of the fluid domain indicating the main processes involved in cavitation: the liquid phase is composed of hydraulic oil and dissolved air, which could be absorbed or released. Furthermore, hydraulic oil can vaporize or condense [4.11].

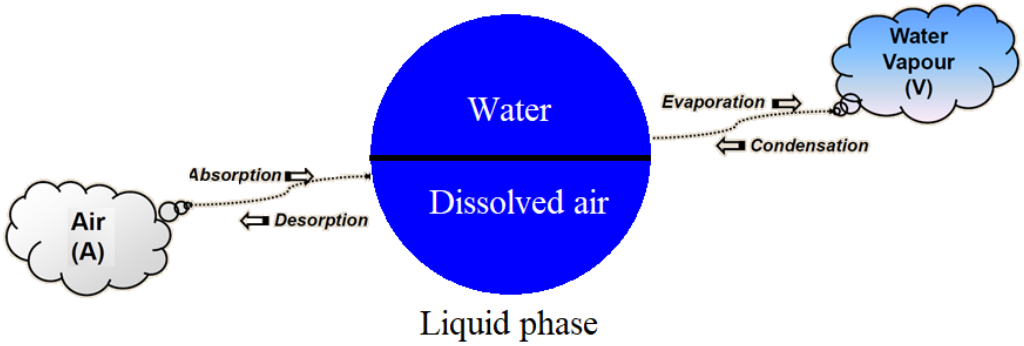

Figure 4.23. Schematic representation of the fluid domain and of the characteristic processes of cavitation.

In order to include both the effects of gaseous and vapor cavitation, a three-phase fluid model consisting of liquid *l*, air *g* and vapor *v* has been used in the CFD simulations. For mass conservation, the sum of the fractions of each phase must be unitary:

$$f_l + f_g + f_v = 1 \tag{4.18}$$

Furthermore, to allow the air to enter into solution with the oil, the liquid phase is modelled as a variable composition mixture formed by hydraulic oil and dissolved air.

4.3.8 Gaseous cavitation

Liquids normally contain a certain amount of dissolved non-condensable gases. Non-condensable gases in a liquid could be found in the dissolved state and as a free gas. The free state

of the non-condensable gases could be due to a premixing of the gas in supply liquid, or from the local injection to the boundary or as an evolution of the non-condensable gas. To include the effects of non-condensable gases, tracking the change in the mass fraction of both dissolved and free gases is needed.

Indicating with $f_{g,g}$ the mass fraction of the gases in free form and with $f_{g,l}$ that of the gases dissolved in the liquid, the mass fraction of the non-condensable gases f_g could be expressed as the sum of the two components:

$$f_g = f_{g,g} + f_{g,l} \tag{4.19}$$

It follows then that the law of conservation of mass applied to the domain, Equation (4.18), becomes:

$$f_l + f_{g,g} + f_{g,l} + f_v = 1 \tag{4.20}$$

The density of the mixture is calculated as:

$$\frac{1}{\rho} = \frac{f_v}{\rho_v} + \frac{f_{g,g}}{\rho_g} + \frac{f_l + f_{g,l}}{\rho_l} \tag{4.21}$$

Where it is assumed that the density of the liquid with the dissolved non-condensable gases is the same as that of the pure liquid.

To allow the variation and interchange of $f_{g,g}$ and $f_{g,l}$ in the computation domain, two convection-diffusion equations have been added in the CFD code: one for non-condensable gases in the gaseous phase, $f_{g,g}$, Equation (4.22), and one for non-condensable gases dissolved in the liquid, $f_{g,l}$, Equation (4.23):

$$\frac{\partial(\rho f_{g,g})}{\partial t} + \nabla \cdot \left(\rho \, \vec{U} \, f_{g,g} - D_{g,g}(\nabla f_{g,g})\right) = \dot{S}_{DA} \tag{4.22}$$

$$\frac{\partial(\rho f_{g,l})}{\partial t} + \nabla \cdot \left(\rho \, \vec{U} \, f_{g,l} - D_{g,l}(\nabla f_{g,l})\right) = -\dot{S}_{DA} \tag{4.23}$$

The total mass of the non-condensable gases is conserved in the computational domain, as could be seen by adding the two equations above.

The term source connects the transition between the two states and the expression is:

$$\dot{S}_{DA} = R_d - R_a = \begin{cases} C_d \rho_g (p_{equil} - p_g)(1 - f_{g,g}) f_{g,l} \\ C_a \rho_g (p_g - p_{equil})(f_{g,l,lim} - f_{g,l}) f_{g,g} \end{cases} \quad (4.24)$$

Where C_d and C_a are empirical coefficients to be determined that control the speed at which the associated phenomenon occurs.

Equation (4.24) establishes that the driving force of the process is the differential equilibrium pressure. The release of air happens when the partial pressure of the gas p_g is below the equilibrium pressure, p_{equil}. Similarly, absorption occurs when the partial pressure of the gas is above the equilibrium pressure.

The absorption constant is lower than the release constant for two reasons. The absorption from the gaseous state to that dissolved in the liquid must overcome the effect of the surface tension, which has a greater resistance. The other reason is that the $p_{equil} - p_g$ pressure difference during release is limited by the maximum p_{equil} value, while it is not during absorption.

The equilibrium pressure is assumed as the sum of the vapor pressure and the partial pressure of the gas, calculated as the product between Henry's constant and the molar mass of dissolved air.

Henry's constant has several formulations.

In accordance with Sazonov and Shaw [4.12], the dimensionless Bunsen coefficient α is defined as "*the volume of gas in saturation, reduced to 273.15 K and 1 bar, which is absorbed by the unit of pure solvent at the measurement temperature and partial pressure of 1 bar*". Considering an ideal gas, it is possible to define Henry's constant as:

$$H^{cp} = \frac{\alpha}{R \cdot T^{STP}} \quad \left[\frac{mol}{m^3 Pa}\right] \quad (4.25)$$

With T^{STP} equal to 273.15 K and R is the universal gas constant.

Henry solubility via liquid-phase mixing ratio, H^{xp}, is defined as:

$$H^{xp} \stackrel{\text{def}}{=} {}^{x}/_{p} \quad \left[\frac{1}{Pa}\right] \quad (4.26)$$

Where x is the molar mixing ratio in the liquid phase. The conversion is:

$$H^{xp} = \frac{\rho}{M} \cdot H^{cp} \quad \left[\frac{1}{Pa}\right] \quad (4.27)$$

With ρ the density of the liquid and M its molar mass. The reciprocal has been used in the calculation of the partial pressure of the gas.

4.3.9 Vapor cavitation

Vapor cavitation has been simulated in CFX using the Zwart model, Paragraph 4.1.4 .

For simplicity, the equations expressing the interphase mass transfer rate per unit volume in case of condensation are reported:

$$\dot{m}_{fg} = F\frac{3r_g\rho_g}{R_B}\sqrt{\frac{2}{3}\frac{|p_v - p|}{\rho_f}}\ sign(p_v - p) \tag{4.28}$$

And in case of vaporization:

$$\dot{m}_{fg} = F\frac{3R_{nuc}(1 - r_g)\rho_g}{R_B}\sqrt{\frac{2}{3}\frac{|p_v - p|}{\rho_f}}\ sign(p_v - p) \tag{4.29}$$

F is an empirical coefficient that determines the intensity of the process and could be different in the case of condensation, F_c, or vaporisation, F_v. For reasons similar to what is described in the paragraph on gaseous cavitation, vaporisation is a process that occurs faster than condensation and this aspect is quantified with the F parameter.

4.3.10 Lumped parameter model

A lumped parameter fluid model has been also developed, in a Matlab® environment, to simulate the behaviour of the fluid in the presence of both gaseous and vaporous cavitation.

This model assumes that for pressures higher than the saturation pressure the entire quantity of gas is completely dissolved in the liquid: consequently, the gas, in the equation of state of the fluid, does not provide a contribution in volume, but only in mass and thus follows the law of compressibility of the liquid. Below the saturation pressure, in accordance with the Dalton-Henry law, a fraction of gas starts to separate and therefore increases the total volume of the fluid, [4.11, 4.13].

The properties of the fluid are described considering three pressure ranges.

- Case 1: $p > p_{SAT}$

The volume fraction *x* of dissolved gas does not contribute to increasing the volume, because the small gas molecules are positioned in the interstices between the larger liquid molecules, but only increases the mass of the liquid. Thus, the density of the fluid consisting of gas and liquid is:

$$\rho_0 = \rho_{L0} + \frac{x}{1-x}\rho_{G0} \tag{4.30}$$

Where *x* represents the volume fraction of dissolved air and ρ_{G0} is the density of the gas and ρ_{L0} that of the liquid in the reference conditions, $p = p_{ATM}$ and $T_0 = 273.15\ K$.

Consider different conditions, with a higher pressure and a different temperature, but with a unitary volume of fluid. The mass remains unchanged, while the volume, considering that the gas is completely enclosed between the liquid molecules, follows the law of compressibility of liquids:

$$V_{liq} = \frac{\rho_{L0}}{\rho_{L(p,T)}} \tag{4.31}$$

The density in these new conditions is given by the ratio between mass and volume:

$$\rho(p,T) = \rho_0 \cdot \frac{\rho_{L(p,T)}}{\rho_{L0}} = \rho_{L(p,T)} + \frac{x}{1-x}\rho_{G0} \cdot \frac{\rho_{L(p,T)}}{\rho_{L0}} \tag{4.32}$$

Consider the compressibility module:

$$B = \rho \frac{\partial p}{\partial \rho} \tag{4.33}$$

Assuming that B remains constant, that the density of the liquid varies negligibly as the temperature varies, by integrating the following expression of density is obtained:

$$\rho(p) = \rho_0 \cdot e^{\frac{p-p_0}{B}} = \left(\rho_{L0} + \frac{x}{1-x}\rho_{G0}\right) \cdot e^{\frac{p-p_0}{B}} \tag{4.34}$$

- Case 2: $p_{VAPL} < p < p_{SAT}$

It is assumed that the gas starts to release at pressures below p_{SAT} and that this process ends at the lower saturation pressure, p_{VAPL}. Since the lower saturation pressure is very low, once this pressure is reached it is assumed that all gas is fully released. The dissolved air fraction behaves exactly as in Case 1, giving a mass but not a volume contribution to the density. The free fraction, on the other hand, expands or compresses as the pressure varies, thus making it necessary to consider the contribution in volume.

The fraction of free air θ follows Henry's law, according to which θ is proportional to the pressure at which the gas is:

$$\theta = \frac{p_{SAT} - p}{p_{SAT} - p_{VAPL}} \tag{4.35}$$

Nevertheless, the first derivative of theta is not continuous: to prevent discontinuities and the related numerical problems, the theta expression has been replaced by a polynomial function with null derivative in p_{SAT} and p_{VAPL}.

To calculate the density, consider a unit volume of liquid under the reference conditions, with a free gas fraction equal to $\theta \cdot x$:

$$\begin{gathered} V_{liq} = 1 \\ \rho_{liq} = \rho_{L0} + \frac{(1-\theta)x}{1-x}\rho_{G0} \\ M_{liq} = \rho_{L0} + \frac{(1-\theta)x\rho_{G0}}{(1-x)} \end{gathered} \tag{4.36}$$

And

$$V_{gas} = \frac{\theta x}{(1-x)}$$

$$\rho_{gas} = \rho_{G0} \tag{4.37}$$

$$M_{gas} = \frac{\theta x \rho_{G0}}{(1-x)}$$

By bringing in generic conditions of pressure and temperature, for the liquid is obtained:

$$V_{liq} = \frac{\rho_{L0}}{\rho_{L(p,T)}}$$

$$\rho_{liq} = \rho_L(p,T) + \frac{(1-\theta)x}{1-x} \cdot \rho_{G0} \cdot \frac{\rho_{L0}}{\rho_{L(p,T)}} \tag{4.38}$$

$$M_{liq} = \rho_{L0} + \frac{(1-\theta)x\rho_{G0}}{(1-x)}$$

Assuming, as in Case 1, that the variation in the density of the liquid as the only temperature varies is negligible. This approximation is no longer acceptable for gas, so it should be done:

- first a temperature change at constant pressure:

$$V_{gas} = \frac{\theta x}{(1-x)} \cdot \frac{T_{AS}}{T_0}$$

$$\rho_{gas} = \rho_{G0} \cdot \frac{T_{AS}}{T_0} \tag{4.39}$$

$$M_{gas} = \frac{\theta x \rho_{G0}}{(1-x)}$$

- then a polytropic transformation from p_0 at constant temperature:

$$V_{gas} = \frac{\theta x}{(1-x)} \cdot \frac{T_{AS}}{T_0} \cdot \left(\frac{p_0}{p}\right)^{1/\gamma}$$

$$\rho_{gas} = \rho_{G0} \cdot \frac{T_{AS}}{T_0} \cdot \left(\frac{p_0}{p}\right)^{1/\gamma} \tag{4.40}$$

$$M_{gas} = \frac{\theta x \rho_{G0}}{(1-x)}$$

By dividing the total mass by the total volume, the equation that provides the density of the fluid as a function of pressure is obtained:

$$\rho = \frac{(1-x)\rho_{L0} + x\rho_{G0}}{(1-x)\cdot e^{\left(\frac{p_0-p}{B}\right)} + \frac{T}{T_0} x\vartheta \left(\frac{p_0}{p}\right)^{\frac{1}{\gamma}}} \tag{4.41}$$

At pressures lower than p_{VAPH}, the hydraulic oil begins to vaporize. There is not a single pressure at which the transition from liquid to vapor occurs, but an interval, because hydraulic oil is composed of several molecules with different vapor tensions. The fluid is then modelled as a uniform mixture of free air, oil vapor and liquid oil. In this pressure range the vapor to liquid mass fraction is defined by a polynomial function:

$$\varphi = \frac{m_V}{m_L} = \begin{cases} 0, & p \geq p_{VAPH} \\ \varphi(p), & p_{VAPL} < p < p_{VAPH} \\ 1, & p \leq p_{VAPL} \end{cases} \tag{4.42}$$

Similarly to before, the density of the fluid could be expressed as a function of pressure and temperature, assuming that the density of the liquid is independent of temperature. It has also been assumed that both the free gas and the vapor phase undergo an isentropic transformation:

$$\rho = \frac{(1-x)\rho_{L0} + x\rho_{G0}}{(1-x)(1-\varphi)\cdot e^{\left(\frac{p_0-p}{B}\right)} + \frac{T}{T_0}\left[\frac{\varphi(1-x)\rho_{L0}}{\rho_{V0}}\left(\frac{p_{VAPH}}{p}\right)^{\frac{1}{\gamma_V}} + x\vartheta\left(\frac{p_0}{p}\right)^{\frac{1}{\gamma_G}}\right]} \tag{4.43}$$

Where:

$$\rho_{V0} = \frac{\widetilde{m}}{\tilde{R}_G \cdot T_0} p_{VAPH} \tag{4.44}$$

- $p < p_{VAPL}$

If the pressure further decreases below the lower vaporization pressure, only the gaseous phase exists, consisting of free air and oil vapor. The density could be determined by setting $\varphi = 1$ in Equation (4.43).

The definition of the upper and lower vaporization pressure is affected by the great uncertainty relating to the chemical composition of the hydraulic oil. The upper value has been set at 0.2 bar, while the lower one has been estimated using the Clapeyron equation relating to one of the components of the oil, the heptadecane, $C_{17}H_{36}$, [4.15].

Table 4.3. Main parameters adopted in the cavitation model.

x	9%	
P_{SAT}	1	[bar]
p_{VAPH}	0.2	[bar]
p_{VAPL}	0.0001	[bar]

Figure 4.24 shows the density of the fluid as a function of pressure. Below the saturation pressure, the density progressively decreases because of the release of the air dissolved in the liquid; the density then decreases further due to the gradual vaporisation of oil.

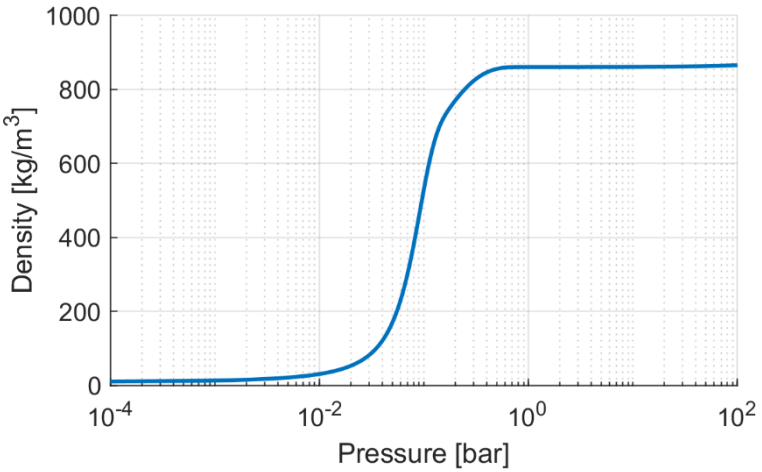

Figure 4.24. Fluid density as a function of pressure expressed in logarithmic scale.

Using this model to predict the mass flow through an orifice where the total upstream pressure is p_T and the static downstream pressure is p_s, the ideal fluid velocity at the restricted section is:

$$c_{id} = \int_{p_S}^{p_T} \frac{dp}{\rho} \tag{4.45}$$

For $p > p_{SAT}$ the integral could be analytically solved, obtaining:

$$c_{id} = \int_{p_S}^{p_T} \frac{dp}{\rho} = -\frac{B}{\rho_0}\left[e^{\frac{p_{ATM}-p_T}{B}} - e^{\frac{p_{ATM}-p_S}{B}}\right] \tag{4.46}$$

For other cases, the integration must take place numerically.

The ideal velocity value must be compared with the value of the sound velocity at the static downstream pressure, whose expression is:

$$c_{sound} = \int \frac{dp}{d\rho} \tag{4.47}$$

Where:

$$\frac{dp}{d\rho} = -\frac{\Psi}{\Pi}\left[(1-x)\left(\frac{1-\varphi}{B} - \frac{d\varphi}{dp}\right)e^{\frac{p_0-p}{B}} + \frac{\partial\varphi}{dp}C_1 p^{-\frac{1}{\gamma}} - \frac{C_1 + \varphi C_2}{\gamma}p^{-1-\frac{1}{\gamma}}\right]^{-1} \tag{4.48}$$

And:

$$\begin{gathered}
\Pi = (1-x)\rho_{L0} + x\rho_{G0} \\
\Psi = \left((1-x)e^{\frac{p_0-p}{B}} + \vartheta x\frac{T}{T_0}\left(\frac{p_0}{p}\right)^{\frac{1}{\gamma}}\right)^2 \\
C_1 = x\frac{T}{T_0}p_0^{\frac{1}{\gamma}} \\
C_2 = (1-x)\,\frac{T}{T_0}p_{VAPH}^{\frac{1}{\gamma}}
\end{gathered} \tag{4.49}$$

The correct speed value to be used in calculating the mass flow rate is the minimum between the speed of sound and the ideal one given by the Equation (4.46).

The trend of the speed of sound, calculated using the Equation (4.47), is shown in Figure 4.25. In general, it is a very high value, but from the graph it is possible to appreciate that for low pressure values, typically those at which cavitation occurs, the speed of sound decreases markedly: it is exactly in this pressure range that it is necessary to compare it with the ideal speed calculated with the Equation (4.46).

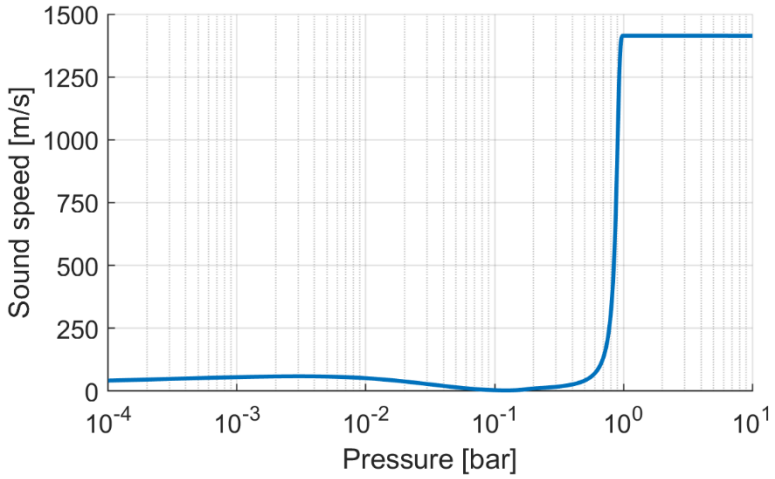

Figure 4.25. Sound speed as a function of pressure.

4.3.11 Experimental activity

An experimental activity has been specifically conducted in order to calibrate the parameters present within the complete cavitation model implemented in ANSYS® CFX and to allow the validation of the lumped parameter model.

The tests have been carried out at the Engineering and Architecture Laboratory of the University of Parma. The ISO hydraulic scheme of the experimental setup is shown in Figure 4.26, while in Figure 4.27 there is the picture of the test bench set up. The models and the characteristics of the sensors used are listed in Table 4.4. The hydraulic oil is an ISO-VG 46 and the test temperature has been set at 40 °C.

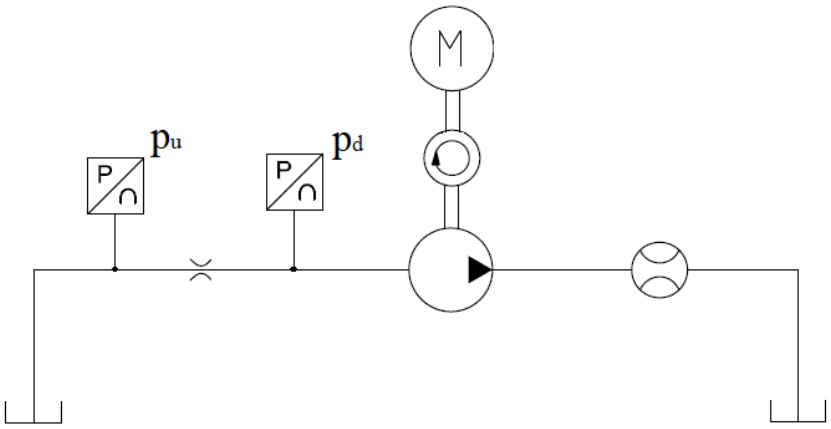

Figure 4.26. ISO scheme of the test bench layout.

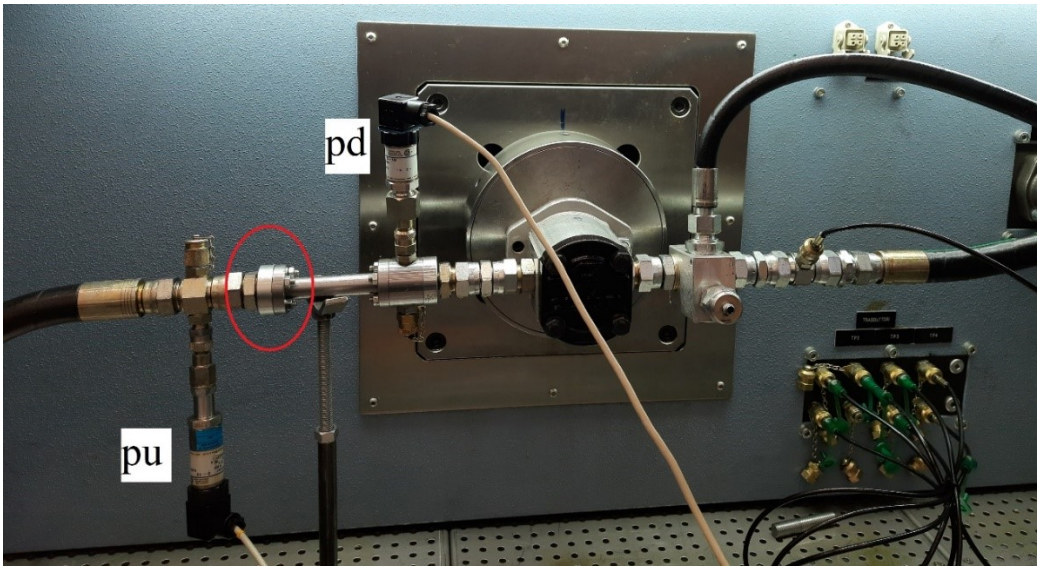

Figure 4.27. Photo of the test bench set up.

Table 4.4. Sensors installed on the test bench and related characteristics.

Variable	Sensor	Model	Main Features
p_u	Pressure Transducer	Wika S-10	0 – 10 barA ±0.5%FS
pd	Pressure Transducer	Wika S-10	0 – 10 barA ±0.5%FS
$\dot{V}_{delivery}$	Flow Meter	VSE VS 1	80 l/min ± 0.3% measured value
ω	Speed sensor	HMB T10FS	accuracy class 0.05

A fixed orifice has been placed upstream of a pump in order to provide a low pressure at the pump inlet due to the pressure drop generated: in Figure 4.27 the orifice is indicated by the red circle. The pressure drop is caused by the fluid speed through the orifice and is controlled by the pump rotational speed. The absolute pressures upstream and downstream of the orifice have been measured, as well as the flow rate passing through the circuit.

In Figure 4.28 the flow rate measured by the flowmeter is shows as a function of the rotational speed of the pump. The flow measurement uncertainty is not displayed on the graph because the interval is very small and would not be visible.

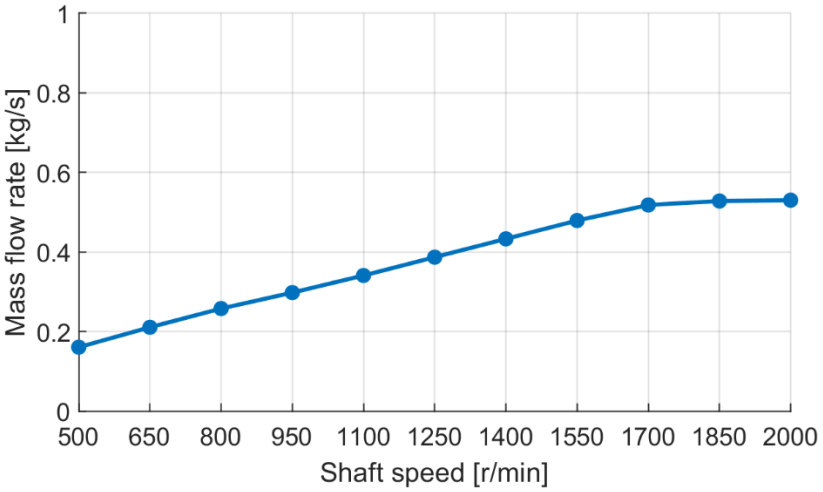

Figure 4.28. Mass flow rate measured experimentally as a function of pump shaft speed.

Analysing the graph in Figure 4.28, up to 1550 r/min the mass flow rate increases linearly with the speed of the pump. In this operating interval the main phenomenon is the release of a fraction of the dissolved gas which however does not negatively affect the mass flow rate in the pipeline. By further increasing the speed the phenomenon of vaporous cavitation has established. The minimum pressure reached downstream of the orifice is limited and so the pressure drop across the orifice does not increase further as shown in Figure 4.29, where the uncertainty of pressure measurement is also reported. Therefore, the mass flow rate remains almost constant, in accordance with the discussion of Martelli et Al. [4.14].

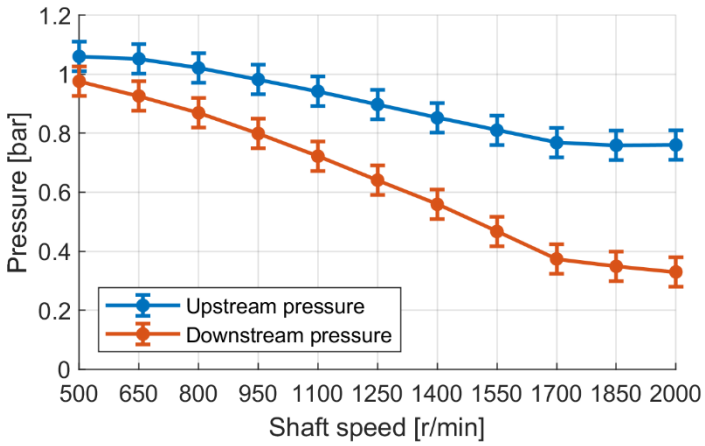

Figure 4.29. Pressure measured experimentally upstream and downstream the orifice.

4.3.12 CFD simulations

The geometry of the pipe is shown in Figure 4.30, where the length of the pipe corresponds to the distance between the two pressure sensors. The most important geometric relations are shown in Table 4.5. Since the geometry is axisymmetric, the CFD simulations have been performed with a 2D geometry.

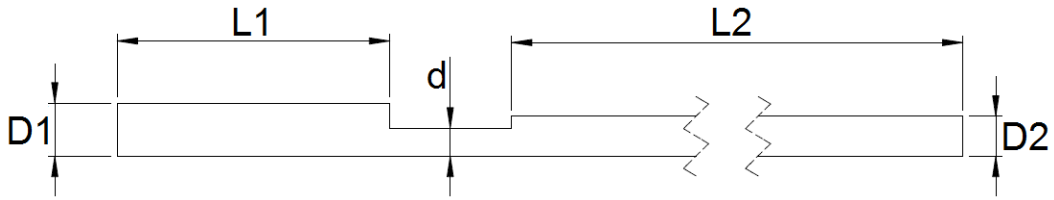

Figure 4.30. Sketch of the tested orifice.

Table 4.5. Geometric features of the orifice

$D1/d$	1.8
$D1/D2$	1.3
$L1/d$	4.9
$L2/d$	12.9

The simulations were carried out with ANSYS® CFX software. The gaseous cavitation model is not present within the software, but has been introduced through the CFX Expression Language (CEL). CEL is a scripting language internal to the main CFD code that allows to perform operations on additional user-defined variables.

The fluid domain consists of a structured mesh, the number of cells of which has been established following a sensitivity analysis of the mesh; the main features of the mesh are reported in Table 4.6. The turbulence model adopted is the standard k-epsilon model. The absolute pressures measured by the sensors during the experimental activity have been imposed as boundary conditions at the inlet and the outlet of the simulated domain.

Table 4.6. Features of the mesh.

Min Element size	Max Element size	Average Element quality	Average Aspect ratio	Average Orthogonal quality	Average Skewness
2.5e-5	3e-4	0.36	7.2	0.96	5.0e-3

In Table 4.7 the parameters used in the model are listed. As regards the vaporization and condensation processes, the two sets of parameters found in the scientific literature and described

in the Paragraph 4.2 have been adopted. In order to correctly model these processes, the definition of the physical and thermodynamic properties of the fluid is essential. Since the reference hydraulic oil is a complex mixture of heavy hydrocarbons, to simplify the properties definition of the vapor, the fluid has been assumed mono component considering one of oil component, the heptadecane $C_{17}H_{35}$, [4.15].

The gaseous cavitation model is quite innovative and in the scientific literature there are no applications with hydraulic oil, but only with water with the values indicated in the Table 4.7. However, the characteristic values of water have been used for the simulations, since they allow to obtain a good agreement with the experimental results.

The C_a absorption coefficient is lower than the C_d release coefficient for two reasons. The absorption process must overcome the effect of surface tension, which opposes greater resistance; and the differential pressure during the release of air is limited by the maximum p_{equil} value, while it is not restricted during absorption.

Table 4.7. Cavitation parameters used in numerical simulations.

	Vapour pressure	**R_b**	**R_{nuc}**	**F_v**	**F_c**	**C_d**	**C_a**
Set A	0.2 bar	10 μm	5e-4	0.9	0.01	2	-0.1
Set B	0.2 bar	10 μm	5e-4	50	0.01	2	-0.1

Figure 4.31 displays the mass flow through the orifice calculated by means of CFD simulations and the comparison with experimental data as a function of the pressure drop. If the effect of vaporous cavitation were not included, the flow rate would be an ever-increasing function; however, even experimentally it is observed that this is not the case. The curves obtained from the simulation are two: one obtained with the parameters of Set A and the other with Set B. Since the two sets differ in the vaporization coefficients until the pressure drop is such as to allow the formation of vapor the two curves are superimposed, as could be seen in the first part of the graph.

With greater pressure drops, vapor is also formed and consequently the vaporization parameters greatly influence the calculation of the mass flow. Set B has a vapor formation coefficient greater than that of Set A and therefore a greater amount of vapor is formed which leads to an underestimation of the mass flow through the orifice. Consequently, Set A is the most accurate allowing to appreciate a good overlap with the experimental data, especially where the flow rate stabilizes and the vaporous cavitation is predominant.

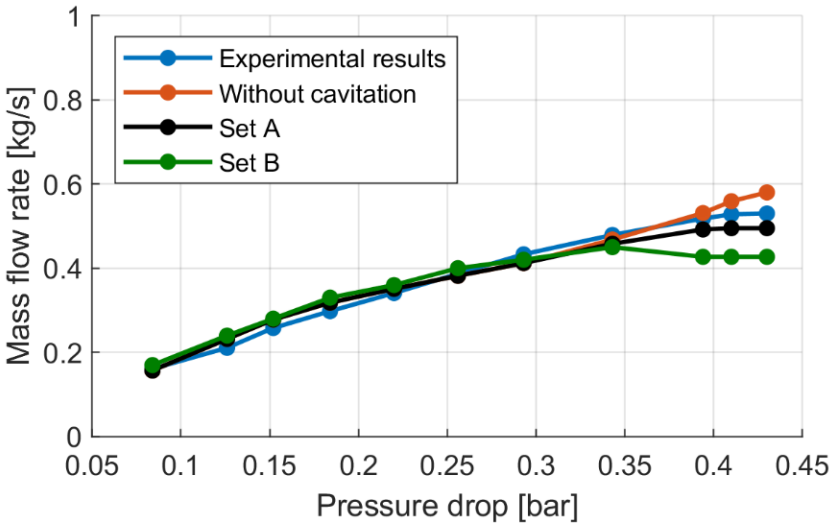

Figure 4.31. Comparison between experimental mass flow rate, CFD simulation results with different cavitation parameters and without cavitation.

Since Set B underestimates the flow rate for larger pressure drop, the following results are relative to Set A.

Figure 4.32 shows the speed of the oil in the geometry considered in the case of a pressure drop of 0.256 bar: it is important to observe the velocity distribution, since it has consequences on the results in terms of pressure distribution and on the formation of the gaseous phase, intended as both air and vapor.

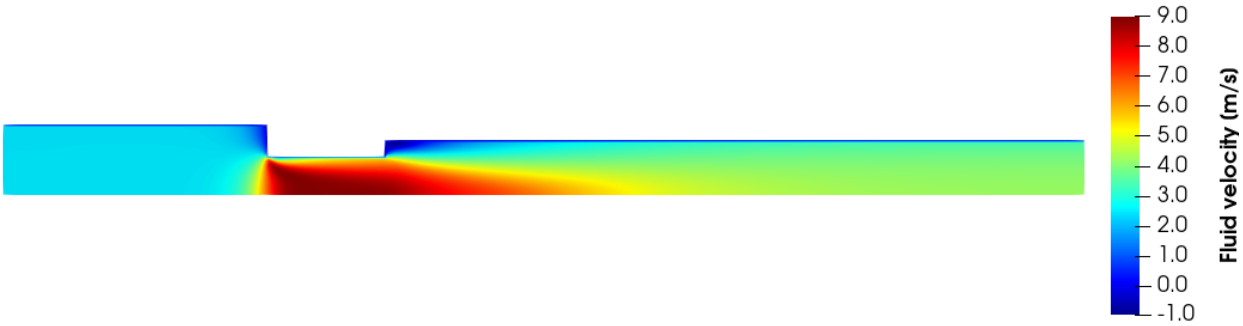

Figure 4.32. Fluid velocity through the orifice. Pressure drop 0.256 bar, Set A of parameters.

The pressure distribution relative to the case of a low pressure drop (0.256 bar) is shown in Figure 4.33. The minimum of pressure is in the converging section, close by the orifice, because of the high speed of the fluid. After the orifice, in the diverging area, the pressure increases due to the reduction in the speed of the fluid and the following conversion of kinetic energy into manometric energy.

Figure 4.33. Pressure distribution through the orifice. Pressure drop 0.256 bar, Set A of parameters.

Figure 4.34 shows the distribution of the free air volume fraction. The amount that is released is small since the pressures reached are not very low. The divergent section of the domain represents a region of stagnation and the velocity of the fluid, shown in Figure 4.32, is even negative. The greatest quantity of free air is concentrated in this area and the direction of the fluid velocity contributes to increasing its concentration.

Figure 4.34. Air volume fraction distribution through the orifice. Pressure drop 0.256 bar. Set A of parameters.

In this operating condition, the minimum pressure reached is not sufficient to also form vapor, but it is necessary to increase the pressure drop across the orifice. Figure 4.35 shows the pressure distribution of the case of pressure drop of 0.43 bar: in this configuration the minimum pressure reached is the saturation pressure at which vapor could also form.

Figure 4.35. Pressure distribution through the orifice. Pressure drop 0.43 bar, Set A of parameters.

Figure 4.36 shows the volume fraction of air. In this case, due to the lower pressure reached, a greater amount of air is released, which tends to be concentrated in the stagnation zone. However, part of the released air remains in free form until the outlet of the domain: this is due both to the low pressure at the outlet which allows the existence of air in free form and to the dynamics of the absorption process which takes more time than release.

Figure 4.36. Air volume fraction distribution through the orifice. Pressure drop 0.43 bar. Set A of parameters.

Figure 4.37 shows the vapor volume fraction that has formed within the domain: as the downstream static pressure decreases, an area of the domain is filled with vapor which narrows the real section where the fluid flows, limiting the mass flow through the orifice.

Figure 4.37. Vapour volume fraction distribution through the orifice. Pressure drop 0.43 bar, Set A of parameters.

These results allowed to validate the set of parameters, providing a good agreement between simulated and experimental data. Set A will subsequently be applied to textured surfaces: validation by orifice is on a much larger geometric scale than engineered surfaces. The physics of the phenomenon at scales of the order of microns could be different. However, carrying out experimental tests regarding cavitation on textured geometries is extremely complex and requires equipment that few laboratories in the world could have; the only possible experimental characterization is therefore on larger geometric scales, such as the motion of the fluid in a pipe.

4.3.13 Lumped parameter model results

Experimentally, the downstream pressure has been acquired at a distance from the orifice equal to about 12 times the diameter of the orifice: to correctly apply the equation of the orifice the pressure value near the outlet section of the orifice is needed, and it has been then calculated through CFD simulations.

The following equation has been used to calculate the mass flow rate through the orifice:

$$\dot{m} = C_d \cdot \Omega \cdot \rho \cdot c \tag{4.50}$$

Where Ω is the cross sectional area of the orifice. The density value ρ used is obtained from Figure 4.24 at the orifice downstream pressure, calculated through CFD simulations.

Figure 4.38 shows a comparison between CFD simulations, the lumped parameter method results and the experimental data. The lumped model predicts the mass flow rate with good accuracy, like the CFD approach. The maximum deviation between the experimental results and the CFD simulations is 7%, while the maximum deviation between the experimental data and the lumped parameter method is 6.4%.

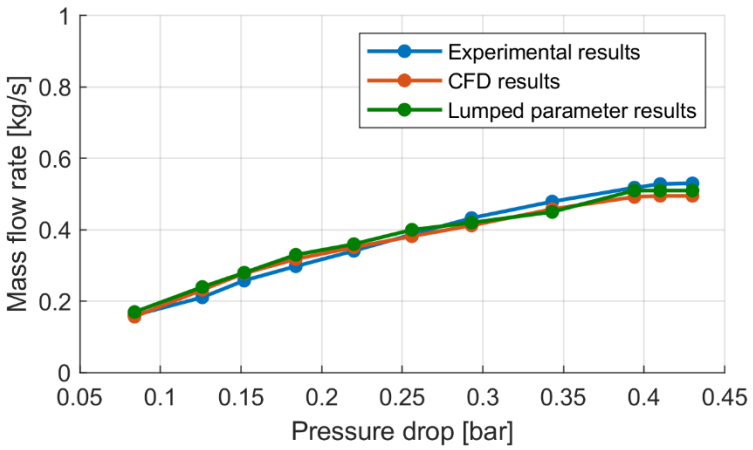

Figure 4.38. Comparison between experimental results, lumped parameter approach and CFD results.

Using the correct fluid velocity value is essential in order to obtain the results of Figure 4.38: the term *c* of the Equation (4.50) is given by the comparison between the ideal speed value, Equation (4.45), and the speed of sound value, Equation (4.47). Adopting the ideal speed expression for the entire range involves a great overestimation of the mass flow rate through the orifice when the vaporous cavitation begins, for pressure drops greater than 0.34 bar, as could be seen in Figure 4.39 by the dashed red line. Nevertheless, in the case of a greater pressure drop, the ideal velocity exceeds

the velocity of sound. In this case, the sound speed must be used: the mass flow rate obtained with the correct value of fluid speed is indicated by the solid green line. The dashed green line represents the mass flow rate calculated with the speed of sound for smaller pressure drops. The results show that the mass flow rate predicted by the lumped parameter model matches with the experimental one using the ideal velocity up to pressure drops of 0.34 bar and the speed of sound for greater pressure drops.

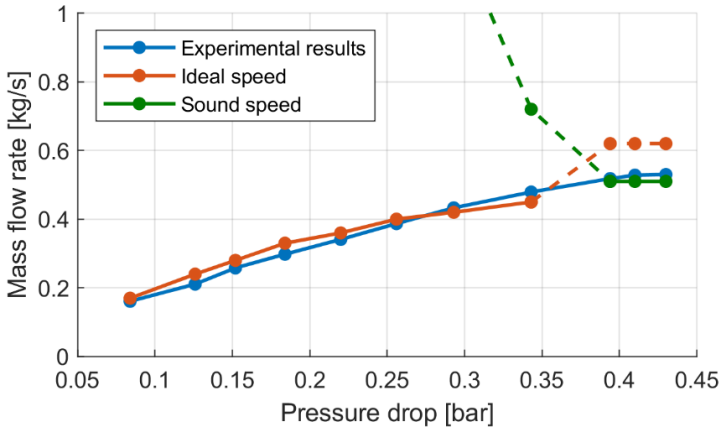

Figure 4.39. Comparison between the results obtained with the ideal speed and that of sound.

To better understand the trend of the speed of sound and the ideal fluid speed, the Figure 4.40 shows the comparison between the two curves. The first graph, Figure 4.40.a, relates to the upstream pressure of 1.0.5 bar when the pressure drop is 0.08 bar: the sound speed is much greater than the idela speed. This case is representative of conditions up to pressure drops of 0.34 bar. When higher pressure drops occur, the total upstream pressure is lower and consequently the ideal and the sound speed become comparable: Figure 4.40.b shows in detail the condition when vapor is formed. At the saturation pressure of 0.2 bar the ideal speed is higher than the sound speed. Using the value of speed of sound is therefore needed in order to correctly calculate the mass flow rate.

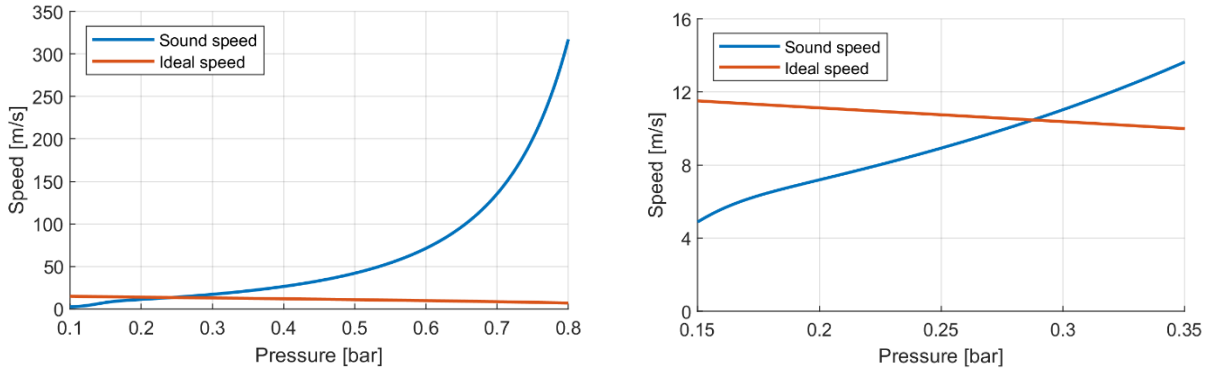

(a) (b)

Figure 4.40. Comparison between ideal speed and sound speed. (a) total upstream pressure 1.05 bar; (b) intersection of the two curves for total upstream pressure of 0.75 bar

List of references

4.1 Nervegna N., Rundo M. Passi nell'oleodinamica. Epics. 2020

4.2 Rundo M., Squarcini R., Furno F. Modelling of a variable displacement lubricating pump with air dissolution dynamics. SAE International. 2018. Doi: 10.4271/03-11-02-0008

4.3 Zhou J., Vacca A., Manhartsgruber B. A Novel approach for the prediction of dynamic features of air release and absorption in hydraulic oils. Journal of Fluids Engineering. 2013. Doi: 10.1115/1.4024864

4.4 Shah Y., Vacca A., Dabiri S. Air release and cavitation modeling with a lumped parameter approach based on the Rayleigh–Plesset equation: the case of an external gear pump. Energies. 2018. Doi: 10.3390/en11123472

4.5 Shah Y., Vacca A., Dabiri S., Frosina E. A fast lumped parameter approach for the prediction of both aeration and cavitation in gerotor pumps. Meccanica. 2018. Doi: 10.1007/s11012-017-0725-y

4.6 McCloy H. Control of Fluid Power: Analysis and Design. Ellis Horwood Ltd. 1980. ISBN: 0131708120

4.7 Zwart P. J., Gerber A. G., Belamri T. A two-phase flow model for predicting cavitation dynamics. Proceedings of the 5th International Conference on Multiphase Flow, Yokohama, Japan. 2004

4.8 Zhou J., Hu J., Jing C. Lumped parameter modelling of cavitating orifice flow in hydraulic systems. Journal of Mechanical Engineering. 2016. Doi: 10.5545/sv-jme.2015.3082

4.9 del Campo D., Castilla R., Raush G. A., Gamez Montero P. J., Codina E. Numerical Analysis of external gear pumps including cavitation. Journal of Fluids Engineering. 2012. Doi: 10.1115/1.4007106

4.10 Casoli P., Scolari F., Rundo M., Lettini A., Rigosi M. CFD analyses of textured surfaces for tribological improvements in hydraulic pumps. Energies. 2020. Doi: 10.3390/en13215799

4.11 Casoli P., Scolari F., Rundo M. Modelling and validation of cavitating orifice flow in hydraulic systems. Sustainability. 2021. Doi: 10.3390/su13137239

4.12 Sazonov V. P., Shaw D. G. Introduction to the Solubility Data Series: 1.5.2. Physicochemical Quantities and Units, A note on nomenclature, points 10 and 11. Introduction to IUPAC-NIST Solubilities Database. 2006

4.13 Casoli P., Vacca A., Franzoni G., Berta G. L. Modelling of fluid properties in hydraulic positive displacement machines. Simulation Modelling Practice and Theory. 2006. Doi: 10.1016/j.simpat.2006.09.006

4.14 Martelli M., Gessi S., Massarotti G., Marani P., Zarotti L. On peculiar flow characteristics in hydraulic orifices. Proceedings of the ASME/BATH 2017 Symposium on Fluid Power and Motion Control, Sarasota, USA. 2017. Doi: 10.1115/FPMC2017-4313

4.15 Reid R., Prausnitz J., Poling B. Properties of Gases and Liquids. McGraw-Hill Education: New York, NY, USA, 2001. ISBN 978-0070517998

Chapter 5. Full cavitation model applications

This chapter shows the simulation results on a computation domain that represents the meatus between the gear wheel and the lateral block. Three texture geometries are proposed, all characterized by the application of partial texturing: a geometry with steps, one with a sequence of square dimples and one with smaller steps.

The simulations are carried out by applying the full cavitation model and allow to know the distribution of the gas phase, both of free air and of vapor, in case it is formed.

Notions are also provided on the squeeze effect and friction forces for different types of texture.

5.1 Initial considerations

The several simulations performed, Chapter 3 and Chapter 4, had the aim of understanding the behaviour of the textured surfaces for different geometric and operational conditions. For this reason, a simple reference domain had been chosen, which could give reliable and fast results. The choice of a simplified domain had also demonstrated very useful for better understanding the consequences of the cavitation phenomenon on such particular geometries and the importance of having a solid model capable of simulating both types of cavitation.

This Thesis activity is aimed at increasing the performance of external gear pumps. The meatus to simulate is the one established between the lateral surface of the gear wheels and the lateral plates. As already mentioned, the lateral plate is the object of study on which a textured surface is realized in order to obtain a greater hydrodynamic bearing capacity such as to oppose the approach between wheel and lateral plate.

Figure 5.1 shows the overlap between the gear wheel and the lateral plate, where the gear wheel has been emptied to better understand the characteristics of the coupling. In addition to the difference between the materials of the two components, there is a discontinuous and periodic coupling during operation, since the gear wheel is not a disc.

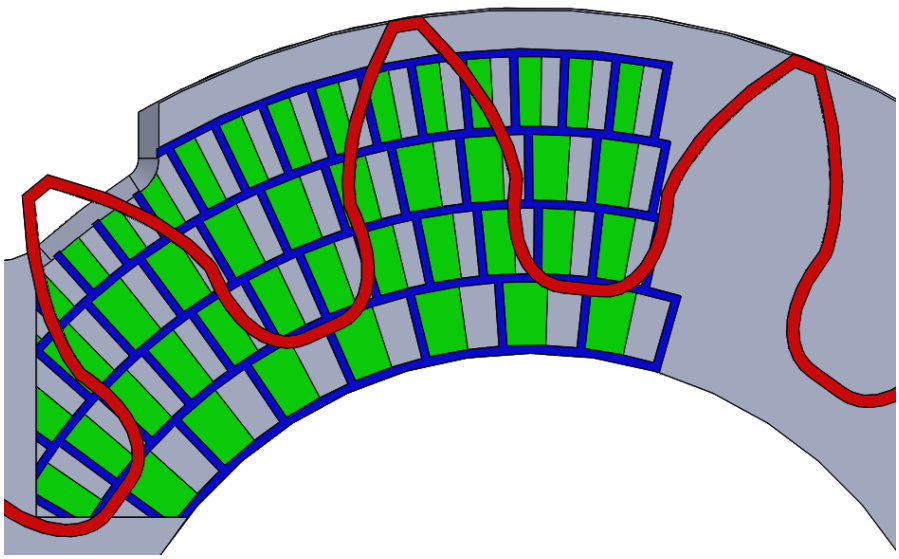

Figure 5.1. Overlap between gear wheel and textured lateral plate.

From the study conducted it is evident that the partial texturing solution is the best geometry configuration in order to obtain a great bearing capacity. For this reason, the geometries selected to conduct a more in-depth study by applying the full cavitation model are characterized by

applications of partial texturing where a grid of recovery channels has been created to delimit circular sectors that have been textured at 60%, as shown in the Figure 5.2.

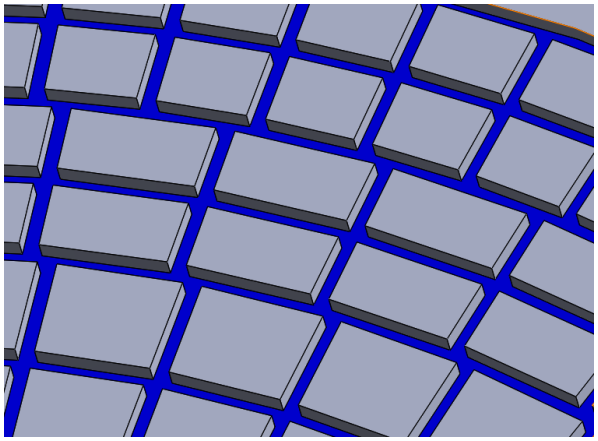

Figure 5.2. Sector geometry. The recovery channels that delimit various sectors are highlighted in blue. Each sector will then be textured to 60%.

The geometries investigated through CFD simulations are the following:

- Geometry A. Steps of 0.01 mm deep and recovery channels 0.2 mm wide and 0.05 mm deep;
- Geometry B. Sequence of square dimples with side 0.1 mm and depth of 0.01 mm. Recovery channels 0.2 mm wide and 0.05 mm deep;
- Geometry C. Steps 0.01 mm deep and recovery channels 0.1 mm wide and 0.05 mm deep. The geometry, similar to type A, has been scaled in order to have a greater number of steps, with the same contact surface.

The simulations have been carried out by applying the fluid model with full dynamic cavitation, whose detailed description is in the Paragraph 4.3: the parameters of the model are those obtained from experimental activity applied on the orifice. The parameters are listed in the Table 5.1:

Table 5.1. Cavitation parameters used in numerical simulations.

	Vapour pressure	**R_b**	**R_{nuc}**	**F_v**	**F_c**	**C_d**	**C_a**
Set A	0.2 bar	0.5 µm	5e-4	0.9	0.01	2	-0.1

The study surface is shown in the Figure 5.3. Since the domain extension of the single tooth is much greater than the dimensional order of the texturization, the geometry has been separated into tooth and rotating seal, in order to reduce the number of elements of the mesh since the solver requires a considerable amount of resources. The division has been made following the red dotted

line in the Figure 5.3: using the principle of superimposition of effects it is possible to have two separate simulations such that the overall effect of the entire tooth is given by the sum of the two contributions. The reason for the division is also practical: the rotating seal is characterized by a continuous coupling between the gear and the lateral plates, while the tooth covers a portion of the lateral plate that varies during rotation. The simulations of the tooth portion have been performed considering a discrete number of positions that the gear could assume during rotation, while the rotating seal part has been simulated in its entirety. The simulations have been performed in ANSYS® CFX.

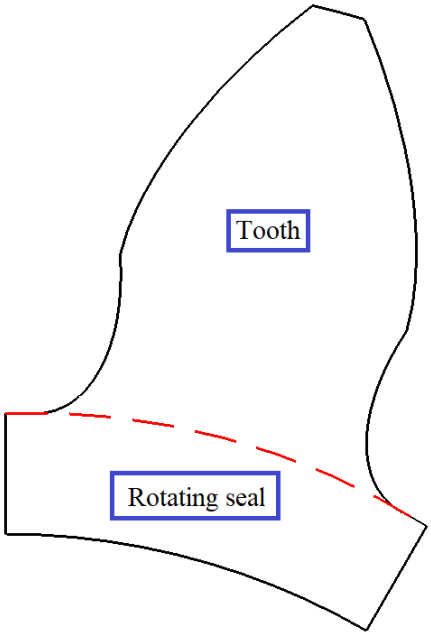

Figure 5.3. Front view of a tooth of a gear wheel showing the separation line between the tooth and the rotating seal.

5.2 Geometry A

The texture consists of a grid of recovery channels 0.2 mm wide and 0.05 mm deep that delimits three main rings of circular sectors inside which steps 0.01 mm deep have been placed.

The dimensions of the sectors have been designed also considering the geometry of the tooth, which being an involute profile, narrows towards the end. Considering the meatus subtended by the single tooth, Figure 5.4, the first two rows of sectors, rings I and II in the figure, have an angular dimension of 6°, while the sectors of the third row have a dimension of 4°. In this way, during the rotation of the tooth on the surface, there are always at least two entire sectors confined in the meatus for each ring that contribute to generate bearing capacity.

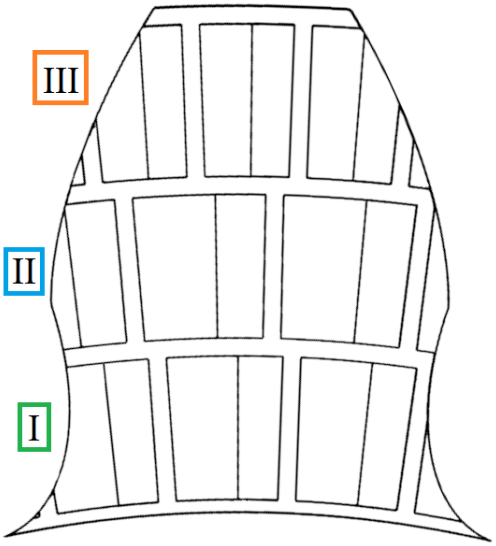

Figure 5.4. Meatus delimited by the tooth with the main rings indicated.

During the rotation of the gear wheel, the geometry of the textured surface between the wheel and the lateral plates varies: the simulations have been carried out considering different angular positions of the wheel spaced 2° from each other. Considering the periodicity of the texturing, it follows that six angular stages are sufficient to obtain the starting position again.

The boundary conditions are open boundary with zero relative pressure for the perimeter walls of the domain, while the upper plane is a moving wall with a no slip condition. The speed of the moving plane is assumed to be 2500 r/min. The fluid motion is assumed to be laminar, due to the low height of the gap and the high viscosity of the hydraulic oil. The oil temperature is assumed to be 40 °C.

The fluid domain has been discretized using a structured mesh, whose characteristics have been established following a sensitivity analysis. Of the different meshes tested, the three most significant are listed in the Table 5.2.

Table 5.2. Main characteristics of the meshes used for the sensitivity test.

	Min Element size	**Max Element size**	**Average Element quality**	**Average Aspect ratio**	**Average Orthogonal quality**	**Average Skewness**
Mesh 1	5e-6	5e-5	5.27e-2	50.43	0.957	0.12
Mesh 2	2e-6	2e-5	8.95	21.22	0.967	8.11e-2
Mesh 3	1e-6	1e-5	0.34	5.35	0.966	7.92e-2

The parameter used to evaluate the influence of the mesh on the numerical results is the force generated by the surface. The Figure 5.5 shows the trend of the force, divided by a reference value for confidential reasons, as the mesh changes: Mesh 2 has a final value that differs only by 2.5% compared to Mesh 3, which has a greater number of elements. For this reason, Mesh 2 has been adopted.

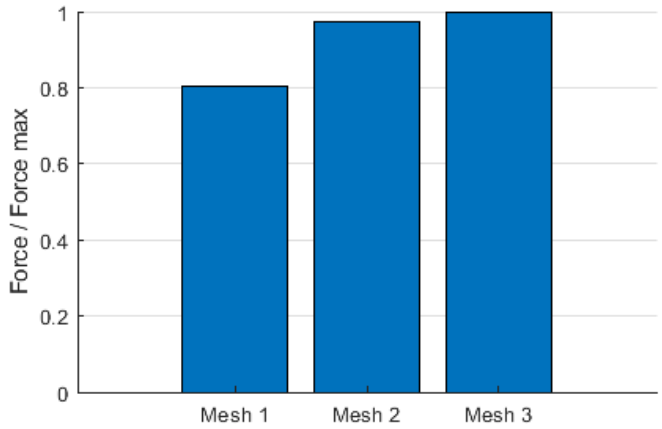

Figure 5.5. Influence of the mesh on the force generated. Position 1, gap 10 μm

The Figure 5.6 shows the absolute pressure contours relating to the six different angular positions, relating to the case of a gap height equal to 10 μm. The direction of rotation of the moving plane is clockwise. Since the moving plane rotates and the no slip condition still applies, the tangential speed rises as the radius increases. This leads to a growth in the hydrodynamic effect due to greater sliding velocity. In the following maps it could be appreciated that in general the greater overpressure is generated in correspondence with the sectors at a greater distance from the center of rotation: the maximum pressure values reached are a few bars, a more than discrete value considering the size of the steps and the fact that it is made in a low pressure area of the lateral plates. The recovery channels are the area where the pressures reach the lowest values and this allows the oil to be recalled from the boundary to bring a greater quantity of lubricant into the meatus, limiting a further decrease in pressure, also confining the effects of local cavitation. With a gap equal to 10 μm the vapor saturation pressure is reached only in very localized small areas and therefore the maps of the vapor volume fraction are not reported: these will be shown for smaller gap values, where the vapor concentration is greater and allows to see better the areas where the vapor is formed.

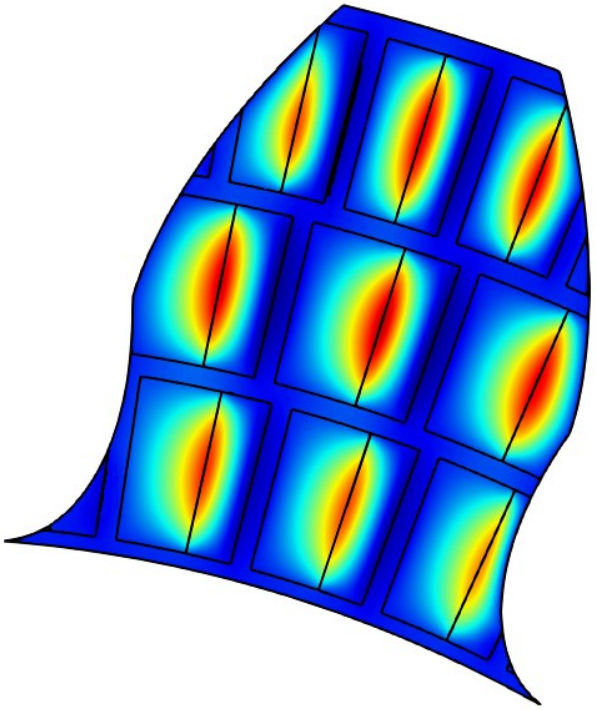

(a)

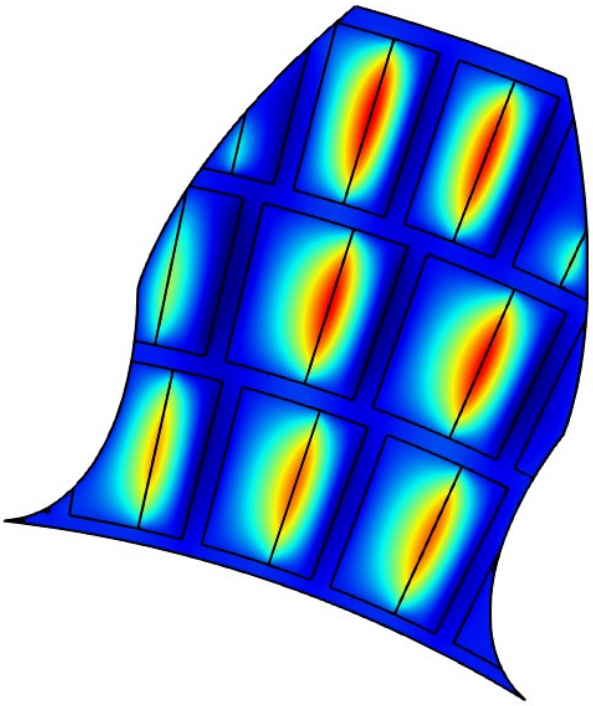

(b)

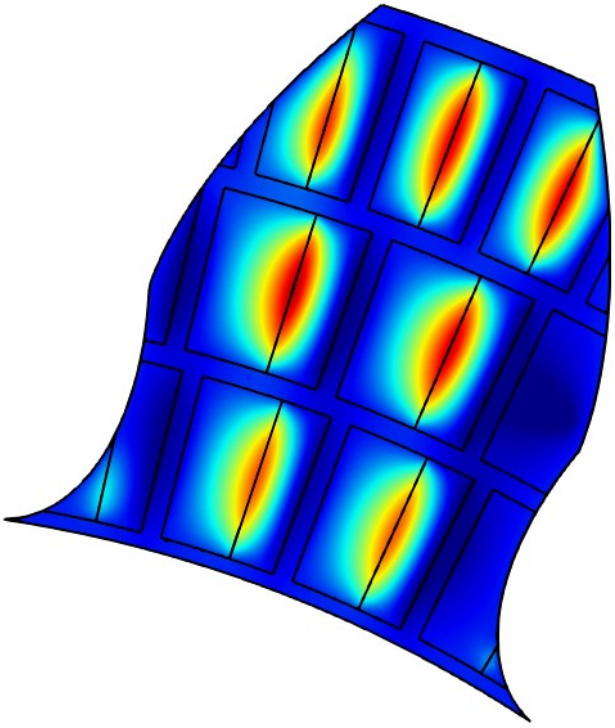

(c)

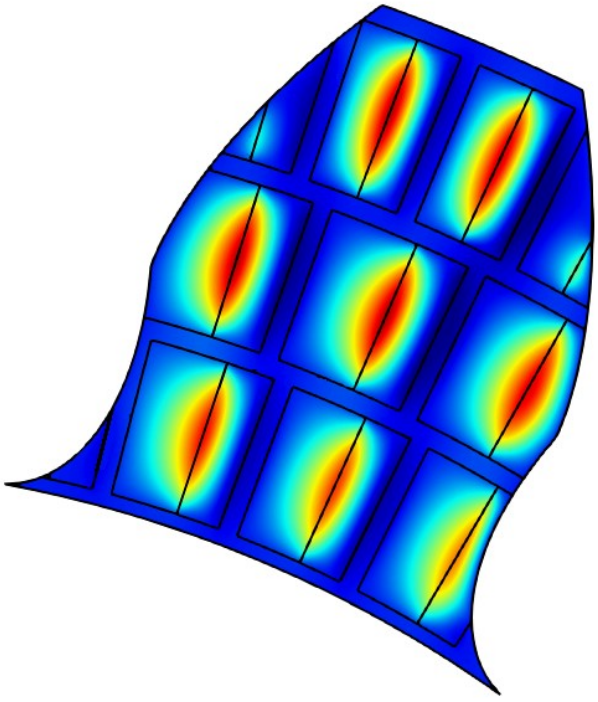

(d)

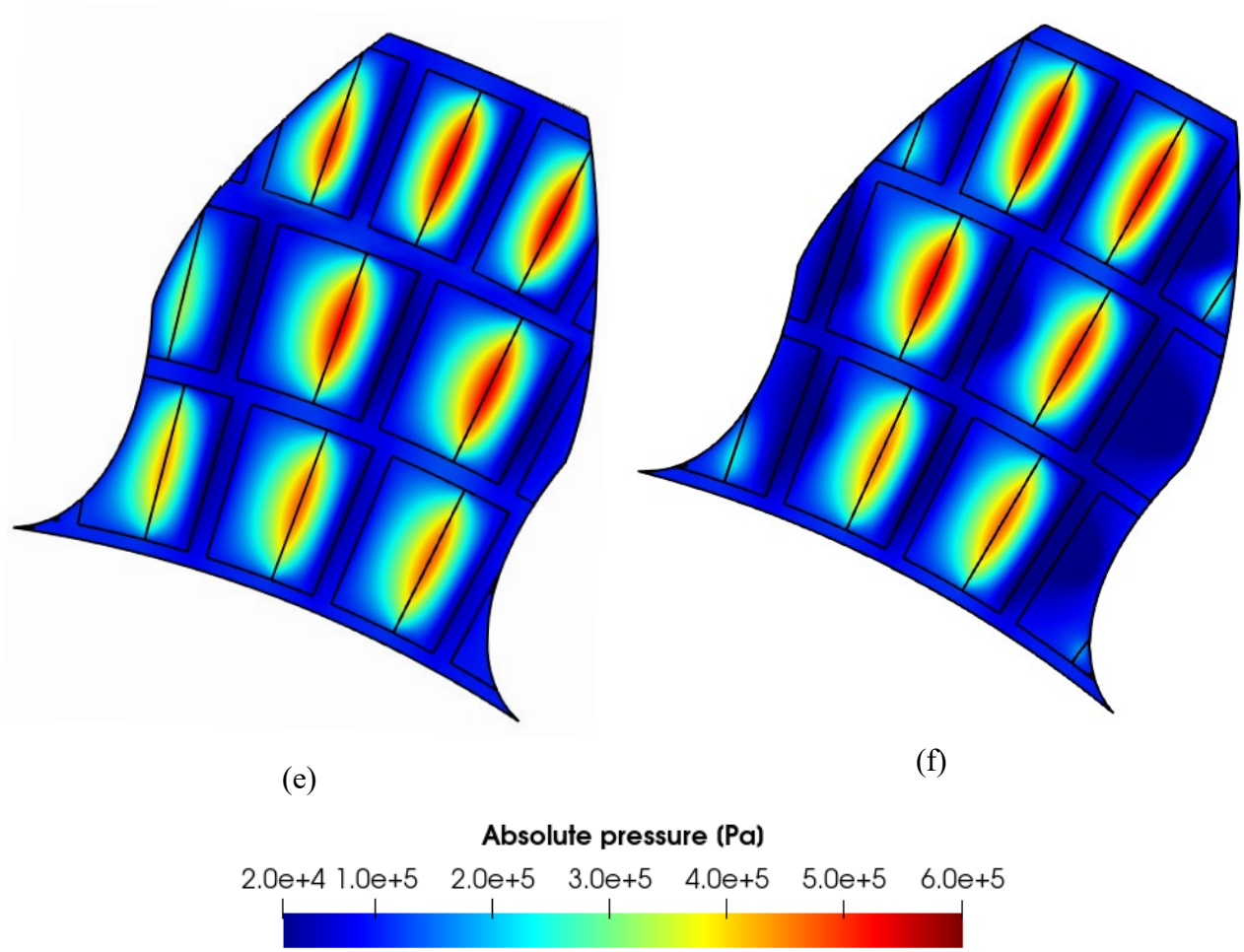

Figure 5.6. Pressure contours. Step width 60% and depth 10 µm. Gap 10 µm and rotating speed 2500 r/min

The Figure 5.7 instead shows the results relating to the gap equal to 3 µm. As already highlighted in the previous chapters, when the gap decreases both the minimum and maximum pressure values are greater. In this configuration, the saturation pressure value is reached, which leads to vaporous cavitation of the oil. In general, this arrangement of the steps allows to obtain high pressure values: locally it is possible to generate an overpressure of even about twenty absolute bars.

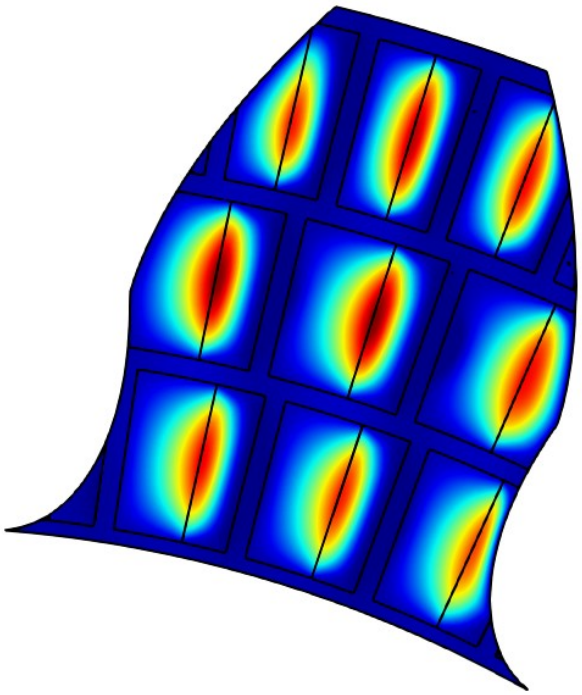

(a)

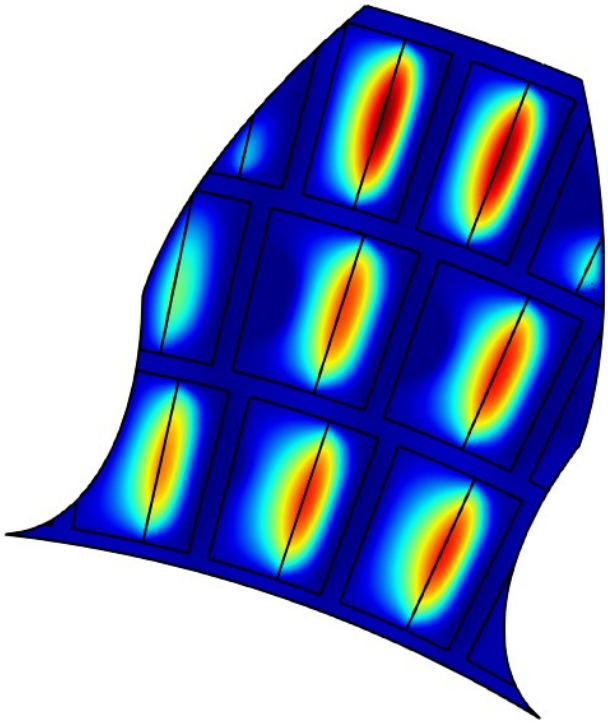

(b)

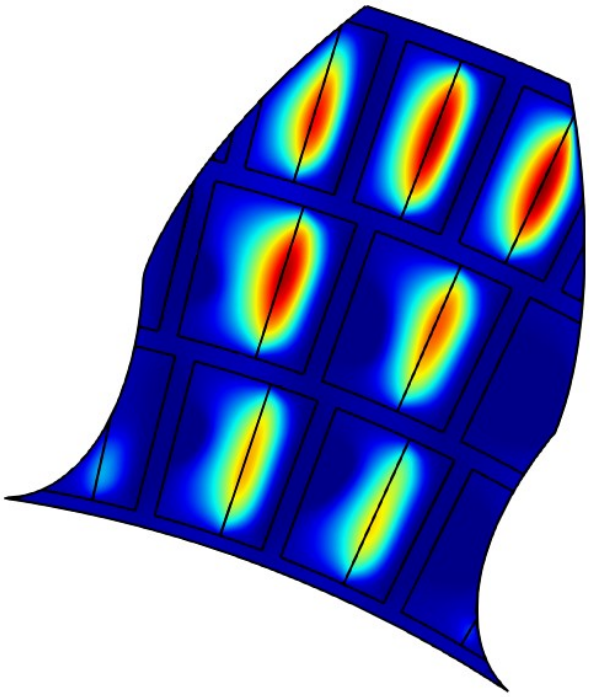

(c)

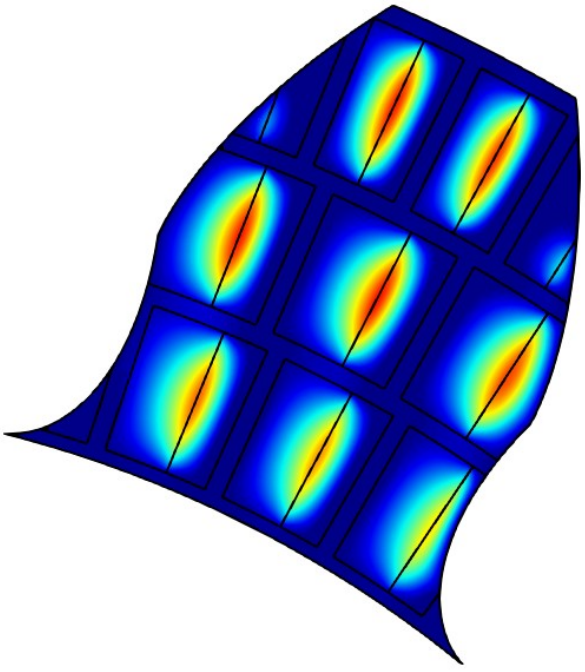

(d)

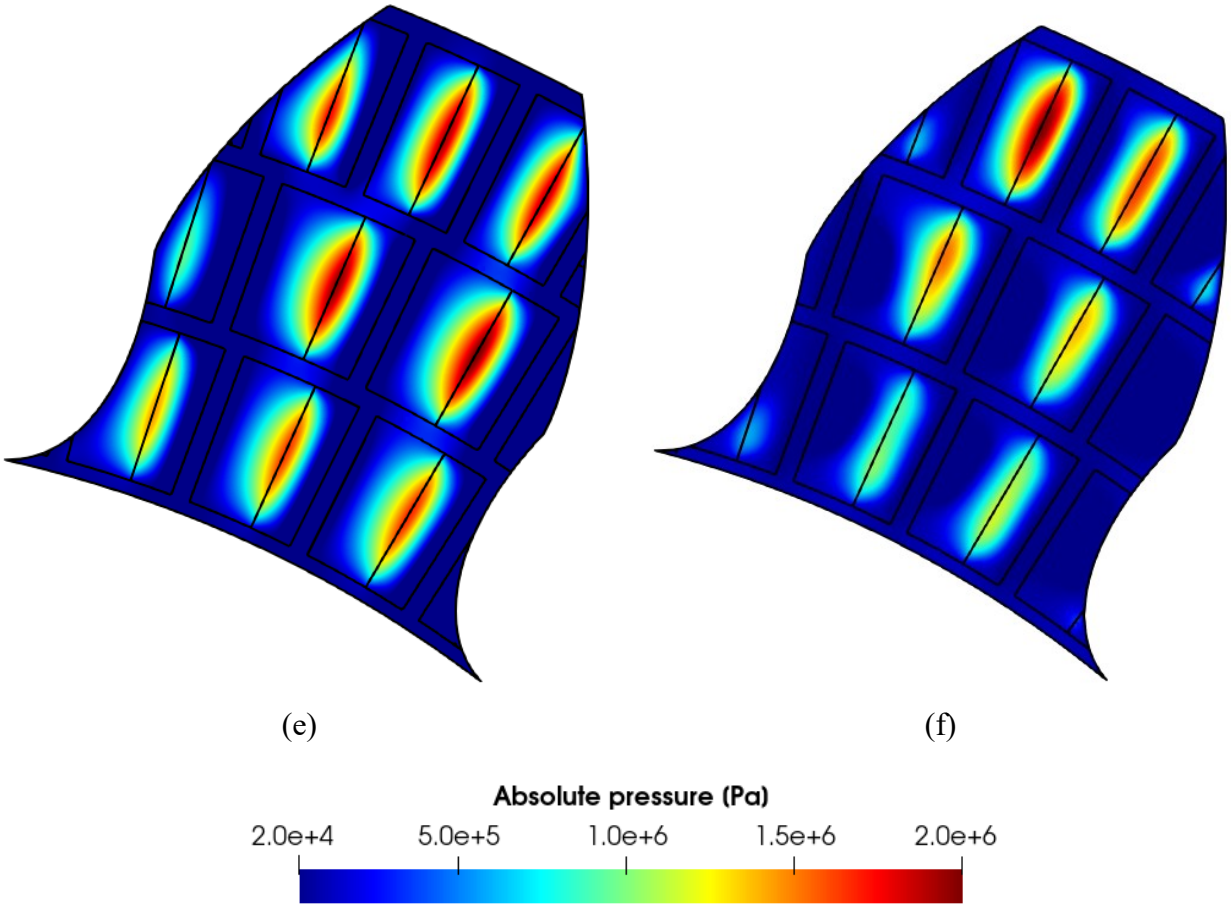

Figure 5.7. Pressure contours. Step width 60% and depth 10 µm. Gap 3 µm and rotating speed 2500 r/min

The Figure 5.8 shows the force generated by the surface in the different positions assumed by the tooth during rotation as the gap varies. For reasons of confidentiality the bearing capacity has been divided by the maximum value obtained. The bearing capacity changes during the rotation according to the angular position of the tooth. The reason for this discontinuity is due to the number of steps present below the tooth which is not always constant in the different positions considered: for example, position 2 has only two steps which contribute to the total force on rings II and III, while in position 1 there are three steps. This trend is maintained for all gap heights, but is enhanced as the gap decreases, for all the angular positions assumed by the gear wheel.

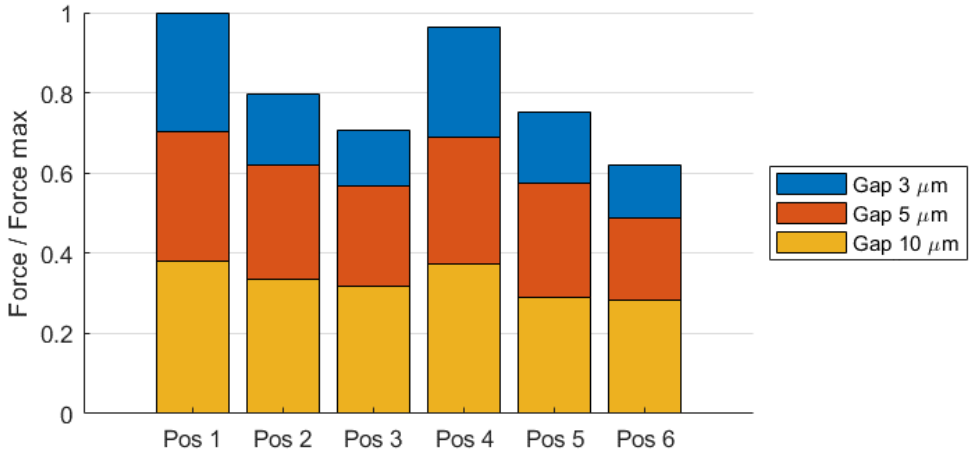

Figure 5.8. Bearing capacity in the different positions studied for different values of the gap.

In the Figure 5.9 the dimensionless force averaged over the six positions as a function of the gap is reported: the trend as the gap decreases is increasing more than linear.

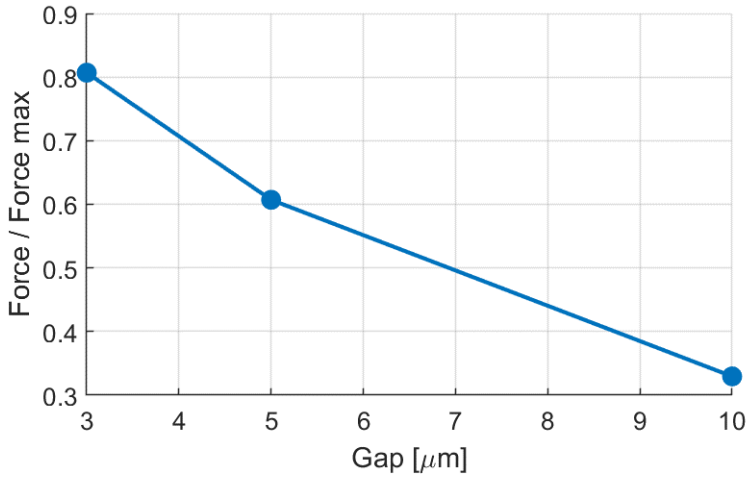

Figure 5.9. Bearing capacity averaged over the six angular positions as a function of the gap.

5.2.1 Rotating seal

Simulations have been also performed on the lateral plate portion called the rotating seal. In this case, unlike the previous ones, the two coupled surfaces, lateral plate and gear wheel, have a continuous coupling.

The geometry considered is like the one created under the tooth and presents angular sectors with an amplitude of 6° separated by recovery channels with the same geometric characteristics described in the previous paragraph.

The simulations have been performed on the entire angular sector corresponding to the portion of the lateral plate in the suction. The Figure 5.10 shows the results relating to a gap of 10 μm and 3 μm.

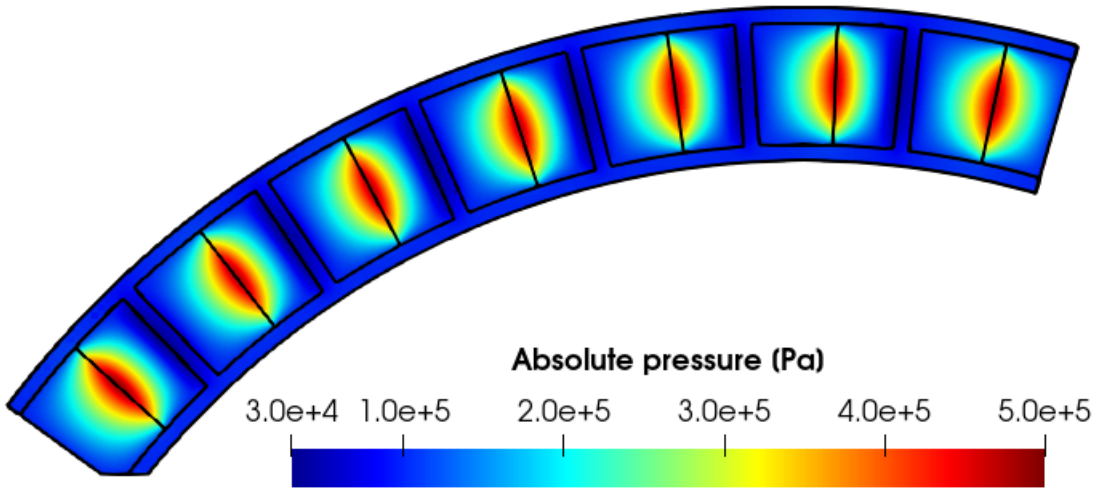

(a)

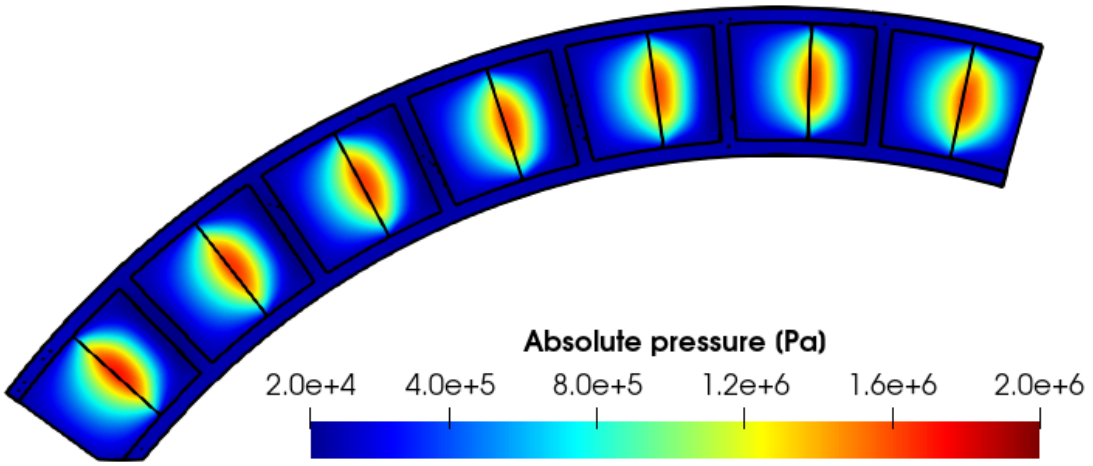

(b)

Figure 5.10. Absolute pressure contour on the moving plane. (a) Gap 10 μm. (b) Gap 3 μm

Also in this case the force expressed by this portion of the surface is such that it increases more than linearly as the gap decreases, as reported in the Figure 5.11a. The Figure 5.11b shows how the force given by the rotating seal is always greater than the average one obtained by the tooth during the rotation. The values are dimensionless by dividing by the maximum force value, which corresponds to that generated by the rotating seal with a gap of 3 μm.

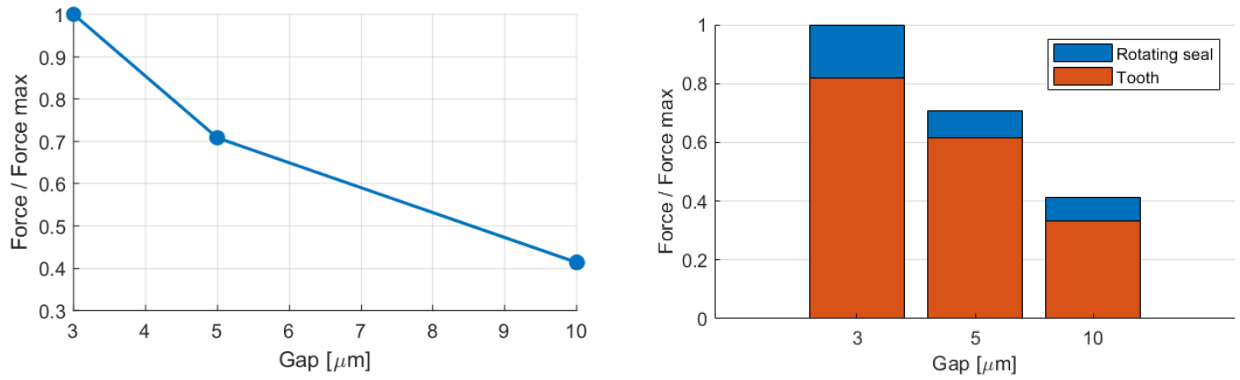

(a) (b)

Figure 5.11. (a) Bearing capacity expressed by the rotating seal as a function of the gap height. (b) Comparison between the bearing capacity of the rotating seal and the average force generated by the tooth.

In conclusion, the total bearing capacity obtainable through this texture geometry is given by the sum of the force generated by the rotating seal plus that obtained by the tooth multiplied by the number of teeth present on the textured surface.

5.3 Geometry B

As Geometry A, this configuration consists of a grid of recovery channels 0.2 mm wide and 0.05 mm deep that delimits three main rings of circular sectors inside which a sequence of square dimples with side 0.1 mm and depth of 0.01 mm have been positioned in the first 60% of the available surface.

The dimensions of the sectors are the same as those of Geometry A: sectors of rings I and II have an angular dimension of 6°, while the third row presents sectors of 4° in width.

Similarly to Geometry A, the boundary conditions are: open boundary on the perimeter walls; moving plane with rotation speed of 2500 r/min and non-slip condition. Oil temperature 40 °C. Also in this case the motion of the fluid is laminar. The mesh is structured with the characteristics of Mesh 3 in the Table 5.2: the size of the elements is smaller than Geometry A due to the minor geometric extension of the dimples compared to the steps.

The Figure 5.12 shows the absolute pressure contours relating to the six different angular positions, relating to the case of a gap height equal to 10 μm. The rotational direction of the moving plane is clockwise. By observing the pressure contours, an overpressure is established in each sector to ensure that the surface generates a positive bearing capacity. However, looking in detail, the magnitude of the overpressure is almost an order of magnitude less than in the case with the steps with the same boundary conditions. Also in this case, since the speed of the moving plane is

rotational, the sliding velocity rises as the radius increases, leading to a growth in the hydrodynamic effect that allows to generate a greater overpressure in correspondence with the sectors at a greater distance from the center of rotation. With a gap equal to 10 μm the vapor saturation pressure is reached only in very localized small areas with the generation of a small amount of vapor.

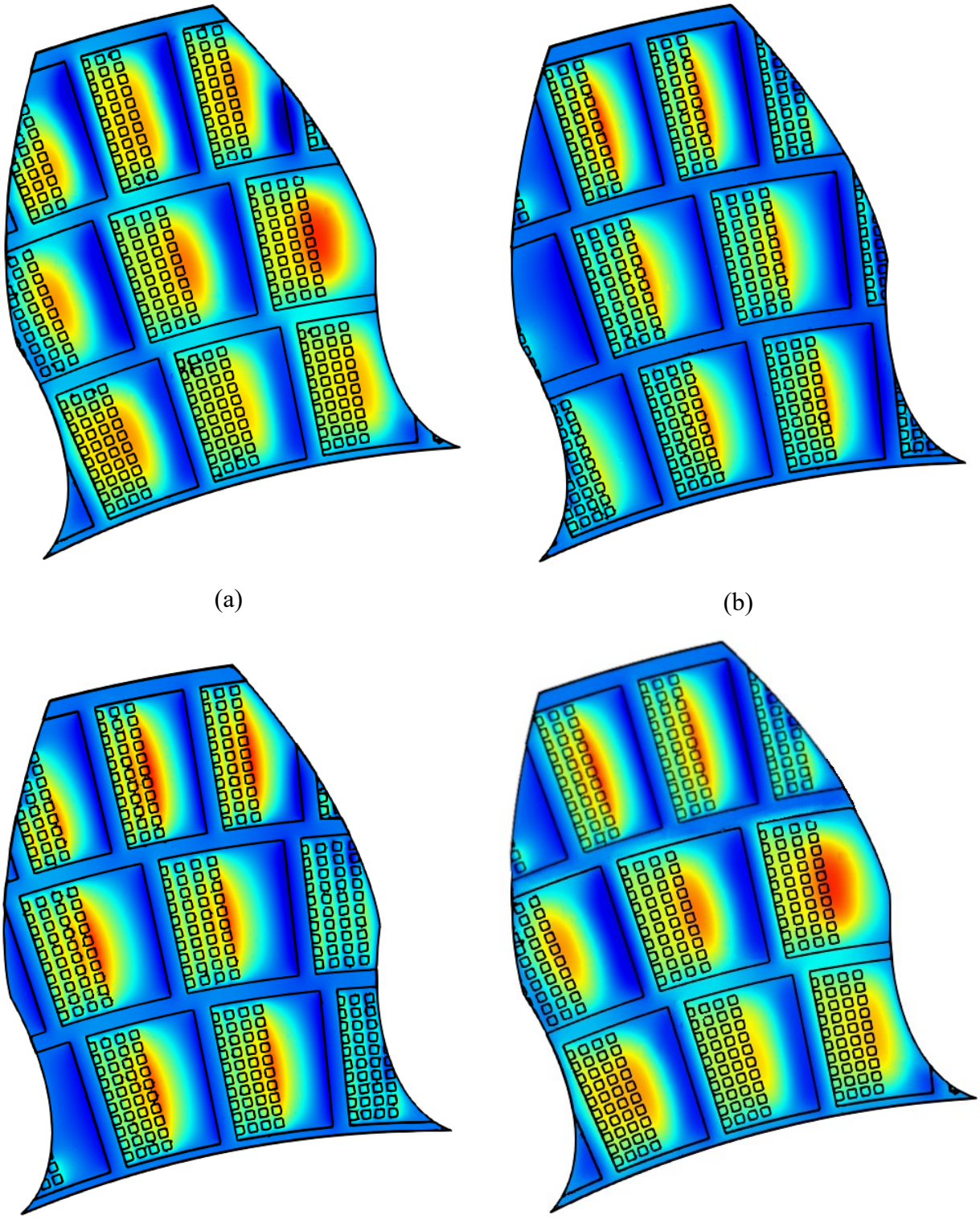

(a) (b)

(c) (d)

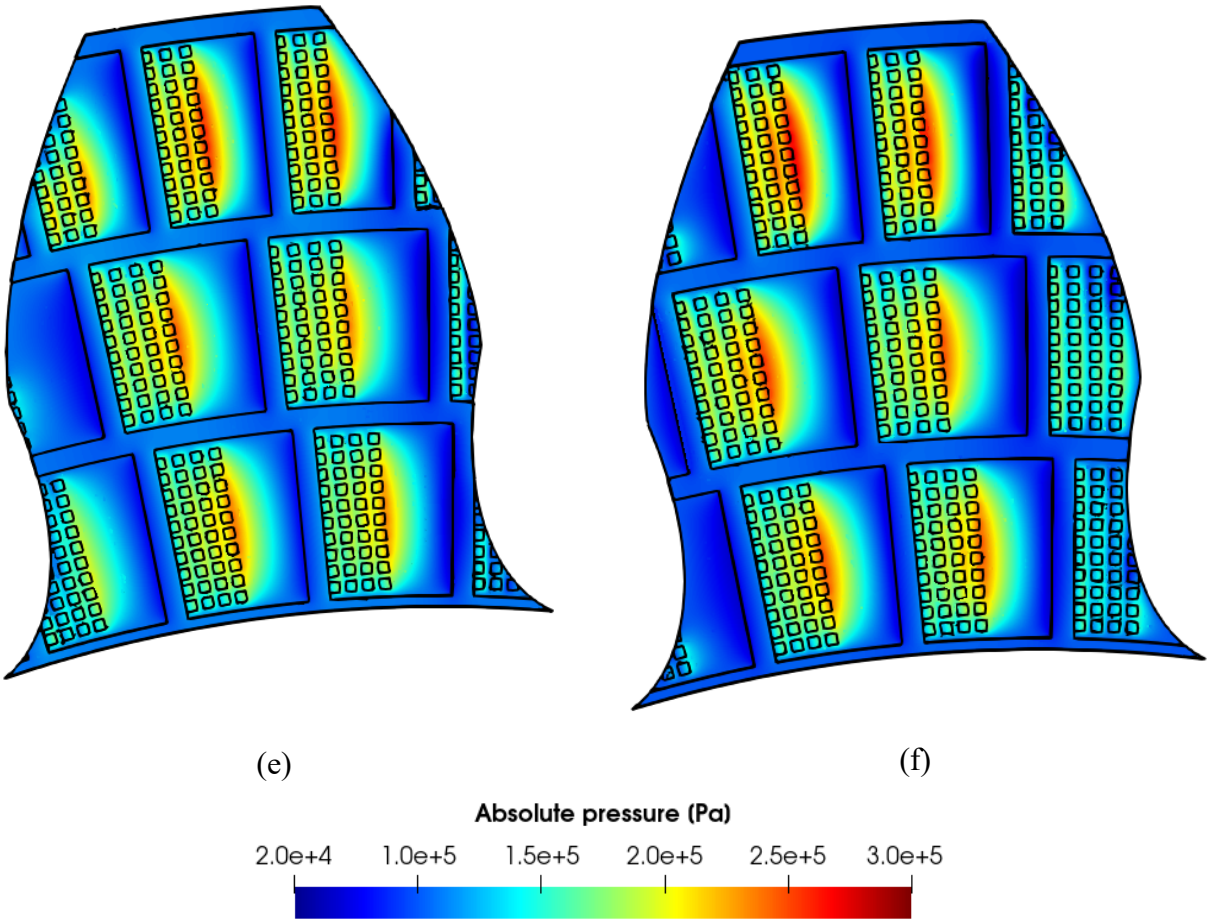

Figure 5.12. Pressure contours. Dimples side 0.1 mm and depth 10 µm. Gap 10 µm and rotating speed 2500 r/min

The Figure 5.13 instead shows the results relating to the gap equal to 3 µm.

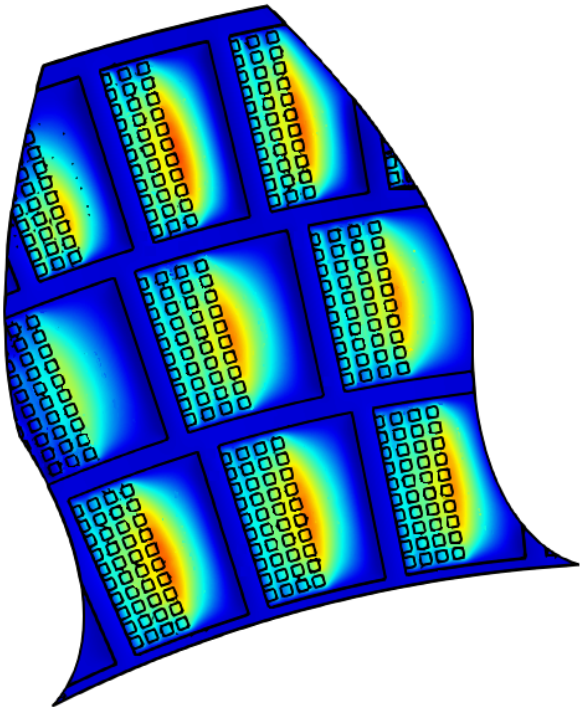

(a)

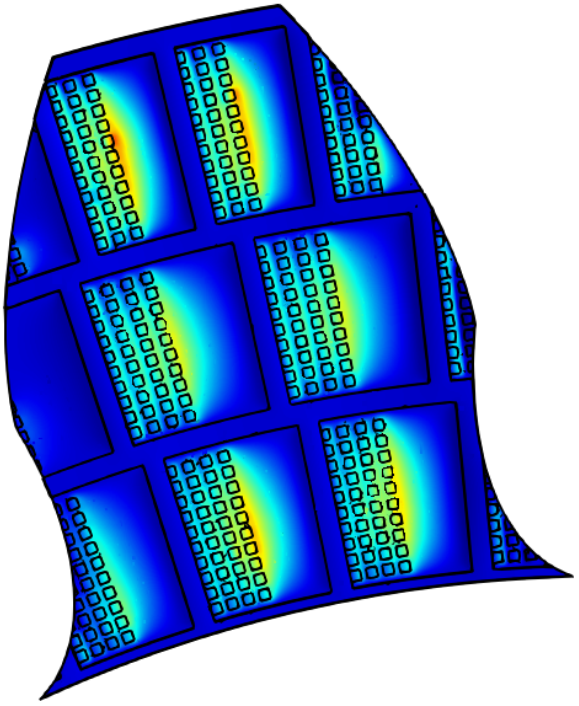

(b)

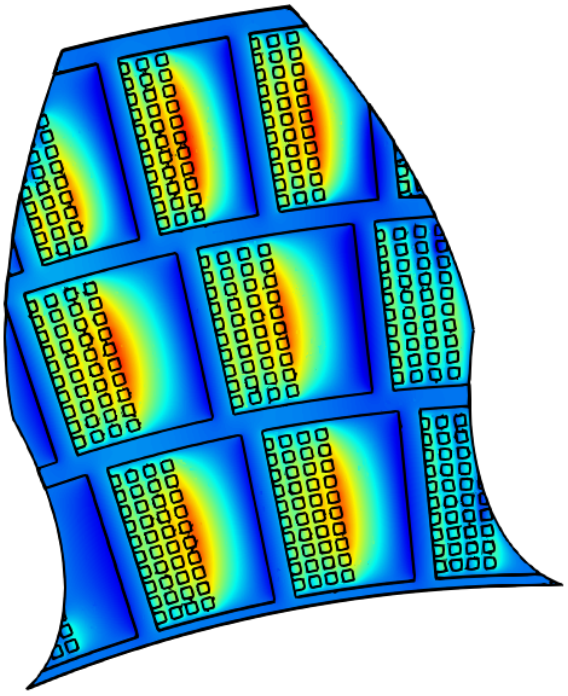

(c)

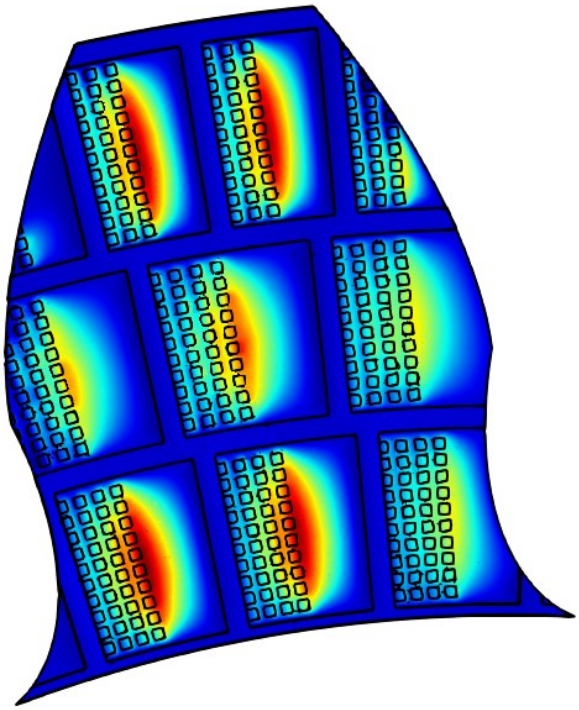

(d)

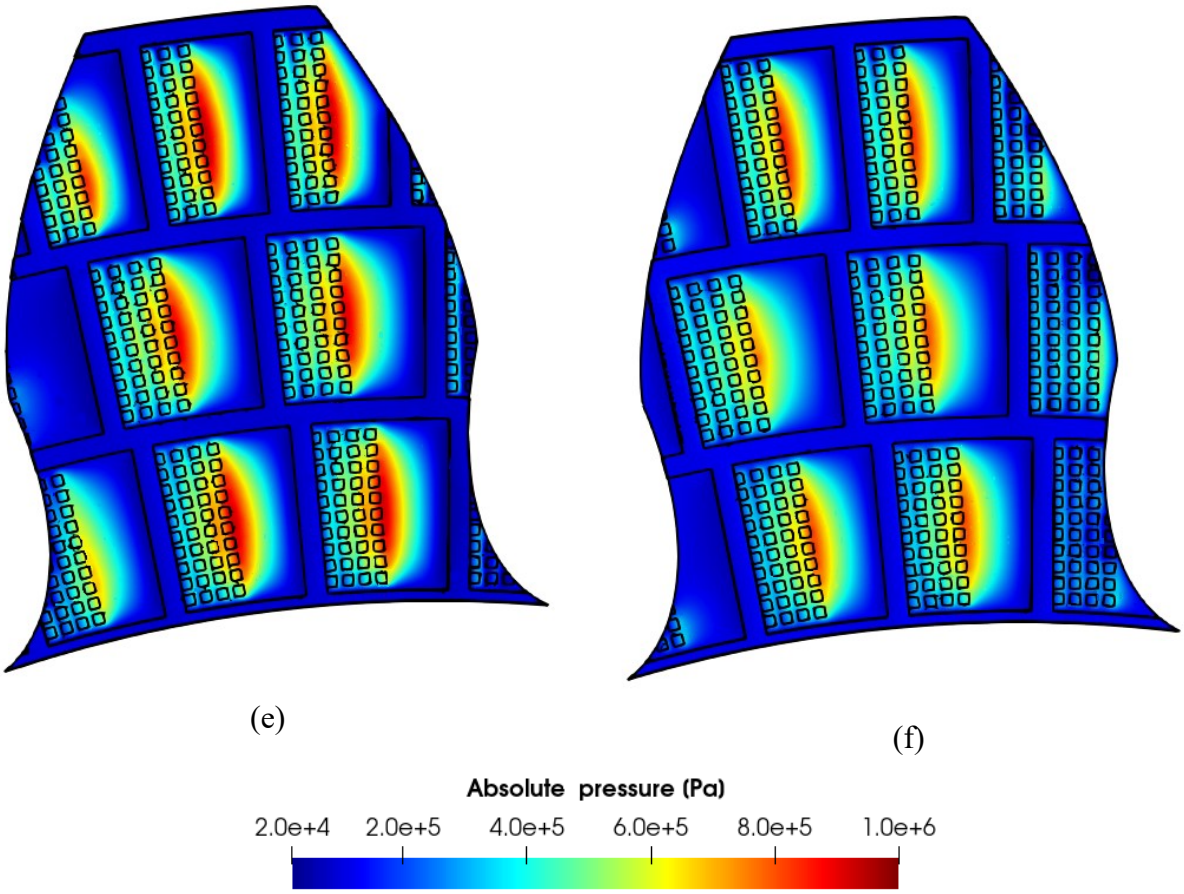

Figure 5.13. Pressure contours. Dimples side 0.1 mm and depth 10 µm. Gap 3 µm and rotating speed 2500 r/min

The Figure 5.14 shows the force generated by the surface in the different positions assumed by the tooth during rotation. For reasons of confidentiality the bearing capacity has been divided by the maximum value obtained. As for Geometry A, the great discontinuity of the bearing capacity is due to the number of steps present below the tooth which is not constant in the different positions considered.

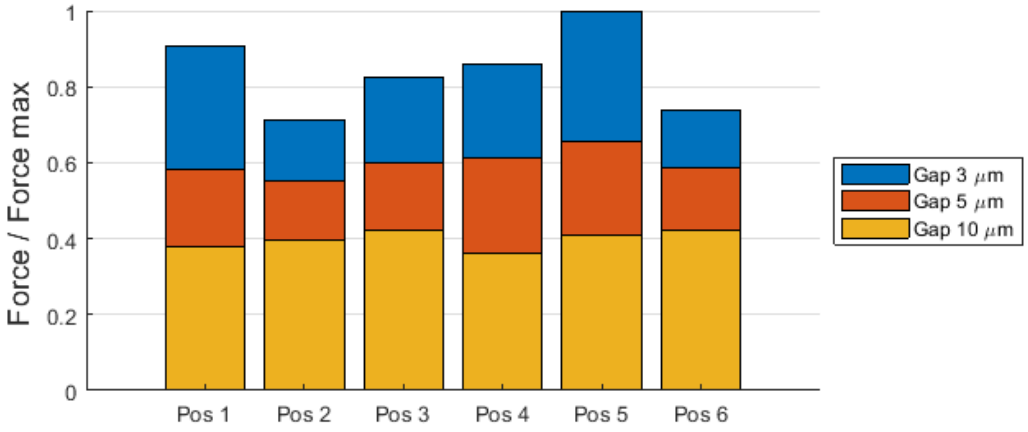

Figure 5.14. Bearing capacity in the different positions considered for different values of the gap.

In the Figure 5.15 the dimensionless force averaged over the six positions is reported: the trend as the gap decreases is increasing more than linear.

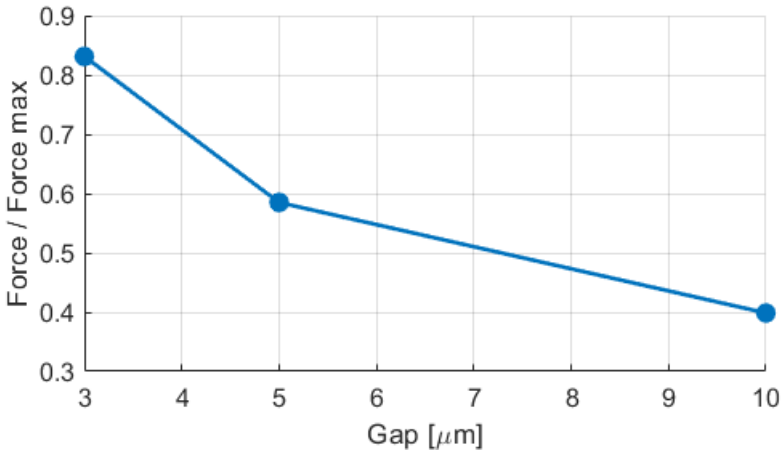

Figure 5.15. Bearing capacity averaged over the six angular positions as a function of the gap.

5.3.2 Rotating seal

Simulations have been also performed on the rotating seal. The geometry created is like the one under the tooth and is characterized by angular sectors with an amplitude of 6° separated by recovery channels with the same geometric characteristics described in the previous paragraph.

The simulations have been performed on the entire portion of the lateral plate in the suction. The Figure 5.16 shows the results relating to a gap of 10 μm and 3 μm.

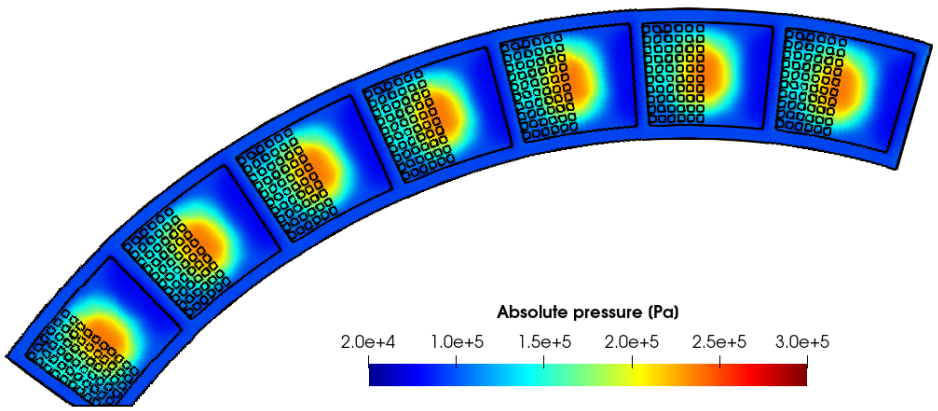

(a)

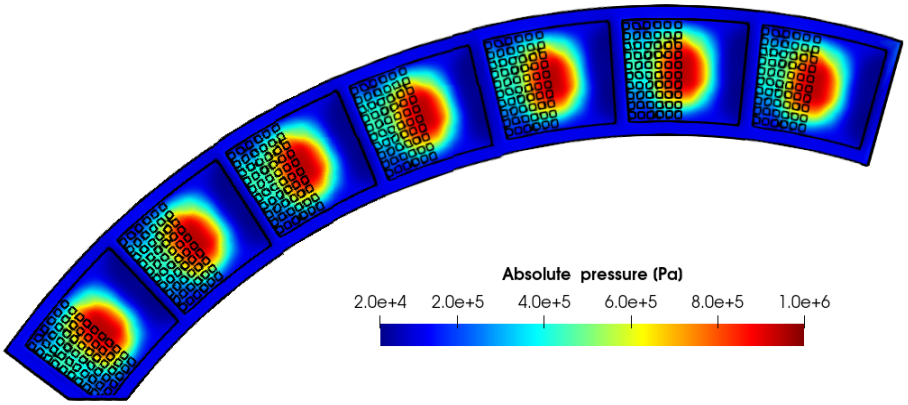

(b)

Figure 5.16. Absolute pressure contour on the moving plane. (a) Gap 10 µm. (b) Gap 3 µm

As already described in previous paragraphs, the bearing capacity generated is increasing more than linearly as the gap decreases, as reported in the Figure 5.18a. The Figure 5.18b shows that the force provided by the rotating seal is greater than the average one obtained by the tooth during the rotation. The values are dimensionless by dividing by the maximum force value, which corresponds to that generated by the rotating seal with a gap of 3 µm.

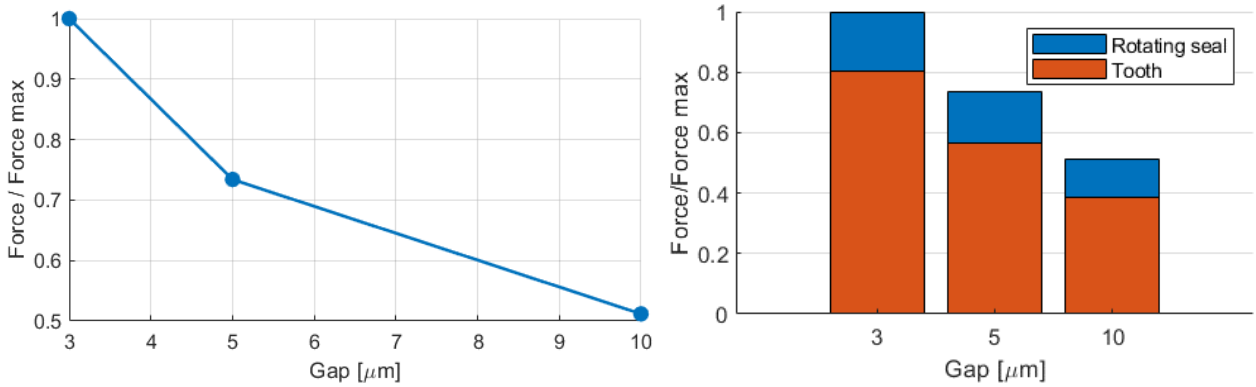

(a) (b)

Figure 5.17. (a) Bearing capacity expressed by the rotating seal as a function of the gap height. (b) Comparison between the bearing capacity of the rotating seal and the force generated by the tooth.

5.4 Geometry C

This geometry has a number of sectors four times higher than Geometry A. The sectors have a radial height halved as well as the angular width is also halved, passing from 6° to 3° and from 4° to 2°. The recovery channels are also half as thick, leaving their depth unchanged. In this configuration, three different simulations with an angular step of 2° are sufficient since the texture has a periodicity of 6°. The Figure 5.18 shows the absolute pressure contours obtained on the moving plane, where the gap is 10 μm. The direction of rotation of the moving plane is clockwise. Also in this case, the higher pressure values are obtained in the steps at a greater distance from the rotation axis, due to the greater relative sliding speed between its coupled surfaces. The low pressure areas, which correspond to portions of the recovery channels, are few and confined towards the ends of the domain; in the more central areas, on the other hand, the pressure tends to be greater than the atmospheric one, due to the bigger number of steps that allow the pressure to be more uniform.

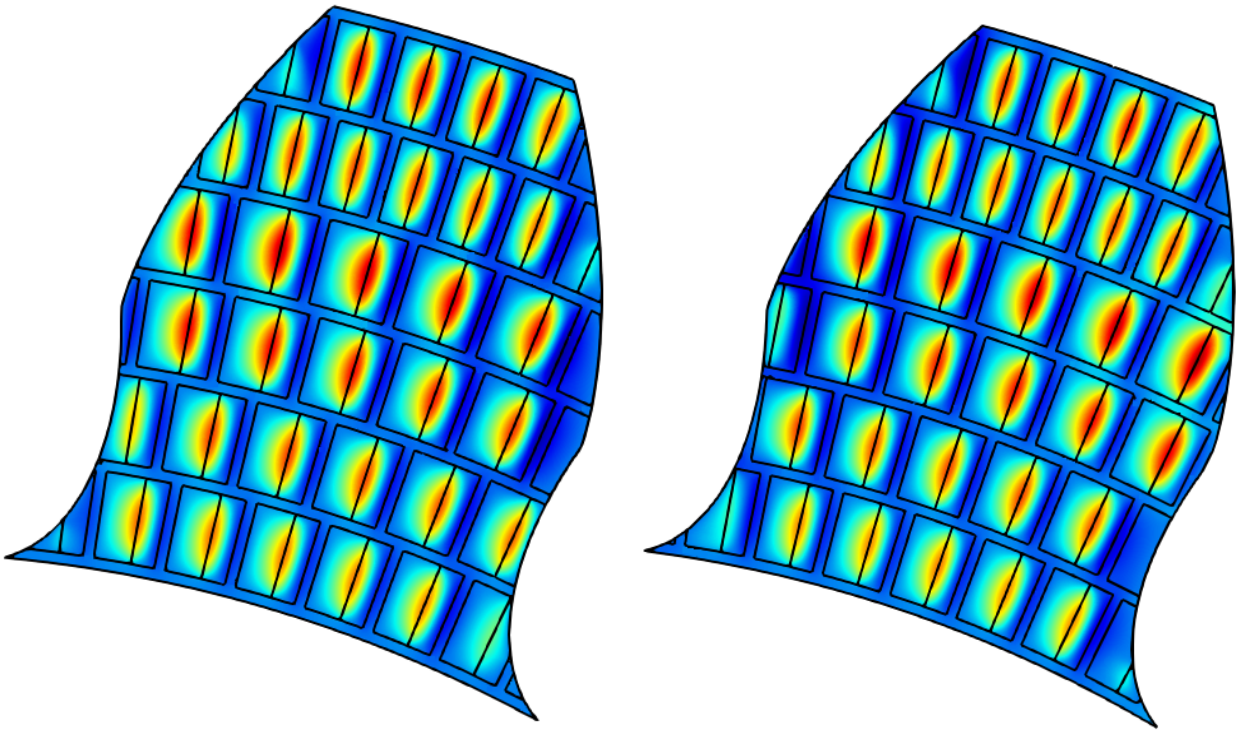

(a) (b)

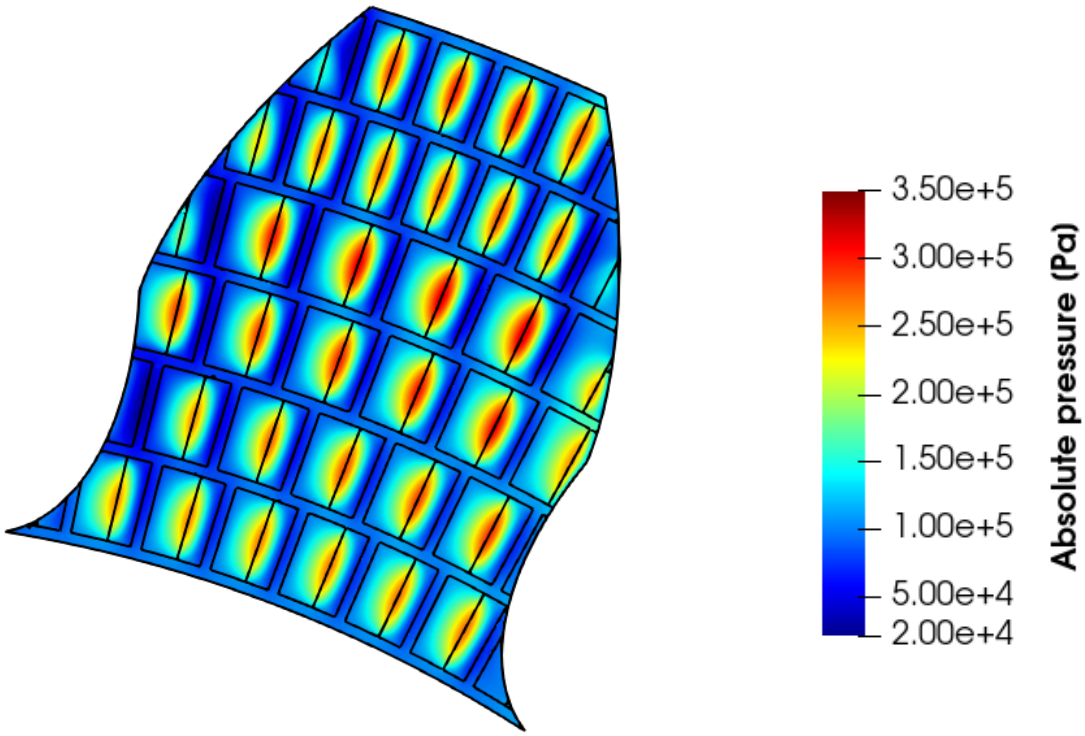

(c)

Figure 5.18. Pressure contours. Step width 60% and depth 10 µm. Gap 10 µm and rotating speed 2500 r/min

The Figure 5.19 shows the absolute pressure contours on the moving plane relative to the case of a gap equal to 3 µm. As already commented in other configurations, when the gap decreases both the minimum and maximum pressure values are greater. As the gap decreases, the textured surface allows for higher pressure peaks; at the same time the minimum pressure decreases to values close to the saturation one, triggering the vaporous cavitation.

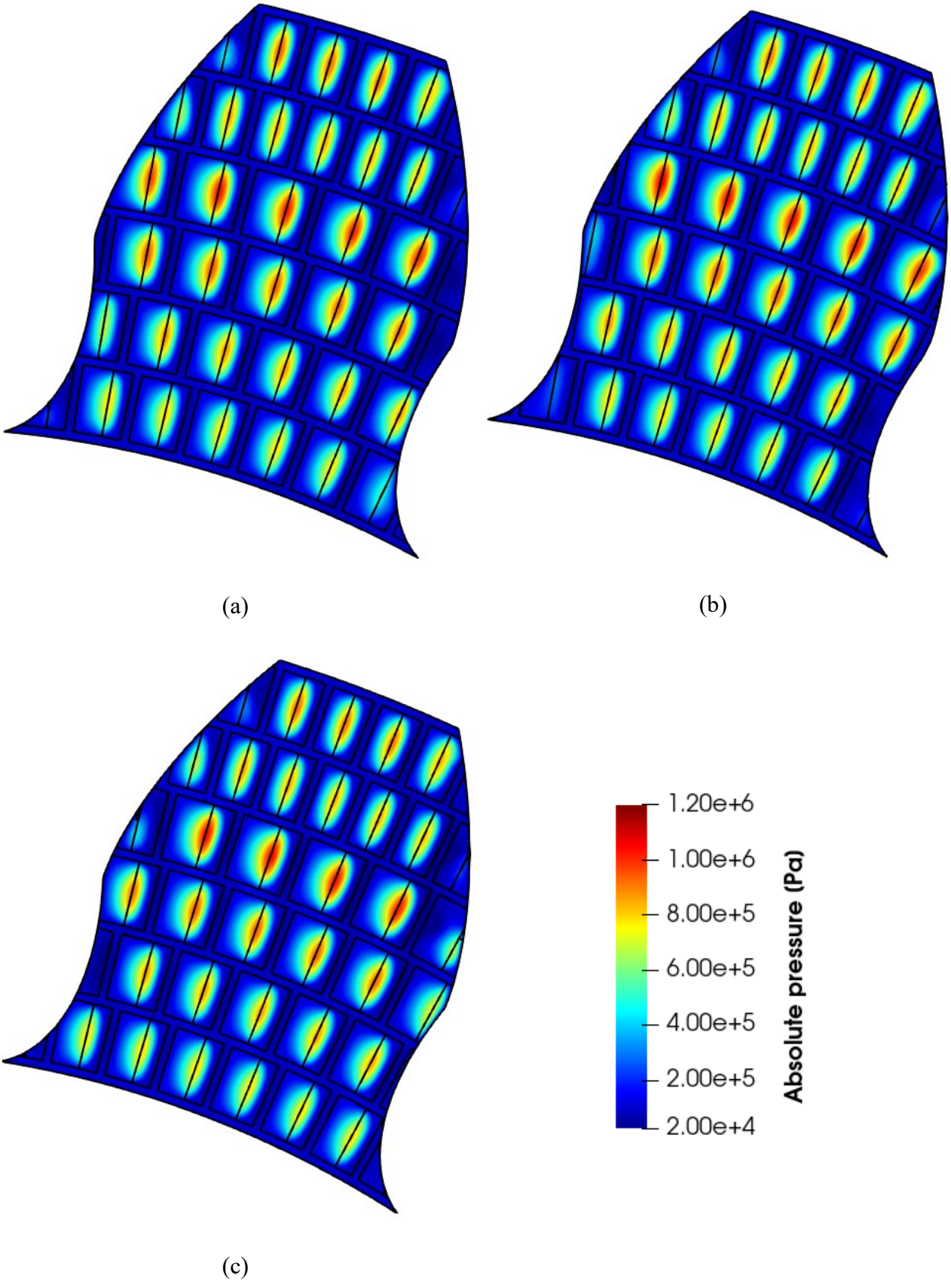

Figure 5.19. Pressure contours. Step width 60% and depth 10 μm. Gap 3 μm and rotating speed 2500 r/min

As in the previous cases, the Figure 5.20 shows the dimensionless force generated by this geometry configuration as a function of the angular position assumed by the tooth for different gap heights. Since the number of steps is greater than in previous configurations, the force generated is more uniform during rotation: in the chart it could be appreciated how the force is almost the same for each angular position and increases as the gap decreases.

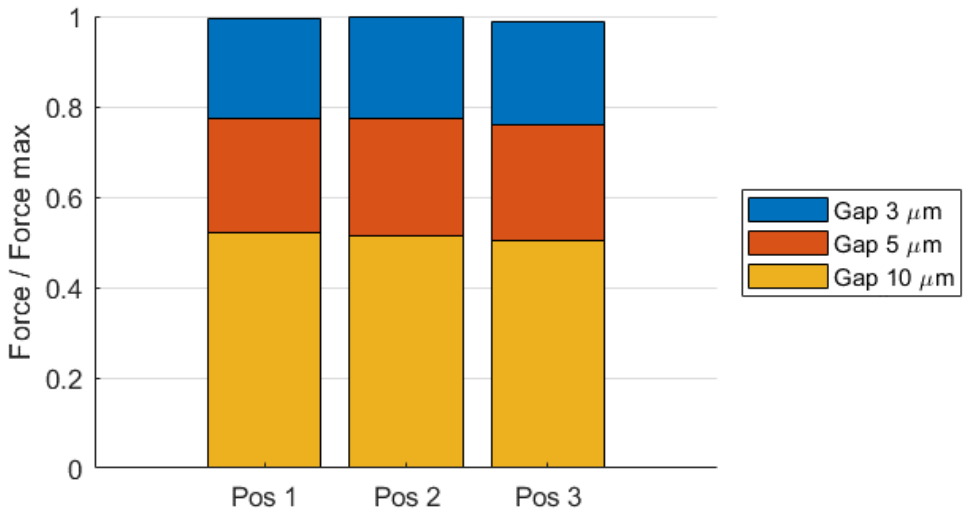

Figure 5.20. Bearing capacity in the different positions studied for different values of the gap.

The Figure 5.21 shows the dimensionless average pressure for Geometry C, which, as already observed in the other geometries, grows more than linearly as the gap decreases.

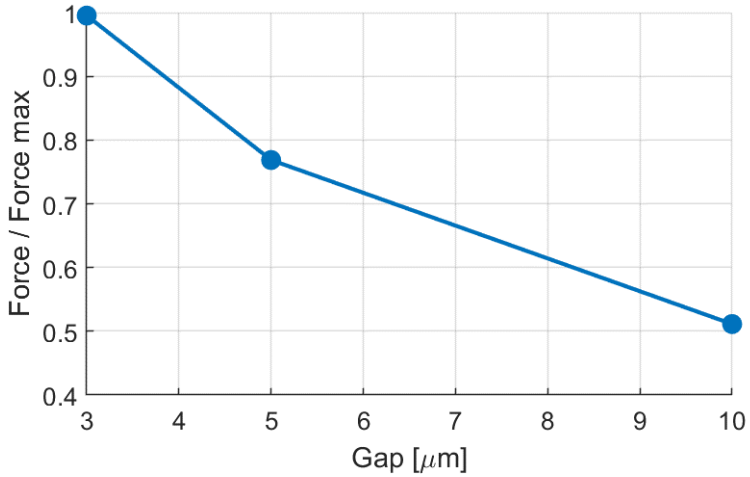

Figure 5.21. Bearing capacity averaged over the three angular positions as a function of the gap.

5.4.3 Rotating seal

Also in this geometric configuration, simulations on the rotating seal have been performed. Since the geometry of the texture is smaller than the others, there are two rows of steps with the same surface area. The Figure 5.22 shows the results relating to a gap of 10 µm and 3 µm.

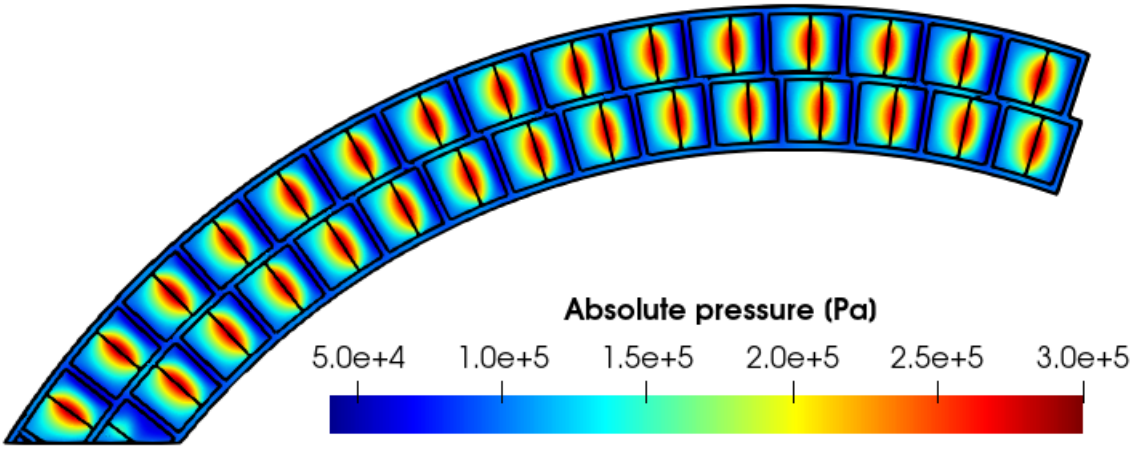

(a)

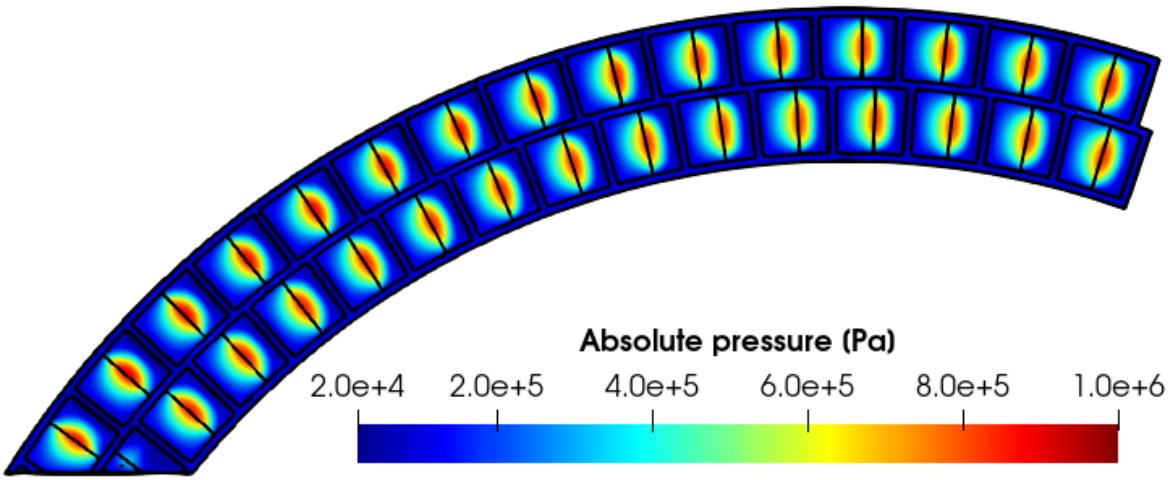

(b)

Figure 5.22. Pressure contour on the moving plane. (a) Gap 10 µm. (b) Gap 3 µm

The force expressed by this portion of the surface increases more than linearly as the gap decreases, as reported in the Figure 5.23a. Figure 5.23b shows the comparison between the force given by the rotating seal and the average one obtained by the tooth during rotation; the values are dimensionless by dividing by the maximum force value, which corresponds to that generated by the

rotating seal with a gap of 3 µm. As with other configurations, the rotating seal generates a greater force.

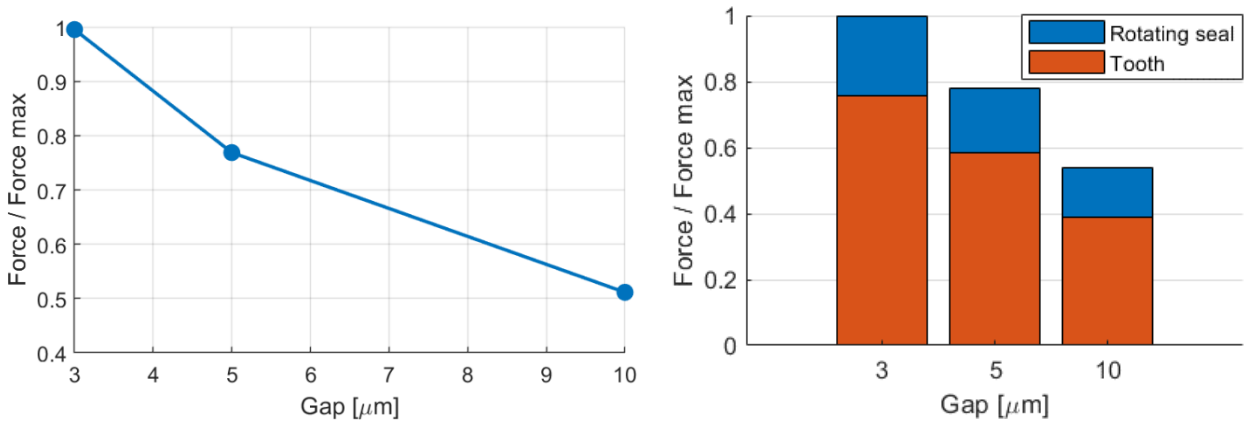

Figure 5.23. (a) Bearing capacity expressed by the rotating seal as a function of the gap height. (b) Comparison between the bearing capacity of the rotating seal and the force generated by the tooth.

5.4.4 Comparison

The Figure 5.24 shows the comparison between the three analyzed geometries. The average force has been divided by the maximum average value, corresponding to the force generated by Geometry A with a gap equal to 3 µm. The graph relates to the portion of the lateral plate under the tooth; the results reflect the considerations made when describing the pressure contours. The geometry capable of generating the greatest bearing capacity is the one characterized by large steps, Geometry A, while the other two provide lower performance and comparable to each other's.

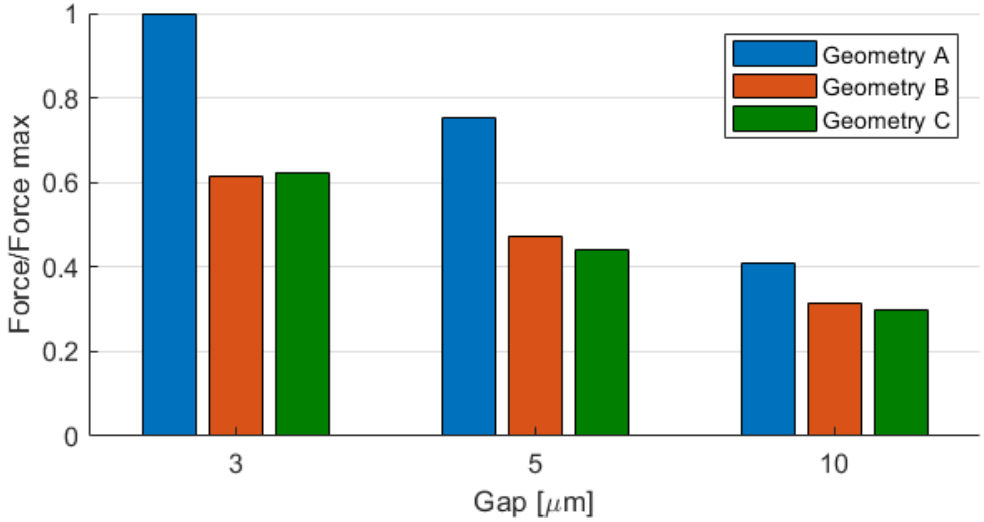

Figure 5.24. Bearing capacity generated by the three analyzed geometries.

5.5 Cavitation considerations

This paragraph describes the potential of the full cavitation model in calculating the volume fractions of released air and generated vapor and predicting the distribution of the gas phase within the domain.

The Figure 5.25 shows the volume fraction of vapor generated in the domain relating to position 2 of Geometry A, with a gap of 3 μm. The vapor tends to concentrate near the recovery channels, since they are the areas where the pressure is lower and reaches the saturation value. Condensation is a dynamic process that requires a longer time than vaporization (the condensation coefficient is two orders of magnitude smaller, Table 5.1): for this reason, the vapor occupies part of the volume of the step before being completely reabsorbed into the liquid, due to the increase in the pressure field hydrodynamically generated by the texture. This also explains why in the contours shown in the Figure 5.7, the pressure field is distorted: vapor is still present at the inlet of the step, which limits the pressurization ramp generated by the hydrodynamic effect, as shown in the portion highlighted in the Figure 5.26.

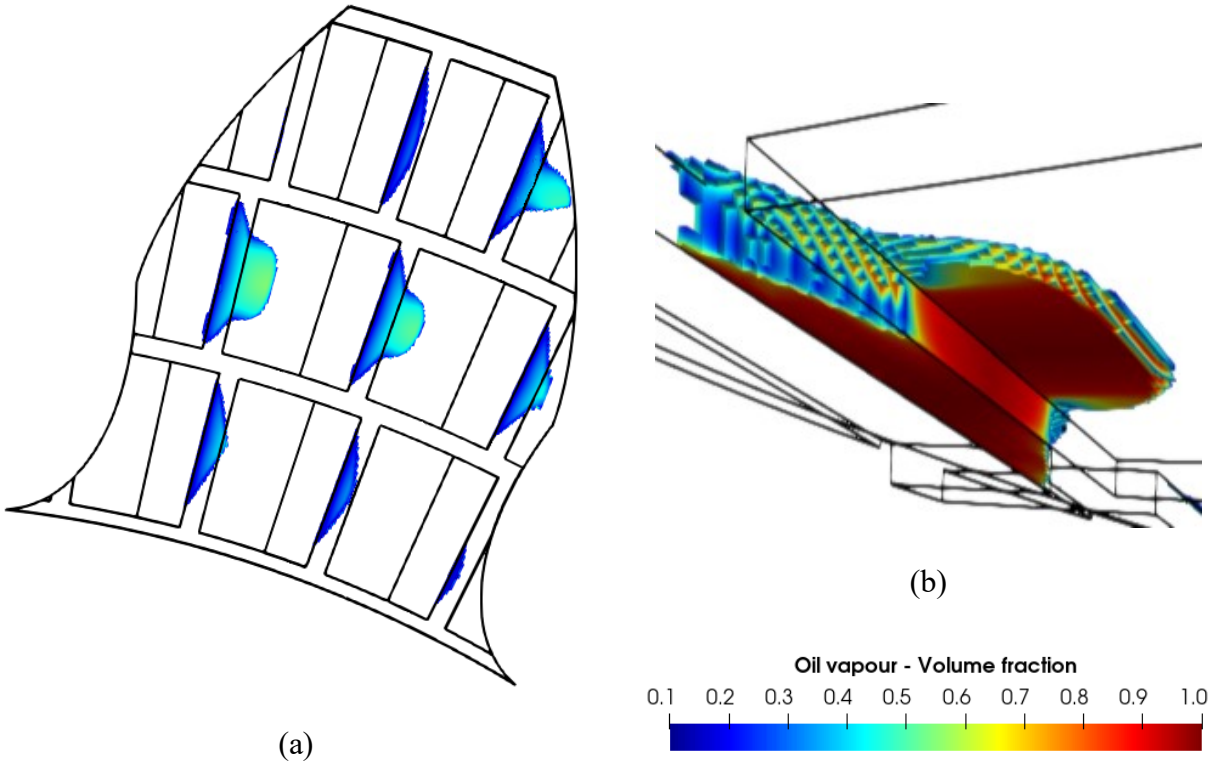

Figure 5.25. Oil vapor volume fraction generated. Position 2, gap 3 μm, rotating velocity 2500 r/min. Only the portions of the mesh where the volume fraction of vapor is greater than 10% are highlighted.

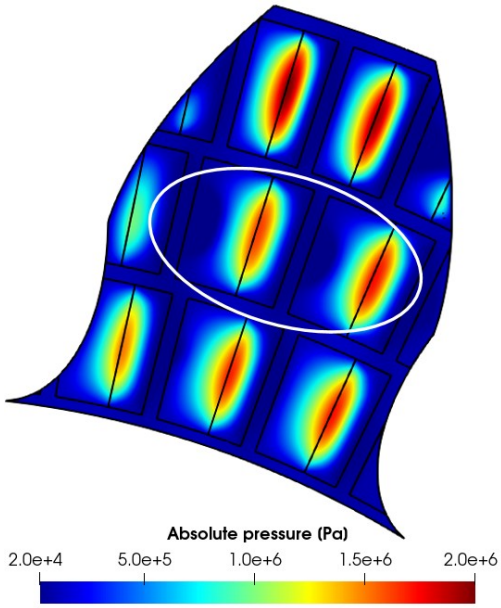

Figure 5.26. Pressure contours of position 2. Gap 3 µm and rotating speed 2500 r/min

In the configuration characterized by the sequence of dimples, Geometry B, the onset of vaporous cavitation occurs in a very localized and slight way only towards the exit from the domain, where the texture is cut by the involute profile of the tooth, as shown in the Figure 5.27.

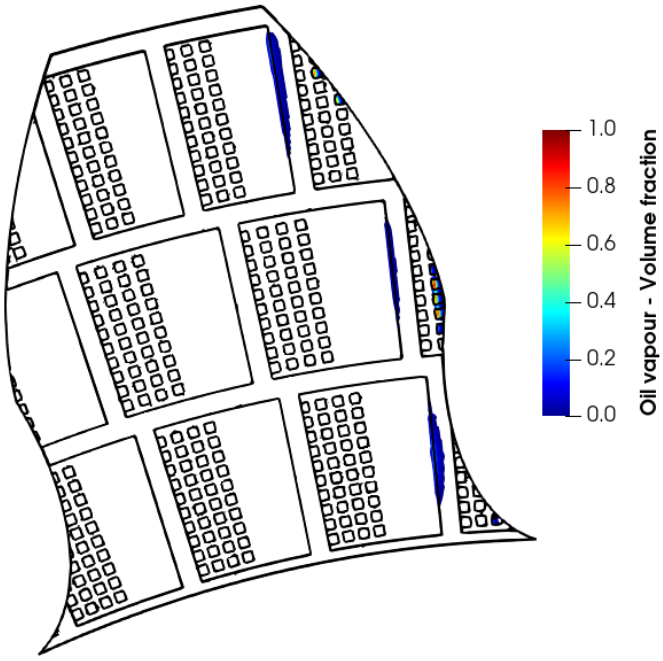

Figure 5.27. Oil vapor volume fraction generated. Position 2, gap 3 µm, rotating velocity 2500 r/min. Only the portions of the mesh where the volume fraction of vapor is greater than 10% are highlighted.

In the configuration characterized by smaller steps, Geometry C, the greater number of sectors allows the pressure field to be more uniform, limiting the onset of vaporous cavitation only where

there are no longer other adjacent steps that locally raise the pressure: this occurs towards the exit from the domain, where the texture is cut by the involute profile of the tooth, as shown in the Figure 5.28.

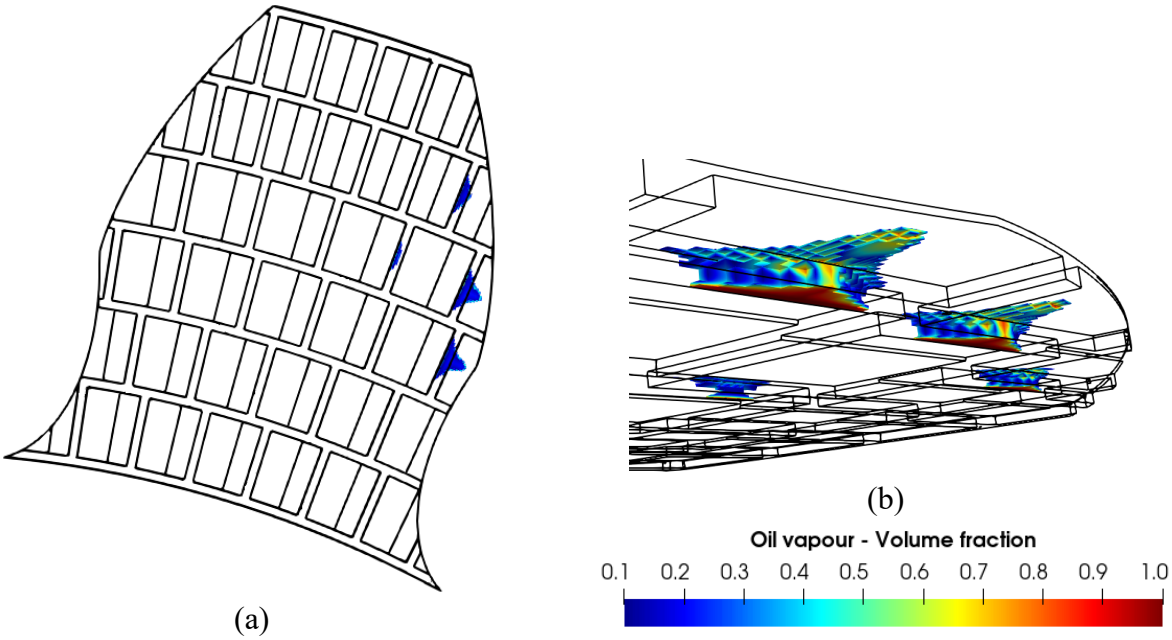

Figure 5.28. Oil vapor volume fraction generated. Position 2, gap 3 µm, rotating velocity 2500 r/min. Only the portions of the mesh where the volume fraction of vapor is greater than 10% are highlighted

The three geometries considered do not require further refinements because the vaporous cavitation occurs in very localized areas, without compromising the bearing capacity given by the hydrodynamic effect.

The Figure 5.26 shows the contours of the volume fraction of free air in one position for each configuration, with a 3 µm gap. In general, the air tends to be more concentrated inside the channels, where the pressure is lower. The motion of the mobile plane drags the air inside the sectors, in particular in the configurations with steps, where the volume fraction is gradually reduced, due to the increase in pressure that allows the air to be reabsorbed into the oil. The reabsorption process is not instantaneous, but requires time, which is greater than that taken by the fluid to move between one sector and the next: consequently, the air release process tends to propagate and the quantity of air released increases towards the exit of the domain in the direction of rotation of the moving plane. Only in the configuration with the square dimples the air remains confined within the channels, since the individual dimples are not in communication with each other, preventing air from occupying them.

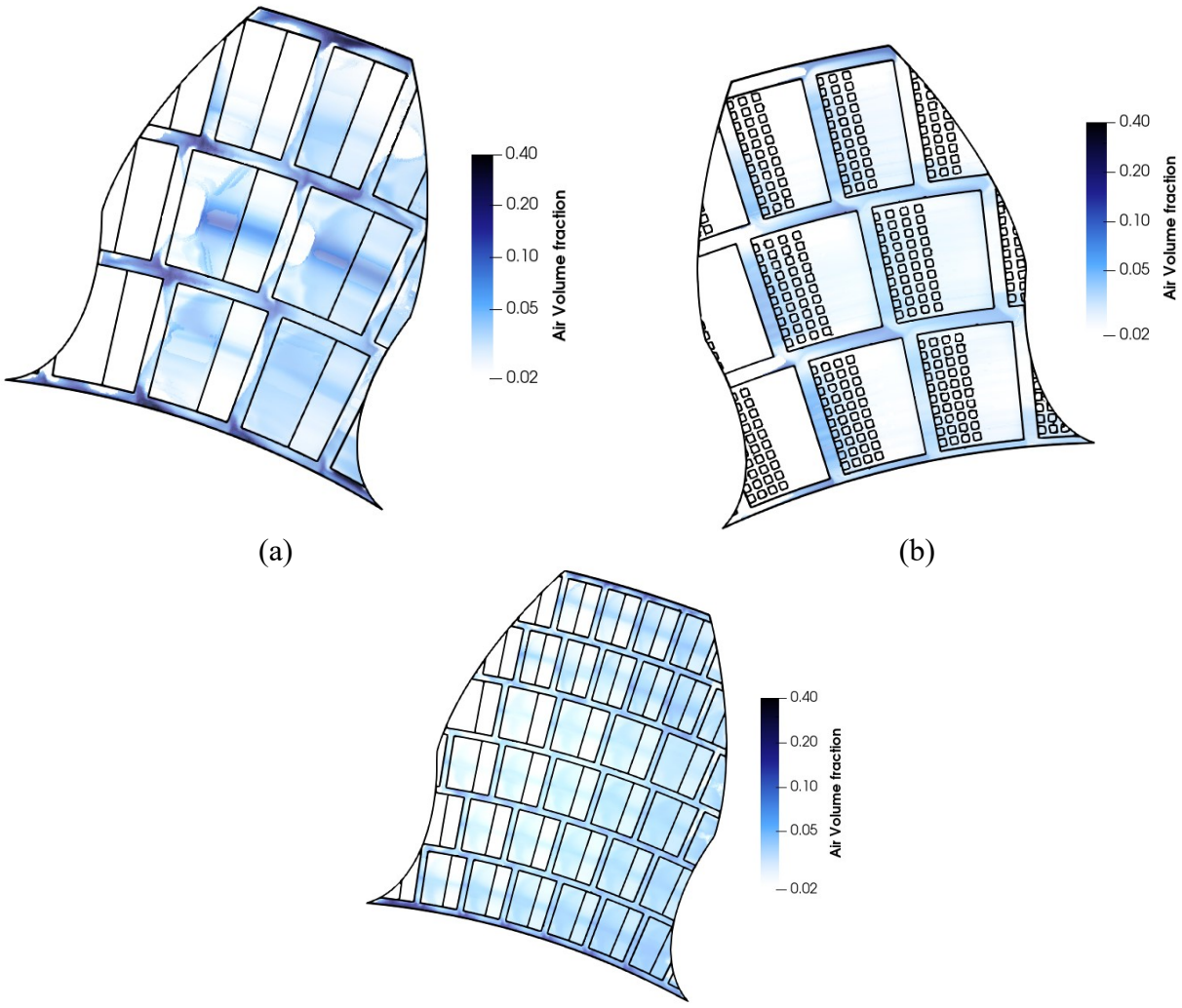

Figure 5.29. Air volume fraction released. Position 2, gap 3 µm, rotating velocity 2500 r/min. Only the portions of the mesh where the volume fraction of air is greater than 2% are highlighted.

The gaseous phase present in the lateral plate portion corresponding to the rotating seal behaves similarly to the tooth. Vapor cavitation is concentrated in the recovery channels and Geometry A is the one that shows a more marked phenomenon. As for the gaseous cavitation, the propagation of the phenomenon occurs and the free air tends to be accumulated towards the exit of the domain, especially for the geometries characterized by steps. Also in these cases, the concentration of free air is very low and does not significantly affect the bearing capacity of the coupling.

5.6 Additional consideration

5.6.5 Squeeze films

In the treatment developed up to now, focusing on the hydrodynamic effects, it has always been assumed that the gap height remains constant during relative sliding. In reality, during the operation of a gear pump, the lateral plates have an oscillating motion that periodically brings them closer to and away from the gear wheels. The Figure 5.30, taken from the researches of Dhar et Al [5.1, 5.2], schematically shows the movement of the lateral plate with respect to the gear wheels; the effect of the movement on the pressure inside the meatus delimited by the gear wheels is reported: if the lateral plate approaches the wheels, the pressure in the gap increases and tends to counterbalance the approach; otherwise, the pressure decreases.

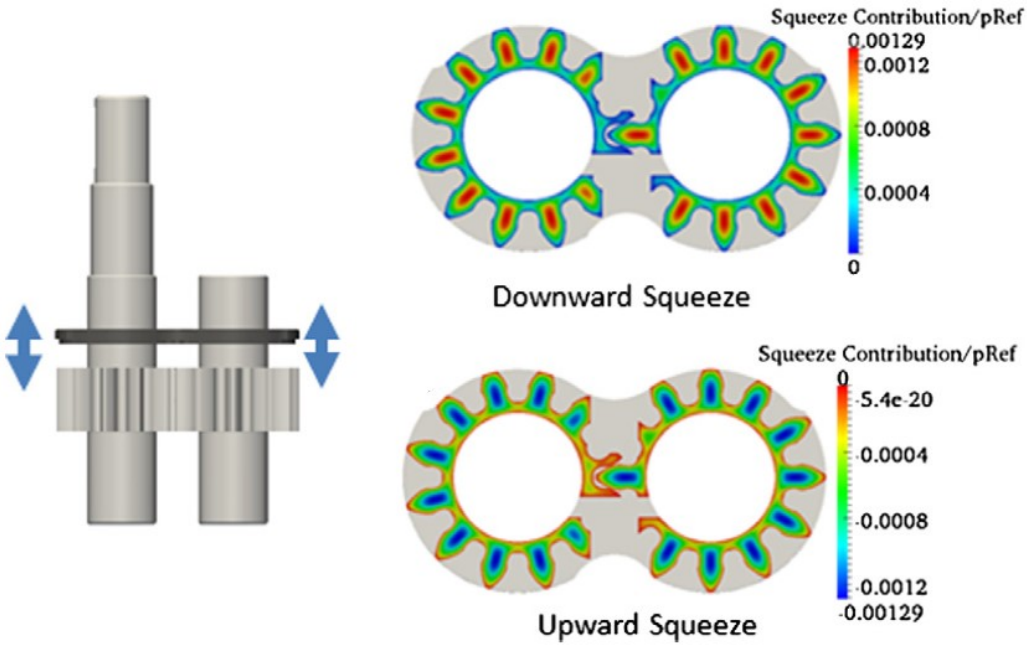

Figure 5.30. Image of the lateral plate motion during the operation of an external gear pump. Pressure contours in case of approaching or moving away of the lateral plate from the gear wheels. Image taken from Dhar et Al. [5.1]

It is therefore a question of analysing how the bearing capacity varies in the case of a lubricating film that changes its thickness over time, i.e. cases in which:

$$\frac{\partial h}{\partial t} \neq 0 \tag{5.1}$$

Where h represents the gap height.

Squeeze film is a term that denotes the condition in which the derivative is negative, that is when the two coupled surfaces are approaching together. A very useful feature of squeeze films is that they produce an increasing, even though temporary, bearing capacity when one of the two surfaces is subjected to a sudden high load. A characteristic application of this effect is adopted by the engine rod bearings which must resist the transient combustion forces. A further aspect of squeeze films is the force generated by the squeeze effect is always opposite to the direction of motion of the two surfaces. This constitutes a damping effect, which allows to limit the approach between the two surfaces, as well as helping to ensure stability to vibrations. To understand better, consider the Reynolds equation, where to analyse the squeeze forces the term $\partial h/\partial t$ is retained and takes priority over the term representing the geometry of the film $\partial h/\partial x$. The Reynolds equation with the squeeze term, assuming that the lubricant is isoviscose and zero entraining velocity, is:

$$\frac{\partial}{\partial x}\left(h^3\frac{\partial p}{\partial x}\right)+\frac{\partial}{\partial y}\left(h^3\frac{\partial p}{\partial y}\right)=12\eta\frac{dh}{dt} \tag{5.2}$$

The Equation (5.2), whose analytical description is reported in [5.3], permits to calculate the pressure range in the gap and could be integrated for a specific geometry in order to predict the bearing capacity and the maximum pressure. Furthermore, it could also be solved with respect to time to know the squeeze time, defined as the time required for the film thickness to reach a critical value.

The Figure 5.31 shows the case of two parallel flat surfaces pressed together: it is possible to observe the pressure distribution which has the maximum exactly in the centre of the surface. The velocity profile of the lubricant escaping the gap, in the two directions *x* and *y*, is also indicated.

The pressure distribution in this case as a function of $\partial h/\partial t$ is:

$$p=\frac{6\eta}{h^3}\frac{dh}{dt}\left(x^2-\frac{B^2}{4}\right) \tag{5.3}$$

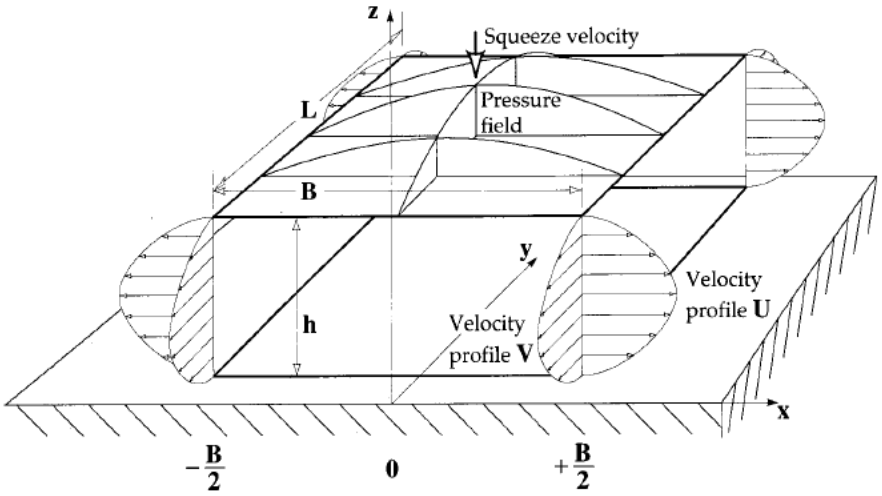

Figure 5.31. Squeeze film between two parallel plates.

To study the squeeze effect applied to the geometry of the tooth of the gear wheel, simulations have been carried out taking as reference the same angular position for each type of texture. In addition, the condition in the absence of texture was also analysed, in order to evaluate what the introduction of the texture involves on the bearing capacity in the presence of squeeze.

Also in this case, as in the previous simulations, the boundary conditions are open boundary on the perimeter walls of the domain. The difference is that the speed of the moving plane is no longer rotational, but translational and approaching. The simulations were carried out with three different speeds: 0.01 mm/s, 0.1 mm/s and 1 mm/s. The initial height of the meatus is equal to 10 μm and the simulation has been performed up to a gap height of 2 μm. The simulations have been performed in transient and the results related to the last simulation step are reported. The convergence criterion of every solution step is that the residuals of each equation are less than 10^{-5}.

The Figure 5.32 shows the static pressure contours relating to the case of squeeze speed 0.1 mm/s. The results are in accordance with Reynold's theory of lubrication and the pressure distribution of Figure 5.31. The maximum pressure value is in the centre of the domain and the pressure field gradually decreases away from the centre. From the contours it is already possible to appreciate that there is a marked difference between the case of two flat plane and those with the texture. The presence of the texture, regardless of the type, increases the average height of the gap. From the Equation (5.3), the pressure is inversely proportional to the gap height: so, a greater height of the meatus reduces the bearing capacity due to the squeeze effect. In particular, the recovery channels represent an escape path for the lubricant that is pressed by the moving plane. This means that the fluid is not confined within the domain and consequently is able to generate a lower bearing

capacity: the high pressure area of the case without texture is greater than the others and also has a higher maximum pressure value, generating a greater force.

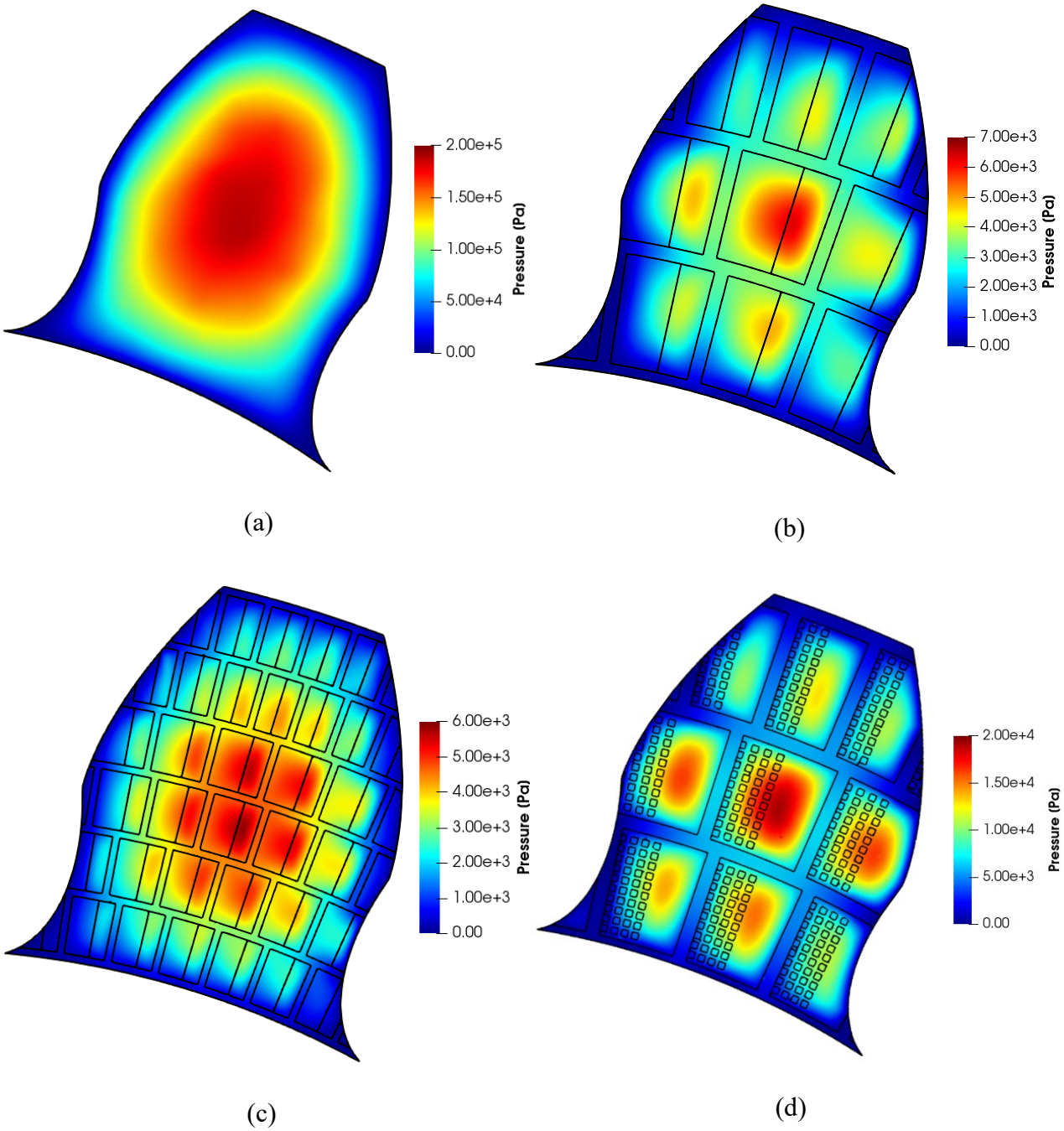

Figure 5.32 Pressure contour of squeeze films for different texture geometry. (a) Flat plane without texture. (b) Steps with depth of 10 µm. (c) Small steps deep 10 µm. (d) Sequence of square dimples with side 0.1 mm and deep 10 µm. Squeeze velocity 0.1 mm/s

The magnitude of the pressure due to squeeze films is much lower than the hydrodynamic effect analysed in detail in the previous paragraphs: it follows that the benefits of introducing a textured surface to the performance of an external gear pump are mainly due to hydrodynamic lubrication.

The Figure 5.33 shows the trend of the bearing capacity as a function of the squeeze speed for the four geometries considered. In accordance with the Equation (5.3), a greater squeeze speed leads to a greater bearing capacity in the coupling and since the relationship is linear, increasing the speed by a factor of 10, the force increases by the same amount. The geometry without texture allows for maximum bearing capacity due to the squeeze effect since the average gap height in lower and fluid is more bounded. The other geometries have significantly lower bearing capacities, among these the type with dimples is the best one since the textured surface is smaller than the other types and therefore has a slightly lower average gap height. For reasons of confidentiality, the force values are dimensionless for the maximum value, corresponding to that obtained from the geometry without texture at the highest squeeze speed.

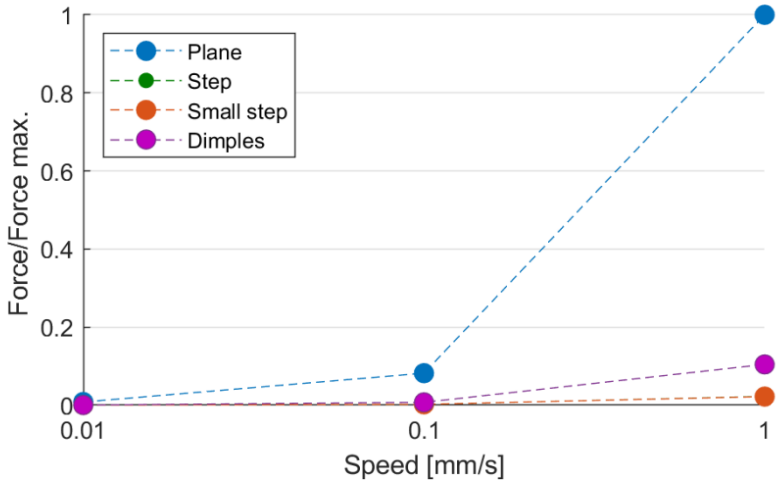

Figure 5.33 Bearing capacity due to squeeze effect as a function of squeeze velocity.

The configurations with steps and small steps generate the same bearing capacity due to squeeze film, and in fact the curves are overlap in the graph of Figure 5.33. The reason is due to the same textured area, as reported in Table 5.3, resulting in identical average gap height. Hence, although there are a greater number of steps in small steps configuration which should confine better the fluid, the behaviour of the coupling is not affected.

Table 5.3. Average texture surface for the configuration considered.

Geometry type	Average texture surface [%]
Step	70.3%
Small step	71.0%
Dimples	39.2%

The results shown refer to the case of approaching surfaces. Under this hypothesis the pressure is always positive. However, in systems where squeeze is present as both positive and negative and the lubricant is liquid, cavitation is unavoidable. Cavitation therefore affects squeeze forces with the formation of compressible bubbles in an incompressible liquid lubricant. Bubbles could also persist or grow by coalescing until the squeeze characteristics of the system are substantially changed. The persistence of bubbles even under temporarily positive pressure of the lubricant is due to the speed of dissolution of the bubbles which is much slower than the speed of bubble formation, as discussed in the paragraph 4.3. The overall effect is to significantly reduce the load capacity from the values calculated by the hydrodynamic theory assuming the absence of cavitation effects [5.4, 5.5]. A model of oscillating compression films with cavitation and bubble formation is described in [5.4]. The Figure 5.34 shows the mechanism of gas bubble accretion in the hypothesis of oscillatory movement of the two coupled surfaces: in the case of negative squeeze, small bubbles are formed, mainly from the release of the gas dissolved in the liquid, which are absorbed in larger bubbles when positive squeeze occurs. A cyclical oscillatory motion condition involves the formation of increasingly larger bubbles of gas, which compromise the bearing capacity of the coupling.

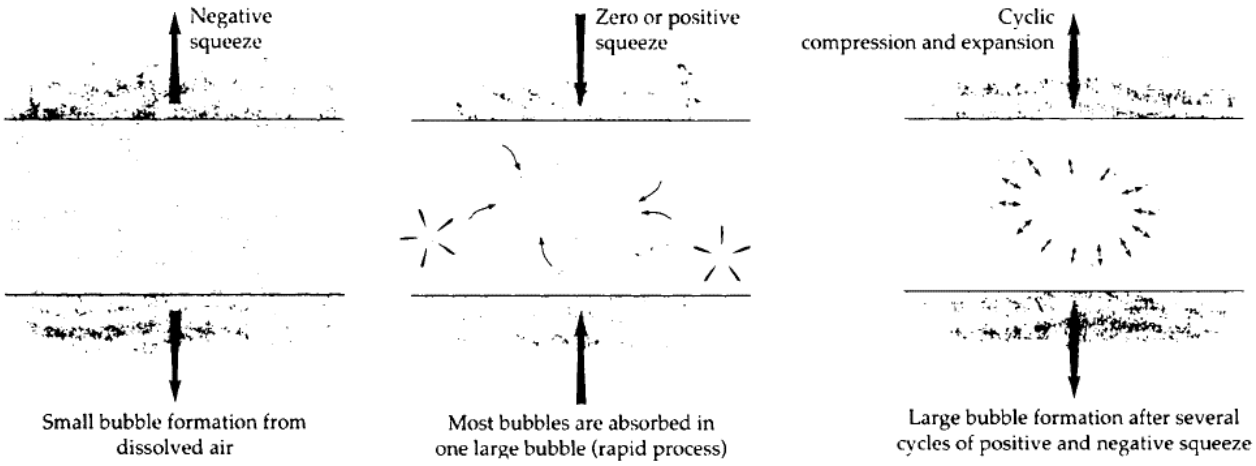

Figure 5.34. Mechanism of bubble accretion under oscillating squeeze.

5.6.6 Friction force

A further aspect to be analyzed concerns the friction force that is established in the lubricated coupling due to the shearing of the lubricant. The friction force is obtained by integrating the shear stress τ on the surface of the entire computation domain Ω:

$$F = \int_{\Omega} \tau d\Omega \tag{5.4}$$

As already mentioned in the paragraph 2.3, the shear stress is defined as a function of the dynamic viscosity and the relative sliding speed between the two coupled surfaces.

$$\tau = \mu \cdot \frac{dv_x}{dy} \tag{5.5}$$

Due to the increased thickness of the fluid film and the additional hydrodynamic bearing capacity effect between the sliding surfaces, the surface texturing produces a reduction in friction. Significant research conducted with the surface structure aims to reduce friction, which from a wear perspective is beneficial as it will lead to a longer life of the material. Tønder [5.6] analytically investigated the effect of dimples on pivoted plain bearings and found that the bearing capacity as well as the film thickness increased significantly, with the consequence of reducing friction. The results on the effect of texture density on friction reduction studied by Tønder have been supported by numerous analytically and experimentally studies. Wang et Al. [5.7] conducted experimental tests on thrust bearing textured with circular dimples in water based lubrication and announce a decrease in the coefficient of friction and the effect is greater as the size and density of the dimples increase. Also, Yu et Al. [5.8] found a decrease in the coefficient of friction in lubricated couplings between textured surfaces for different texture geometries.

The analysis in this Thesis was focused on the torque required to keep the moving plane in rotation, studying the same geometries considered in the analysis of the squeeze effect. The Figure 5.35 shows a graph of the torque trend as the gap varies, where the values have been divided by the maximum one for reasons of confidentiality. In confirmation of what is reported in the scientific literature, a coupling between textured surfaces allows to reduce friction and consequently reduce the torque exerted by the fluid on the moving surface. The reduction of friction is greater in the configurations that have the steps because they are geometries that allow to increase the average height of the fluid meatus.

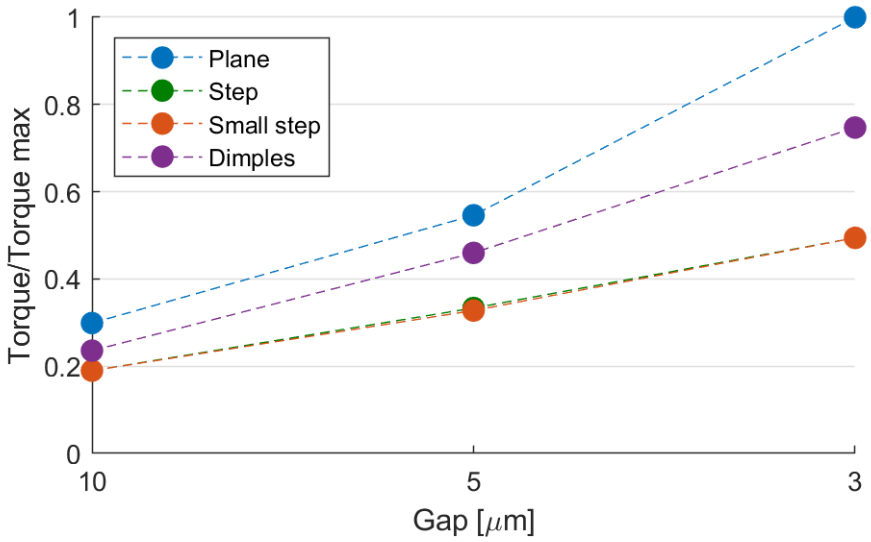

Figure 5.35. Friction torque as a function of gap height for the different texture geometry.

List of references

5.1 Dhar S., Vacca A. A fluid structure interaction-EHD model of the lubricating gaps in external gear machines: Formulation and validation. Tribology International. 2013. Doi: 0.1016/j.triboint.2013.02.008

5.2 Dhar S., Vacca A. A novel CFD – Axial motion coupled model for the axial balance of lateral bushings in external gear machines. Simulation Modelling Practice and Theory. 2012. Doi: 10.1016/j.simpat.2012.03.008

5.3 Stachowiak G. W., Batchelor A. W. Engineering tribology. Third edition. 2006. ISBN 978-0-7506-7836-0. Doi: 10.1016/B978-0-7506-7836-0.X5000-7

5.4 Haber S., Etsion I. Analysis of an oscillatory oil squeeze film containing a central gas bubble. ASLE Transactions. 1985. Doi: doi.org/10.1080/05698198508981619

5.5 Parkins D. W., Stanley W. T. Characteristics of an oil squeeze film. Transactions ASME, Journal of Lubrication Technology. 1982. Doi: doi.org/10.1115/1.3253268

5.6 Tonder K. Dimpled pivoted plane bearings: Modified coefficients. Tribology International. 2010. Doi: 10.1016/j.triboint.2010.08.001

5.7 Wang X., Kato K., Adachi K., Aizawa K. Loads carrying capacity map for the surface texture design of SiC thrust bearing sliding in water. Tribology International. 2003. Doi: 10.1016/S0301-679X(02)00145-7

5.8 Yu H., Wang X., Zhou F. Geometric shape effects of surface texture on the generation of hydrodynamic pressure between conformal contacting surfaces. Tribology Letters. 2010. Doi: 10.1007/s11249-009-9497-4

Chapter 6. Experimental activity

This chapter describes in detail the wide experimental activity carried out.

Information on laser technology is provided and samples realized are shown, with also the measurements made using an optical profilometer.

The discussion continues by illustrating the many experimental tests performed, paying attention to the difficulties encountered during the tests. A paragraph discussing the results is present at the end of the chapter.

6.1 Laser technology

A laser source is a device capable of generating a beam of electromagnetic waves characterized by having a single frequency and limited divergence. These characteristics have allowed and favoured the spread of laser applications to various sectors, from industrial to medical or IT.

In the industrial field, a laser source is used for the transfer of energy to the workpiece: the resulting increase in temperature could lead to melting and vaporization of the material. It follows that all industrial laser processes are of the thermal type.

There are several processes that could be carried out using a laser source: the main ones are cutting, welding, hardening and marking operations.

Electromagnetic radiation has a dual nature: corpuscular and undulatory. Light could be considered as made up of energetic particles, called photons, of zero mass, but capable of transporting energy and momentum. However, it could also be considered as a wave characterized by an electric and magnetic field that varies over time and space, described analytically by Maxwell's equations and schematically represented in Figure 6.1.

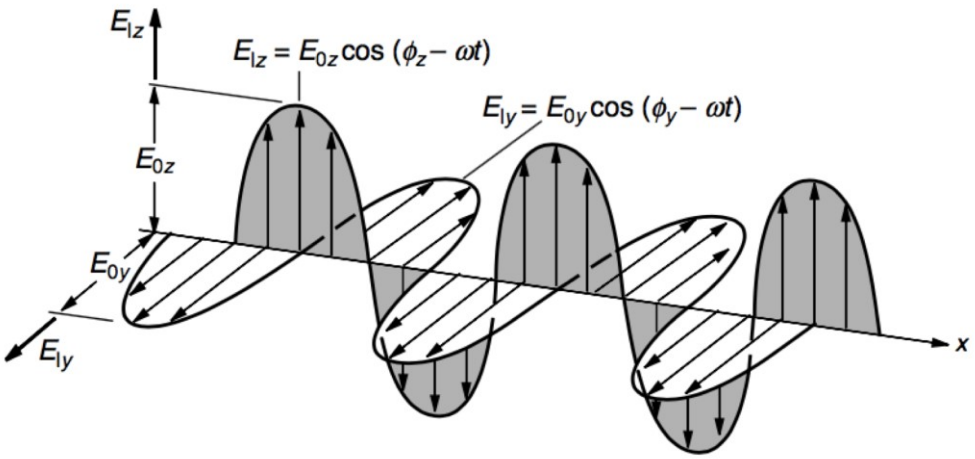

Figure 6.1. Schematic representation of an electromagnetic wave.

The properties required by a laser beam are monochromaticity and low divergence. The monochromaticity allows the laser beam to concentrate all the energy on a single wavelength; the low divergence of the laser allows the beam to be focused on a limited area. These properties permit to achieve a high focusability through lenses to obtain a beam with a greater amplitude by concentrating it on a smaller section.

The energy associated with a photon flux is given by Planck's law:

$$E = h \cdot f \tag{6.1}$$

Where h is Planck's constant and f is the frequency of the electromagnetic radiation. From Planck's law it emerges that the energy of a photon flux could only assume discrete values, that is, it is quantized, since it could only assume multiple values of the frequency.

What happens is a direct consequence of the atomic model: even atoms could only assume specific energy levels. Considering two energy levels, of which E_1 the one at a lower energy level and E_2 the one at the higher level, three scenarios could occur:

- Absorption: there is absorption of a photon by an atom when a photon, colliding with the atom, annihilates and gives its energy to the latter.
- Spontaneous emission: when an atom that is in the energy state E_2 decays to the energy level E_1 there is the emission of a photon.
- Stimulated emission: the phenomenon occurs when an atom is in the E_2 state and is reached by a photon. In this case, the atom decays at the E_1 level releasing two photons equal to the initial one.

The latter phenomenon is very advantageous because by multiplying the photons it allows to obtain a more intense electromagnetic radiation.

In order to emit a laser beam, the material used for generation must be in a population inversion condition, that is, it must have more atoms at the highest energy level, $N_2 > N_1$. This condition is not thermodynamically stable, since a system tends to move into a configuration that minimizes energy. The Boltzmann's relation, Equation (6.2), allows to calculate the populations at different energy levels in conditions of thermodynamic equilibrium:

$$\frac{N_2}{N_1} = e^{\left(-\frac{E_1 - E_2}{K_B T}\right)} \tag{6.2}$$

Where K_B is Boltzmann's constant.

To achieve population inversion, energy must be supplied to the medium to move many atoms from the lowest to the highest energy level: this process is called energy pumping. There are several pumping techniques:

• Electric discharge: it is used for active media in the gaseous phase. Two electrodes are placed inside the volume of gas and the flow of electrons transfers energy to the gas obtaining the population inversion.

• Optical pumping: used in solid active media. A light source generates a flux of photons which, passing through the active medium, provide the energy necessary to obtain the population inversion.

• Chemical pumping: population inversion is achieved using particular chemical compounds (excimers).

• Junction between semiconductors.

In addition to population inversion, it is also necessary to amplify the electromagnetic radiation by means of an optical resonance: with this technique it is possible to obtain laser sources of high intensity with the advantage of maintaining a limited size of the equipment; in fact, in the absence of a resonant cavity, the intensity of the laser beam is proportional to the length of the active medium. The active medium is placed between two mirrors creating a resonant cavity, as shown in Figure 6.2. The photon flux is continuously bounced from the mirrors inside the active medium, consequently undergoing further amplifications. Of the two mirrors, only one is completely reflective, while the other allows part of the radiation to exit, generating the actual laser beam.

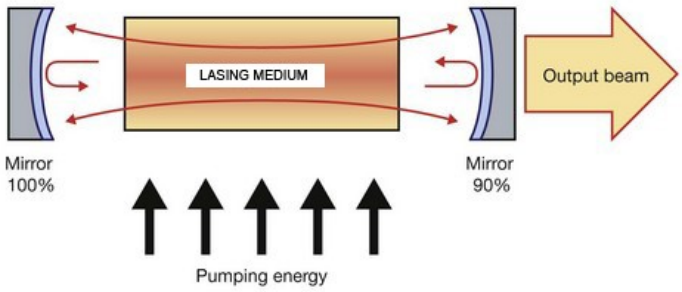

Figure 6.2. Representation of a resonant cavity.

In reality, for industrial applications the sources of interest are systems with three or four energy levels: systems with two levels present the problem of not obtaining population inversion, since at most an equal population could be obtained on both levels, $N_1 = N_2$.

In systems with three energy levels, represented in Figure 6.3, the energy supplied by pumping allows the population to be moved to a level higher than the laser level (that is the upper lasing level, *ULL*), and then quickly decays to the laser level. The inversion of the population is obtained between the lower lasing level, *ULL,* and the ground level, thus allowing the emission of the laser. The decay time between the *ULL* and the ground must be greater than the time required to pass from the pump level to the *ULL*, in order to ensure population inversion. The ground level is the most populous and to achieve population inversion it is necessary to move a great number of atoms to the *ULL* level, an operation that requires a lot of energy.

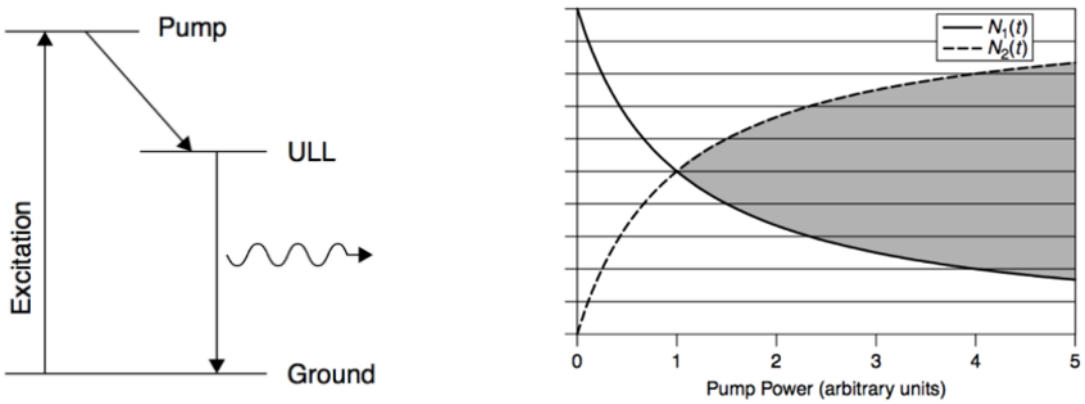

Figure 6.3. Three energy level laser system.

To overcome this drawback, systems with four energy levels have been developed and it is shown in Figure 6.4. There is an additional energy level (lower lasing level, *LLL*) in which the population is smaller than that in the ground. The levels between which the stimulated emission takes place are less populous than the three-level system and this allows to obtain the population inversion as soon as power is supplied to the pumping system.

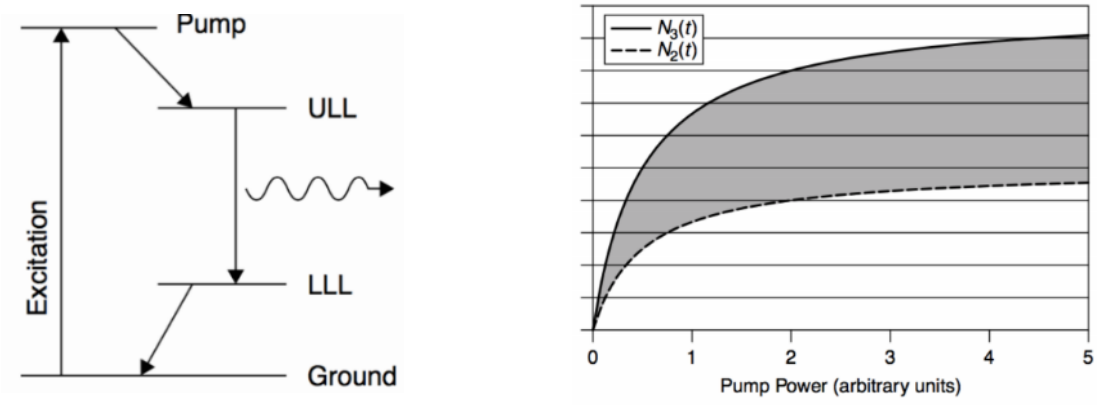

Figure 6.4. Four energy level laser system.

The main laser sources used industrially are:

• CO_2 laser: composed of a gaseous mixture of carbon dioxide, nitrogen and helium and pumping takes place via electronic flow. Historically they have been the most widespread in the industrial field, but now new types are supplanting this category. They are characterized by high power, low overall efficiency (up to 10%), and are mainly used for cutting and welding.

• Nd:YAG laser: uses a solid state source, a crystal. It has been the most widespread technology for metal cutting and welding since the wavelength of the beam (1064 nm) is better absorbed in metals than the CO_2 laser. These sources also have a low total efficiency.

• Diode laser: characterized by good efficiency. However, the quality of the beam is limited: suitable for performing heat treatments since the beam that is not properly concentrated allows to generate heat in a diffused area on the working piece.

• Fiber laser: characterized by high power associated with good beam efficiency and quality. Still expensive technology that limits its diffusion, but lately it is expanding.

• Disc laser: very recent technology that in the industrial field is in competition with the fiber laser since they have similar features. This type is also characterized by high power, good beam quality and good total efficiency.

The laser sources could be divided into two categories according to the time profile of the beam: in continuous mode, Figure 6.5, or in pulsed mode, Figure 6.6. In continuous mode, the power is emitted constantly over time. In the pulsed regime, the emission is discontinuous with discrete pulses in the time domain, allowing for very high peak powers. The pulsed speed could be further subdivided on the basis of the duration of the pulses: long 0.1 ÷ 50 ms, short 1 ÷ 200 ns and ultrashort 30 fs ÷ 30 ps.

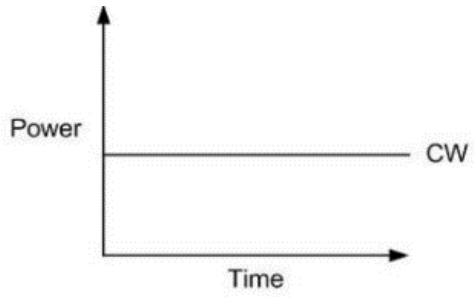

Figure 6.5. Continuous regime.

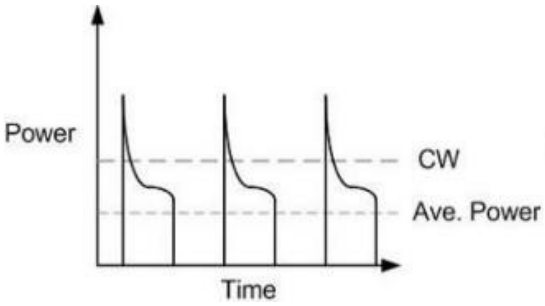

Figure 6.6. Pulsed regime.

6.2 Pieces realized

The numerical simulations carried out in the Chapter 5 have permitted to identify five different geometries to conduct experimental tests in order to evaluate the effectiveness of the texturing.

The five geometries are characterized by partial texturing applications where a grid of recovery channels has been created in order to delimit circular sectors that have been textured to 60%. Only one configuration does not present the recovery channels: it has also been decided to realize this samples to experimentally verify the need to introduce the channels on the lateral plates, as validation of the numerical results.

The five geometries are the following:

- Type A. Steps deep 0.01 mm and recovery channels of 0.05 mm depth and 0.2 mm wide. The Figure 6.7 shows a portion of the lateral plate: the steps are highlighted in green, while the channels in blue.

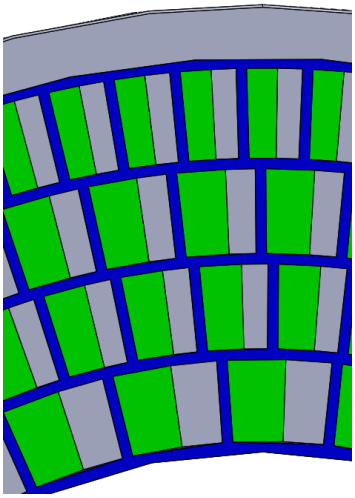

Figure 6.7. Geometry characterized by steps (in green) and recovery channels (in blue).

- Type B. Steps deep 0.01 mm and recovery channels of 0.1 mm depth and 0.2 mm wide. The front view is the same as the Figure 6.7.
- Type C. Steps deep 0.01 mm e no recovery channels. This configuration is shown in Figure 6.8.

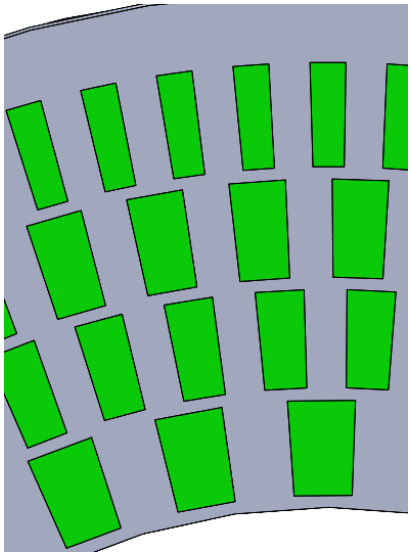

Figure 6.8. Geometry characterized by the presence of only steps, highlighted in green.

- Type D. Sequence of square dimples with side 0.1 mm and depth 0.01 mm. Recovery channels of 0.05 mm depth and 0.2 mm wide.

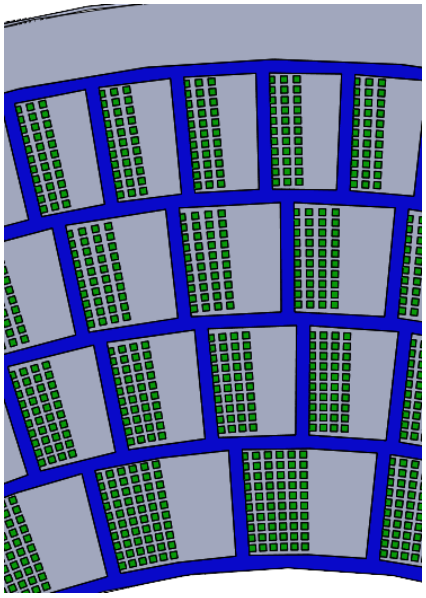

Figure 6.9. Geometry characterized by the sequence of dimples in each sector (in green) and recovery channels (in blue).

- Type E. Steps deep 0.01 mm and recovery channels of 0.05 mm depth and 0.1 mm wide. The geometry, similar to type A, has been scaled in order to have a greater number of steps, with the same contact surface. The Figure 6.10 shows a portion of the lateral plate: the steps are highlighted in green, while the channels in blue.

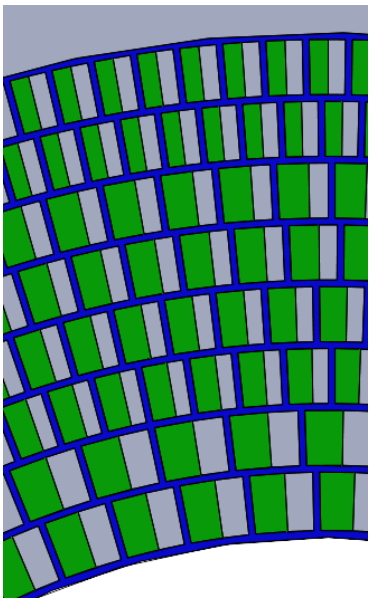

Figure 6.10. Geometry characterized by the small steps (in green) and recovery channels (in blue).

- Type F. Steps deep 0.05 mm and recovery channels of 0.1 mm and 0.2 mm wide. Also in this configuration the front view is the same as the Figure 6.7.

The geometries have been made on the portion of lateral plates of external gear pumps corresponding to the suction area.

The lateral plates have been processed by laser marking, with the support of the company SISMA S.p.A. which, thanks to its competence and experience, has provided the best machining parameters to obtain the geometries that are as close as possible to those theorized.

A 20W fiber laser source in pulsed regime has been adopted, equipped with an f160 focal system. Details regarding the processing parameters can not be disclosed for confidentiality reasons.

6.3 Measurements with optical profilometer

The samples made have been measured, before the experimental tests, using an optical profilometer in order to verify that the geometry obtained is the desired one. The profilometer, present at the Department of Engineering and Architecture of the University of Parma, is a Taylor Hobson CCI MP-L, whose characteristics are listed in the Table 6.1:

Table 6.1. Features of the optical profilometer.

Measurement type	3D non-contact
Measurement mode	Coherence Correlation Interferometry (CCI)
Repeatability of surface RMS	< 0.02 nm [0.2 Å]

Of all the samples made, two for each type have been measured on the profilometer. It has been verified that the laser processes are very repeatable and this allows not to measure every piece realized. Therefore, the measurements related to a single sample will be shown.

The laser marking generates some burr on the perimeter of the removed surface: in general, the height of the burr is proportional to the depth of the processing. In order to evaluate the quantity of burr produced, the measurements on the profilometer have been carried out on the samples just marked. Subsequently, a manual polishing operation has been performed to completely remove the burr.

6.3.1 Type A

In the Figure 6.11a a photograph of a sample of lateral plate of Type A is presented. The Figure 6.11b shows the 3D surface obtained from the measurement of the optical profilometer, restricted to a portion of the textured surface of a Type A sample. It is possible to see the burr formed on the perimeter of the steps and channels. The Figure 6.12 shows the profile on a cross section of the surface: the depths indicated in the table are calculated respect to the unmachined surface. This image is useful to estimate the value of the burr: the maximum height of the burr is 41.9 µm and is very narrow, equal to 0.05 mm.

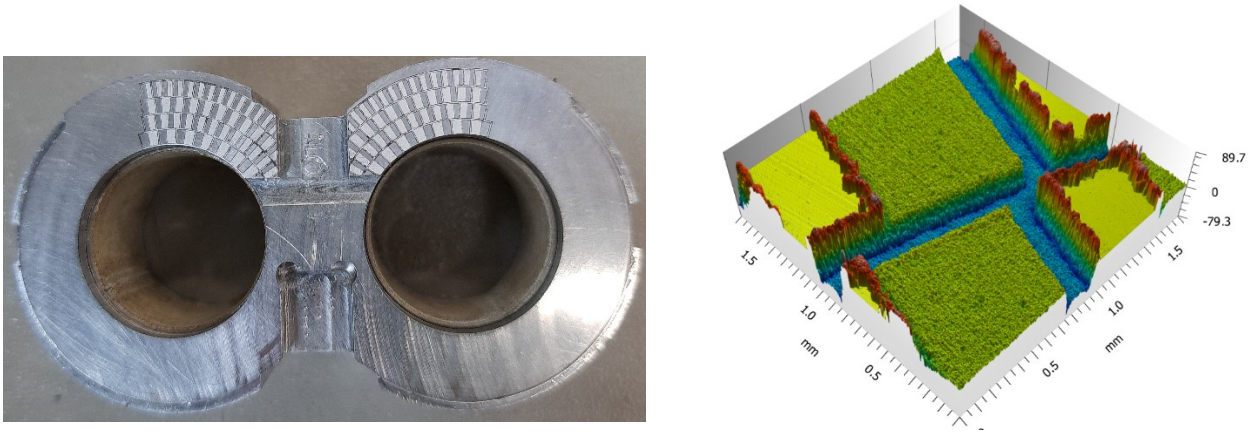

(a) (b)

Figure 6.11. (a) Photo of the lateral plate. (b) 3D profile measured immediately after laser texturing.

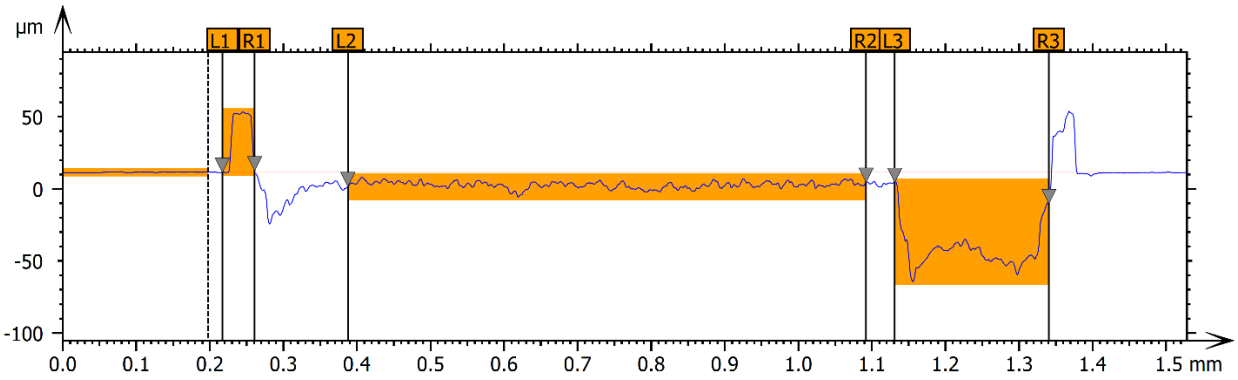

Parameters	Unit	Step 1	Step 2	Step 3
Maximum height	µm	41.9	17.1	75.7
Mean height	µm	26.1	8.79	53.9

Figure 6.12. Surface profile on a cross section of the raw sample.

The Figure 6.13 shows the 3D profile of the same sample after a mechanical polishing process. With this process the burr is completely eliminated and the quality of the laser processing could be

better appreciated. The steps are very well defined. Also, the channels have almost perfect vertical walls. The Figure 6.14 again shows the profile on a cross section of the surface. The steps have an average depth of 10.4 µm, confirming that the laser processing parameters are perfectly calibrated. The channels, on the other hand, have an arched geometry on the bottom: this is due to the laser processing of the perimeter of the sectors which, in order to be as defined as possible, required an additional laser pass on the perimeter, producing a greater depth of the recovery channels. The average depth of the channels reaches 55 µm, with maximum depths of 69 µm. The irregularity of the shape of the channels does not represent a problem since their function is to allow the oil to be recalled in the low pressure areas. Hence, a larger cross section improves the functionality of the channel.

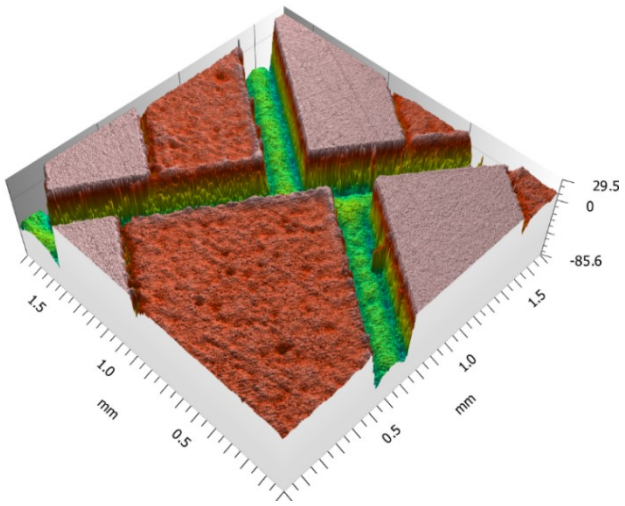

Figure 6.13. 3D profile measured after the mechanical polishing process.

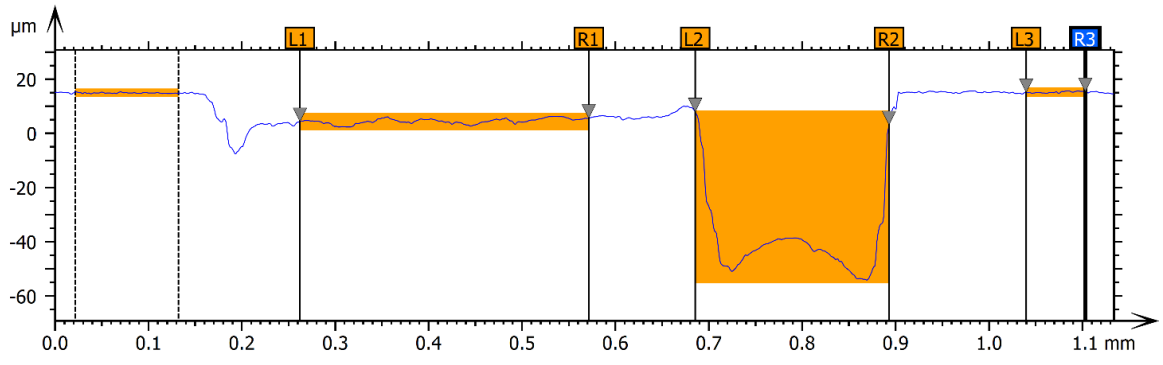

Parameters	Unit	Step 1	Step 2	Step 3
Width	mm	0.310	0.208	0.0649
Maximum height	µm	12.6	69.1	0.812
Mean height	µm	10.4	55.4	0.286

Figure 6.14. Surface profile on a cross section of the polished sample.

6.3.2 Type B

Type B present the same geometric imprint as Type A, but with channels twice as deep. In Figure 6.15a a picture of a lateral plate is presented. The Figure 6.15 shows the 3D surface, while the Figure 6.16 displays the profile along a cross section. Since the depth of the channels is greater than in the previous case, the amount of burr formed is much more, with an average height of 70.1 µm (in Type A it was 41.9 µm).

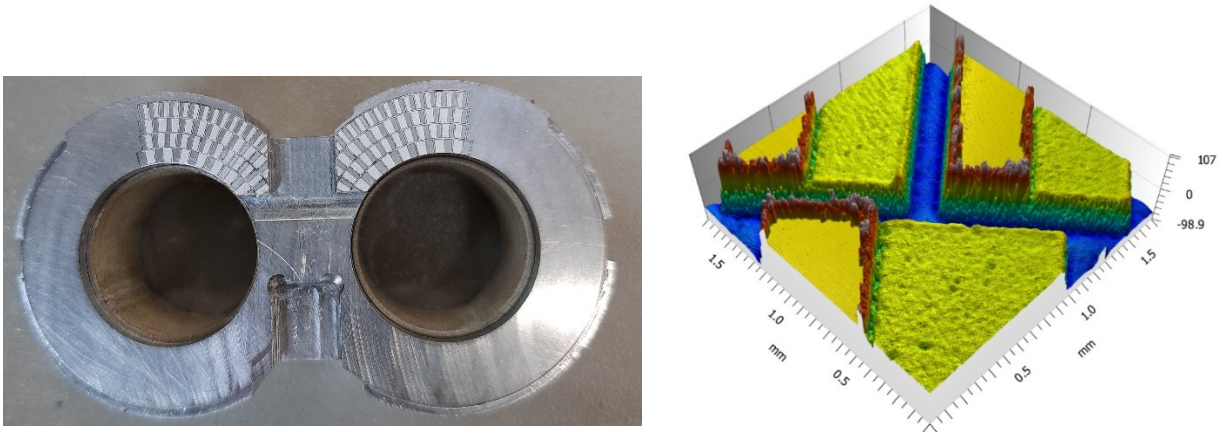

(a) (b)

Figure 6.15. (a) Photo of the lateral plate. (b) 3D profile measured immediately after laser texturing.

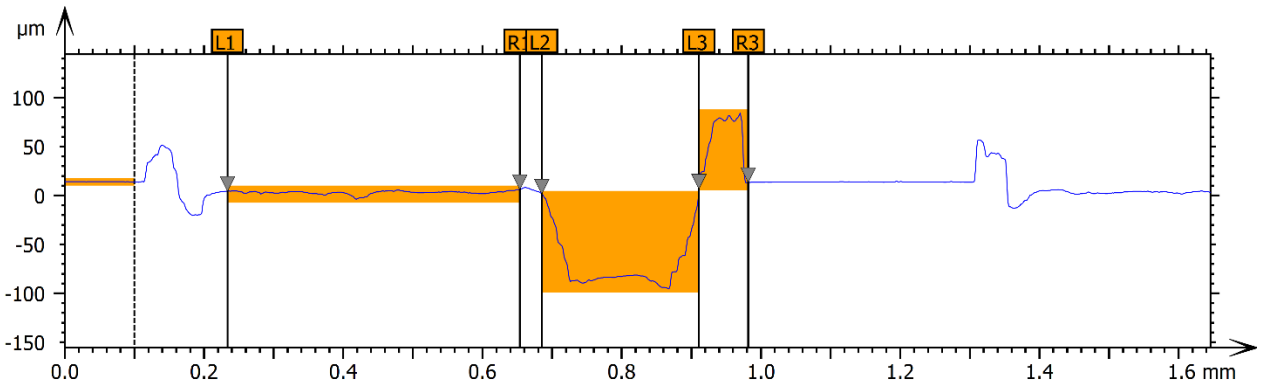

Parameters	Unit	Step 1	Step 2	Step 3
Width	mm	0.421	0.226	0.0722
Maximum height	µm	17.8	110	70.1
Mean height	µm	11.1	84.9	45.1

Figure 6.16. Surface profile on a cross section of the raw sample.

The Figure 6.17 shows the same sample after polishing which allowed to completely eliminate the burr. The average depth of the steps is 8.47 µm, while the maximum depth of the channels is 102 µm. Also in this case the cross section of the channels, Figure 6.18, is affected by the laser marking necessary to correctly define the geometry of the sectors and assumes the characteristic

curved shape. It is also worthy of appreciation that the surface quality of the bottom of the steps is very good, as in the previous case, since the processing parameters to laser the steps are the same.

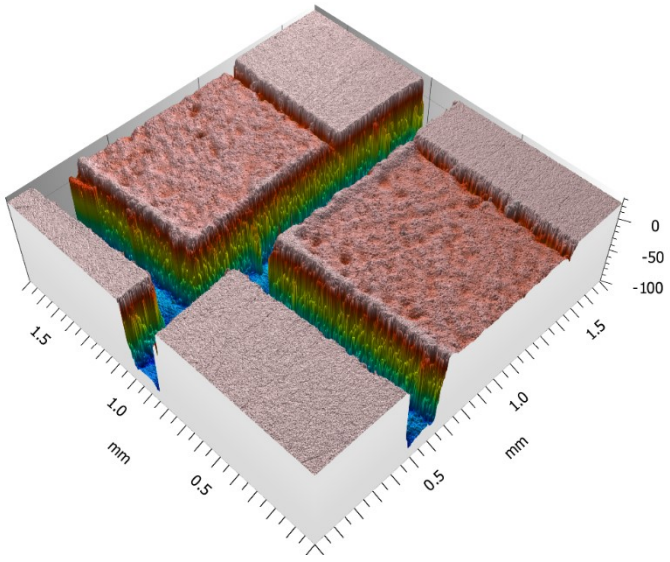

Figure 6.17. 3D profile measured after the mechanical polishing process.

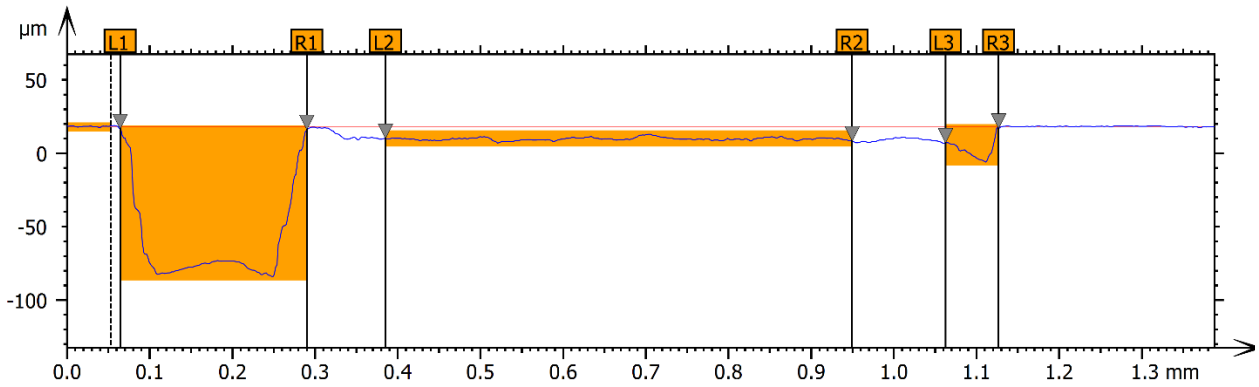

Parameters	Unit	Step 1	Step 2	Step 3
Width	mm	0.228	0.566	0.0651
Maximum height	µm	102	11.2	24.3
Mean height	µm	79.1	8.47	16.2

Figure 6.18. Surface profile on a cross section of the polished sample.

6.3.3 Type C

Figure 6.19a displays a picture of one lateral plate realized. This configuration has only the steps, and no channels, as clearly visible in the photo of Figure 6.19a. The 3D surface is reported in Figure 6.19b, while the cross section is shown in the Figure 6.20. Since the recovery channels are not present, the burr that is formed is lower than previous configurations, since a lower quantity of material is removed: as confirmation, the maximum height of the burr is only 13 µm, more than 5 time lower than Type B.

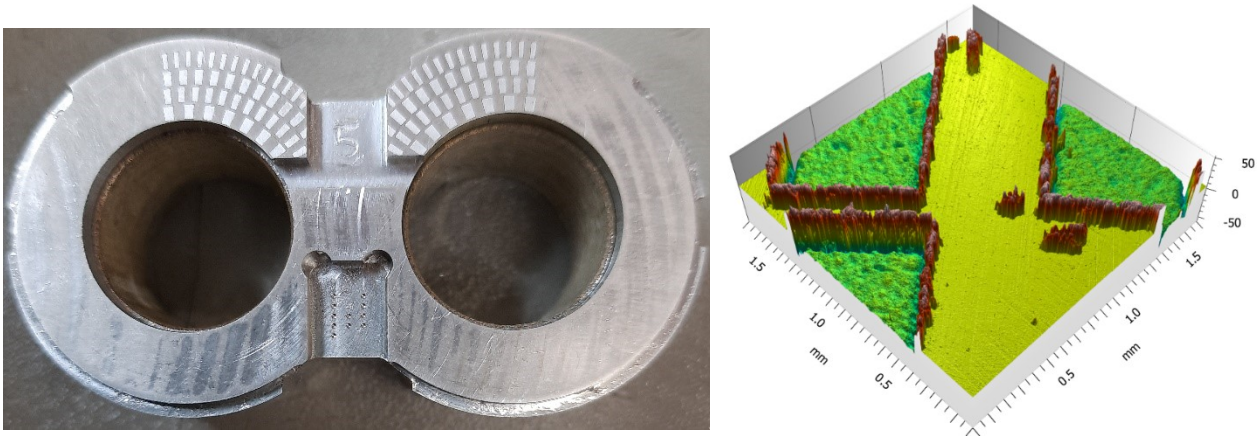

(a) (b)

Figure 6.19. (a) Photo of the lateral plate. (b) 3D profile measured immediately after laser texturing.

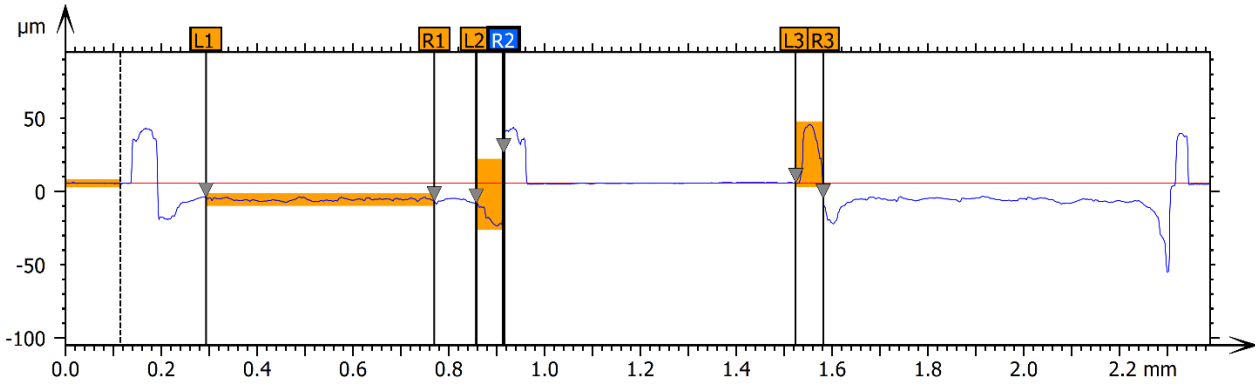

Parameters	Unit	Step 1	Step 2	Step 3
Width	mm	0.477	0.0591	0.0579
Maximum height	µm	13.1	29.3	39.7
Mean height	µm	11.3	21.7	23.1

Figure 6.20. Surface profile on a cross section of the raw sample.

After the polishing process the surface also appears without burr. The analysis of the profile shows how the steps have the same geometric characteristics of the previous cases, since the identical processing parameters have been used.

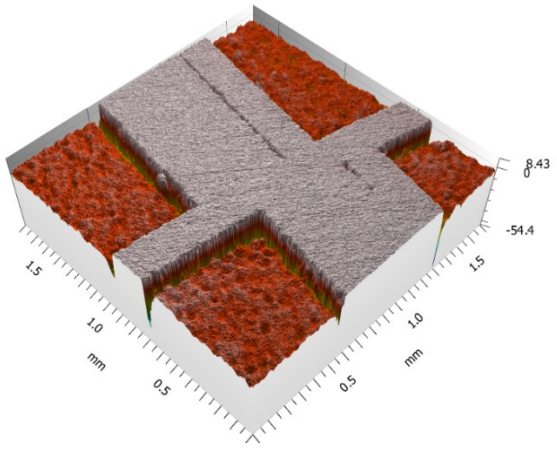

Figure 6.21. 3D profile measured after the mechanical polishing process.

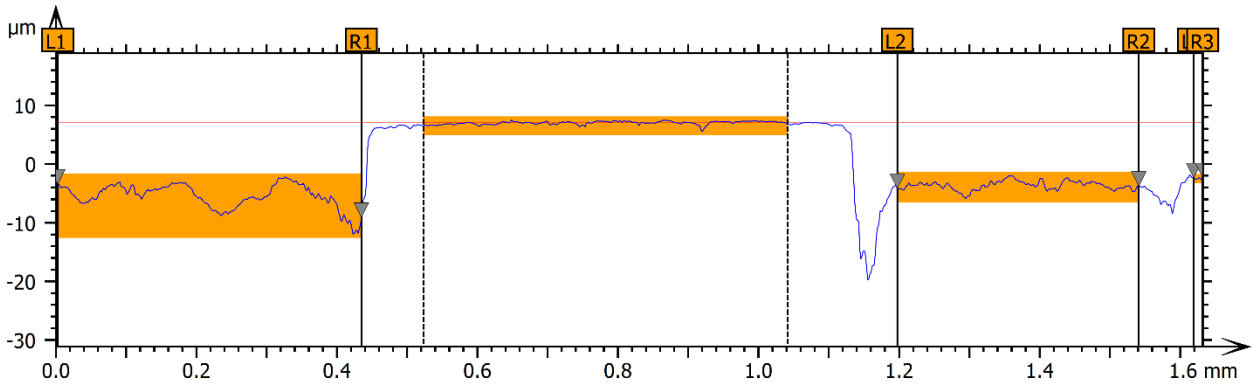

Parameters	Unit	Step 1	Step 2	Step 3
Width	mm	0.434	0.346	0.0145
Maximum height	µm	19.0	12.9	9.67
Mean height	µm	12.5	10.7	9.49

Figure 6.22. Surface profile on a cross section of the polished sample.

6.3.4 Type D

Type D has a different conformation compared to the previous ones: instead of the steps there is a succession of dimples with a square section of 100 µm side and 10 µm deep. The recovery channels have a width of 200 µm and a depth of 50 µm. A picture of the lateral plate is displayed in Figure 6.23a. The Figure 6.23b shows the 3D surface obtained with the profilometer. The laser process produces burr on the perimeter of the removed surface: this involves a considerable amount of burr where the dimples are present, as they are very close to each other. The profile obtained is plotted in Figure 6.24. The height of the burr is about 50 µm and from this image it is also difficult to distinguish the dimples.

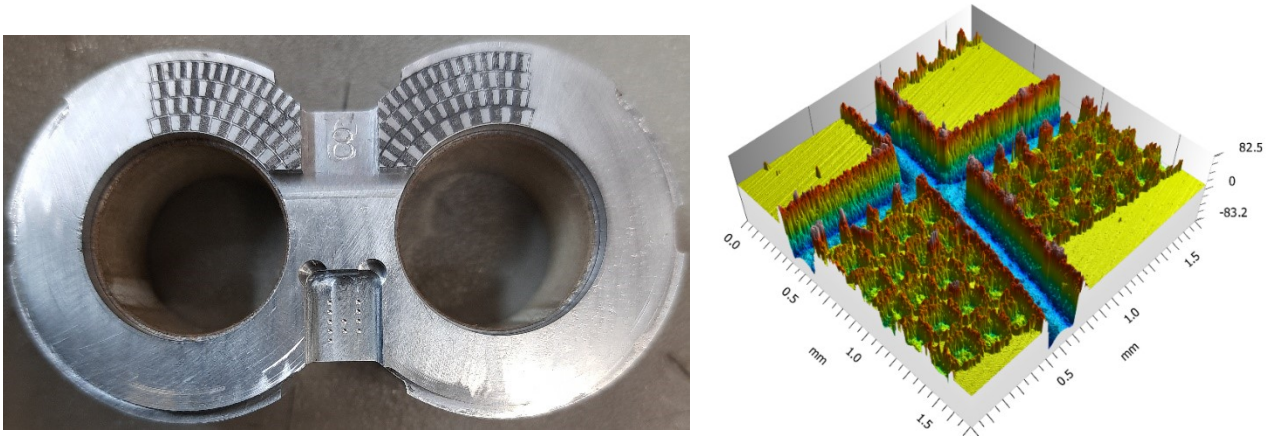

(a) (b)

Figure 6.23. (a) Photo of the lateral plate. (b) 3D profile measured immediately after laser texturing.

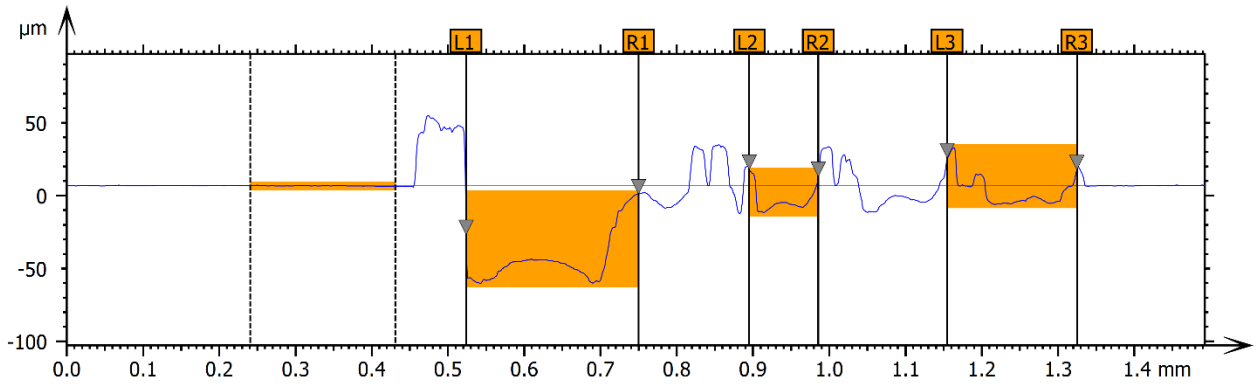

Parameters	Unit	Step 1	Step 2	Step 3
Width	mm	0.228	0.0915	0.171
Maximum height	µm	67.1	18.4	12.7
Mean height	µm	49.7	10.2	3.76

Figure 6.24. Surface profile on a cross section of the raw sample.

The Figure 6.25 shows the 3D surface after the polishing process, but it is evident that it was not enough to completely remove the large amount of material present on the surface. The profile on the cross section, in the Figure 6.26, allows to measure a residual height of the burr of about 5.77 µm. The channels have width and depth in agreement with what has been hypothesized, as well as the dimples.

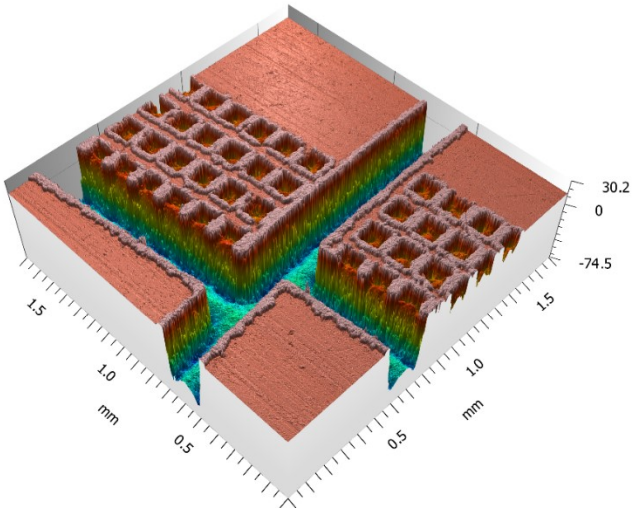

Figure 6.25. 3D profile measured after the mechanical polishing process.

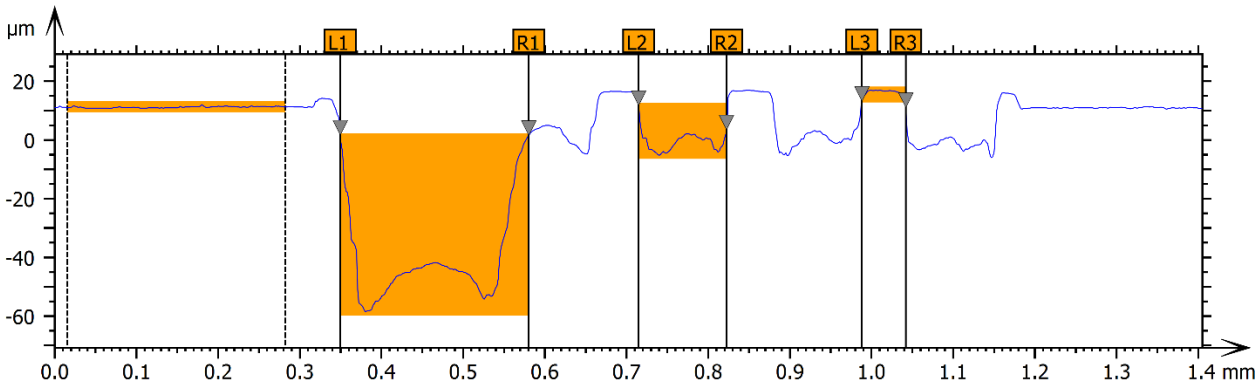

Parameters	Unit	Step 1	Step 2	Step 3
Width	mm	0.232	0.110	0.0548
Maximum height	µm	69.7	16.4	5.77
Mean height	µm	51.8	11.7	5.06

Figure 6.26. Surface profile on a cross section of the polished sample.

6.3.5 Type E

This configuration has steps and channels similar to those of Type A. The photograph of the lateral plate is visible in Figure 6.27a. The Figure 6.27b shows the 3D surface just created, while in the Figure 6.28 it is possible to observe the profile on a cross section. The maximum height of the burr is about 42 µm.

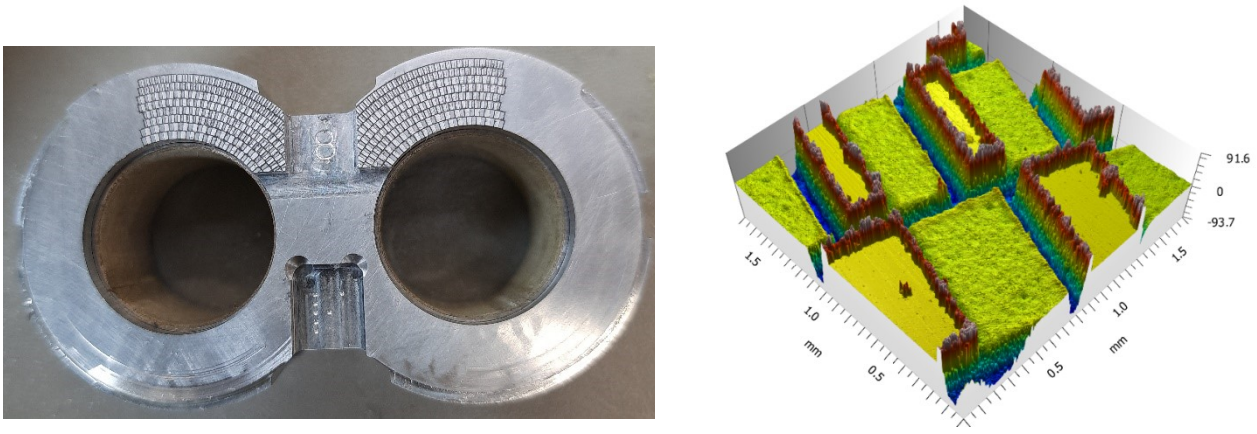

(a) (b)

Figure 6.27. (a) Photo of the lateral plate. (b) 3D profile measured immediately after laser texturing.

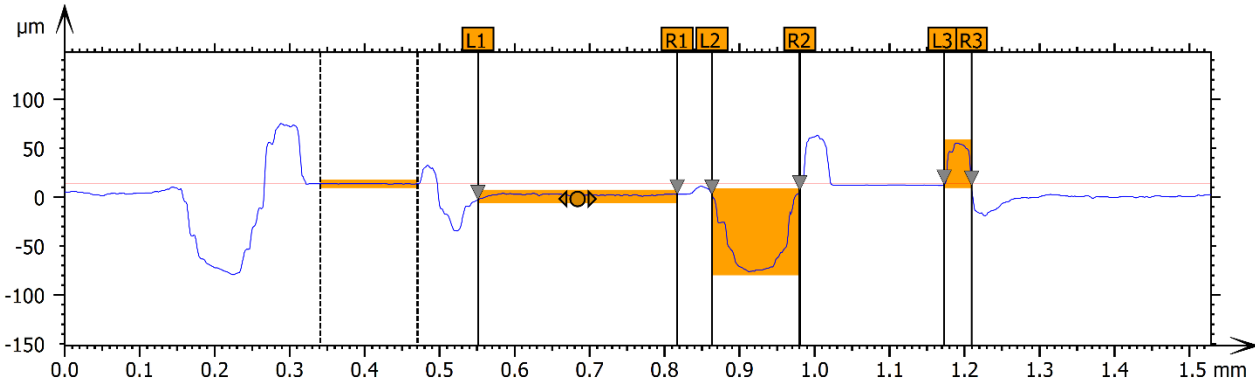

Parameters	Unit	Step 1	Step 2	Step 3
Width	mm	0.267	0.119	0.0377
Maximum height	µm	16.4	89.8	41.8
Mean height	µm	11.4	63.8	30.2

Figure 6.28. Surface profile on a cross section of the raw sample.

By mechanically removing the burr, the surface appears very clean and well defined, Figure 6.29. The steps are on average 9.6 µm deep and the channels are 120 µm wide and 57 µm deep, Figure 6.30, just like the theoretical dimensions.

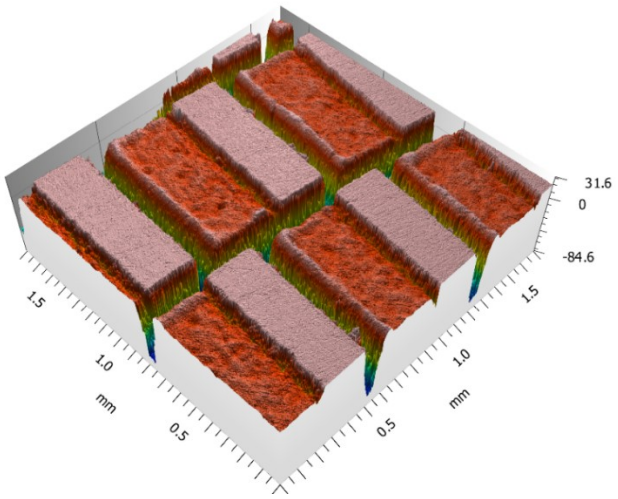

Figure 6.29. 3D profile measured after the mechanical polishing process.

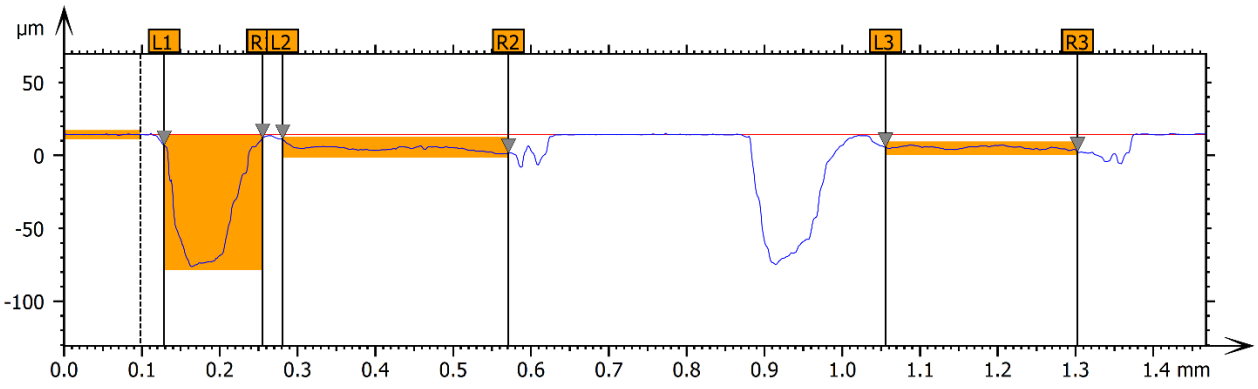

Parameters	Unit	Step 1	Step 2	Step 3
Width	mm	0.127	0.291	0.248
Maximum height	µm	90.5	13.2	11.6
Mean height	µm	56.5	9.62	8.93

Figure 6.30. Surface profile on a cross section of the polished sample.

6.3.6 Type F

This typology is similar to Type B, but has 40 µm deep steps, Figure 6.31. This geometry has been created in a second phase of the experimental activity and only the measurements made after the mechanical polishing are available. The texture appears very precise and well defined, as could be seen from the profile on a cross section, Figure 6.32. The channels have a width of about 250 µm and a maximum depth of 120 µm; the steps have an average depth of 44 µm.

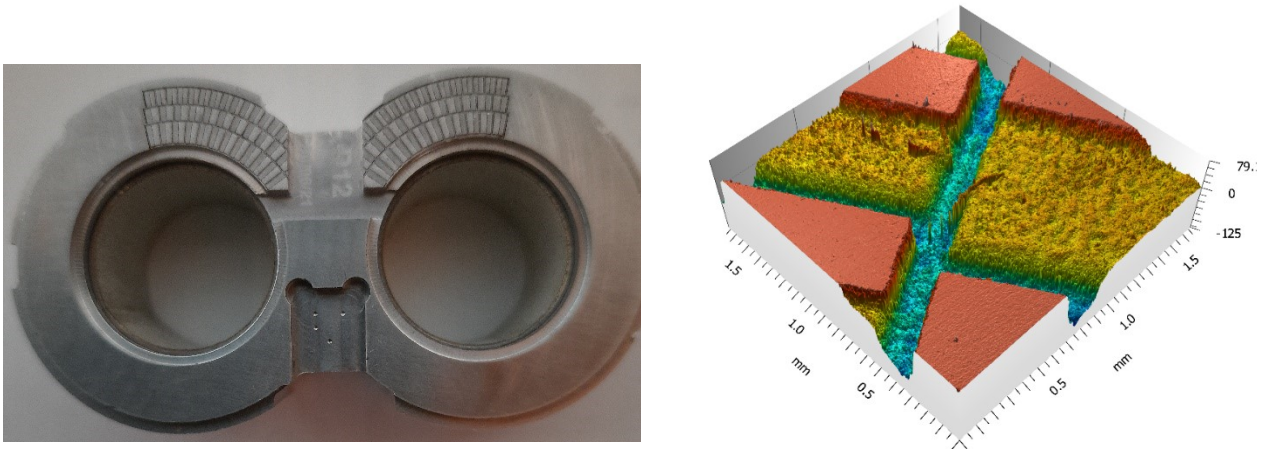

(a) (b)

Figure 6.31. (a) Photo of the lateral plate. (b) 3D profile measured immediately after laser texturing.

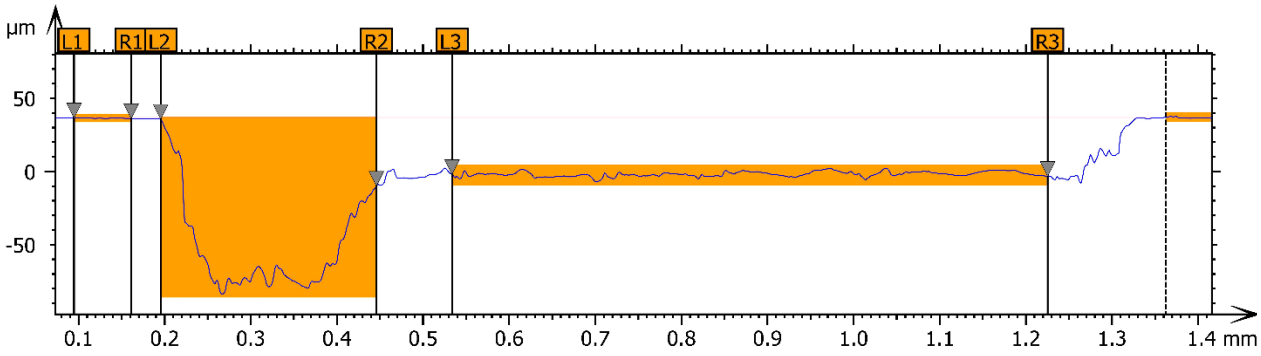

Parameters	Unit	Step 1	Step 2	Step 3
Width	mm	0.0667	0.251	0.693
Maximum height	µm	0.674	120	44.0
Mean height	µm	0.395	88.9	38.6

Figure 6.32. Surface profile on a cross section of the polished sample.

6.4 Experimental tests

The lateral plates realized and whose measurements are shown in the paragraph 6.3, have been inserted inside external gear pumps. The pumps belong to group 2 and are made by Casappa S.p.A. The functional characteristics are listed in the Table 6.2:

Table 6.2. Characteristics of the tested pumps.

Displacement	21.14 cc/rev	
Pressure	Max continuous	260 bar
	Max discontinuous	280 bar
	Max peak	300 bar
Max speed	4000 r/min	

In order to verify that the surface texturing could actually contribute to increasing the performance of external gear pumps, a test procedure has been planned, also agreed with the Casappa company, based on their great experience.

To assess whether the performance of a pump with textured lateral plates is better than a traditional pump, endurance tests should be performed. During this type of test, by keeping the characteristic quantities monitored, such as the suction and discharge pressures, the absorbed torque and the rotation speed, a decrease in the overall efficiency of the pump is generally observed after many working cycles. In fact, in long-term tests and in severe conditions, there is a progressive removal of material from the lateral plates, due to insufficient hydrodynamic lubrication inside the meatus between gear wheels and lateral plates, generating seizure conditions. The wear of the lateral plates means that a greater flow rate flows back towards the suction, with a consequent loss of volumetric efficiency. The hydromechanical efficiency is also negatively influenced by the seizure of the pump, since when the components are in contact the absorbed torque increases.

The seizure tests require activities with a very long time duration, indicatively they could also last two or three consecutive days; unfortunately, in the laboratory of the Department of Engineering and Architecture of the University of Parma it is not possible to perform tests of this duration. The strategy adopted is based on solutions that tend to reduce the time of seizure, voluntarily reducing the effectiveness of hydrodynamic lubrication between gear wheels and lateral plates inside the pump.

A possible way to limit the test time is to couple the lateral plates with non-brushed gear wheels, that is, they do not have a fillet radius on the side of each tooth. The Figure 6.33a shows the entire

gear wheel present in this type of pump and the other images show two variants of the tooth side: in the Figure 6.33b a tooth with non-brushed side (sharp edge) is visible, while the Figure 6.33c shows a tooth with a fillet radius, normally used in gear pumps. Later in the text the gear wheels with sharp edges will be indicated with the abbreviation NoSp, while the standard wheels with STD. In the image, the fillet radius has been deliberately increased to emphasize it and make it more visible. The chamfer on the side of each tooth allows the oil to be conveyed inside the meatus and also permits the tooth of the wheel to behave exactly like a slider moving on a fixed surface, generating hydrodynamic bearing capacity. On the other hand, the edge side of the tooth is very sharp and, in case of contact with the lateral plate, removes a greater amount of material, wearing out the component and worsening the performance of the pump in less time.

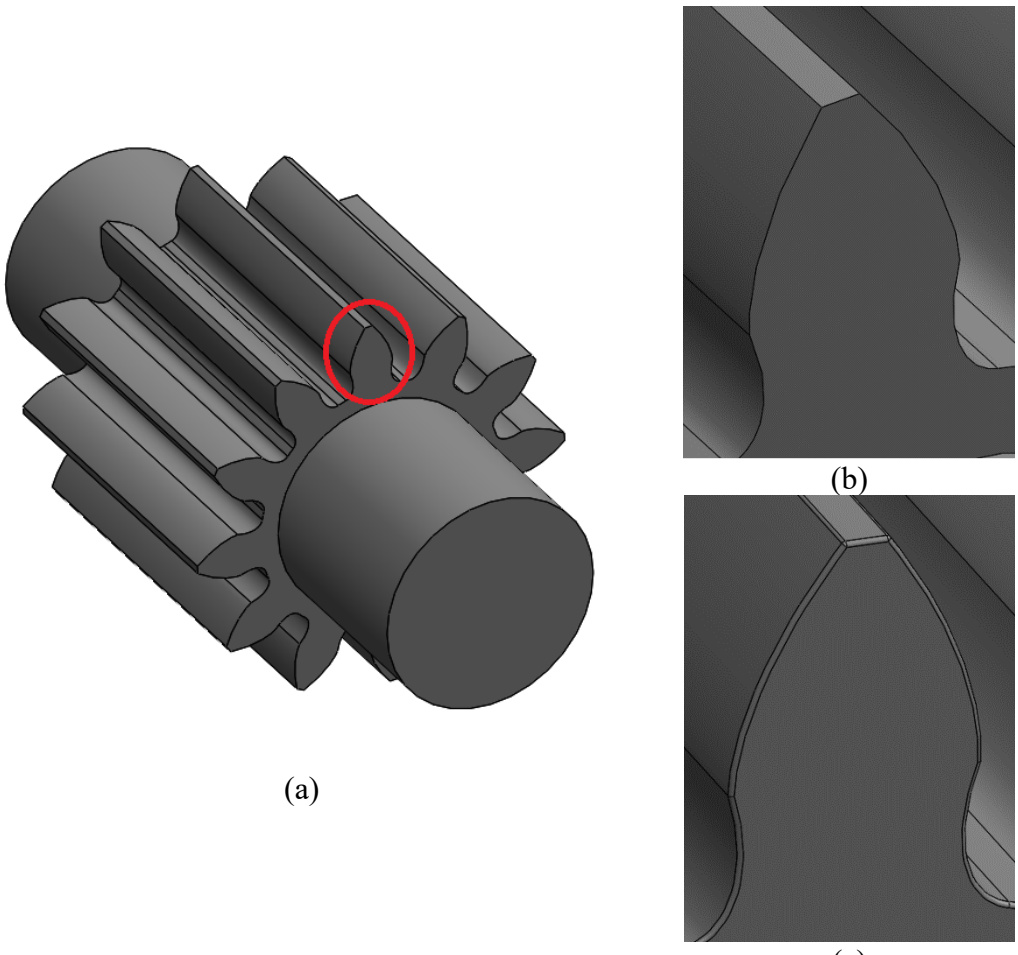

Figure 6.33. (a) Gear wheel of a group 2 pump. (b) Sharped edge tooth, NoSp. (c) Smoothed edge tooth, STD.

The whole experimental activity took a long time, especially to arrive at defining a test cycle that would allow to quickly get to seizure.

Before even testing the textured pumps, the analysis focused on pumps with standard lateral plates and NoSp wheels: this configuration represents the starting point with which comparisons have been subsequently made with the various types of textures.

Once the seizure conditions have been obtained, the pumps with the textured lateral plates have been tested with the same working cycle. The test strategy is to compare the overall efficiency of the baseline with those of pumps with textured lateral plates: if after the same cycle, the overall performance of a pump with textured components is greater than the efficiency of the baseline, an increase of the pump performance has been obtained.

In a pump, energy losses could impact the delivered flow rate or the absorbed torque. Both contributions could be analysed separately through the volumetric and hydromechanical efficiency. Leakages and losses due to compressibility of the fluid are quantified by the volumetric efficiency, defined for a pump as:

$$\eta_v = \frac{Q}{n \cdot V_d} \tag{6.3}$$

Where Q is the delivered flow rate, n the pump rotational speed and V_d the machine displacement.

Losses due to friction, both due to surfaces in relative motion and to the viscosity of the fluid, cause a higher torque absorption and are quantified by the hydromechanical efficiency, defined as:

$$\eta_{hm} = \frac{V_d \cdot (p_i - p_d)}{T} \tag{6.4}$$

Where p_i and p_d are respectively the suction and discharge pressures, while T is the absorbed torque.

The overall efficiency of the machine is given by the product of the two efficiencies:

$$\eta_g = \eta_v \cdot \eta_{hm} \tag{6.5}$$

The type of test adopted allows to obtain an indirect measure of the effectiveness of the surface texturing. Since the geometric dimensions of the textures are very small it is not possible to directly measure the hydrodynamic bearing capacity generated by the surface, moreover inside gear pumps.

However, from the numerous tests carried out with the tools and equipment available in the laboratory of the University of Parma, the test strategy adopted has proved useful for evaluating the

effectiveness of a textured surface, also allowing to appreciate the differences given by the distinct geometries created.

6.4.7 Measurement uncertainty

The efficiencies curves that will be shown are also completed by the measurement uncertainty. Measurement uncertainty is a number associated with the result of a measurement that expresses the dispersion of the values that could be attributed to the measurand.

In most cases the measurand y is not measured directly, but is determined by other N quantities x_i by means of a functional relation f:

$$y = f(x_1, x_2, x_3 \dots x_N) \tag{6.6}$$

Where the variables x could in turn be measurands or parameters dependent on other measurements.

Since each quantity x has been acquired with a measuring instrument having its own uncertainty, it is possible to calculate the combined uncertainty of the quantity y by applying the law of propagation of uncertainty, Equation (6.7):

$$i = \sqrt{\sum_{i=1}^{p} \left(\frac{\partial f}{\partial x_i}\right)^2 i^2(x_i)} \tag{6.7}$$

Where: $\frac{\partial f}{\partial x_i}$ is the partial derivative of the computed function with respect to a single independent measured quantity x_i, e $i(x_i)$ is the uncertainty of measurement of the variable x_i. The propagation law of uncertainty is valid if all the inputs x_i are uncorrelated or independent quantities.

6.4.8 Circuit layout

The experimental tests have been performed in the laboratory of the Department of Engineering and Architecture of the University of Parma.

The Figure 6.34 shows the photo of the test bench set up with a pump being tried out, while the Figure 6.36 shows the ISO diagram of the circuit layout, indicating the sensors installed.

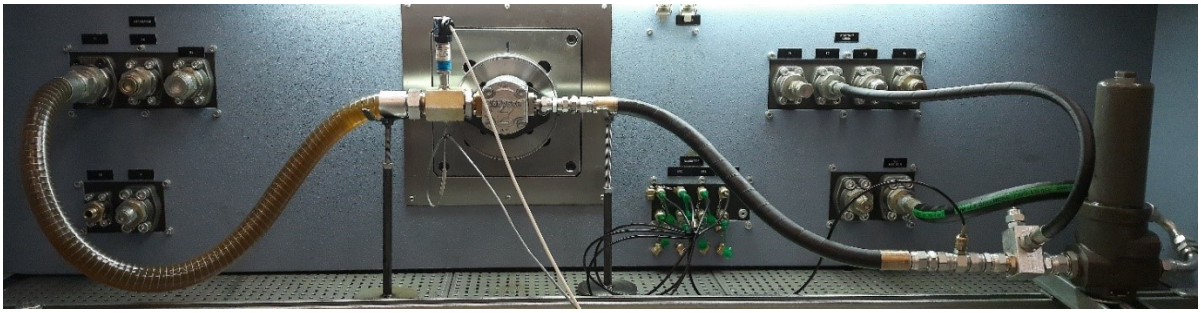

Figure 6.34. Photo of the test bench set up.

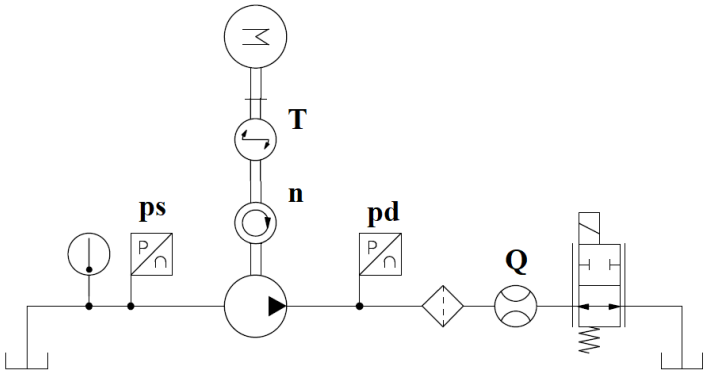

Figure 6.35. ISO scheme of the circuit layout.

The Table 6.3 lists the models of the sensor used and their main characteristics.

Table 6.3. Sensors installed on the test bench and relative characteristics.

Variable	Sensor	Model	Main Features
p_s	Pressure Transducer	Wika S-10	0 – 10 barA ±0.5%FS
p_d	Pressure Transducer	Danfoss MBS 1250	0 – 400 bar ±0.5%FS
Q	Flow Meter	VSE VS 1	0-80 l/min ± 0.3% measured value
n	Speed sensor	HMB T10FS	accuracy class 0.05
T	Torque sensor	HMB T10FS	accuracy class 0.05

6.4.9 Running in

Before being tested, each hydraulic pump needs to be run in. During the first start up, the hydraulic machine is usually driven into rotation by an external motor and it is made to work in the presence of gradually increasing pressure differences between the ports, up to values close to the maximum allowed. In these conditions the gear wheels, under the action of the loads originating

from the fluid pressure, come into contact with the body of the machine in the area near the low pressure port and, since the wheels themselves are made of a material having greater hardness than the body, they remove a certain amount of material from it. The delicate running in operation described above, of fundamental importance for the proper functioning of the machine in its subsequent life, essentially produces an alteration of the geometry of the body which, combined with the eccentric position assumed by the wheels during operation, determines the shape of the head meatus.

The chosen running in cycle is performed at a rotation speed of 1000 r/min. Gradually, the pressure at the pump delivery port is increased to 20 bar, maintained for a time sufficient to remove material from the body, and then it is again brought to zero pressure. The quantities of interest (suction pressure, delivery pressure, delivery flow rate and absorbed torque) are acquired at half the maximum pressure reached. This procedure is repeated several times by increasing the delivery pressure by 20 bar up to a pressure of 240 bar. The oil temperature has been set at 50 °C. The Table 6.4 provides a complete overview of the running in conditions.

Table 6.4. Running in conditions.

Running-in pressure	20	40	60	80	100	120	140	160	180	200	220	240
Acquisition pressure	10	20	30	40	50	60	70	80	90	100	110	120

The running in cycle consists of many steps since originally it was not known the influence of using NoSp gear wheels on the overall performance. The first pumps to be run in have non-textured lateral plates. Actually, the use of NoSp gear wheels does not involve any significant variation in the performance of the machine during the running in: the Figure 6.36 shows the volumetric and hydromechanical efficiencies trends between standard pumps and pumps with NoSp gear wheels inside. Regarding the volumetric efficiency, there is an excellent overlap between the two curves; the comparison of the hydromechanical efficiency shows small deviations at very low pressures, but anyway the uncertainty bands are overlapped. For confidential reasons the value of each graph has been divided by a reference value in order to make the maximum value equal to 0.9: however, the trend remains respected. This technique will also be adopted for the other graphs.

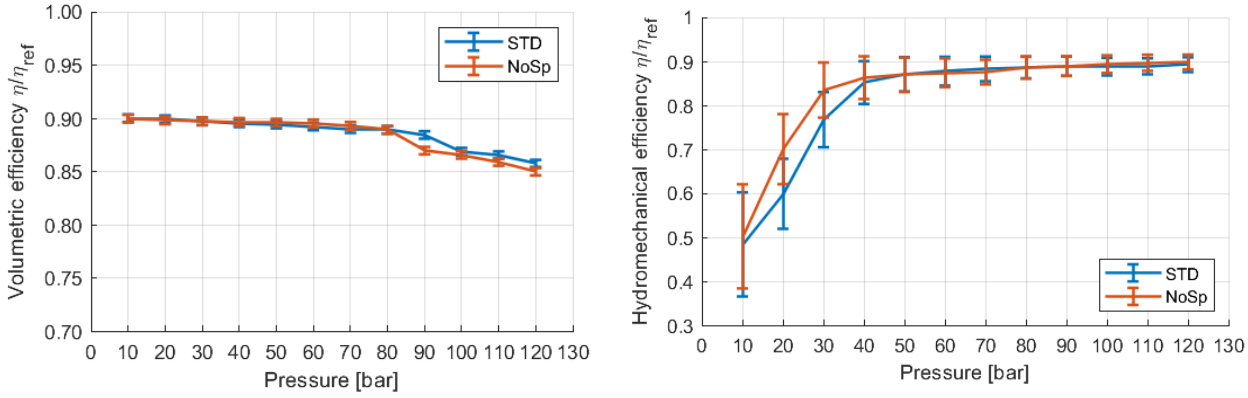

(a) (b)

Figure 6.36. Comparison between volumetric (a) and hydromechanical (b) efficiency between a standard pump and one with NoSp gear wheels. Non-textured lateral plates.

Since the use of NoSp gear wheels does not affect performance after the running in, the pumps with textured lateral plates inside and with NoSp gear wheels have been also run in with the same working cycle. For clarity, the Table 6.5 summarizes the types of textures created.

Table 6.5. Type of textured pumps to be tested.

Type	Geometry
A	Steps deep 0.01 mm and recovery channels of 0.05 mm depth and 0.2 mm wide
B	Steps deep 0.01 mm and recovery channels of 0.1 mm depth and 0.2 mm wide
C	Steps deep 0.01 mm e no recovery channels
D	Sequence of square dimples with side 0.1 mm and depth 0.01 mm. Recovery channels of 0.05 mm depth and 0.2 mm wide
E	Steps deep 0.01 mm and recovery channels of 0.05 mm depth and 0.1 mm wide
F	Steps deep 0.05 mm and recovery channels of 0.1 mm and 0.2 mm wide

The Figure 6.37 shows the trend of the volumetric efficiency for a pump of each type of texturing compared with the performance of the non-textured baseline with NoSp gear wheels. There is a little variability on point values, but it is very limited; however, one type of texture has a trend in volumetric efficiency that is always lower than the others and with respect to the baseline. This configuration is the one that presents the succession of square dimples within the circular sector. This anomaly is also found by analyzing the hydromechanical performance trend, shown in the Figure 6.38 for the same pumps of the previous chart. Again, the Type D configuration has

increasingly lower efficiencies than the others, which instead have comparable results with the baseline. Each plot has been divided by a reference value of η for confidential reasons.

The cause for the different behavior of the type D may be due to the greater quantity of metal burr produced by laser processing that has not be completely removed with the mechanical polishing process. During the first start up the gear wheels encounter greater friction, since they rub on the peaks of the burr, requiring greater torque from the electric motor, with a consequent decrease in hydromechanical efficiency. The burr also contributes to increasing the average height of the meatus between wheels and lateral plates, allowing a greater amount of oil to flow back towards the suction, decreasing the volumetric efficiency. In any case, the difference between this configuration and the others is not such as to justify damage to the pump following the running in.

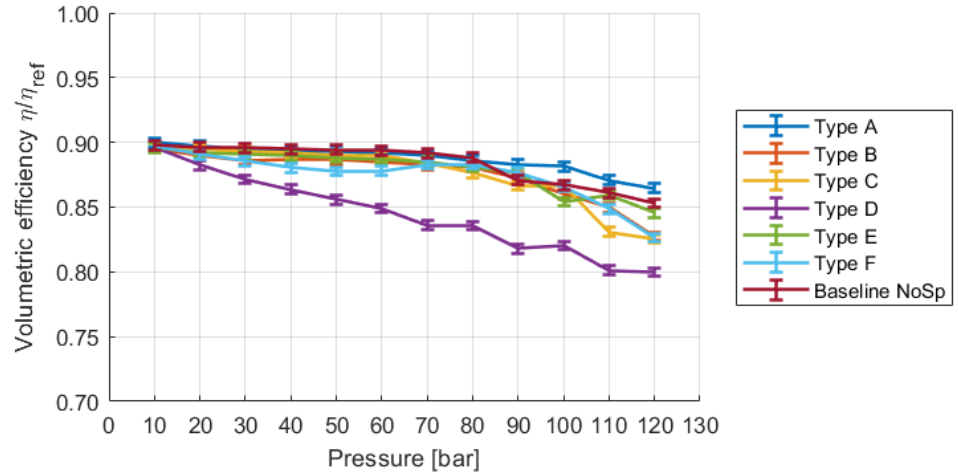

Figure 6.37. Volumetric efficiency for pumps with textured lateral plates during the running-in phase. Comparison with baseline. NoSp gear wheels.

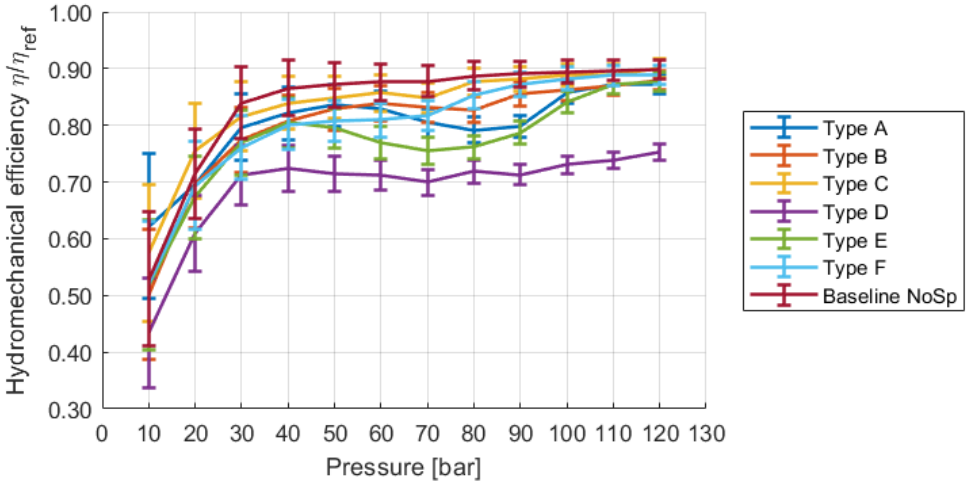

Figure 6.38. Hydromechanical efficiency for pumps with textured lateral plates in the running-in phase. Comparison with baseline. NoSp gear wheels.

The graphs show the trend of only one sample per type of texture to avoid having too many overlapping curves and making the graphs difficult to understand. In fact, more pumps have been tested to evaluate the repeatability of the results. In the Figure 6.39 a bar graph shows the trend of the volumetric performance of four equal samples, belonging to type A, subjected to the same running in cycle; the uncertainty bands have not been added because they are of very small amplitude and practically not visible. The samples have very concordant trends, except for small deviations at higher pressures, but they always remain on very high values. The Figure 6.40 reports a similar graph, but referred to the hydromechanical efficiency with uncertainty bands: also in this case the agreement of the values is high. The other types of textures have the same concordances between many samples and it is therefore possible to conclude that the pumps have excellent repeatability.

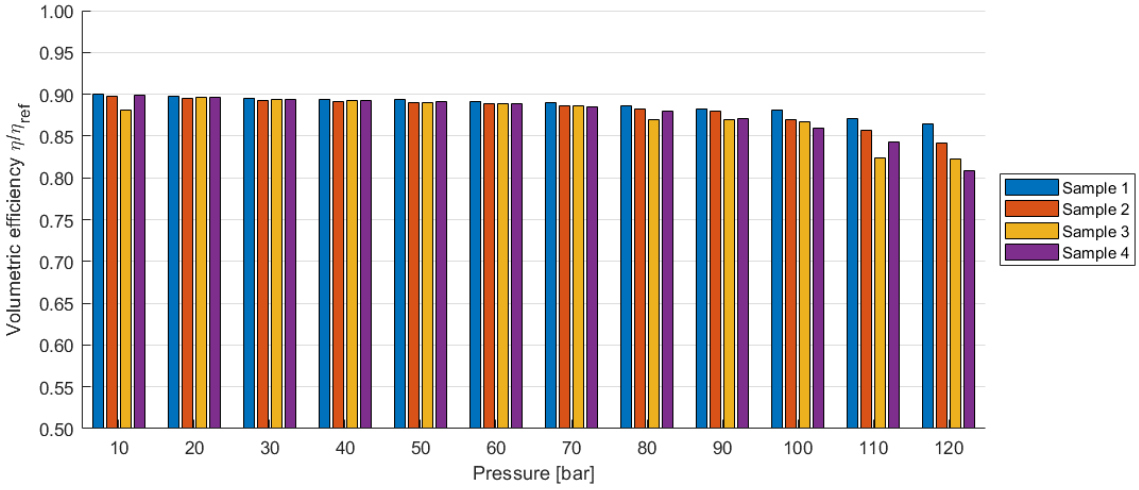

Figure 6.39. Volumetric efficiency of four samples of type A after the running-in.

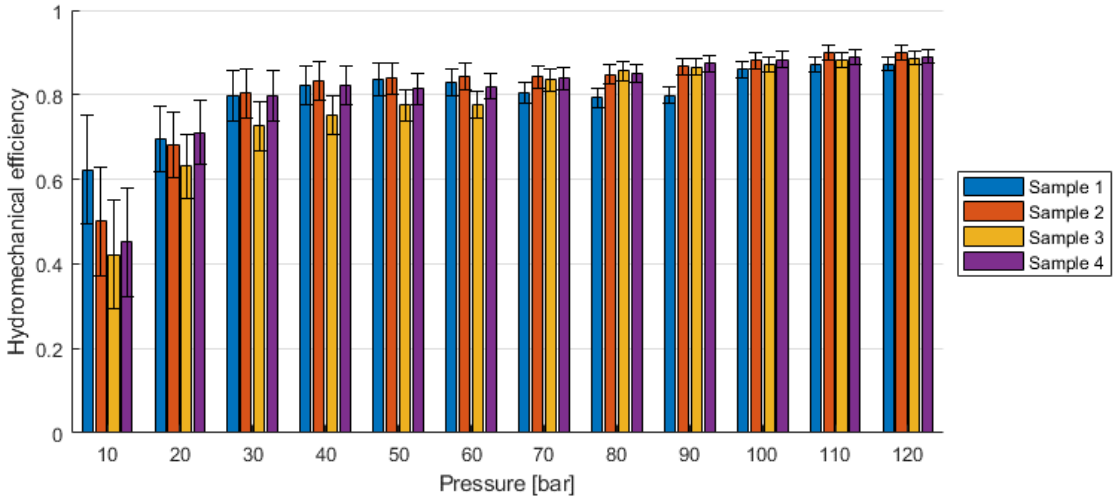

Figure 6.40. Hydromechanical efficiency of four samples of type A after the running-in.

6.4.10 Baseline – Test cycle

The pumps belonging to the baseline (without texture and with NoSp gear wheels) and already run in have been subjected to a working cycle that provides for a progressive tightening of the operating conditions, in order to identify the seizure conditions. Not knowing in advance the operating conditions such as to induce the pumps to seize, it has been decided to proceed gradually. In a first phase, the quantities of interest are acquired for the calculation of the volumetric and hydromechanical efficiency at increasing speeds from 1000 r/min to 2500 r/min; for each rotation speed the pressure imposed on the delivery increases from 120 bar to 240 bar with steps of 20 bar: the Table 6.6 summarizes the test conditions of the pumps. The oil temperature is set at 50 °C.

Table 6.6. Test conditions.

Pump speed [r/min]	**Pressure [bar]**						
	120	140	160	180	200	220	240
1000	✓	✓	✓	✓	✓	✓	✓
1500	✓	✓	✓	✓	✓	✓	✓
2000	✓	✓	✓	✓	✓	✓	✓
2500	✓	✓	✓	✓	✓	✓	✓

The Figure 6.41 shows the trends of the volumetric efficiency as a function of the delivery pressure for different rotation speed: the solid line represents a pump with NoSp wheels, while the dashed line represents a standard pump, STD wheels. The efficiencies curves are completely overlapping and the performance of pumps with NoSp wheels is greater than the standard ones. The explanation could be that the absence of the fillet radius on the side of the tooth conveys a smaller amount of oil into the meatus, which could flow back towards the suction; moreover, without the fitting, the hydrodynamic bearing capacity of the meatus is lower, decreasing the average height of the gap, with consequent lower losses due to leakage. All these factors combine to slightly increase the volumetric efficiency. Similarly, the Figure 6.42 shows the hydromechanical efficiency curves for the same two pumps: also in this case the efficiencies are completely equivalent, also considering the greater amplitude of the uncertainty band.

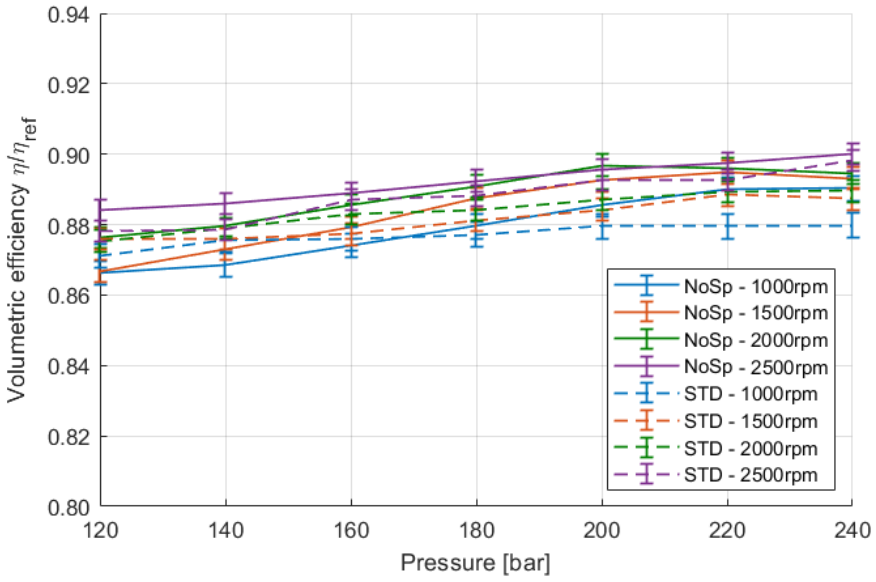

Figure 6.41. Volumetric efficiency as a function of delivery pressure for different rotational speeds. Solid line represents a pump with NoSp gear wheels; dashed line a standard pump. Oil temperature 50 °C

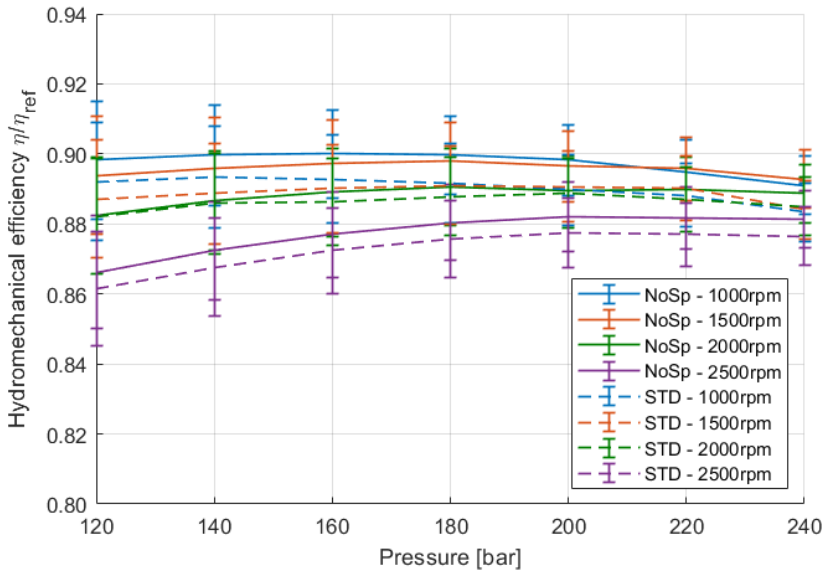

Figure 6.42. Hydromechanical efficiency as a function of delivery pressure for different rotational speeds. Solid line represents a pump with NoSp gear wheels; dashed line a standard pump. Oil temperature 50 °C

Considering the excellent performance values obtained during this first test phase, it was necessary to significantly modify the test conditions, in order to induce seizure of the components in a short time. The test conditions have been modified by increasing the rotation speed up to 3400 r/min and setting the oil temperature at 70 °C. As before, the data have been acquired at pressures from 120 bar to 240 bar, with an increment of 20 bar. Moreover, to better check and highlight if any internal damage occurred, the pumps have been subjected to a further working cycle at decreasing speed, but at the same pressure values. Seizure may occur in the most severe conditions, i.e. at high

speed and pressure, but may not be immediately visible from efficiencies. By decreasing the rotation speed it is possible to check if there is a difference between the acquisitions and to quantify it. The Table 6.7 and Table 6.8 summarize the new test conditions.

Table 6.7. Test conditions relating to Cycle I

Pump speed [r/min]	Pressure [bar]						
	120	140	160	180	200	220	240
1000	✓	✓	✓	✓	✓	✓	✓
1500	✓	✓	✓	✓	✓	✓	✓
2000	✓	✓	✓	✓	✓	✓	✓
2500	✓	✓	✓	✓	✓	✓	✓
3000	✓	✓	✓	✓	✓	✓	✓
3400	✓	✓	✓	✓	✓	✓	✓

Table 6.8. Test conditions relating to Cycle II

Pump speed [r/min]	Pressure [bar]						
	120	140	160	180	200	220	240
3400	✓	✓	✓	✓	✓	✓	✓
3000	✓	✓	✓	✓	✓	✓	✓
2500	✓	✓	✓	✓	✓	✓	✓
2000	✓	✓	✓	✓	✓	✓	✓
1500	✓	✓	✓	✓	✓	✓	✓
1000	✓	✓	✓	✓	✓	✓	✓

Figure 6.43 and Figure 6.44 show the volumetric efficiency trends relative to two baseline samples, while Figure 6.45 and Figure 6.46 show the hydromechanical efficiencies for the same two pumps. The efficiencies obtained with the Cycle I are displayed in a continuous line, while those obtained with the Cycle II are plotted in a dashed line. As the speed decreases, the efficiencies of the Cycle II show progressively higher differences. However, the differences are not that marked and the pump can not be defined seized. Therefore, the test strategy needs some further modification.

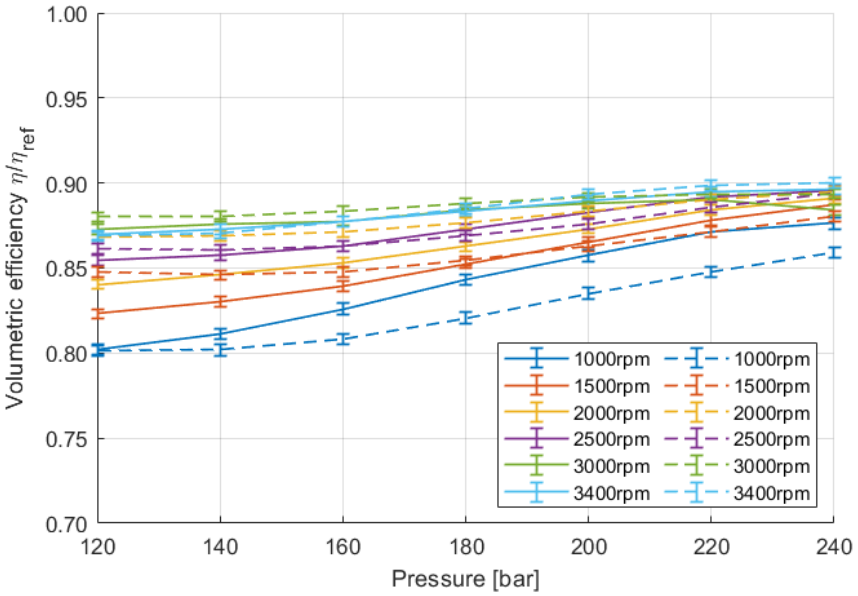

Figure 6.43. Baseline Sample 1. Volumetric efficiency as a function of delivery pressure for different rotational speeds. Solid line represents the results obtained with Cycle I; dashed line those obtained with Cycle II. NoSp gear wheels. Oil temperature 70 °C

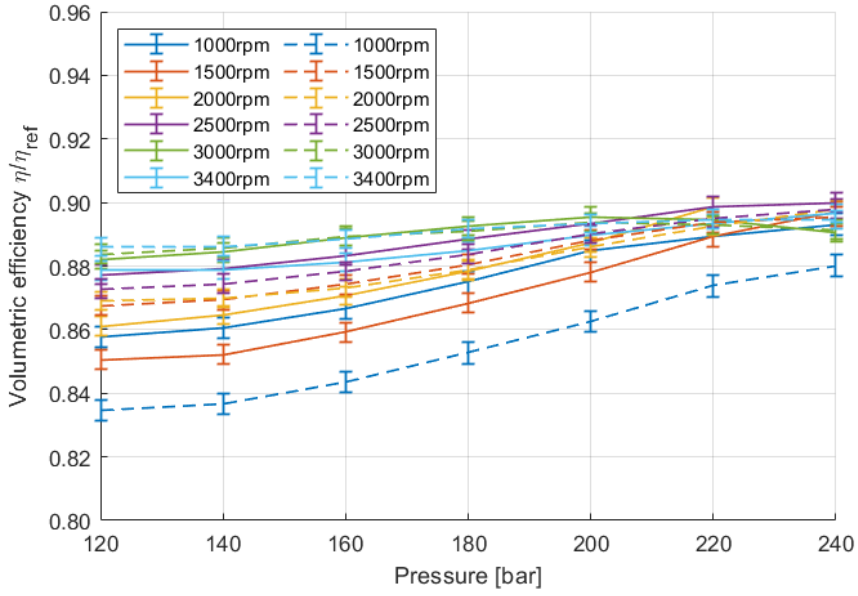

Figure 6.44. Baseline Sample 2. Volumetric efficiency as a function of delivery pressure for different rotational speeds. Solid line represents the results obtained with Cycle I; dashed line those obtained with Cycle II. NoSp gear wheels. Oil temperature 70 °C

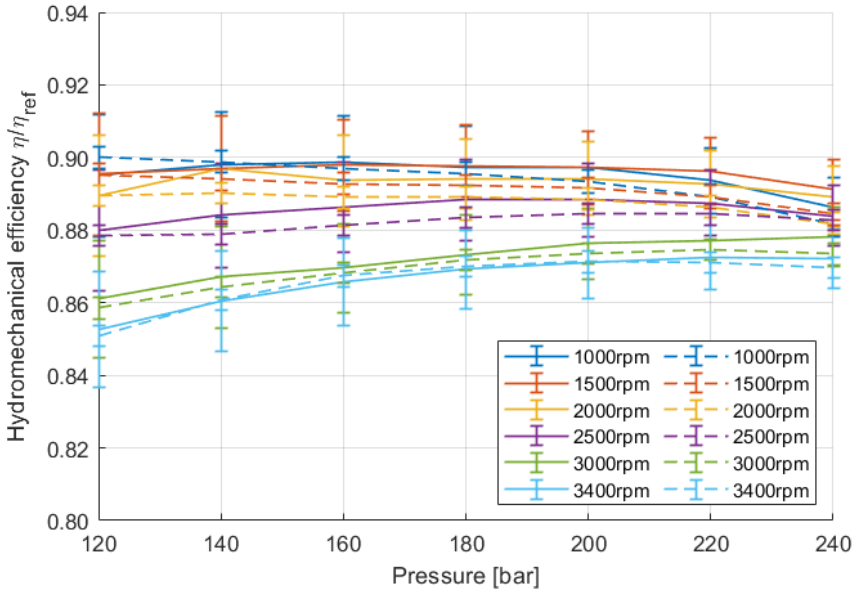

Figure 6.45. Baseline Sample 1. Hydromechanical efficiency as a function of delivery pressure for different rotational speeds. Solid line represents the results obtained with Cycle I; dashed line those obtained with Cycle II. NoSp gear wheels. Oil temperature 70 °C

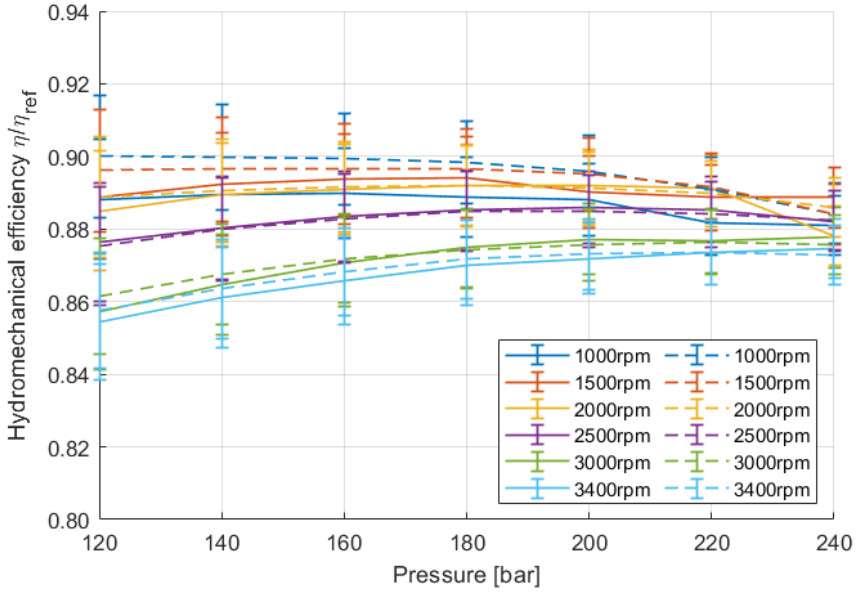

Figure 6.46. Baseline Sample 2. Hydromechanical efficiency as a function of delivery pressure for different rotational speeds. Solid line represents the results obtained with Cycle I; dashed line those obtained with Cycle II. NoSp gear wheels. Oil temperature 70 °C

The efficiencies graphs are useful for evaluating the trend as a function of pressure for different rotation speed; however, when the curves are numerous, the graphs are difficult to read and interpret. To overcome this drawback, it has been decided to introduce a synthetic parameter that allows to quickly assess whether there is a significant deviation of the curves during the two cycles. The parameter is the average global efficiency, given by the average of the global efficiency calculated for each test point *n*, Equation (6.8).

$$\eta_g = \frac{\sum_n (\eta_v \cdot \eta_{hm})}{n} \tag{6.8}$$

Using this parameter, two values are obtained graphically represented in Figure 6.47a for the first sample and in Figure 6.47b for the second. For confidential reasons, the overall efficiency of each plot has been divided by the same reference value in order to have the identical scale: this permit to appreciate that Sample 2 has a slightly lower overall efficiency than Sample 1. However, for each sample, the global efficiencies with Cycle I and Cycle II are practically the same and therefore the two pumps are to be declared healthy.

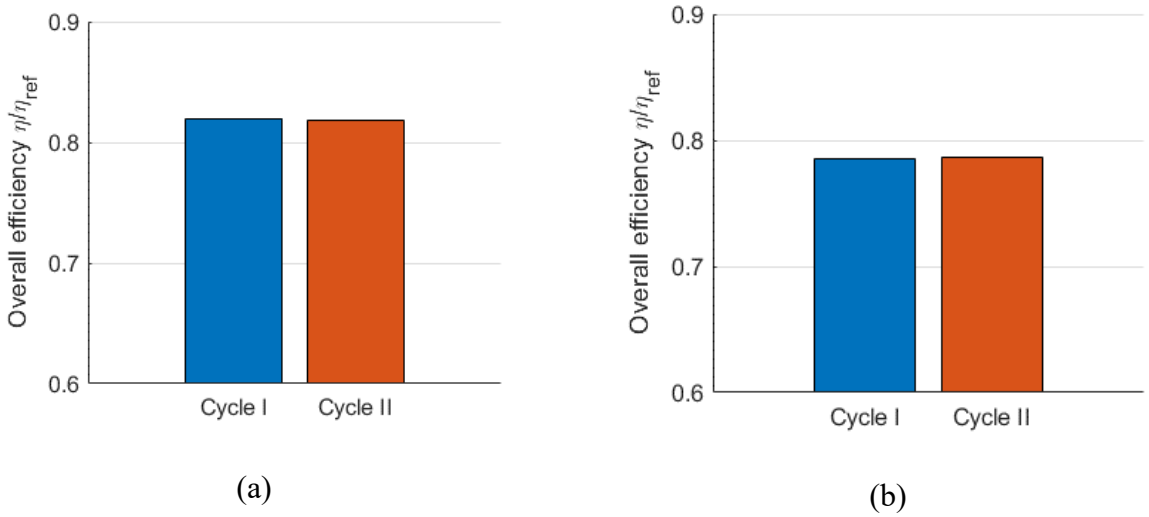

Figure 6.47. Average overall efficiency relative to Cycle I and Cycle II. (a) Baseline sample 1. (b) Baseline sample 2.

At this point the two baseline pumps tested were disassembled to observe the condition of the lateral plates. The monitoring of volumetric and hydromechanical efficiencies alone may not be sufficient to identify the onset of seizure: there may be situations in which the efficiencies have significant variations only after a longer time, or when the wear of the lateral plates is very high. The Figure 6.48 shows the photo of the lateral plates of Sample 1: confirming what was obtained with the performance analysis, the two lateral plates show very slight scratches, probably mainly due to the start of the pump. When the pump starts from a standstill, there is still no hydrodynamic bearing capacity inside the meatus between gear wheels and lateral plates such as to avoid direct contact: the consequence is to create small scratches on the lateral plates that absolutely do not affect the performance of the pump.

Figure 6.48. Photos of the lateral plates of the baseline pump 1 after Cycle I and Cycle II

Not being able to further tighten the test conditions due to the limitations of the test bench, it has been decided to modify the lateral plates, reducing the surface on the gear wheel side. In this type of pump, the lateral plates are balanced, i.e. the delivery pressure also acts on the back of the lateral plates which are thus pressed against the wheels, to reduce losses due to leakage into the gap. Reducing the surface on one side of the component causes an imbalance with a consequent greater thrust of the lateral plates towards the wheels. In this way, the hydrodynamic bearing capacity inside the meatus must counteract a greater force and therefore its failure is more likely. The diameter where the bushing is placed has been partially increased: the Figure 6.49 shows a lateral plate where the removed portion has been highlighted. It took several attempts with increasing radii to achieve the optimal configuration. The value of the radius can not be disclosed for confidential reasons.

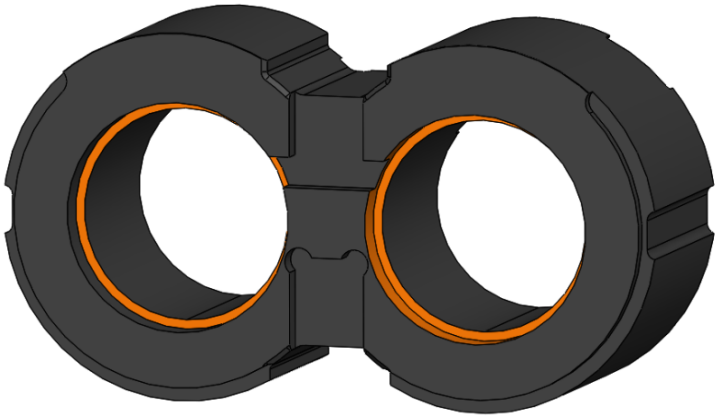

Figure 6.49. Lateral plates with the removed portion highlighted.

Three samples with modified balanced lateral plates have been tested with Cycle I and Cycle II. The Figure 6.50 shows the variation in the overall efficiencies of the three samples after the two cycles: all the samples show marked decreases in the overall performance, with reductions between 5% and 10%, as indicated in Table 6.9. It could also be concluded that the repeatability of the tests is high.

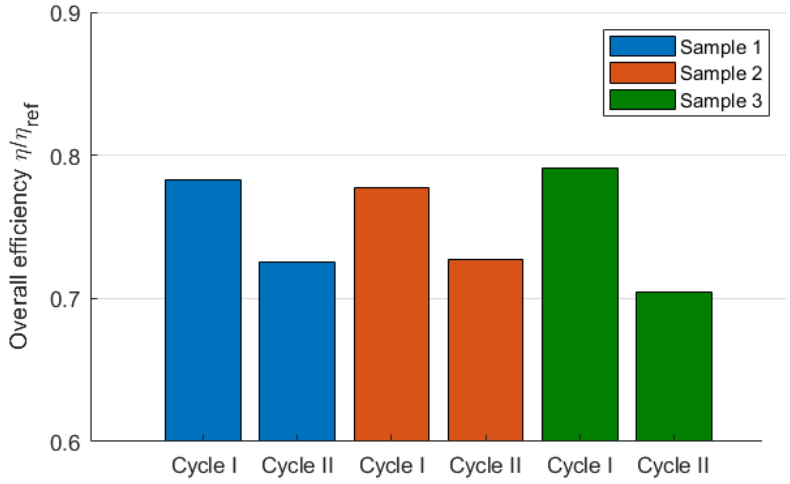

Figure 6.50. Overall efficiency calculated for Cycle I and Cycle II for three samples. NoSp gear wheels, lateral plates with modified balancing.

Table 6.9. Percentage decrease in overall efficiency.

Sample 1	-6.50%
Sample 2	-5.69%
Sample 3	-9.68%

As a further confirmation, the Figure 6.51 shows the trends of the volumetric and hydromechanical efficiency of the first sample for different rotational speed. In particular, about the volumetric efficiency, there is a progressively growing difference between the curves of the Cycle II from the first as the rotation speed decreases. The hydromechanical efficiency, on the other hand, does not undergo significant variations: the explanation may be that once the seizure has occurred, the gear wheels and the lateral plates are no longer in contact with each other, with the result that the pump does not absorb more torque.

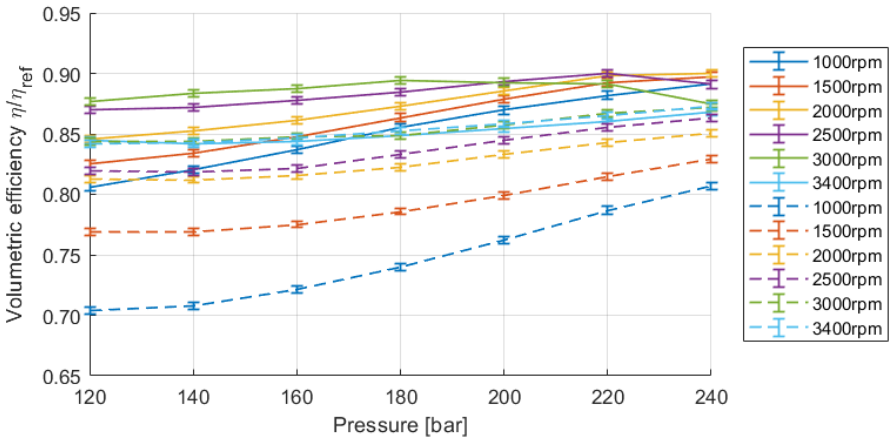

Figure 6.51. Baseline sample 1. Volumetric efficiency as a function of delivery pressure for different rotational speeds. Solid line represents the results obtained with Cycle I; dashed line those obtained with Cycle II. NoSp gear wheels, lateral plates with modified balancing. Oil temperature 70 °C

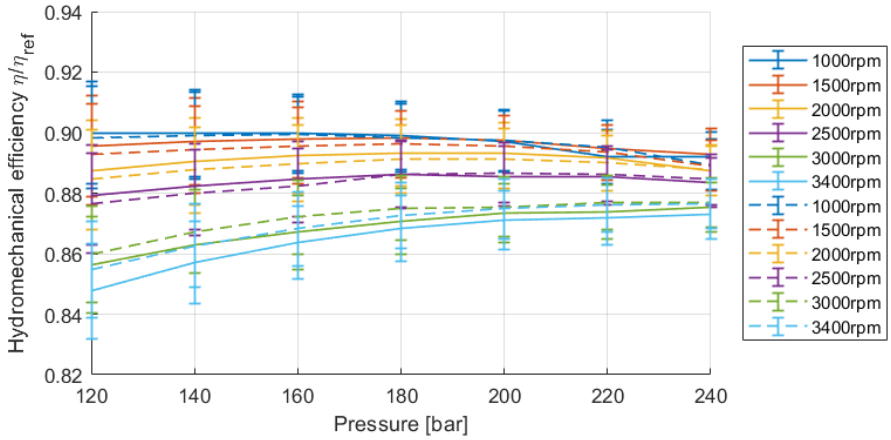

Figure 6.52. Baseline sample 1. Hydromechanical efficiency as a function of delivery pressure for different rotational speeds. Solid line represents the results obtained with Cycle I; dashed line those obtained with Cycle II. NoSp gear wheels, lateral plates with modified balancing. Oil temperature 70 °C

The Figure 6.53 shows the photographs of two lateral plates present within Samples 1 and Sample 2, focused on the low pressure area, taken after Cycle II. Signs and scratches, even deep ones, are very evident on the components, confirming a strong and lasting contact between wheels and lateral plates, a symptom of very marked seizure.

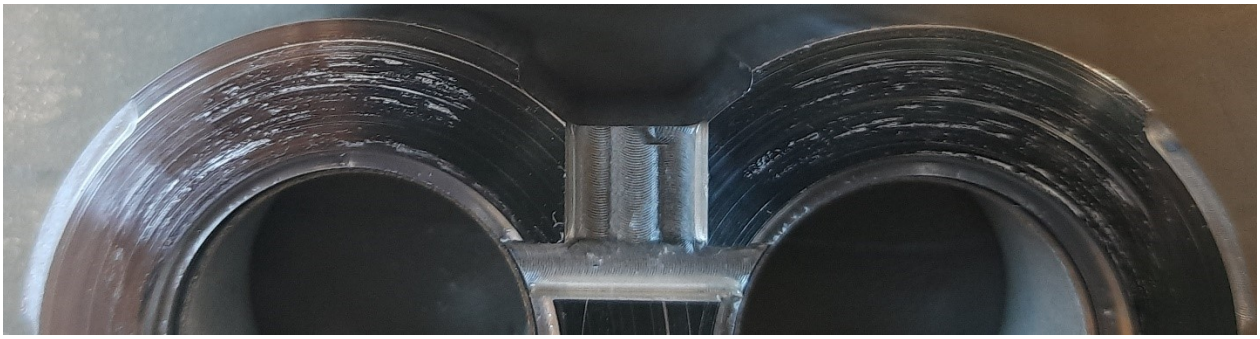

(a)

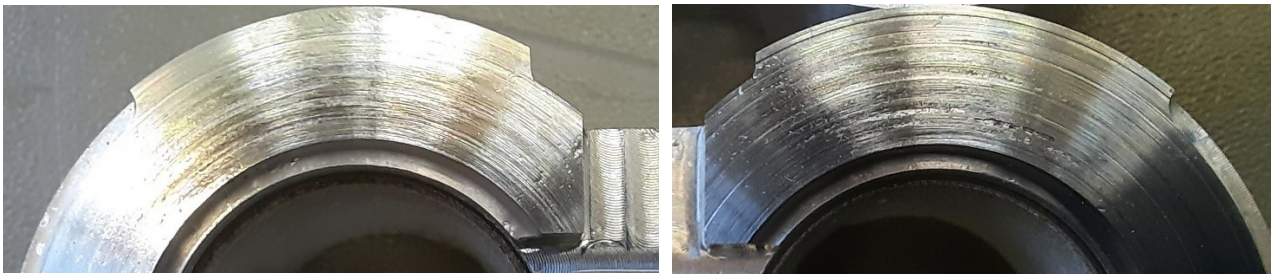

(b) (c)

Figure 6.53. (a) Photo of a baseline lateral plate, sample 1, detail on the suction. (b) and (c) Detail of the suction area of the lateral plates of sample 2

Samples of pumps with STD gear wheels and lateral plates with modified balance (equal to that used in the baseline) have also been tested. These tests are important to understand the effective influence of NoSp gear wheels, under the same working conditions. The standard pumps have been subjected to the same working cycle, consisting of Cycle I and Cycle II. The results are shown in the Figure 6.54, where the global efficiency of the three samples with NoSp gear wheels and a sample of standard pump is reported. The standard pump, despite having a global efficiency value slightly lower than one with NoSp gear wheels, does not show any drop in efficiency between the two cycles, that is, it does not get seized. The conclusion therefore is that to induce seizure in quick test times, the use of NoSp gear wheels is essential.

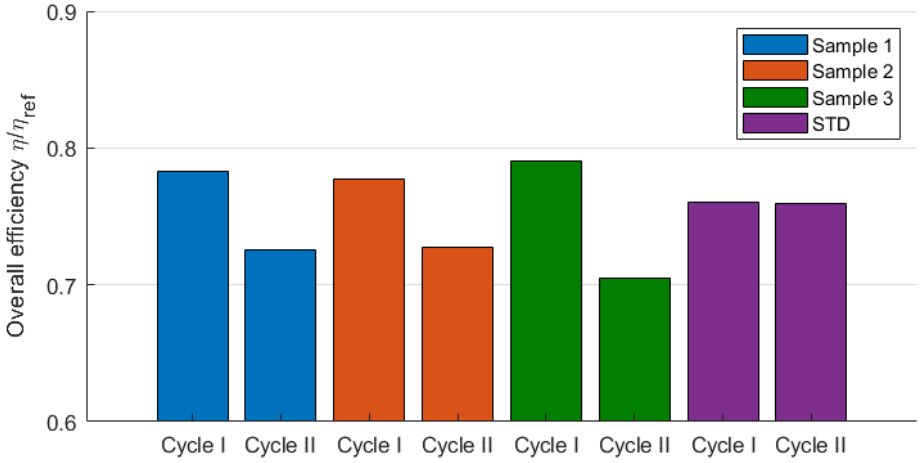

Figure 6.54. Overall efficiency calculated for Cycle I and Cycle II for three baseline samples. Comparison with a standard pump with STD gear wheels. Lateral plates with modified balancing.

The Figure 6.55 shows a photograph of a lateral plate placed inside the standard pump, taken after Cycle II. Unlike the previous images, the lateral plate appears with slight superficial scratches, such as not to affect the performance of the pump.

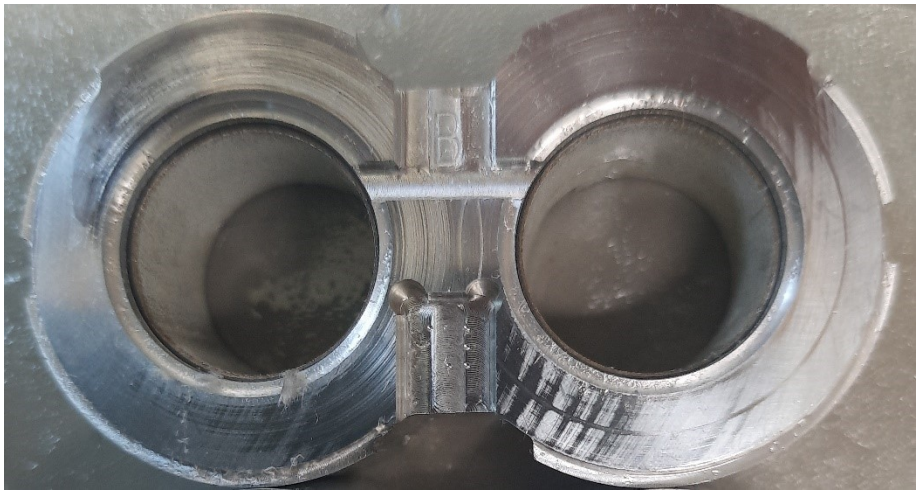

Figure 6.55. Photo of a baseline lateral plate of an STD pump, with brushed wheels and lateral plates with modified balancing.

6.4.11 Textured pumps

Pumps with textured lateral plates have been tested with the test cycle adopted with the baseline, in first place with the standard lateral plate balancing and using NoSp gear wheels. Since this type of lateral plate has never been tested, it is necessary to evaluate the values of the global efficiency to know if they are comparable with the baseline: the surface texturing aims to increase the performance of the pump, therefore the overall efficiency must be at least similar to that of the baseline. The Figure 6.56 shows the overall efficiencies, divided by a reference value, of a sample for each type of texture during Cycle I and Cycle II: no pump exhibits drastic decreases in efficiencies, in a very similar way to baseline pumps, Figure 6.47. Type D, the configuration with the sequence of square dimples, is the one that has the lowest values among all types; the reason could be very similar to what has already been highlighted during the running in of this type of texture. The Type F sample is not present in the chart, because it was made later in the experimental phase and has already been created with the modified balancing.

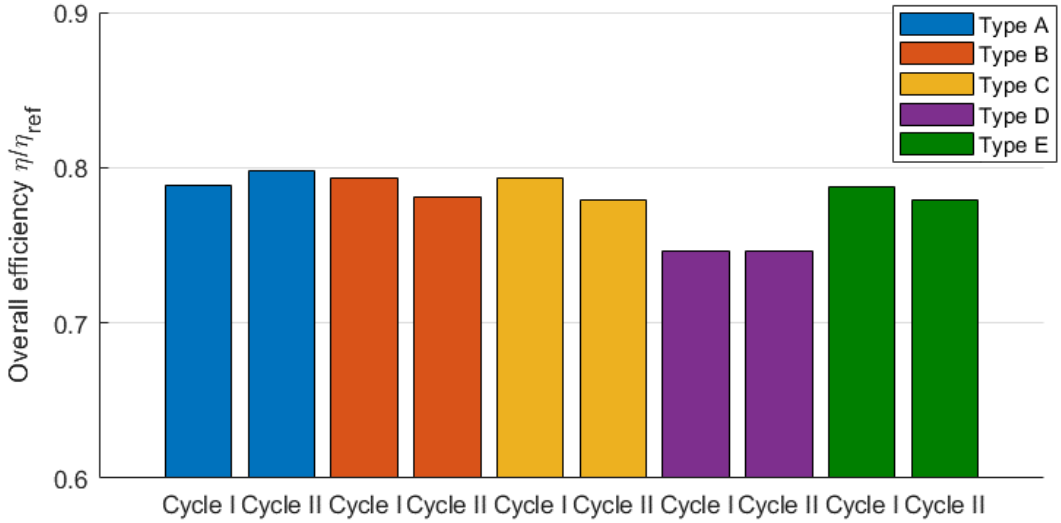

Figure 6.56. Overall efficiency calculated after Cycle I and Cycle II for each samples of texture. Standard lateral plates balancing.

Seizure does not occur on lateral plates with standard balance, exactly as with the untextured samples, therefore, pumps with textured lateral plates have been tested with lateral plates with modified balance (always with NoSp gear wheels). Overall, two pumps have been tested for each type of texture, except for type F of which only one sample was available. The Figure 6.57 shows an overview of the test results on all tested pumps. The values have been dimensionless for confidentiality reasons.

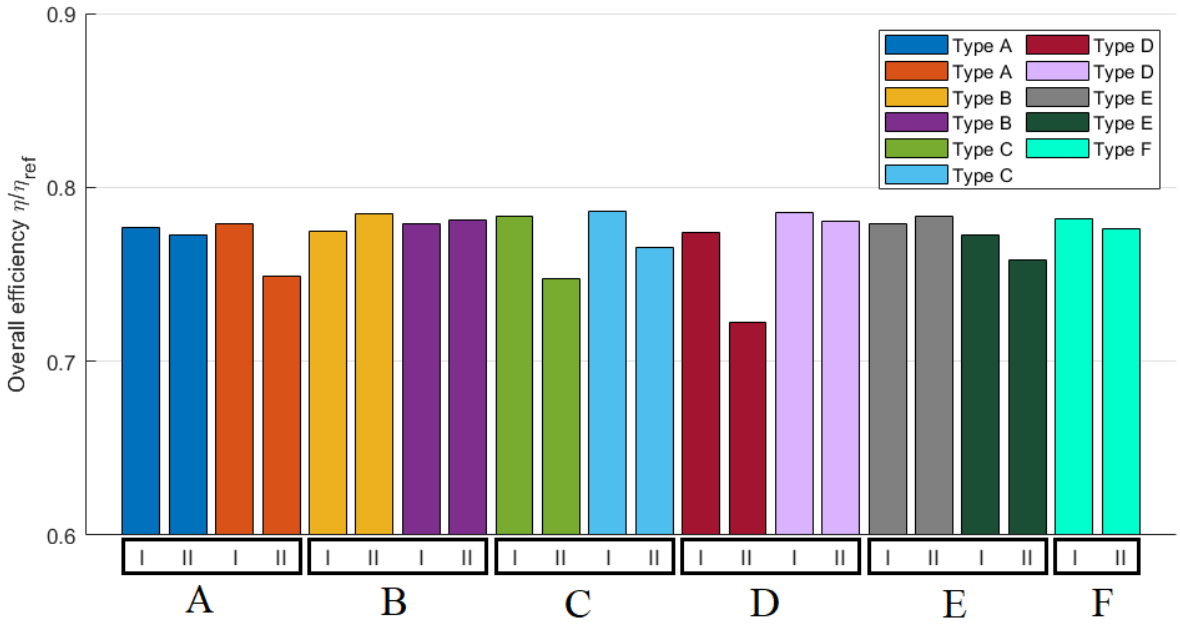

Figure 6.57. Overall efficiency calculated after Cycle I and Cycle II for each samples of texture. Modified lateral plates balancing and NoSp gear wheels.

The Table 6.10 indicates the percentage variations of the overall efficiency between Cycle I and Cycle II for all the pumps tested; data for baseline pumps are also reported to facilitate comparison.

Table 6.10. Percentage loss between Cycle I and Cycle II.

	Type A	Type B	Type C	Type D	Type E	Type F	Baseline
Sample 1	-0.43%	1.21%	-4.04%	-5.97%	0.45%	-2.27%	-6.50%
Sample 2	-3.39%	0.22%	-2.56%	-0.57%	-1.68%	–	-5.69%
Sample 3							-9.68%

6.5 Discussion

By analyzing the results obtained, it is possible to appreciate the differences between the several texture configurations. There are also marked differences between different samples of the same type: many pumps are needed to evaluate the repeatability of the results, which for cost reasons it was not possible to produce. Despite this, all samples tested showed better performance than the baseline. Type B is the one that does not show any drop in overall efficiency during the two working cycles. All the other types show decreases in the overall efficiency, less than the baseline, with strong differences between the two tested samples.

Type C is characterized by the absence of recovery channels. From the simulations carried out, the channels allow to delimit sectors independent of each other in order to obtain positive bearing capacity, as described in the Paragraph 3.3.2 . In confirmation of what has been obtained numerically, this configuration, being devoid of channels, is the one that, among all the types, has shown the greatest losses in terms of overall performance.

Type B, the best at the end of the tests, is characterized by a step geometry, which gave the greatest results from the simulations, and with deeper channels than the other samples. The greater depth of the channels allows a greater quantity of oil to flow towards the low pressure areas, providing more lubricant to the meatus. This aspect is also a confirmation of what was highlighted during the numerical analysis.

The other types present results that are not easy to interpret, since one sample has a very low efficiency compared to the second. This is mainly due to the test conditions, which are very severe. In order to carry out the tests in the university laboratory it was essential that the seizure took place quickly and unfortunately this led to the modification of the lateral plates balance. The texture geometries that already emerged from the numerical simulations as the least performing, in particular the type D, present samples with marked decreases in the overall efficiency.

Types A, E and F have had slight decreases in the overall efficiency, but it is not possible to distinguish the differences given by the various surface geometries.

The Figure 6.58 shows the photographs of two lateral plates belonging to type A and type E in the case of Sample 2 for both configurations. The wear levels are very high with deep scratches on the entire face of the component: the mechanical action of the NoSp gear wheels was such as to completely remove the steps made on the lateral plate, leaving only the grid of recovery channels. These samples, which have a clear decrease in the overall performance, are therefore to be declared seized.

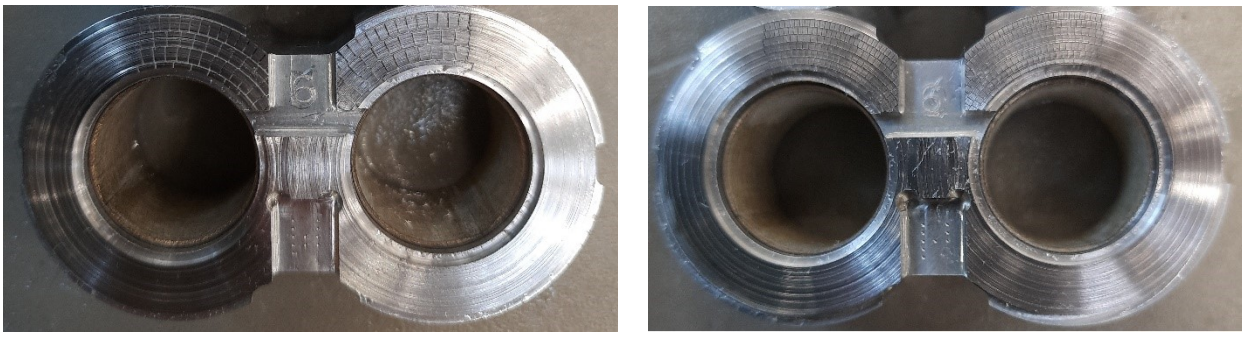

(a) (b)

Figure 6.58. Photographs of Type A and Type E lateral plate after Cycle II.

Instead, the photograph of type F is shown in the Figure 6.59a. This configuration is characterized by deeper steps and therefore, despite the severe test conditions, the geometry made on the lateral plates remained and is clearly visible, proving to withstand very demanding working conditions. Measurements have been carried out with an optical profilometer to evaluate the surface conditions: the Figure 6.59b reports the 3D profile of a portion of the surface, which appears slightly damaged, with only some surface scratches.

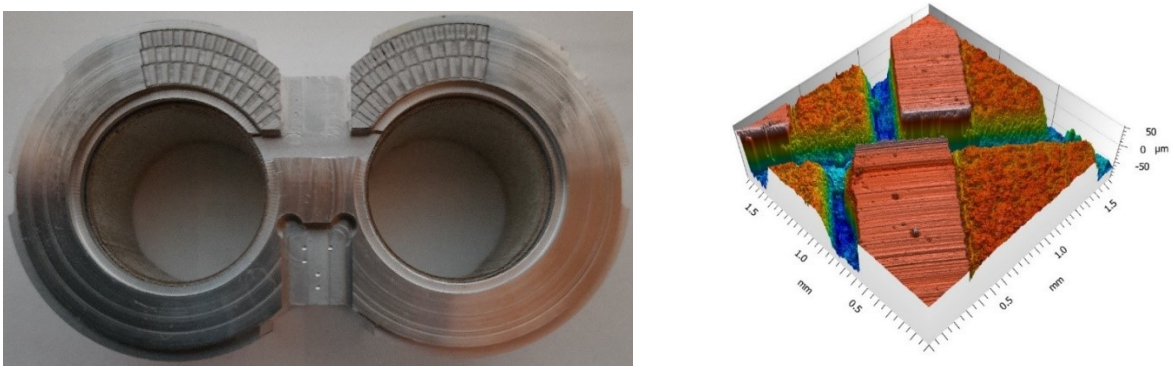

(a) (b)

Figure 6.59. (a) Photograph of a Type F lateral plate. (B) 3D profile measured whit an optical profilometer.

Type B, which did not show any decrease in the overall efficiency, has been subjected to a further test in order to identify when the abrupt decrease in efficiency happens. The test consists in repeating Cycle I and Cycle II one more time. The Figure 6.60 shows the non-dimensional global efficiencies relative to the two samples: Sample 1 has an efficiency that remains approximately constant, while Sample 2 shows a sudden drop in efficiency after the third cycle, with a decrease of 4.07%.

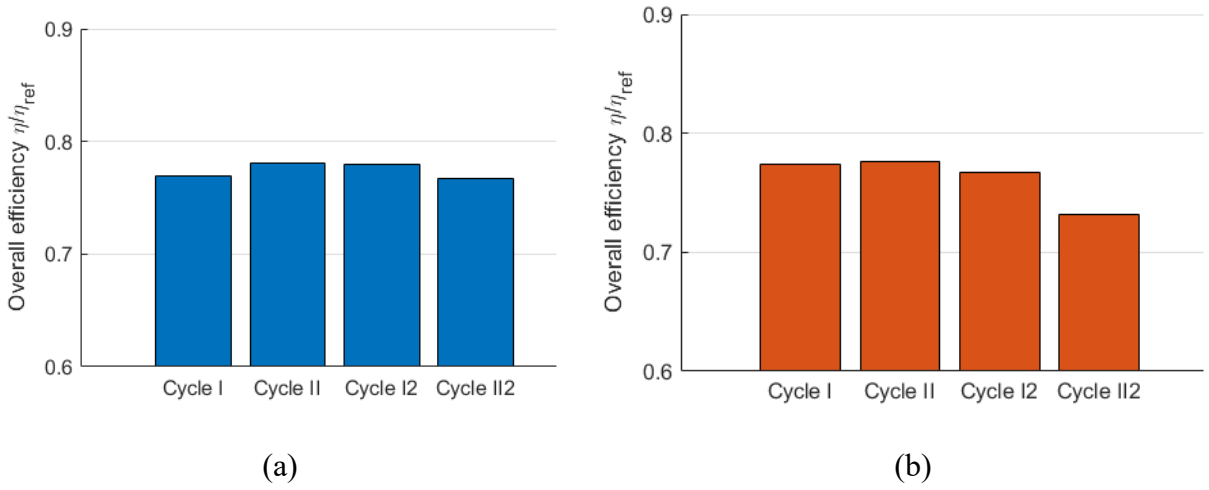

Figure 6.60. Overall efficiency for Type B. (a) Sample 1. (b) Sample 2.

The Figure 6.61 shows a lateral plate of Sample 2 after the further test: also in this case it appears heavily worn, with only the channels still clearly visible.

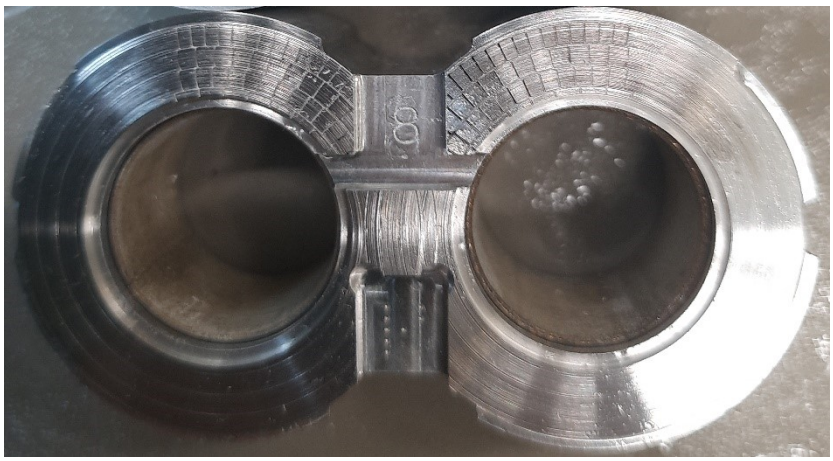

Figure 6.61. Photograph of a sample 2 lateral plate after Cycle II2

All the configurations allowed to obtain better results, in terms of efficiency, compared to the baseline pumps without texture.

It is important to notice that when seizure is reached, given the very severe test conditions, the textured surface is strongly altered by the mechanical action of the gear wheels, leaving in most cases only the recovery channels. The fact that pumps with textured lateral plates when they come to seizure have higher efficiencies than baselines means that even the grid of recovery channels alone allows for better lubrication of the coupling, which is now in boundary lubrication condition.

From the experimental tests it emerges that the best configuration is the one characterized by steps and with the deeper recovery channels, Type B, also confirming the considerations made after the numerical analysis. Future activity will be focused on this configuration, providing for further experimental tests by inserting textured lateral plates inside traditional pumps, with STD gear wheels and balanced lateral plates. The activity will be of endurance tests, lasting a few days, and it will be possible to compare the performance of pumps with texturing with those of standard pumps.

Summary and Conclusions

The main target of this research activity was the development of techniques for increasing the hydrodynamic bearing capacity in the meatus within external gear pumps.

The creation of textured surfaces on the lateral plates has been investigated in order to generate an additional bearing capacity within the meatus between gear wheels and lateral plates. The fluid meatus analysis was carried out by means of CFD analysis. Numerical simulations made it possible to evaluate the effect that the creation of a textured surface on the lateral plates has in increasing the hydrodynamic load capacity of the lubricated coupling.

The simulations were performed changing the geometric characteristics and the arrangement on the lateral plate of the textured surface and allowed to identify the best solutions on which to concentrate a wide experimental activity in order to validate the simulation results.

Laser technology was chosen to produce the samples, because it is very versatile and at the same time guarantees excellent repeatability of processing. The samples were subsequently measured with an optical profilometer to verify the geometric characteristics obtained.

The experimental activity was long and complex, especially for the identification of a working cycle that allow to reach critical operating conditions in a short time, which also required the modification of some components.

The experimental tests, entirely carried out at the Department of Engineering and Architecture of the University of Parma, have provided encouraging results, showing in general an increase in the performance of a pump with textured components inside compared to a traditional one.

In conclusion, this Thesis provides a contribution to the study of applications of engineered surfaces in the industrial field. The results obtained are promising and create the basis for future developments. Research in the field of hydraulic machines is complex and constantly evolving with the introduction of more and more sophisticated electrical and hydraulic solutions that require the development of ever more efficient and performing components for the future.

Acknowledgments

The author would like to thank the company Casappa® S.p.A. for the support provided throughout the activity of this Thesis.

The author would like to thank Prof. Paolo Casoli for the opportunity to get involved in a Ph.D. Course on such an interesting topic.

The author would like to thank the company SISMA S.p.A. for support during sample making using laser technology.